

**Effects of Aging on Microstructure and Mechanical Properties of
Lead Free Solder Materials**

by

Sudan Ahmed

A dissertation submitted to the Graduate Faculty of
Auburn University
in partial fulfillment of the
requirements for the Degree of
Doctor of Philosophy

Auburn, Alabama
December 15, 2018

Keywords: lead-free solder, aging, constitutive models, mechanical properties,
microstructure, and nanoindentation

Copyright 2018 by Sudan Ahmed

Approved by

Jeffrey C. Suhling, Chair, Quina Distinguished Professor of Mechanical Engineering
Hareesh V. Tippur, McWane Professor of Mechanical Engineering
James S. Davidson, Gottlieb Endowed Professor of Civil Engineering
Michael J. Bozack, Professor of Physics

Abstract

Lead free solder materials are widely used in the electronic packaging industry due to environmental concerns. However, experimental testing and microstructural characterization have revealed that Sn-Ag-Cu (SAC) lead free solders exhibit evolving properties that change significantly with environmental exposures such as isothermal aging and thermal cycling. This dissertation addresses those changes in the microstructure and properties of lead free solders by conducting four different projects.

In the first project, three new SAC_Bi lead free solder materials recommended for high reliability applications have been chemically analyzed and then mechanically tested in order to determine the nine Anand parameters. The alloys are referred to as Ecolloy (SAC_R), CYCLOMAX (SAC_Q), and Innolot by their vendors. For each alloy, three different microstructures were explored using different cooling profiles as well as subsequent isothermal aging. The nine Anand parameters were determined for each unique solder alloy from a set of uniaxial tensile tests performed at several strain rates and temperatures. Testing conditions included strain rates of 0.001, 0.0001, and 0.00001 (sec⁻¹), and temperatures of 25, 50, 75, 100, and 125 °C. The mechanical properties and the values of Anand parameters for these new SAC-Bi alloys were compared with those for standard SAC105, SAC305, and SAC405 lead free alloys.

In the second project, nanoindentation methods were utilized to explore the creep behavior, and aging effects of SAC305 solder joints at several elevated testing temperatures from 25 to 125 °C. A special high temperature stage and test protocol was used within the nanoindentation system

to carefully control the testing temperature, and make the measurements insensitive to thermal drift problems. Solder joints were extracted from 14 x 14 mm PBGA assemblies (0.8 mm ball pitch, 0.46 mm ball diameter). For all the experiments, only single grain solder joints were used to avoid introducing any unintentional variation from changes in the crystal orientation across the joint cross-section. After extraction, the single grain solder joints were subjected to various aging conditions. Nanoindentation testing was then performed on the aged specimens at five different testing temperatures ($T = 25, 50, 75, 100, \text{ and } 125 \text{ }^\circ\text{C}$). In order to understand creep response of the solder joints at different temperatures, a constant force at max indentation was applied for 900 sec while the creep displacements were monitored. With this approach, creep strain rate was measured as a function of both temperature and prior aging conditions. Nanoindentation pile-up effects, although insignificant at room temperature, were observed during high-temperature testing and corrections were made to limit their influence on the test results.

The changes in solder mechanical behavior that occur during isothermal aging are a result of the evolution of the SAC solder microstructure. In the third part of this dissertation, new procedures were developed to capture solder microstructure while the sample is being heated inside an oven (in-situ aging study). The heating stage and scanning probe microscopy (SPM) facility within a nanoindentation system were utilized to achieve the goal. The sample was kept within the nanoindentation system and exposed to a high temperature aging using the heating stage present in the instrument. In particular, aging was performed at $T = 125 \text{ }^\circ\text{C}$ for up to 26 hours, and the topography of the microstructure of a fixed region (10×10 microns) was continuously scanned using the SPM system and recorded after one hour time intervals. Image analysis software was

utilized to quantify microstructural changes (total area, number and average diameter of IMC particles, interparticle spacing etc.) with respect to aging time.

In the last project, the board level thermal cycling reliability of Super Ball Grid Array (SBGA) packages has been investigated by simulation and experimental testing. Nanoindentation and strain gauge based CTE (coefficient of thermal expansion) measurement methods were utilized to extract mechanical and thermal properties of different layers of a 31 mm SBGA package such as substrates, mold, die, solder mask, Cu-pad, solder, adhesive material etc. Extensive microscopic study was performed to understand the construction of SBGA package, FR-4 and Megtron6 PCB laminates. Finite element modeling was used to predict the reliability of SBGA assemblies for different PCB laminate materials. The FEA results have been validated through correlation with thermal cycling accelerated life testing experimental data.

Acknowledgments

I would like to express my sincere gratitude to my major professor Dr. Jeffrey C. Suhling for his continuous supervision and untiring support throughout my PhD study at Auburn University. I am grateful for getting the opportunity to work with a mentor like him. He is one of my role models and a source of inspiration. I am also grateful to my advisory committee members including Dr. Hareesh V. Tippur, Dr. Michael J. Bozack, and Dr. James Davidson for their insightful discussion about this research work. Special thanks are extended to my friends and co-workers Dr. Jordan Roberts, Dr. Safina Hussain, Dr. Muhannad Mustafa, Dr. Munshi Basit, Dr. Nusrat Jahan Chhanda, Dr. Md. Hasnine, Dr. Nianjun Fu, Dr. Quang Nguyen, Promod Chowdhury, Abdullah Fahim, Md Mahmudur Rahman Chowdhury, Mohammad Alam, ChienChih Chen, Jing Wu, Jun Chen, KM Rafidh Hasan, Mohd Aminul Hoque, Kamrul Hasan, and John Marcell for their friendship and support.

I am also grateful to my family members especially to my mother Most. Shamsun Nahar and my brother Shanto Ahmed for their continuous support throughout my life. Finally I would like to dedicate this dissertation to my loving and supportive wife Khalida Harun.

Table of Contents

Abstract.....	ii
Acknowledgments.....	v
CHAPTER 1	1
INTRODUCTION.....	1
1.1 Overview of Solders in Microelectronics	1
1.2 Lead Free Solders	2
1.3 Candidates for Alternative Lead Free Solders	2
1.3.1 Tin.....	3
1.3.2 Chromium (Cr).....	4
1.3.3 Nickel (Ni)	4
1.3.4 Zinc (Zn).....	5
1.3.5 Cobalt (Co).....	5
1.3.6 Bismuth (Bi).....	5
1.3.7 Antimony (Sb)	6
1.3.8 Germanium (Ge).....	6
1.3.9 Sn-Ag-Cu System	6
1.4 Mechanical Properties of Lead Free Solders	7
1.4.1 Tensile Properties (Stress-Strain Behavior).....	8
1.4.2 Creep.....	11
1.4.3 Nanoindentation	13
1.5 Objectives of This Research	17

1.6	Organization of the Dissertation	18
CHAPTER 2		20
LITERATURE REVIEW		20
2.1	Introduction.....	20
2.2	Effects of Isothermal Aging on Mechanical Properties of Solder	21
2.3	Application of Anand Model for Solder Joint	23
2.4	Reduction of Aging Effect by Dopant	24
2.5	Nanoindentation on SAC Solder Joints	28
2.6	Effects of Aging on the Microstructure of Solder	30
2.7	Summary	37
CHAPTER 3		40
EXPERIMENTAL PROCEDURE		40
3.1	Introduction.....	40
3.2	Uniaxial Test Sample Preparation	40
3.3	Uniaxial Tensile Testing System	44
3.4	Typical Testing Data and Data Processing	45
3.5	Microstructure Study	47

3.6	Sample Preparation for Nanoindentation.....	50
3.7	Nanoindentation Machine and Test Procedures	53
3.8	Measurement of Elastic Modulus and Hardness.....	55
3.9	Summary and Discussion.....	58
CHAPTER 4		59
EFFECTS OF AGING ON MECHANICAL PROPERTIES AND ANAND		
PARAMETERS OF SAC-Bi ALLOYS		59
4.1	Introduction.....	59
4.2	Anand Viscoplastic Constitutive Model	60
4.2.1	Review of Anand Model Equations (1D)	60
4.2.2	Uniaxial Stress-Strain Theoretical Response.....	63
4.2.3	Procedure for Determining the Anand Model Parameters from Uniaxial Stress Strain data	64
4.3	Chemical Composition of the SAC-Bi Alloys.....	65
4.4	Effects of Aging on SAC_R (Ecolloy)	66
4.4.1	Stress-Strain Data for Various Temperature and Strain Rates.....	67
4.4.2	The Anand Parameters for SAC_R.....	72
4.4.3	Stress-Strain Data Comparison (SAC_R and SAC105)	78
4.4.4	Microstructure Analysis.....	79
4.5	Effects of Aging on SAC_Q (CYCLOMAX).....	84

4.5.1	Stress-Strain Data for Various Temperature and Strain Rates.....	84
4.5.2	The Anand Parameters for SAC_Q.....	90
4.5.3	Stress-Strain Data Comparison (SAC_Q and SAC305).....	94
4.5.4	Microstructure Analysis.....	95
4.6	SAC-Bi Alloy Innolot.....	98
4.6.1	Stress-Strain Data for Various Temperature and Strain Rates.....	98
4.6.2	The Anand Parameters for Innolot.....	100
4.7	Comparison of the Microstructure of SAC_R, SAC_Q and Innolot	103
4.7.1	Comparison of Stress-Strain Data of SAC-Bi Alloys with Traditional SAC Alloys.....	104
4.8	Summary and Discussion.....	106
CHAPTER 5		108
CHARACTERIZATION OF SAC SOLDER JOINTS AT HIGH TEMPERATURE USING NANOINDENTATION		108
5.1	Introduction.....	108
5.2	Sample Preparation for High Temperature Nanoindentation	109
5.3	High Temperature Nanoindentation System and Test Procedures	111
5.4	Pile-up Correction for High Temperature Nanoindentation Tests.....	116
5.5	Measurement of Creep Behavior	119

5.6	High Temperature Nanoindentation Test Matrix.....	123
5.7	Effects of Test Temperature.....	124
5.8	Effects of Aging.....	128
5.9	Summary and Discussion.....	134
CHAPTER 6		135
EVALUATION OF AGING INDUCED MICROSTRUCTURAL EVOLUTION IN LEAD FREE SOLDERS USING SCANNING PROBE MICROSCOPY.....		135
6.1	Introduction.....	135
6.2	Effects of Aging on the Microstructure of SAC305 Solder.....	136
6.3	In-situ Imaging Process.....	139
6.4	SPM Image of SAC305 Solder	140
6.5	Measurement of Area and Number of IMC.....	142
6.6	Measurement of Particle Diameter	144
6.7	Changes in Microstructure During Aging.....	147
6.8	Study Using SEM	154
6.9	Discussion of IMC Evolution During Aging.....	159
6.10	Fitting Equation	162

6.11	Comparison Between SPM and SEM Results with Mechanical Properties	164
6.12	Distribution of IMC Particles.....	166
6.13	Summary	175
CHAPTER 7		177
CHARACTERIZATION OF SBGA PACKAGE FOR RELIABILITY ANALYSIS.....		177
7.1	Introduction.....	177
7.2	Nanoindentation on SBGA Package.....	177
7.3	Measurement of Thermal Property (CTE).....	185
7.4	Microstructure of FR-4 and Megtron-6 PCBs	187
7.5	FEA Model for SBGA Package.....	191
7.6	Summary and Discussion.....	197
CHAPTER 8		199
CONCLUSIONS		199
8.1	Literature Review.....	199
8.2	Experimental.....	200
8.3	Effects of Aging on Mechanical Properties and Anand Parameters of SAC-Bi Alloys..	200
8.4	Characterization of SAC Solder Joints at High Temperature Using Nanoindentation....	201

8.5	Evaluation of Aging Induced Microstructural Evolution in Lead Free Solders Using Scanning Probe Microscopy	202
8.6	Characterization of SBGA Package for Reliability Analysis	203
8.7	Summary	205
8.8	Future Work	206
	REFERENCES	208

List of Figures

Figure 1.1 Elastic Modulus and Coefficient of Thermal Expansion (CTE) of Tin as a Function of Crystal Orientation [1]	4
Figure 1.2 Market Share of Lead Free Solder.....	7
Figure 1.3 Typical Tensile Test Response of a Ductile Material	10
Figure 1.4 Typical Creep Curve.....	12
Figure 1.5 Berkovich Tip.....	14
Figure 1.6 Vickers Tip.....	15
Figure 1.7 Cube-Corner Tip.....	15
Figure 1.8 Conical Tip.....	16
Figure 1.9 Spherical Tip.....	17
Figure 3.1 Equipment used for Specimen Preparation	41
Figure 3.2 Water Quenched (WQ) Cooling Profiles	42
Figure 3.3 Heller 1800EXL Reflow Oven.....	42
Figure 3.4 Reflow (RF) Cooling Profiles	43
Figure 3.5 Solder Uniaxial Test Specimens.....	44
Figure 3.6 X-Ray Inspection of Solder Test Specimens (Good and Bad Samples)	44
Figure 3.7 Mechanical Test System with Uniaxial Sample.....	45
Figure 3.8 SAC Stress-Strain Curve and Material Properties.....	46
Figure 3.9 Empirical Model Fit to Solder Stress-Strain Curves	47

Figure 3.10 Grinding and Polishing Machine.....	48
Figure 3.11 OLYMPUS BX60 Optical Microscope.....	48
Figure 3.12 Zeiss Polarized Light Microscope.....	49
Figure 3.13 JEOL JSM-7000F Field Emission SEM.....	49
Figure 3.14 Zeiss EVO 50 SEM.....	50
Figure 3.15 iNEMI Test Board and BGA Package.....	52
Figure 3.16 IsoMet 1000 Precision Cutter.....	52
Figure 3.17 Hysitron TI950 TriboIndenter.....	53
Figure 3.18 SAC305 Solder Joint after Nanoindentation Testing.....	54
Figure 3.19 An example of the loading profile used during nanoindentation testing.....	55
Figure 3.20 An example of the load-displacement curve obtained after nanoindentation testing.....	56
Figure 4.1 Stress-Strain Curves for SAC_R (WQ).....	68
Figure 4.2 Stress-Strain Curves for SAC_R (RF).....	69
Figure 4.3 Stress-Strain Curves for SAC_R (RF+Aging).....	70
Figure 4.4 UTS of SAC_R at Different Strain Rates and Test Temperatures.....	71
Figure 4.5 Comparisons between Anand Model Predictions and Experimental Data (SAC_R, WQ).....	75
Figure 4.6 Comparisons between Anand Model Predictions and Experimental Data (SAC_R, RF).....	76

Figure 4.7 Comparisons between Anand Model Predictions and Experimental Data (SAC_R, RF+3 Months Aging).....	77
Figure 4.8 Stress-Strain Curve Comparisons for SAC_R.....	78
Figure 4.9 Stress-Strain Curve Comparisons for SAC105	79
Figure 4.10 Comparisons of Stress-Strain Curves for SAC_R and SAC105	79
Figure 4.11 Sn-Bi phase diagram.....	80
Figure 4.12 SEM Images for SAC_R Microstructure (SEI).....	82
Figure 4.13 SEM Images for SAC_R Microstructure (BSE)	83
Figure 4.14 Stress-Strain Curves Obtained for SAC_Q (WQ).....	85
Figure 4.15 Stress-Strain Curves Obtained for SAC_Q (RF, No Aging).....	86
Figure 4.16 Stress-Strain Curves Obtained for SAC_Q (RF, 3 Months Aging).....	87
Figure 4.17 UTS of SAC_Q at Different Strain Rates and Test Temperatures.....	88
Figure 4.18 Comparison between Anand Model Predictions and Experimental Data for SAC_Q (WQ).....	91
Figure 4.19 Comparison between Anand Model Predictions and Experimental Data for SAC_Q (RF, No Aging).....	92
Figure 4.20 Comparison between Anand Model Predictions and Experimental Data for SAC_Q (RF, 3 Months Aging).....	93
Figure 4.21 Stress-Strain Curves for SAC_Q with and without Prior Aging.....	94
Figure 4.22 Stress-Strain Curves for SAC305 with and without Prior Aging.....	95
Figure 4.23 Comparison of Stress-Strain Curves for SAC305 and SAC_Q.....	95

Figure 4.24 SEM Image for SAC305 Microstructure (a) Low Magnification (500X) and (b) High Magnification (2000X)	97
Figure 4.25 SEM Image for SAC_Q Microstructure (a) Low Magnification (500X) and (b) High Magnification (2000X)	97
Figure 4.26 SEM Image for Aged SAC_Q Microstructure (a) Low Magnification (500X) and (b) High Magnification (2000X)	97
Figure 4.27 Stress-Strain Curves for Innolot	99
Figure 4.28 Comparison between Anand Model Predictions and Experimental Data for Innolot (WQ)	102
Figure 4.29 Microstructure of the SAC-Bi Solder Alloys	103
Figure 4.30 Comparison of Stress-Strain Curves of New SAC-Bi Alloys with SAC105 and SAC405 (a) WQ Samples and (b) (RF Samples).....	105
Figure 4.31 Variation of Strength for Different Temperatures.....	105
Figure 5.1 Sample Preparation for High Temperature Nanoindentation	110
Figure 5.2 (a) Multi-Grain Solder Joint, (b) Single Grain Solder Joint.....	111
Figure 5.3 High Temperature Nanoindentation System	112
Figure 5.4 Solder Joint Sample in the High Temperature Stage in (a) Open and (b) Close Conditions	113
Figure 5.5 Permanent Indentation After Testing	114
Figure 5.6 Loading Profile Used for Nanoindentation Creep Tests	115
Figure 5.7 Load-Displacement Curve Obtained from a Nanoindentation Creep Test	115
Figure 5.8 3D SPM image of a single indent.....	117

Figure 5.9 2D SPM Topography data for a single indent.....	117
Figure 5.10 SPM topography data for a single indent and pile-up measurement.....	118
Figure 5.11 Nanoindentation creep displacement on SAC305.....	119
Figure 5.12 Variation of creep strain rate with holding time for SAC305 solder joint.....	120
Figure 5.13 Variation of stress with holding time for SAC305 solder joint.....	121
Figure 5.14 Creep strain rate vs. applied stress plot obtained from nanoindentation creep experiment.....	122
Figure 5.15 Creep strain rate vs. applied stress plot using Garofalo creep model.....	123
Figure 5.16 SAC305 Solder Joint after Nanoindentation Testing at Different Temperatures....	124
Figure 5.17 Nanoindentation load vs. indentation depth curves.....	125
Figure 5.18 Nanoindentation Creep Displacement vs. Time Curves.....	125
Figure 5.19 Variation of Applied Stress with Time During Constant Loading.....	126
Figure 5.20 Variation of Creep Strain Rate with Applied Stress.....	127
Figure 5.21 Creep strain vs. stress curves extrapolated to a lower stress level	127
Figure 5.22 Indents on SAC305 solder joints in no aging conditions obtained at (a) 25 °C, (b) 50 °C, (c) 75 °C, (d) 100 °C, and (e) 125 °C	129
Figure 5.23 Indents on SAC305 solder joints at different aging conditions obtained at (a) 25 °C, (b) 50 °C, (c) 75 °C, (d) 100 °C, and (e) 125 °C.....	130
Figure 5.24 Effects of Aging on Creep Response at 25 °C.....	131
Figure 5.25 Effects of Aging on Creep Response at 50 °C.....	132
Figure 5.26 Effects of Aging on Creep Response at 75 °C.....	132
Figure 5.27 Effects of Aging on Creep Response at 100 °C.....	133
Figure 5.28 Effects of Aging on Creep Response at 125 °C.....	133

Figure 6.1 Microstructure of SAC305 Solder (a) Before Aging and (b) After Aging.....	137
Figure 6.2 Location Based Variation in the Microstructure of SAC305 Solder.....	139
Figure 6.3 SPM Sample, (a) on Preform, (b) Final Polished Sample.....	140
Figure 6.4 SPM Topography Image of a Typical SAC305 Sample Showing β -Sn Dendrite, Subgrain Boundaries, and Eutectic Region (No Aging).....	141
Figure 6.5 Initial Topographies of the Studied SAC305 Samples Before Aging.....	142
Figure 6.6 Image Processing Steps for IMC Particle Area Calculations (a) After Outlining All the Particles (b) Binary Image and (c) Final Image from ImageJ.....	144
Figure 6.7 A Schematic Representation of An IMC with Several Possible Exposed Area Above The Surface Layer.....	145
Figure 6.8 Side And Top View of An Ideal Spherical IMC Particle Showing Actual And Apparent Diameters.....	145
Figure 6.9 (a-s) Example SAC305 microstructural evolution observed by SPM imaging (Aging at T = 125 °C).....	151
Figure 6.10 Changes in IMC Particle Diameter with Aging Time	153
Figure 6.11 Changes in IMC Particle Number with Aging Time.....	153
Figure 6.12 Variation in Total IMC Particle Area with Aging Time	154
Figure 6.13 Monitored Regions in The Short Term Aging Experiments with SEM (Red Boxes Indicate Regions Used for Analytical Analysis).....	156
Figure 6.14 Example SAC305 Short Term Microstructural Evolution Observed by SEM Microscopy (Aging at T = 125 °C).....	158
Figure 6.15 Example SAC305 Long Term Microstructural Evolution Observed by SEM Microscopy (Aging at T = 125 °C).....	159
Figure 6.16 Schematic of Solute Concentration in Front of A Small and a Large Particle [114].....	160

Figure 6.17 Schematic Representation of a Dislocation Passing IMCs (Orowan Looping) [115].....	161
Figure 6.18 Changes in IMC Particle Diameter with Aging Time.....	163
Figure 6.19 Variation of IMC Particle Diameter with Aging Time (SPM, Short Term Aging).....	164
Figure 6.20 Variation of IMC Particle Diameter with Aging Time (SEM, Short Term Aging).....	165
Figure 6.21 Variation of IMC Particle Diameter (Short Term and Long Term Aging Data).and Mechanical Strength with Aging Time.....	166
Figure 6.22 Distributions of IMC Particle Sizes After Various Aging Times.....	170
Figure 6.23 (a) SAC305 Microstructure and (B) Region Selected for FIB Analysis.....	170
Figure 6.24 SAC305 Microstructure (a) After Platinum Coating and (b) After FIB Analysis ..	171
Figure 6.25 FIB Images of SAC305 Solder Showing the IMC Particles Underneath the Surface	175
Figure 7.1 Cross Section of SBGA Package and a Few Examples of Indents.	179
Figure 7.2 (a) High Load Transducer and Stage, (b) Low Load Transducer and Stage.....	180
Figure 7.3 Loading Profile Used for Cu Pad, Heat Sink, Cu Ring, and Si Die	181
Figure 7.4 Loading Profile Used for Solder Joint.....	182
Figure 7.5 Loading Profile Used for Solder Mask.....	182
Figure 7.6 Loading Profile Used for Die Attach Adhesive	183
Figure 7.7 Loading Profile Used for Mold Compound.....	183
Figure 7.8 Nanoindentation Load-Displacement Curves (a) Bowing and (b) No Bowing in the Unloading Curve.....	184
Figure 7.9 Vishay Strain Gage Signal Processing Equipment.....	186

Figure 7.10 SEM Image of the Cross Section of (a) FR-4 and (b) Megtron-6 PCB	189
Figure 7.11 Images of FR-4 Laminate at Higher Magnifications.....	190
Figure 7.12 Images of Megtron-6 Laminate at Higher Magnifications.....	191
Figure 7.13 Schematic Cross Section of the SBGA Package	192
Figure 7.14 3D Finite Element Model of the SBGA Package.....	193
Figure 7.15 Accumulated plastic work (MPa) contours plot for the solder joints of FR-4 board	195
Figure 7.16 Failure analysis results showing the locations of the cracks	196

List of Tables

Table 1.1 Property Requirement for Solders	2
Table 4.1 Chemical Compositions of the Solder Alloys.....	66
Table 4.2 UTS Values of SAC_R.....	72
Table 4.3 Anand Parameters for SAC_R.....	73
Table 4.4 UTS values of SAC_Q.....	89
Table 4.5 Anand Parameters for SAC_Q.....	90
Table 4.6 UTS values of Innolot.....	100
Table 4.7 Anand Parameters for Innolot.....	101
Table 5.1 Equivalent creep strain rates at 15 MPa stress level	128
Table 6.1 IMC Particle Diameter of Different Locations After Different Aging Duration	152
Table 7.1 A Summary of the Nanoindentation Test Results	185
Table 7.2 CTE Measurement Results for the PCBs.....	187
Table 7.3 Geometry of a 35 mm SBGA package	192
Table 7.4 Material Properties of Different Layers used During Simulation.....	194
Table 7.5 Characteristic life of a 31 mm SBGA package during thermal cycling	194

CHAPTER 1

INTRODUCTION

1.1 Overview of Solders in Microelectronics

In the world of electronic materials, solder plays an important role in the interconnection and assembly of Si chip (or die). As a joining material, in electronic assemblies, solder provides electrical and mechanical connections between the semiconductor device (Si die) and the bonding pad. It also helps to dissipate the heat generated from the Si-chip [1].

Historically, tin-lead solder alloys are used as primary interconnect material in electronic packaging. The eutectic (63Sn-37Pb) tin-lead alloy was very attractive to the electronic industries due to its low melting temperature (183 °C), which allows the soldering process compatible with most of the substrate materials and devices. Aside from the fact of being inexpensive, lead (Pb) provides many technical advantages to tin-lead solders that includes 1) prevents allotropic transformation of beta tin to alpha tin at low temperature, 2) lower the surface tension of the solder and thus enhance wetting, and 3) increase corrosion resistance of the solder by formation of a oxide film which is insoluble and impervious to chemical attack etc.[1, 2].

However, lead is poisonous to human being as well as animals. According to a recent study, lead (Pb) in the child's blood could cause serious problem in neurological and physical development. Although the consumption of lead in electronic devices is minimal, we cannot ignore its harmful effect. As a result, despite of all the advantages of tin-lead solders, governments all over the world are imposing regulations against the use of lead in the electronic devices [1, 2].

1.2 Lead Free Solders

While selecting the lead free alternative, it is important to consider that the properties of the lead free solder must be comparable to the Sn-Pb solder. The performance requirements of solder alloys, for microelectronics applications, are very strict. In general, the lead free solder alloy must have a desired level of electrical and mechanical properties, melting temperature, wetting capability on most common PCB substrates etc. while at the same time must not enhance assembly cost. A brief summary of the important properties of lead free solder required for manufacturing as well as long-term reliability are presented in Table 1.1.[1, 3]

Table 0.1 Property Requirement for Solders

Properties Required for Manufacturing	Properties Required for Long-Term Reliability
Melting/liquidus temperature	Electrical conductivity
Wettability (of copper)	Thermal conductivity
Cost	Coefficient of thermal expansion
Environmental friendliness	Shear properties
Availability and number of suppliers	Tensile properties
Manufacturability using current processes	Creep resistance
Ability to be made into balls	Fatigue properties
Copper pick-up rate	Corrosion and oxidation resistance
Recyclability	Intermetallic compound formation
Ability to be made into paste	

1.3 Candidates for Alternative Lead Free Solders

About 69 different alloys were proposed as an alternative to the Sn-Pb solder. Most of these are Sn based solder where Sn is the main constituent along with one, two or even three other minor elements. These minor elements are added mainly to 1) decrease the melting temperature and 2) improve wetting and reliability of the solder [1]. The properties of Sn and the effects of different alloying elements on the Sn based solder alloys are described below:

1.3.1 Tin

The melting temperature of elemental Sn is 231 °C. One of the main reasons of choosing Sn as the principle component in the lead free solder for electronic applications is its ability to spread and wet a number of various different substrates. In the solid state, tin can have two different phases or crystal structures 1) white or β -Sn with tetragonal crystal structure and 2) gray or α -Sn with diamond cubic crystal structure. At the room temperature the thermodynamically stable phase is β -Sn. Upon cooling, when the temperature goes below 13 °C (allotropic transformation temperature), α -Sn becomes the thermodynamically stable phase. The allotropic transformation of β -Sn to α -Sn, results a significant volume change (around 27%) causing blistering of the tin surface, cracking or disintegration. This phenomenon is mainly a surface event and often referred as ‘tin pest’. The low ductility of α -Sn is another reason of causing blistering and cracking of the tin after the transformation [1, 4, 5]. Although the equilibrium temperature for β -Sn to α -Sn is 13 °C, the transformation occurs only after a significant undercooling and an extensive incubation period as long as several years. For example, no ‘tin pest’ was found on a SAC387 bulk sample after storing at -40 °C for 5 years [5]. Presence of heterogeneous nuclei, also known as seeding, can considerably accelerate the kinetics of the transformation. The possibility of $\beta \rightarrow \alpha$ transformation in a actual solder joint is even limited due to the constraints (component and substrate) on the both side of the joint [4, 5].

Addition of other elements, as an impurity, can affect the allotropic transformation. For example, the presence of Pb, Bi, Sb, Cu, Ge and Si inhibit $\beta \rightarrow \alpha$ transformation while the presence of As, Zn, Al and Mg promote the transformation [4, 5].

Sn has a body centered tetragonal crystal structure (β -Sn), at room temperature, which is anisotropic. Hence, tin shows an anisotropic thermal (e.g. CTE) and mechanical (e.g. elastic modulus) properties as shown in Figure 1.1. As a result, during thermal cycling experiment, cracking occurs along the grain boundaries [1].

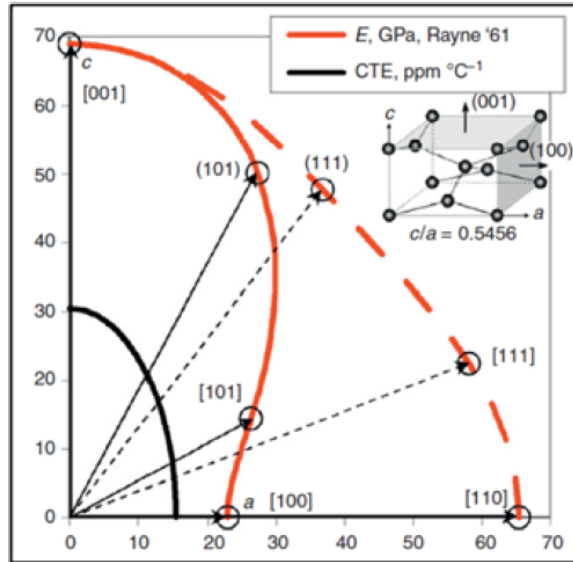


Figure 0.1 Elastic Modulus and Coefficient of Thermal Expansion (CTE) of Tin as a Function of Crystal Orientation [1]

1.3.2 Chromium (Cr)

Cr helps to improve shear ductility after long term aging. Besides, it also suppresses Kirkendall void formation in the solder joints [6].

1.3.3 Nickel (Ni)

Among all the micro-alloy additives, Ni is one of the most common elements. Addition of Ni improves the fluidity of SAC solders. Ni also improves the high strain rate properties of solder joints. For example, the drop strength of SAC alloys can be significantly improved by Ni addition. Although Ni does not have any significant influence

on the creep properties of the solder, it inhibits Cu diffusion and thus reduce the thickness of Cu_3Sn intermetallic compound (IMC). The Ni addition greater than 0.01 wt% could suppress the growth of Cu_3Sn IMC even after long term (2000 hours) aging. Since Cu_3Sn IMC is very brittle, the growth of Cu_3Sn layer is very critical for the brittle failure of the solder joints. Addition of Ni on SAC solder causes to form more stable $(\text{Cu}, \text{Ni})_6\text{Sn}_5$ IMC which act as a barrier layer and suppress the growth of Cu_3Sn layer. Therefore, by reducing the thickness of brittle Cu_3Sn layer, Ni helps to improve share strength of the solder joints. Ni also helps to improve strength by refining solder microstructure [7].

1.3.4 Zinc (Zn)

While Ni reduces only the formation Cu_3Sn , Zn doping can retard both Cu_3Sn and Cu_6Sn_5 IMC's in SAC solders. Zn also helps to improve the interface quality after multiple reflow and high temperature aging. Addition of 1.5% Zn in SAC207 solder could refine Ag_3Sn and Cu_6Sn_5 IMC's and hence increase strength by dispersion strengthening [6].

1.3.5 Cobalt (Co)

Co helps to reduce the growth of Cu_3Sn layer during high temperature aging. Addition of small amount of Co (<0.1 wt%) can improve the properties of SAC solders. Co increases the number of nucleation sites and hence significantly refine the grains of SAC305 solder. Thus it helps to improve shear strength of the solder joints [6].

1.3.6 Bismuth (Bi)

If added in small amount, Bi can improve the wetting ability and reduce melting temperature of lead free solder alloys. It also increases strength of the bulk solder and inhibit the large Ag_3Sn formation in the bulk solder. It is recommended to avoid Pb

contamination in the solder before using Bi as an additive. Because Bi can react with Pb to form a brittle IMC at the grain boundary and reduce strength significantly. If present in excess amount, Bi can cause solidification crack due to the increase in the gap between solidus and liquidus temperature [6].

1.3.7 Antimony (Sb)

Sb improves mechanical properties of lead free solders but it is toxic in nature. A small percentage (0.5 wt%) of Sb can improve drop test reliability of SAC solder joints [8]. Besides, Sb also helps to enhance strength of the solder by solid solution strengthening [7].

1.3.8 Germanium (Ge)

Ge doped solders shows low Cu dissolution from the Cu pad and hence suitable for the wave soldering process. Ge significantly improve wetting properties of the lead free solders and refine the solder microstructure. As a result, Ge addition improves the strength and ductility of the lead free solder [8].

1.3.9 Sn-Ag-Cu System

Among the various lead free solder candidates, Sn-Ag-Cu alloys have gained a significant interest in the academia as well as in the industry because of their superior mechanical properties, relatively low melting temperature, and good solderability or wetting properties [9, 10]. A graphical representation of the market share of different lead free solders is presented in Figure 1.2. It is clear from the figure that Sn-Ag-Cu alloys are dominating in the lead free solder market.

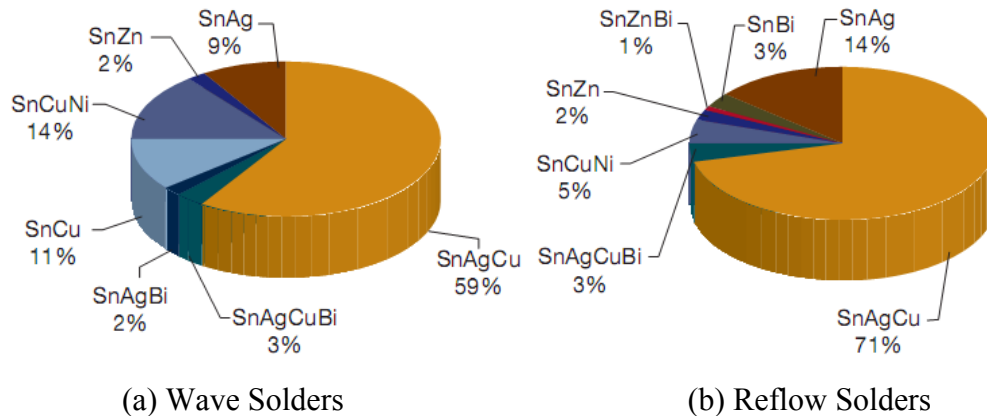


Figure 0.2 Market Share of Lead Free Solder

(https://www.ameslab.gov/files/LeadFreeSolder_Foundation.pdf)

During the initial stages of the development of lead free solder, eutectic Sn-Ag-Cu alloy (SAC387: 95.5Sn-3.8Ag-0.7Cu) was most popular. But, due to the cost of the patent by Iowa State University and the higher Ag%, SAC305 (96.5Sn-3.0Ag-0.5Cu) was seen to be advantageous over SAC387. Moreover the performance of SAC305 is similar to that of the eutectic Sn-Ag-Cu alloy. As a result, the electronic industry has chosen SAC305 to use in most of the lead-free applications [6]. Due to the increased price of Ag, the cost of SAC305 solder bar has increased about 3 times in the past 10 years [6]. Besides, the mechanical properties of the lead free alloy is not stable during the long time exposure at an elevated temperature (aging effect). It has been reported previously, that isothermal aging causes a significant reduction in the reliability of the lead free solder joints [11]. As a result, people are now looking for a low cost alternative with better reliability than SAC305.

1.4 Mechanical Properties of Lead Free Solders

In an electronic device, a number of different types of engineering materials exists in a close proximity. For example, a printed circuit board (PCB) is typically a glass fiber

reinforced polymer (composite material), a die is a semiconductor material which is often encapsulated in a plastic or a ceramic, and the tracking and the solder joints are metallic materials. Solder joints are used to create an electrical circuit by mounting chips and components on the PCB. Hence an ideal solder joint should have a good conductivity to transmit electrical signals and at the same time, adequate strength to provide mechanical support and connection. Hence, mechanical properties of solder joints are critically important to ensure reliability of the electronic products. Among all the mechanical properties, tensile, fatigue, and creep performance of the solder are critically important. Thus an accurate measurement of mechanical properties and development of constitutive equations for solder materials are required in mechanical design, process optimization and reliability assessment.

1.4.1 Tensile Properties (Stress-Strain Behavior)

Although in real life, actual solder joints are rarely under uniaxial tensile load, these properties are required for design purpose. Tensile properties help to determine the response of a material under uniaxial tension loading. Tensile tests provide us information about several material properties, such as ultimate tensile strength (UTS), yield strength (YS), effective elastic modulus (E), elongation, etc. The tensile behavior of a material is commonly described by a stress-strain curve. A tensile test experiment typically provide a load-elongation curve which is then converted into a stress-strain curve using following equations:

$$\sigma_e = \frac{F}{A_o} \quad (1.1)$$

$$\epsilon_e = \frac{\Delta L}{L_o} = \frac{L_f - L_o}{L_o} \quad (1.2)$$

Where, F is the applied load, A_0 is the initial cross-sectional area, L_0 is the initial length, L_f is the final length (after deformation), σ_e is the engineering stress, and ϵ_e is the engineering strain. Since the change in physical shape is negligible, for most of the cases, ‘engineering’ stress-strain curves are used instead of ‘true’ stress-strain curves. A typical stress-strain curve for a ductile material is presented in Figure 1.3. As shown in the figure, stress and strain shows a linear relationship at the beginning of the test. In this linear portion of the curve, stress and strain follows a particular relationship known as Hook’s Law which is described as:

$$\sigma = E\epsilon \quad (1.3)$$

Where E is the effective elastic modulus which is defined by the slope of the initial portion of the stress-strain curve. No plastic deformation occurs in the linear elastic part of the stress-strain curve. Hence theoretically, within the linear portion, if the stress is released, the material should come back to its original shape (zero deformation). However, for a viscoplastic material like solder, time dependent plastic deformation or creep occurs even with a small load (below yield stress). As a result, the value of effective elastic modulus, obtained from stress-strain curve, is typically smaller than the value of modulus measured from a dynamic measurement technique like ultrasonic or acoustic method. The rapid wave propagation, in a dynamic technique, mostly eliminates any inelastic deformation [12-14].

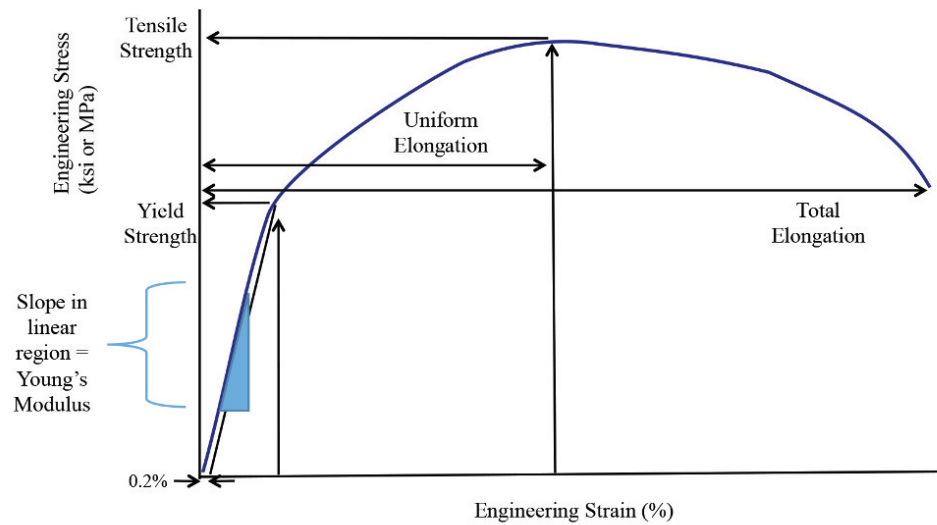


Figure 0.3 Typical Tensile Test Response of a Ductile Material

[<https://www.thefabricator.com/article/metalsmaterials/getting-to-know-more-about-the-metal-you-are-forming>]

Eventually, after a certain period of time the stress-strain curve become nonlinear. This nonlinearity is caused by the stress induced inelastic deformation or plastic flow of the material. In this stage, the atoms of the test specimen undergoes a rearrangement among themselves and moves to a new equilibrium position. In a crystalline material, like solder, this rearrangement is caused by dislocation motion. The point where the curve begins to show a nonlinear behavior or inelastic plastic flow is called yield point and the stress associated with the point is known as yield strength (YS). Since it is difficult to identify the exact stress that caused the plastic flow, YS is typically defined as the stress required to cause 0.2% plastic deformation. Yield strength of a material can be determined from the stress-strain curve by drawing a line parallel to the initial linear portion but 0.2% offset from the origin. The stress associated with the intersection of the parallel line and the stress-strain curve is the yield strength of the material. The ultimate tensile strength (UTS) or tensile strength is defined as the maximum stress obtained from a uniaxial tension

test. After UTS, the decrease in stress (as shown in Figure 1.3) is due to the localized deformation also known as necking in the test sample. If the test continues beyond the UTS, the test sample will eventually break or fail. The stress associated with it is called failure strength and strain at the failure point is known as total elongation (Figure 1.2).

1.4.2 Creep

Creep deformation refers to the time dependent plastic flow or deformation of a material that occurs when the material is exposed to a constant load, typically below yield strength, for a long period of time. Creep deformation becomes significant when the material operates at a high homologous temperature (T_h), which is defined by the ratio of operating temperature (T) and the melting temperature (T_m) of the material.

$$T_h = \frac{T}{T_m} \quad (1.4)$$

Creep deformation becomes the dominant failure mode in a metallic material if T_h is greater than $0.5T_m$. [15]. The melting temperature of lead free SAC solder is around 217 °C (490 K) causing T_h for the alloys, for room temperature (298 K) operating conditions, is $0.61T_m$. As a result, lead free SAC solder alloys display creep deformation even in room temperature operating condition. Due to the mismatches of the coefficient of thermal expansion (CTE) of silicon chip and other assembly materials used in an electronic package, solder joints are remain under mechanical stress. These mechanical stresses can cause time dependent creep deformation of solder materials. In microelectronic packaging, creep deformation is regarded as one of the major failure mechanisms of solder joints [16].

Creep test is typically conducted by applying a constant uniaxial load on the test specimen at a particular temperature. During the test, deformation of the test specimen is

recorded as a function of test time and the result of the creep test is presented as a ‘creep strain’ vs. ‘time’ plot. The extent of creep deformation significantly depends on the applied stress level and the test temperature. Figure 1.4 represents a typical creep curve which consists of three distinct regions, after the initial jump, namely, primary, secondary, and tertiary regions.

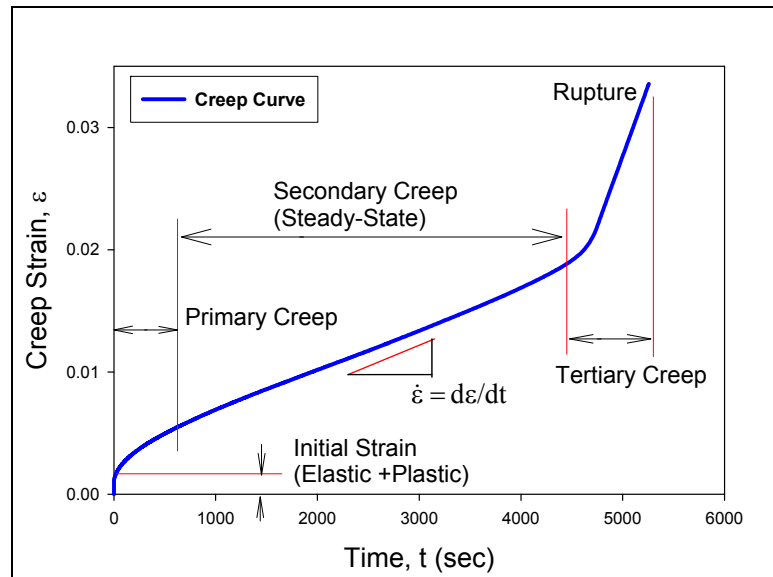


Figure 0.4 Typical Creep Curve.

Every creep test begins with an initial strain which corresponds to the instantaneous response (mostly elastic) of the material due to the applied force/load. In the primary creep stage, the material starts to deform with at a high strain rate (high slope at the beginning of the primary region) and then the strain rate decrease gradually with increasing time. This is due to the work hardening of the material which resists deformation. Eventually, with increasing test time, the creep strain rate reaches to a steady state stage which is known as steady state creep or secondary creep region. The constant creep rate, in the secondary stage, is due to the dynamic balance between strain hardening and recrystallization [17]. The strain rate in the secondary stage is very important since very often researchers use

this parameter in the finite element simulations to predict reliability of the solder joints under different test conditions. After secondary creep, the material enter into the tertiary creep region followed by an immediate rupture. Tertiary region begins when the strain rate start increasing abruptly from the constant value.

1.4.3 Nanoindentation

Indentation testing is a technique where a hard tip, with known mechanical properties, is pressed into the surface of a test sample to extract the test sample's properties. The load applied on the indenter tip caused it to penetrate into the test sample surface. When the applied load reaches to the user specified value, it can be held for a certain period of time (for creep properties) or remove instantaneously (for hardness and elastic modulus). Removal of the applied load leaves an impression or indent on the sample surface.

Nanoindentation (NI) is a kind of indentation testing where the penetration length is measured in nanometer. The development of the NI technique has been motivated by the miniaturization of the engineering materials as well as the development of the nanostructured materials. Since the area of the indenter tip is well defined (known geometry), the indent area can be easily determined from the tip penetration depth from the sample surface. Elastic modulus, hardness and creep properties of a material can be obtained from indentation load displacement data [18].

Because of having very high hardness and elastic modulus, diamond is typically used to make indenter tip. Indenter tips are available in different shape and the choice of indenter tip shape depends on the type of required information from a NI test. Five major types of indenter geometry and their applications are described below (<https://literature.cdn.keysight.com/litweb/pdf/5990-4907EN.pdf>):

Berkovich Tip: This is the most common indenter tip and used to measure mechanical properties using a NI technique. The shape of a Berkovich tip is similar to a three sided pyramid where the faces meet at a single point (Figure 1.5). The tip can maintain its self-similar geometry to a significantly small scale. The center to face angle of the tip is 65.3° .

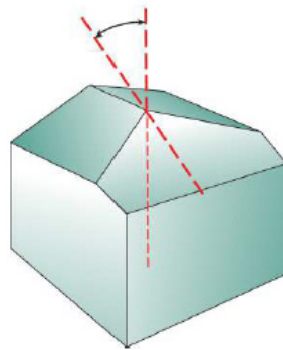


Figure 0.5 Berkovich Tip.

The tip can be manufactured easily and used for a very long time without any damage. The tip shape is ideal for most of the most indentation testing purposes. It introduces plastic deformation at a very small loads which generated meaningful data to measure hardness and elastic modulus. Some common application of a Berkovich tip are: Bulk material, Polymers ($E' > 1\text{GPa}$), Micro-electromechanical System, Thin Film, Scratch Testing, Wear Testing, In-situ Imaging etc.

Vickers Tip: The Vickers tip has the shape of a four sided pyramid with 68° center to face angle as shown in Figure 1.6. Vickers tip can be used for Bulk Material, Films and Foils, Wear Testing, Scratch Testing etc.

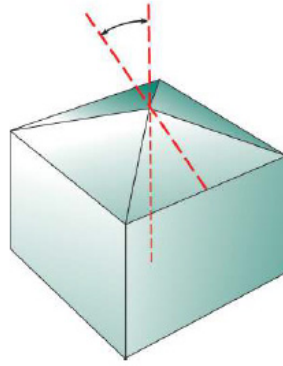


Figure 0.6 Vickers Tip.

Cube-Corner Tip: The shape of a Cube-Corner tip is similar to a three sided pyramid with all the three faces perpendicular to each other as in the corner of a cube [Figure 1.7]. The center to face angle is 34.3° which is very low compared to the other type indenter tips discussed earlier.

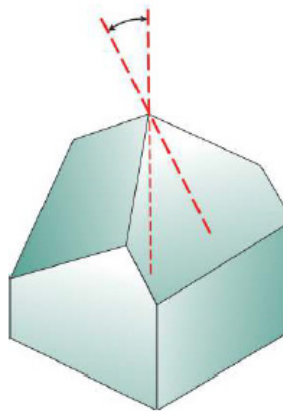


Figure 0.7 Cube-Corner Tip.

Due to the higher sharpness, the stress and strain under the indenter tip is very high which causes cracks, especially in brittle material, around the indent impression. These cracks can be used to determine fracture toughness of the material at small scale. Cube-Corner tip can be used for Thin Films, MEMS, Fracture Toughness, Scratch Testing, Wear Testing, In-situ Imaging etc.

Conical Tip: The Conical tip has the shape of a cone as shown in Figure 0.8. Because of the simplicity of its symmetric geometry and the absence of sharp edges, which cause complications due to stress concentration, Conical tips are very attractive for finite element modeling and simulations. However, Conical tips are rarely used for small scale NI experiments. The primary reason is the difficulties in manufacturing a conical diamond with a very sharp tip. Since the tip is not very sharp, a very high load is required to create a permanent indent or plastic deformation on the surface of a test specimen. Conical tips can be used in Scratch Testing, Wear Testing, In-situ Imaging etc.

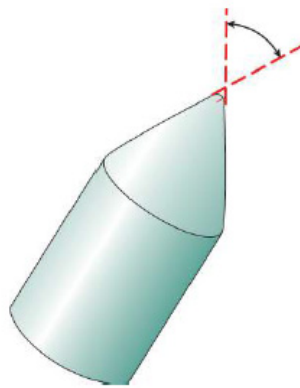


Figure 0.8 Conical Tip.

Spherical Tip: The contact stress for a spherical tip is very small causing only elastic deformation at the beginning of the indentation experiment. With increasing the amount of applied load, the tip penetrates inside the surface causing a transition from elastic to plastic deformation. As a result, spherical tip can be used to determine yielding, work hardening, and to recreate tensile stress-strain curve from indentation test. An image of a Spherical tip is shown in Figure 1.9. Spherical tips are commonly used for MEMS applications.

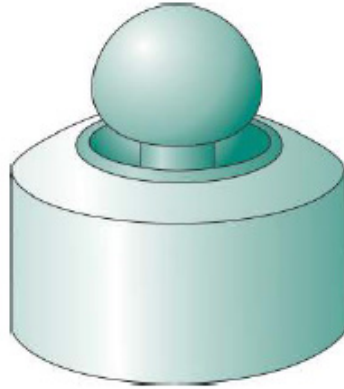


Figure 0.9 Spherical Tip.

1.5 Objectives of This Research

The motivation of this research is to systematically study the effects of aging on mechanical behavior of lead free solder alloys and to develop new constitutive equations and reliability models that include aging effects to predict solder joint reliability in microelectronic packaging. The following objectives will be achieved in this research:

- (1) Investigate the chemical composition and uniaxial tensile properties of three new doped solder ball materials SAC_R (EcolloyTM), SAC_Q (CYCLOMAXTM), and Innolot
- (2) Perform uniaxial tensile tests for lead free solders over a wide range of temperatures, strain rates, and aging conditions;
- (3) Examine mechanical properties of lead free solders of interest and explore the effects of aging on them;
- (4) Develop a novel approach to capture and quantify the changes in solder microstructure while the sample is subjected to heating inside the chamber (In-situ aging study).

- (5) Established a systematic approach to perform nanoindentation on solder joints at elevated temperatures.
- (6) Develop appropriate loading profile/test parameters to perform nanoindentation on different materials used in a BGA package.
- (7) Utilized nanoindentation technique to record elastic modulus and creep properties of solder joints, Cu pad, IMC layer, solder mask, die, heat sink, 3D printed silver traces on a glass substrate etc. at different test temperatures and aging conditions.
- (8) Compare reliability of a 31 mm SBGA package (on FR-4 and Megtron 6 PCB) and performed failure analysis.

1.6 Organization of the Dissertation

This dissertation is based on the Effects of Aging on Microstructure and Mechanical Properties of Lead-free Solder Materials and is presented in the following chapters:

Chapter 1: Introduction to lead free solders alloys and mechanical properties of solder materials.

Chapter 2: Literature review on isothermal aging effects, mechanical properties, nanoindentation on SAC solder joints, nanoindentation at elevated temperature, microstructural evolution during aging of SAC alloys, life prediction and reliability models of electronic packages, based on IMC coarsening, of lead free solder materials.

Chapter 3: Description of experimental procedure, sample preparation, uniaxial tensile and nanoindentation creep tests, data processing and quantitative analysis.

Chapter 4: Study on the mechanical properties as well as Anand viscoplastic constitutive model parameters and the effects of aging on the properties, model parameters, and the microstructure of three new Bi-doped lead free solder materials.

Chapter 5: Investigation on the effects of test temperature and aging time on the nanoindentation creep response of lead free SAC305 solder joints

Chapter 6: Study on the evolution of the microstructure of SAC305 as a function of aging time.

Chapter 7: Characterization of mechanical properties of different layers of SBGA package using nanoindentation and failure analysis study the package.

Chapter 8: Summary and conclusions of the dissertation.

CHAPTER 2

LITERATURE REVIEW

2.1 Introduction

When an electronic assembly is subjected to temperature changes, the solder joints in the assembly remain under mechanical stress due to the mismatch in the coefficient of thermal expansion (CTE) of the printed circuit board (PCB) and the component. Hence mechanical properties of the solder material are critical to ensure reliability of the package. Historically, 63/37 Sn-Pb solder is most commonly used material for solder joint. In recent days, the electronic packaging industry has widely transitioned to Pb-free solders due to environmental concerns. Among the diversity of Pb-free solders, the Sn-Ag-Cu (SAC) alloys have become the most popular and are often considered to be the standard lead-free alloys. NEMI (National Electronics Manufacturing Initiative) recommended to replace Sn-Pb solders by eutectic Sn-Ag-Cu solder in reflow processing and eutectic Sn-Cu solder in wave soldering [19]. Depending on the percentage of silver (Ag), there are several types of SAC alloys available in the market. Solder joint fatigue life under thermal cycling has been shown to increase with increasing Ag content in the SAC solders joints, due to improved mechanical properties and increased fatigue resistance [20]. However, the drop performance of electronic assemblies with SAC Pb-free solder joints is often reduced when increasing the Ag content in the SAC solder [21]. Low silver content solders are increasingly used in electronic assembly for handheld electronic products to improve the drop performance of the solder joints and to lower costs. Hence, there are trade-offs based on the silver content, and no one SAC alloy is typically suitable for all applications.

Solder joint fatigue that occurs during thermal or mechanical cycling is often the predominant failure mode exhibited by lead free electronic assemblies. Thus, engineers must have accurate constitutive equations and failure criteria for lead free solder materials for use in mechanical design and reliability assessment

The microstructure of a lead free solder, which depends on solidification profile and thermal aging after solidification, strongly controls its mechanical properties. Thermal aging causes changes in the microstructure and hence the mechanical response of lead free solders. Changes in mechanical response include reductions in the initial effective elastic modulus, yield stress, and ultimate strength, as well as increased creep rates.

2.2 Effects of Isothermal Aging on Mechanical Properties of Solder

Ma, et al. [15] have reviewed the literature on the mechanical behavior of lead free solders. Several researchers have studied the effect of Ag content on the mechanical, thermal, fatigue performance of SAC alloys. For example, Che, et al. [22] have measured stress-strain curves for various SAC alloys at different strain rates, while Zhu, et al. [23] have measured the mechanical properties of SAC305 at different strain rates and temperatures.

The mechanical properties of a lead free solder are strongly influenced by its microstructure, which is controlled by its thermal history including solidification rate and thermal aging after solidification. Due to aging phenomena, the microstructure, mechanical response, and failure behavior of lead free solder joints in electronic assemblies are constantly evolving when exposed to isothermal aging and/or thermal cycling environments. Such aging effects are greatly exacerbated at higher temperatures typical of

thermal cycling qualification tests. However, significant changes occur even with aging at room temperature [23].

Aging effects on the constitutive and failure behaviors of lead free solders have been studied extensively by several prior researchers [11, 24-36]. In early investigations, the mechanical properties and creep behavior of SAC alloys were shown to be severely degraded by prior exposure to room temperature (25 °C) and elevated temperature (50, 75, 100, and 125 °C) aging [11, 24-28]. The measured stress-strain data demonstrated large reductions in stiffness, yield stress, ultimate strength, and strain to failure (up to 50%) during the first 6 months after reflow solidification. After approximately 10-20 days of aging, the lead free solder joint material properties were observed to degrade at a slow but constant rate. In addition, even more dramatic evolution was observed in the creep response of aged solders, where up to 10,000X increases in the secondary creep rates were observed for aging up to 6 months. The aged solder materials were also found to enter the tertiary creep range (imminent failure) at much lower strain levels than virgin solders (non-aged, tested immediately after reflow solidification).

Mustafa, et al. [29] have studied the aging-induced changes occurring in the cyclic stress-strain behavior of lead free SAC solders for both tension/compression and shear loadings. Using the developed approaches, the influence of aging on the fatigue life of lead free alloys was also examined [30]. Zhang and coworkers [31-33] have shown that large reductions in the thermal cycling reliability of BGA test assemblies occurs when they are subjected to aging prior to accelerated life testing. Motalab, et al. [34, 35] have included aging effects in the Anand constitutive model and energy density based failure criterion for SAC solders, and then used these theories with finite element analyses to predict the

thermal cycling life of aged BGA assemblies. Good correlations were achieved with the measured lifetimes from references [31, 32]. Finally, Lall, et al. have studied the high strain rate behavior of SAC solders subjected to aging [20]. Other groups have also noted the strong effects of aging, and extensive listing of references can be found in [11, 24-36].

2.3 Application of Anand Model for Solder Joint

In the electronic packaging industry, it is important to be able to make accurate predictions of board level solder joint reliability during thermal cycling exposures. The Anand viscoelastic constitutive model is often used to represent the material behavior of the solder in finite element simulations. This model is defined using nine material parameters, and the reliability prediction results are often highly sensitive to the Anand parameters. The viscoplastic constitutive equations proposed by Anand [37] have become popular for rate-dependent deformation of metals at high temperatures. They were initially developed for structural metals, but have been adopted for microelectronic solders (Sn-Pb and lead free) for homologous temperatures in excess of $0.5T_m$. The so-called Anand model has been widely applied for the solder stress-strain relations in finite element simulations of electronic packages, where solders undergo small elastic deformations and large viscoplastic deformations. For example, Che, et al. [38] have considered multiple constitutive theories, and then demonstrated that the Anand equations were well matched with predictions of lead free solder fatigue life. In addition, Pei and coworkers [39] have calculated the nine parameters of the Anand model by conducting tensile testing of Sn3.5Ag and Sn3.8Ag0.7Cu lead free solders at several temperatures and strain rates.

Mysore, et al. [40] have found the Anand material parameters for SAC305 (Sn3.0Ag0.5Cu) lead free solder alloy by performing double lap shear tests. They

suggested that the Anand parameters for solder joint samples are significantly different than those measured by testing of bulk solder specimens. In addition, Motalab, et al. [41] have evaluated the Anand parameters for SAC305 solder using two approaches, including stress-strain testing and creep testing. Bai and coworkers [42] suggested a modified approach for SAC305 (Sn3.0Ag0.5Cu) lead free solder where strain rate and temperature dependent values were included for Anand model parameter h_0 . The Anand model constants for SAC105 (Sn1.0Ag0.5Cu) lead free solder have been reported by Amagai, et al. [43] and Kim, et al. [44].

2.4 Reduction of Aging Effect by Dopant

Addition of 4th element in the SAC solder is known as doped SAC alloy. Dopants (microalloy additions) play an important role to control microstructure and mechanical properties of the alloy. Dopants have been found to strongly influence the properties and behaviors of lead free solders. For example, addition of Bismuth (Bi) as a dopant has been demonstrated to have several beneficial effects. Bi helps to reduce solidification temperature, increases strength by means of precipitation hardening, and also helps to reduce IMC (Intermetallic Compound) layer thickness in lead free solder materials [45]. The Effect of Bi on the mechanical properties of a SAC (Sn3.5Ag0.9Cu) alloy was investigated by Matahir and coworkers [46]. They reported that the shear strength increased with increasing Bi addition up to 2 wt%. Beyond that point, the shear strength decreased with increasing Bi%. Improved shear strength might attribute to the role of Bi on the morphology of microstructure and distribution of dominant IMC (Ag_3Sn). Reduction of strength at higher Bi content was due to the evolution of Bi rich phase and

fragmentation of the IMC. Pandher, et al. [47] also reported that addition of 2% Bi in SAC alloys improves wetting and alloy spreading.

Zhao, et al. [48] found that addition of 0.02% Ni to SAC105 increased the formation of NiCuSn IMC and reduced the localized grain size at solder/NiAu pad interface. In addition, the effects using various doped elements (i.e. Co, Fe, In, Ni, Zn and Cu) in SAC305 BGA solder joints on Cu pads were studied by Sousa, et al. [49]. They concluded that addition of low levels of Zn had a significant beneficial effect on the interfacial IMC. Lee and coworkers [50] found that micro-alloying SAC alloys with Ni and Bi improved thermal fatigue life and drop impact resistance. Yeung, et al. [51] studied a novel lead-free solder SACQ. Based on drop test, thermal cycling, and finite element simulation, they conclude that the doped alloy has improved board level reliability when compared to SAC105. Additional literature publications on the effects of dopants have been reviewed in reference [28].

Sun et. al. [52] reviewed the effects of different alloying elements (Mn, Fe, Bi, Ni, In, Zn, Ga, Sb, Mg,) Rear Earth (RE) Elements (Ce, La, Y, Er, Pr, Nd, Yb,) and nanoparticles (Al_2O_3 , Al, TiO_2 , ZnO, ZrO_2 , CNT, Graphene, CeO_2 , TiB_2 , Ni-Coated CNT, Mo, SiC, SrTiO_3 , Co) on melting temperature, wettability, mechanical properties, microstructure, interfacial reaction and Sn whiskers.

For SAC305 solder, average width of eutectic region was found as $6.8 \pm 2.8 \mu\text{m}$ and grain size of β -Sn was $24.8 \pm 5.9 \mu\text{m}$. Indium (In), helps to refine IMC and Sn-rich phase as well as makes the microstructure more uniform. Titanium (Ti) can significantly reduce Sn grain size and width of eutectic region by heterogeneous nucleation of IMC's. Iron (Fe) forms large FeSn_2 IMC which has a weak interface with β -Sn matrix. Magnesium (Mg)

helps to coarsen eutectic region. Addition of Al in SAC105 refines β -Sn dendrites and enlarge eutectic regions. Besides, it also prevent Ag_3Sn and Cu_6Sn_5 and forms two new IMC Ag_3Al and Al_2Cu . Zn also helps to refine β -Sn dendrites significantly. Ni was found to reduce the size of Sn-rich phase and refine the microstructure. Since Antimony (Sb) has higher affinity towards Sn, presence of Sb reduces the driving force to form Cu-Sn IMC's resulting a narrow IMC layer in the solder joint. Sb also helps to refine IMC grain size.

RE elements can significantly refine the microstructure of SAC solders. Er can reduce the particle size of Ag_3Sn and Cu_6Sn_5 whereas Pr and Nd refine β -Sn dendrites and IMC particle size by forming uniformly dispersed fine RESn_3 . These fine particles act as heterogeneous nucleation sites during solidification. However, excessive amount of RE elements will cause to form bulk RESn_3 phase which has a negative effect on mechanical properties. La, Ce and Y also have a similar effect on solder microstructure.

Al and Ni nanoparticle was found to reduce IMC particle size, spacing and IMC layer thickness by forming very fine and uniformly dispersed Sn-Ni-Cu and Sn-Sg-Al IMCs. Addition of small amount of Fe nanoparticles refine the microstructure and forms FeSn_2 phase. Al_2O_3 nanoparticles increase the size of eutectic region and reduce Ag_3Sn particle size. TiO_2 and SiC nanoparticle reduces the size and spacing between Ag_3Sn particles. SrTiO_3 nanoparticle reduces the size of Ag_3Sn and Cu_6Sn_5 particles by promoting the rate of nucleation during solidification. ZnO suppresses Ag_3Sn and Cu_6Sn_5 IMC formation and reduces β -Sn grain size by 22%.

The Effect of dopants on the aging induced changes in microstructure was also studies by a number of scientists. Sadiq et. al. [53] worked with different Lanthanum (La) doped SAC305 alloys and recorded the changes in microstructure and mechanical

properties during isothermal aging at 150 °C for 6 different aging conditions (i.e. 0 , 10, 25, 50, 100 and 200 hours). They reported that La drastically reduces the IMC particle size and also significantly inhibit the growth of IMC particles during isothermal aging. Based on polarized light image they found that in as cast condition, grain size of SAC305 was ~8 mm and was significantly reduced (~1 mm) after La addition. From the graph presented in that paper, it is also clear that aging doesn't have any significant influence in average grain size.

In another study, Lee et. al. [54] studied the effect of Lanthanum (La) addition and high temperature storage on the microstructure and microhardness of Sn-3.5Ag solder joints. Their experimental results confirms that addition of La refine the solder microstructure. They explained that during solidification of the solder, LaSn_3 compounds form at the beginning and provide extra nucleation sites for Ag_3Sn IMC to grow resulting a refine microstructure. Addition of La was also found to reduce the thickness of IMC layer after soldering as well as isothermal aging. They also reported that La addition helps to improve microhardness and thermal resistance of solder joints.

Hao et. al. [55] studied the effects rare earth element Er addition on the evolution of microstructure of lead free eutectic SAC (Sn-3.8Ag-0.7Cu) solder joints during isothermal aging. Aging was conducted at 170 °C for 4 different holding periods (i.e. 0, 200, 500 and 1000 hours). The authors measured the thickness of IMC layer of Sn-3.8Ag-0.7Cu and Sn-3.8Ag-0.7Cu-0.15Er alloy after different aging duration. They found that Er addition reduces the thickness of IMC layer in as reflowed condition and also significantly reduces the growth during aging. They argued that Er combines with Sn to form ErSn_3 IMC and reduces the activity of Sn which subsequently suppress the formation of Cu_6Sn_5

IMC layer. They also observed that ErSn_3 IMCs formed during solidification of solder act as a heterogeneous nucleation site for Ag_3Sn and Cu_6Sn_5 precipitates. The increase in nucleation sites results a refinement of Ag_3Sn and Cu_6Sn_5 particles. Addition of Er also found to make the microstructure more uniform and reduce the coarsening rate of the IMCs during isothermal aging.

Witkin [56] and Delhaise et al. [57] studied the effect of aging of Bi doped SAC alloys. In both study, the authors reported an elimination or at least reduction of aging induced degradation in SAC-Bi alloys.

2.5 Nanoindentation on SAC Solder Joints

Most prior work on solder mechanical behavior and aging effects has involved tension, compression, and shear testing of miniature bulk solder specimens. Sample geometries have included traditional uniaxial tensile specimens, small cylinders in compression, lap shear specimens, and Iosipescu shear specimens. A more limited number of researchers have examined aging effects by mechanical loading of solder joints [58-61]. These studies have involved shearing of custom fabricated solder ball arrays [58-60], as well as impression creep experiments [61].

Nanoindentation techniques [18] have recently become popular for measuring mechanical properties and creep deformation behavior of extremely small material samples, and several investigators [62-75] have applied them to lead free solders. Early solder nanoindentation studies included room temperature measurements of the elastic modulus E and hardness H of β -Sn dendrites, eutectic phases, and individual Ag_3Sn and Cu_6Sn_5 intermetallic compounds [66-69]. Hasnine et.al. [62-65], have examined aging effects in SAC solder joints extracted from PBGA assemblies using nanoindentation. Their

results showed that the aging induced degradations of the room temperature mechanical properties (modulus, hardness) of single grain SAC joints were of similar magnitudes to those seen previously by testing of larger “bulk” solder specimens with hundreds of grains. However, the degradation of the creep response, while still significant (15-100X increase), was less in the solder joints relative to larger uniaxial tensile specimens (200-7500X increase). This was due to the single grain nature of the joints considered, and the lack of the grain boundary sliding creep mechanism. They also tested very small tensile specimens (10 mm long) with 10-20 grains, and the creep degradation results were similar to the single joint specimens.

Knowledge of elevated temperature behavior, especially creep behavior, is critical to understanding solder joint reliability in thermal cycling and accelerated life testing. Elevated temperature nanoindentation measurements of modulus and hardness of bulk SAC305 and SAC357 solder samples were performed by Gao, et al. [70], and Han and coworkers [71]. In addition, the latter authors also examined the sensitivity of the creep response of lead free solder to temperature. Sadiq, et al. [72] have investigated the nanoindentation elastic modulus and hardness of β -Sn and eutectic phases within a SAC305 solder joint at temperatures ranging from 45-85 °C. Another solder nanoindentation study over a larger temperature range (25-150 °C) was performed by Lotfian, et al. [73], where they reported the mechanical properties of the constituent phases of SAC397 solder joints. Marques, et al. [74, 75] used nanoindentation to study mechanical properties and creep behavior of SAC305 solder joints over a wide temperature range (25-175 °C). Based on finite element simulations, they also developed a method to correlate nanoindentation creep results with uniaxial creep data.

Nanoindentation pile-up, defined by an uplift of material near the edges of an indent, is often observed in testing of solders [67-69, 72, 73]. Pile-up depends significantly on the work hardening ability of the material [76]. For a material that easily work hardens, the top surface near the indent will be hardened during the deformation and thus will prevent pile up by resisting upward flow of the material. Prior researchers have used different techniques to include the pile-up area in their measurement. Kese, et al. [77] proposed a semi ellipse method for pile up correction, which was based on the assumption that the pile-up contact area had a semi-elliptical shape. While some researchers [69, 72, 78] have used the Kese, et al. method, others [68] have used FEA simulations to guide pile-up corrections.

2.6 Effects of Aging on the Microstructure of Solder

Due to their low melting temperatures, solders are exposed to high homologous temperatures in most product applications. Thus, there is a continuous state of active diffusion processes in the solder alloys, and their microstructures are inherently unstable and will continually evolve during normal operating temperature conditions of electronic packaging assemblies. High temperature storage, which is also known as isothermal aging, of the solder alloys causes a significant change in the microstructure leading to a degradation of mechanical properties. Chou [79] studied the effect of isothermal aging on microstructure of Sn-Pb and lead free SAC solder joints. He reported a significant phase coalescence of eutectic Sn-Pb solder joint after aging.

Xu et. al. [80] measured the thickness of IMC layer of different Sn-Pb alloys with different surface finishes after isothermal and thermal cycling aging. Based on their

experimental results they had proposed an integrated model to predict the IMC layer growth under different isothermal aging and thermal cycling environment.

Ubachs et. al. [81] developed a model to predict microstructural evolution during isothermal aging of Sn-Pb alloy by numerical simulation. They focused their study on a fixed region and compared experimental observation of phase growth during isothermal aging at 150 °C, for 0 to 15 hours, with the predicted phase growth by simulation.

In recent days, electronic industries are moving towards lead free solders due to the growing concern about environment. Effect of aging in lead free solder is even more significant. Sahaym et. al. [82] examined the evolution of microstructure of bulk SAC105 and SAC305 solder during isothermal aging at 150 °C. They observed the changes of identical region after 4 different aging durations (0 hr., 110 hr., 194 hr., and 310 hr.). In as reflowed condition, they found that the microstructure is consisted of several pro-eutectic colonies of β -Sn grains surrounded by eutectic regions. Most of the grains in a pro-eutectic colony has low angle ($<15^\circ$) boundaries with the neighboring grains. They reported that after 310 hours of aging, the average size of IMC precipitates has increased from 0.35 μm to 2.5 μm and the average grain size has increase from 4.5 μm to 7.5 μm .

The authors also observed that a small percentage ($\sim 10\%$) of β -Sn grains, especially those near the eutectic region, has went through recrystallization during isothermal aging. They claimed the stress on the β -Sn grains, due to the growth of IMC particle, is responsible for the recrystallization. The extent of recrystallization was less in SAC105 than in SAC305 due to the relative difference in IMC volume fraction. Although not mentioned clearly in the text, it is evident from their graph that the number of high angle grain

boundary has been reduced and low angle grain boundary has been increased after aging for 100 hours.

Maleki et. al. [83] studied the evolution of microstructure of SAC405 and pure Sn during isothermal aging at 150 °C after 144 hours and 296 hours. They also performed Mechanical testing (shear test) to correlate changes in microstructure and mechanical properties. Sample size was approximately $1 \times 0.3 \times 0.3$ mm and it was attached to Cu-pad. They reported that in as-reflowed condition, the microstructure of SAC405 was consisted of ~70 vol% of eutectic phase and ~30 vol% of β -Sn dendrite, whereas the mean diameter of IMC particles and interparticle distance was ~250nm and ~630 nm, respectively. Average particle size increases with aging time due to Ostwald ripening. During IMC growth, they attributed bulk diffusion to be the main rate controlling mechanism. On the other hand, aspect ratio decreases and interparticle spacing increases with aging due to the driving force to reduce surface energy. Electron backscatter diffraction (EBSD) analysis confirmed the presence of large grains (~200 μ m) in SAC405 solder before aging. After 296 hours of aging at 150 °C they didn't find any significant change in grain size and orientation. On the other hand, pure tin has a fine grain (~10 μ m) microstructure before aging which grows significantly during aging and become ~200 μ m after aging. They attributed the reduction of mechanical properties during aging for SAC 405 to the IMC's coarsening whereas for pure Sn to the grain coarsening.

Telang et. al. [84] worked on the effects of aging at 150 °C on microstructure, especially grain size and grain-boundary misorientation, of several alloys including Pure Sn (ingot and reflowed), Eutectic Sn-3.5Ag (ingot), Eutectic Sn-3.8Ag-0.7Cu (ingot), Sn-1.6Ag (solder ball), Sn-3.0Ag (solder ball), and Sn-3.0Ag-0.6Cu (solder ball). For Sn-

3.5Ag alloy they studied three different aging conditions (i.e. 0, 200, and 400 hours.) whereas for rest of the alloys they studied two different aging conditions (i.e. 0. and 200 hours). Before aging, grain size of pure Sn ingot and Reflowed Pure Sn was 50-150 μm (equiaxed) and 100-250 μm (equiaxed), respectively. After aging for 200 hours, the grain size of pure Sn for both condition was $>500 \mu\text{m}$ with irregular shape. They found ledges, in SEM image, along the grain boundary (confirmed by polarized light microscopy) of sample after aging. According to the authors, these ledges were formed due to anisotropic nature of thermal expansion coefficient (CTE) of Sn grain. After aging, when the sample was taken out from the oven, different grains contracted with different magnitudes leading to the ledges. They also argued that the extent of contraction depends on the size and the orientation of the grain. Before aging, the sample had smaller grain size. As a result, when the sample was kept inside the oven, difference in expansion of different grains was relatively small. This resulted small ledges along the grains of as reflowed sample. Although the grain boundaries moved during the aging process, these ledges were retained throughout the experiment.

After comparing the microstructure of eutectic Sn-Ag (3.5% Ag) ingot with pure Sn ingot, they found that Sn-Ag alloy has a much finer (10-30 μm) grain size, which was very stable. Aging of Ag-Sn alloy did not cause any significant grain growth due to the pinning effect of Ag_3Sn IMC particles. On the other hand, the grain size of SAC (Sn-3.8Ag-0.7Cu) ingot was similar to that of Sn-Ag ingot (10-30 μm). But, aging for 200 hours caused a significant growth in the grain size ($\sim 120 \mu\text{m}$) of the alloy. Although not stated clearly in the text, it is evident from the misorientation histogram that the extent of misorientation, among the grains, for the both alloys decrease with increasing aging time.

From their experimental observations the authors also have discussed the effect of Ag and Cu on preferred grain orientation and grain size.

Allen et. al. [85] studied two near eutectic lead free SAC solders (bulk Sn-3.5Ag-0.9Cu and SAC405 joint). They used 3 different aging temperatures (152, 177, and 201 °C) and 5 different aging durations (0, 1, 2, 4, and 8 weeks). They measured the density of IMC particle after different aging conditions and based on their experimental results they conclude that the rate controlling mechanism for coarsening is volume diffusion ($n=3$). They also reported that the coarsening kinetics of eutectic SAC solder is slower than that of eutectic Sn-Pb solders.

Kumar et. al. [86] worked with SAC105 and SAC305 alloys. For isothermal aging experiments, they polished a bulk reflowed solder samples and then aged the samples at 150 °C in high vacuum (to prevent oxidation). After different aging intervals (i.e. 0, 110, 194, 220, and 330 hours) they captured the SEM image of the same region, of any particular sample, to quantify the coarsening behavior of the IMC's. They found that the growth rate of Cu_6Sn_5 particles are much faster than Ag_3Sn particles, due to the higher diffusivity of Cu than Ag in Sn matrix. Besides, the fraction of Ag_3Sn particles was significantly higher than Cu_6Sn_5 particles. Hence, they decided to focus their study on the coarsening of Ag_3Sn particles only. The authors introduced a new parameter named as explicit parameter ' $C_{\text{Ag}}D_{\text{Ag}}t/T$ ', where C_{Ag} and D_{Ag} are solubility and diffusivity of Ag in Sn matrix, respectively, to capture the thermomechanical history of a lead free solder during isothermal aging. Utilizing this parameter, they predicted coarsening rate of Ag_3Sn particles, during isothermal aging, and then compared with the experimental observations. They conclude that the model could efficiently measure thermomechanical history during

isothermal aging and thermomechanical cycling (TMC) below 200 cycles. After 200 cycles the IMC particles undergo dissolution and re-precipitation/redistribution which can't be captured properly by this model. In addition to coarsening, during isothermal aging, they also had observed recrystallization near the eutectic region. They explained that the growth of IMC particles might play an important role in recrystallization.

Besides bulk solder samples, researchers have also explored the effect of aging on the actual solder joints. Chauhan et. al. [87] monitored the effect of isothermal aging at 100 °C on phase coarsening and evolution of SAC305 solder joint. They used image processing software to quantify size, interparticle spacing and volume fraction of Ag_3Sn and Cu_6Sn_5 IMC's. Impact of these changes on secondary creep response was modeled using multiscale creep model. The authors performed their experiments in 4 different aging conditions (0, 24, 600, and 1000 hours.) and presented average results of 3 samples (solder joint) for each aging condition. They found that the size of Ag_3Sn increases monotonically with increasing aging time whereas the size of Cu_6Sn_5 decreased after 600 hours of aging. They didn't find any significant change in Sn grain morphology after 1000 hours (41 days) of aging.

Yang et. al. [88] prepared solder joints using 2 different soldering methods (laser and infrared soldering) and captured the evolution of microstructure during aging up to 190 °C for times up to 300 days. They reported that the evolution is consisted of the growth of IMC's and the Cu-Sn layer near the interface. Although they had studied two different initial microstructure, obtained from 2 different soldering methods, aging at 190 °C caused the final microstructures to be the same.

Chiu et. al. [89] examined the effect of aging time and temperature on the board level reliability during the drop test of lead free SAC solder joints. They reported that Kirkendall void formation, at the interface of Cu pad and Cu₃Sn IMC, is the main reason for getting lower drop reliability during drop test.

Fix et. al. [90] explored the effect of aging time (0 to 1000 hours) and temperatures (125 to 175 °C) on the microstructure of SAC405 solder joint. They have confirmed a significant growth of Ag₃Sn and Cu₆Sn₅ IMCs with aging time. The authors modeled phase growth based on Ostwald ripening mechanism. They conclude that a growth exponent $n = 3$, which indicated volume diffusion as the growth rate controlling mechanism, matches very well with the experimental growth rate data.

The effect of aging at 150 °C on the evolution of eutectic Sn-Ag solder joint for up to 800 hours was studied by Ahat et. al. [91]. From experimental results, they conclude that the thickness of IMC layer increases linearly with square root of aging time. Choi et. al. [92] investigated the effect of different soldering and aging time on the interface layer of Sn-3.5Ag solder and Cu substrate. They used the same solder joint to age at 130 °C for different time duration up to 800 hours. They found that thickness of IMC layer continues to grow with increasing aging duration. However, the growth behavior of IMC layer during aging strongly depends on the initial morphology and hence on the soldering time.

Akhtar et. al. [93] studied the evolution of microstructure near the interface of a solder joint during isothermal aging at 150 °C, for four different aging durations (0, 250, 500, and 1000 hours). They used SAC305 solder joint (ball diameter 500 μm) with two different surface finishes (Immersion Gold (ImAu) and Immersion Tin (Sn)). Image analysis software ImageJ was used to measure the thickness of the IMC layer. They also calculated

the activation energy based on the measured thickness data. They found that the thickness of the IMC layer increases with increasing aging time. Besides, the morphology of the IMC layer, for both surface finishes, change from scallop type to layer type after the aging treatment. Based on their calculations they found that the activation energy of SAC305/ImSn system was less than SAC305/ImAu system resulting a higher IMC layer growth rate in SAC305/ImSn system.

A comparative study was performed by Berthou et. al. [94] where the authors compared the failure mechanism of BGA packages with SAC305 solder joints subjected to two different conditions: (a) accelerated thermal cycling (ATC) between -55 to 125 °C and (b) thermal storage at 80, 125, and 150 °C for 1000 hours. During ATC, they found recrystallization of big Sn grains to small grains in the regions of high stress accumulation. Cracks initiates and grows at interface of the new recrystallized grains. On the other hand, thermal storage for 1000 hours caused a significant growth of IMC layer near the interface as well as the IMCs in the bulk. They didn't reported any recrystallization after thermal storage.

2.7 Summary

In this chapter, the existing literature on the effects of aging on the mechanical properties and the microstructure of lead free solder was extensively discussed. The mechanical properties of a solder are strongly influenced by its microstructure, which is controlled by its thermal history including its solidification rate and thermal exposures after solidification. Aging of lead free solders leads to degradations in their constitutive and failure behaviors. For example, research in the literature has shown that aging leads to large reductions in solder material properties including shear strength, elastic modulus,

nanoindentation joint modulus and hardness, high strain rate mechanical behavior, creep response, and Anand model parameters. Other studies have shown that aging causes severe degradations in uniaxial cyclic stress-strain curves and fatigue life, shear cyclic stress-strain curves and fatigue life, fracture behavior, drop reliability, and thermal cycling reliability.

Dopants have been found to strongly influence the properties and behaviors of lead free solders. For Example, Bi helps to reduce solidification temperature, increases strength by means of precipitation hardening, helps to reduce IMC (Intermetallic Compound) layer thickness, and also reduce aging induced degradation of mechanical properties in lead free solder materials. Ni helps to improve thermal fatigue life and drop test performance by refining Sn grain size and reducing the IMC layer formation near the Cu pad. The effects of rear earth (RE) elements and nanoparticle addition on the properties of lead free solder was also discussed in this chapter.

Nanoindentation methods have shown great potential for characterizing solder materials and aging effects at the joint scale. Nanoindentation is mainly used to extract elastic modulus and hardness of solder joints. Some of the prior works have also used nanoindentation technique to characterize the creep properties although most of the nanoindentation experiments, on solder joints, were conducted at room temperature.

The changes in solder mechanical behavior are a result of the evolution of the SAC solder microstructure that occurs during aging. The most well-known and widely observed changes are coarsening of the Ag_3Sn and Cu_6Sn_5 intermetallic compounds (IMCs) present in the eutectic regions between beta-Sn dendrites. Several researchers have proposed

empirical models to describe the growth of these secondary phase particles as a function of aging temperature and aging time, and related this growth to mechanical property changes.

CHAPTER 3

EXPERIMENTAL PROCEDURE

3.1 Introduction

The specimen preparation and testing techniques are presented in this chapter. Micro-scale uniaxial tensile specimens were prepared in a rectangular shaped hollow glass tube using a vacuum suction method. The test specimens were then cooled either by a water quenched profile or an industry standard reflow profile. Typical dimension of the uniaxial tensile specimens were 80 (length) \times 3 (width) \times 0.5 (height) mm. Uniaxial tensile tests were performed using a micro tension torsion testing system.

Solder joints were typically extracted from 14 x 14 mm PBGA assemblies (0.8 mm ball pitch, 0.46 mm ball diameter) that are part of the iNEMI Characterization of Pb-Free Alloy Alternatives Project. After extraction, a typical sample mounting and polishing procedure was followed to make the solder joints suitable for nanoindentation tests. Since the properties of SAC solder joints are highly dependent on crystal orientation, polarized light microscopy techniques was utilized to determine the orientation of the tested joints. For all the experiments, only single grain solder joints were used to avoid introducing any unintentional variation from changes in the crystal orientation across the joint cross-section.

3.2 Uniaxial Test Sample Preparation

Initially, bulk solder material is melted in a quartz crucible using circular heating elements (see Figure 3.1). The heater in the melting process is excited using a digital controller, which uses feedback from a thermocouple attached on the crucible. The solder

is drawn into the glass tube by inserting one end into the molten solder in the crucible, and then applying suction to the other end using a rubber tube connected to a vacuum source. The amount of solder drawn into the tube is controlled using a regulator on the vacuum line. After the desired amount of solder fills the tube, it is solidified by quenching in a room temperature water bath.

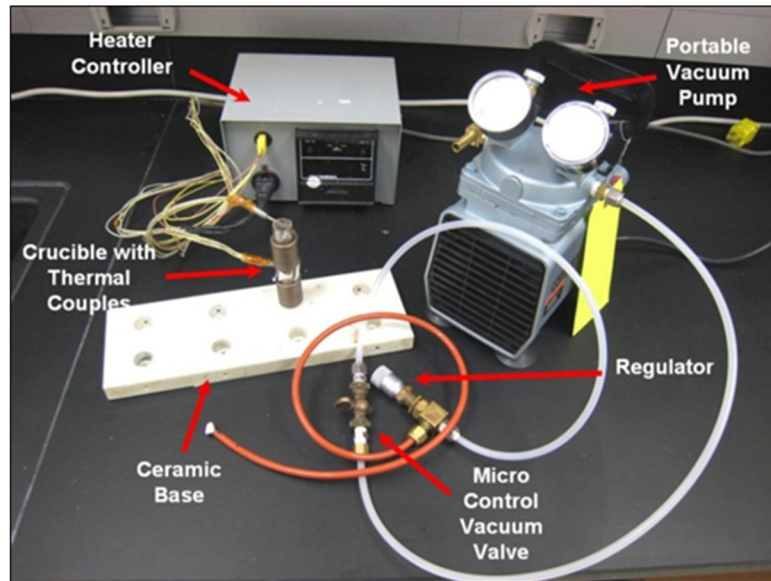


Figure 3.1 Equipment used for Specimen Preparation

Tensile specimens were prepared using two different solidification profiles.

- 1) Water quenched (WQ) solidification profile, leading to fine microstructures and the upper limits of the mechanical properties for each alloy.
- 2) Reflowed (RF) solidification profile, leading to a coarse microstructure very similar to an actual solder joints. The solder test specimens were passed through a controlled heating and cooling chamber using a SMT (surface mount technology) reflow oven.

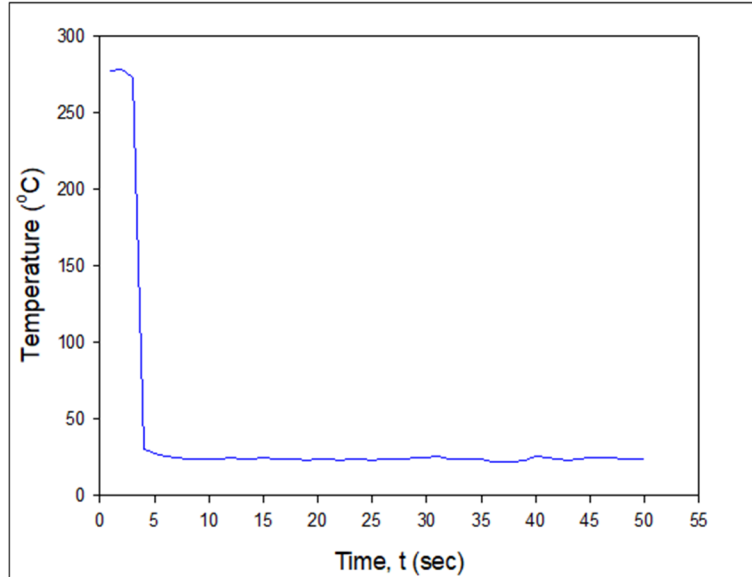


Figure 3.2 Water Quenched (WQ) Cooling Profiles

The temperature vs. time variations for the WQ profile is shown in Figure 3.2. For the samples with reflowed profile, test specimens were initially prepared using WQ profile and then the samples within the glass tubes were sent through a 9 zone Heller 1800EXL reflow oven (Figure 3.3).



Figure 3.3 Heller 1800EXL Reflow Oven

Inside the oven, solder samples were re-melted and experienced to a pre-set temperature profile which is very similar to that used for the actual solder joints. The reflow temperature profile used in this study is presented in Figure 3.4.

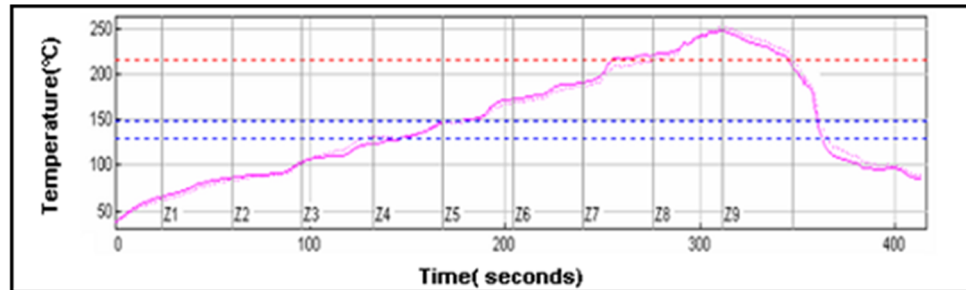


Figure 3.4 Reflow (RF) Cooling Profiles

A typical glass tubes filled with solder and final solder samples after extraction from the glass tubes are shown in Figure 3.5. Glass has lower coefficient of thermal expansion (CTE) compared to solder. As a result, for some solder alloy and cooling rate combinations, solidified solder samples were easily pulled out from the glass tube due to the difference is the CTE of glass and solder. Another way followed to extract the solder sample from the glass tube is by carefully breaking the glass. The tubes in this work had a length of 120 mm, and a cross-sectional area of 3.0 x 0.5 mm. A thickness of 0.5 mm was chosen since it matches the height of typical BGA solder joints. The nominal dimensions of the final test samples were 80 x 3 x 0.5 mm. The specimens were stored in a low temperature freezer after the water quenched/reflow process to minimize any aging effects. The solder microstructure has been verified to be consistent throughout a specimen volume, and from specimen to specimen by cross-sectioning. A micro-focus x-ray system was used to inspect the samples for the presence of flaws (e.g. notches and external indentations) and/or internal voids (non-visible). Specimens with no flaws and voids were

generated using proper experimental techniques, and Figure 3.6 illustrates x-rays scans for good and poor specimens.

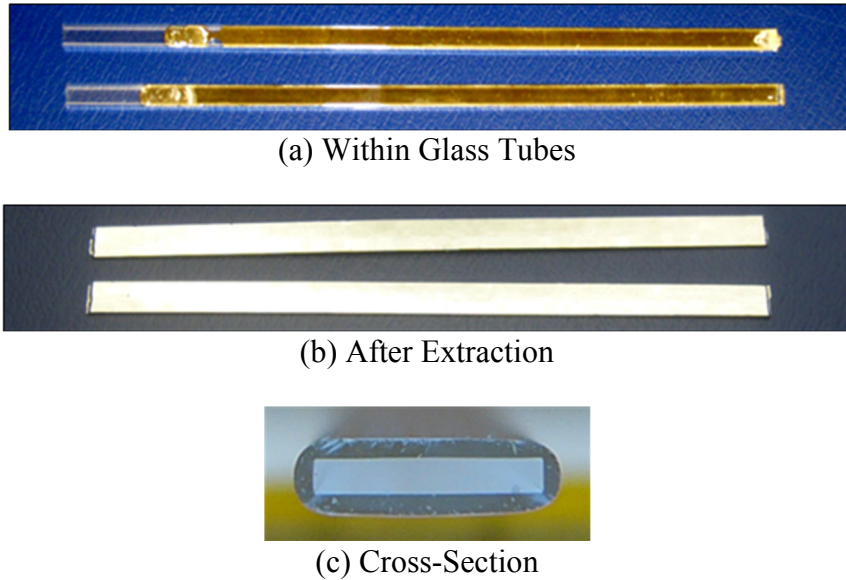


Figure 3.5 Solder Uniaxial Test Specimens

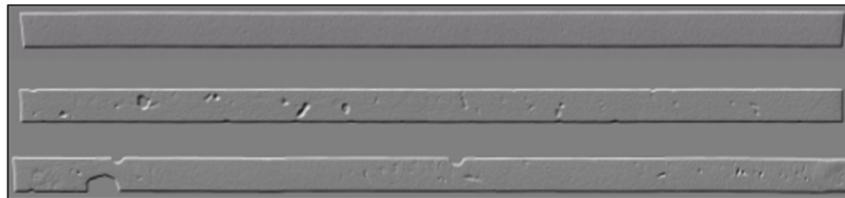


Figure 3.6 X-Ray Inspection of Solder Test Specimens (Good and Bad Samples)

3.3 Uniaxial Tensile Testing System

The tension/torsion thermo-mechanical test system (Wisdom Technology MT-200) used to perform the stress-strain tests in this study is presented in Figure 3.7. This instrument is optimized for loading small specimens such as thin films, solder joints, gold wire, fibers, etc. It provides an axial displacement resolution of 0.1 micron. Samples can be tested over a temperature range of -185 to +300 C using supplemental environmental chambers added to the system.

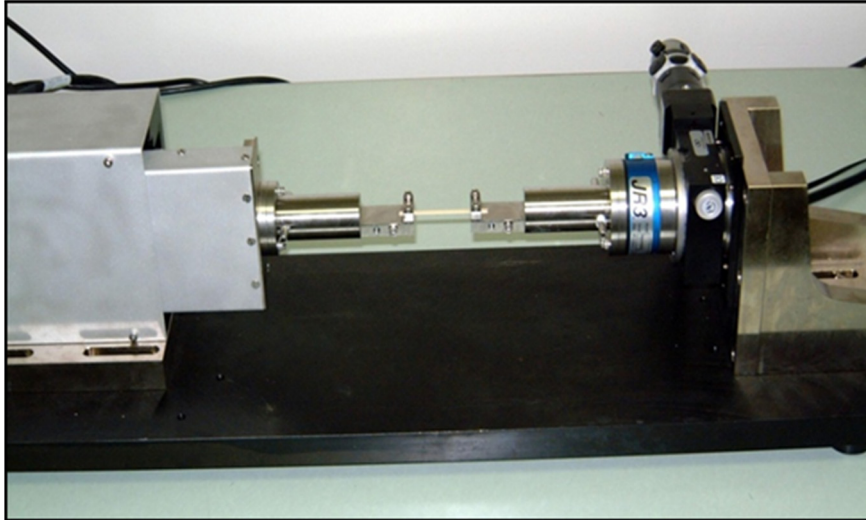


Figure 3.7 Mechanical Test System with Uniaxial Sample

Forces and displacements were measured in the uniaxial tests, and the axial stress and axial strain were calculated using

$$\sigma = \frac{F}{A} \quad \varepsilon = \frac{\Delta L}{L} = \frac{\delta}{L} \quad (3.1)$$

where F is the measured uniaxial force, δ is the measured crosshead displacement, σ is the uniaxial stress, ε is the uniaxial strain, A is the original cross-sectional area, and L is the chosen specimen gage length (initial length between the grips). In order to ensure an uniaxial stress state, the gage length of the specimen was kept as 60 mm (thus the length to width ratio was 20 to 1).

3.4 Typical Testing Data and Data Processing

Typical Test Data

A typical SAC solder tensile stress strain curve is illustrated in Figure 3.8. The standard material properties are labelled on the graph including the effective elastic modulus E (initial slope of the stress-strain curve). This effective modulus is rate dependent since solder behavior is viscoplastic. The value of the effective modulus will

become the true elastic modulus as the testing speed is increased to the limit of infinite strain rate. The yield stress σ_Y (YS) is defined using the typical definition of the stress level that results in a permanent strain of $\epsilon = .002 = 0.2\%$ upon unloading. The maximum (saturation) stress on the stress-strain curve is the ultimate tensile strength σ_u (UTS). As shown the figure, the stress-strain curve for the solder material has an elastic region at the beginning, a small transition region followed by a plastic region. As the strain becomes significantly high, localized deformation takes place which is also known as necking. Necking causes a visible reduction in cross-sectional area and a drop in the applied load, near the end of the stress strain curve, leading towards a rupture.

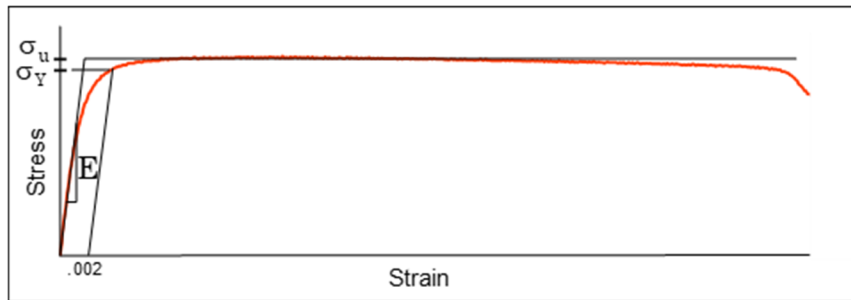


Figure 3.8 SAC Stress-Strain Curve and Material Properties

Stress-Strain Data Processing

Figure 3.9 illustrates a typical set of 5 solder stress strain curves measured for the same alloy under similar environmental and aging conditions. In this work, a four parameter hyperbolic tangent empirical model

$$\sigma = C_1 \tanh(C_2 \epsilon) + C_3 \tanh(C_4 \epsilon) \quad (3.2)$$

has been used to represent the “average” stress-strain curve through a set of experimental data (red curve in Figure 3.9). Material constants C_1 , C_2 , C_3 , and C_4 are determined through

regression fitting of the model to experimental data. The effective elastic modulus E at zero strain is calculated from the model constants using

$$E = \sigma'(0) = C_1 C_2 + C_3 C_4 \quad (3.3)$$

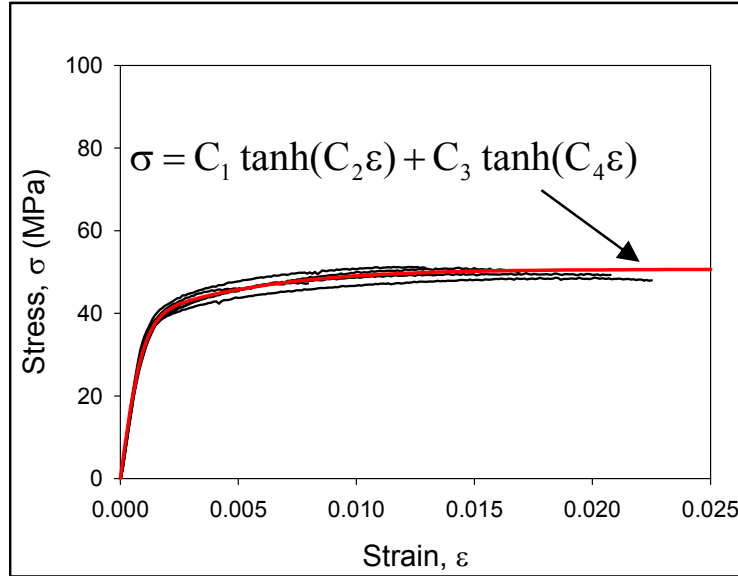


Figure 3.9 Empirical Model Fit to Solder Stress-Strain Curves

3.5 Microstructure Study

For microstructure analysis, the fabricated solder samples were cut into small pieces and potted in epoxy. Details of the preparation process included mechanical grinding with several SiC papers (#320 to #400, #600, #800 and #1200) in a rotating metallographic disc as shown in Figure 3.10. The final polishing was conducted with 0.02 μm colloidal silica suspensions where BUEHLER MasterMet 2 was the abrasive solution and BUEHLER ChemoMet was the polishing cloth. This procedure resulted in mirror finish samples suitable for optical microscopy, Scanning Electron Microscopy (SEM), as well as nanoindentation. Microstructure analysis of the solder alloys was performed on the mounted and polished testing coupons by using an OLYMPUS BX60 Optical Microscope

(Figure 3.11), Zeiss Polarized Light Microscope (Figure 3.12), Zeiss EVO 50 Scanning Electron Microscope (SEM) (Figure 3.13) and a JEOL JSM 7000F Field Emission SEM (Figure 3.14). In addition, EDS (Energy-Dispersive X-ray Spectroscopy) was employed to explore the chemical composition of different phases in the microstructure.

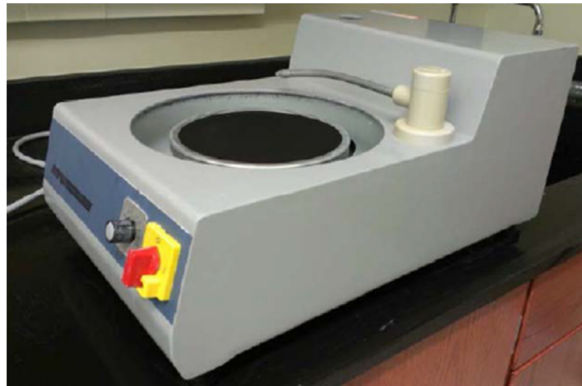


Figure 3.10 Grinding and Polishing Machine



Figure 3.11 OLYMPUS BX60 Optical Microscope

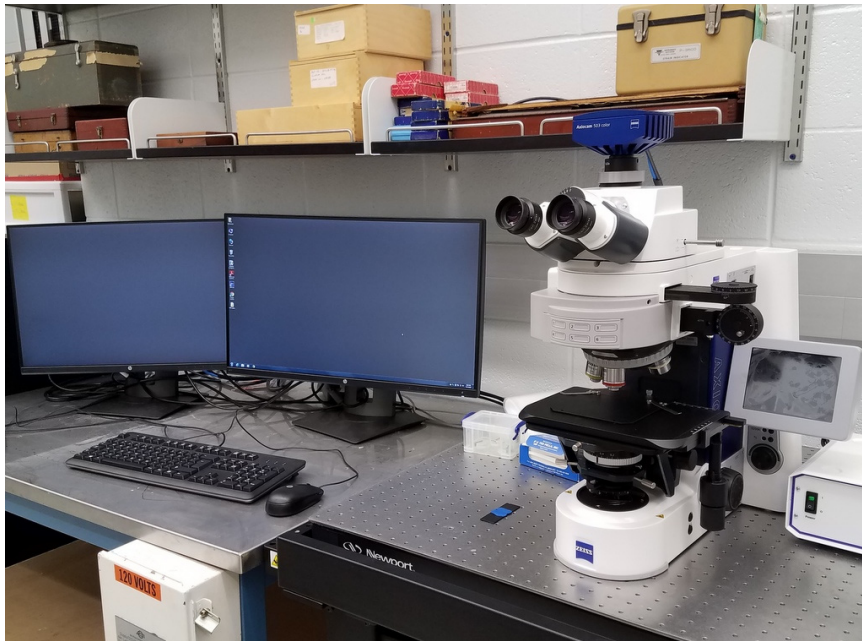


Figure 3.12 Zeiss Polarized Light Microscope



Figure 3.13 JEOL JSM-7000F Field Emission SEM

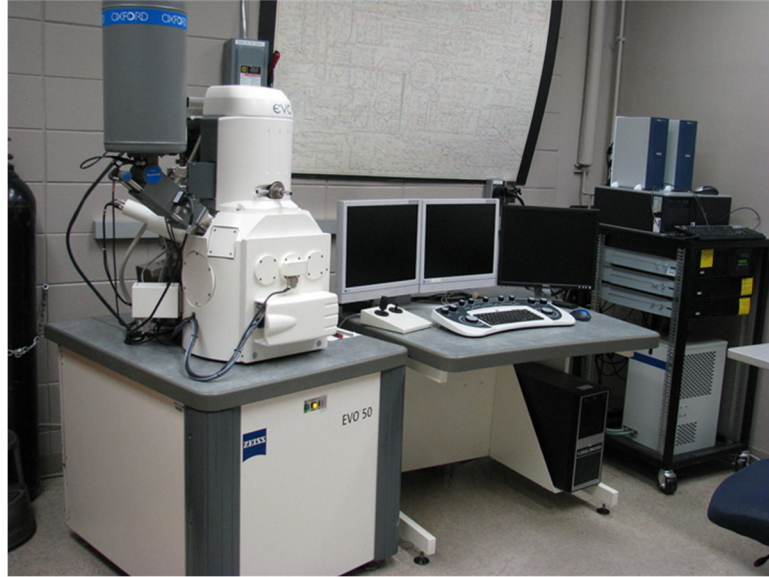


Figure 3.14 Zeiss EVO 50 SEM

3.6 Sample Preparation for Nanoindentation

SAC305 (96.5Sn-3.0Ag-0.5Cu) lead free solder joints were extracted from PBGA assemblies (Amkor CABGA, 14 x 14 mm, 192 balls, 0.8 mm ball pitch, 0.46 mm ball diameter) that were assembled for the iNEMI Characterization of Pb-Free Alloy Alternatives Project (Figure 3.15). Prior to cross sectioning, the PBGA test assemblies were stored in a freezer at $T = -10\text{ }^{\circ}\text{C}$ to minimize any aging effects after board assembly. The assembled PBGA components were cut out from the test boards and then cross-sectioned using BUEHLER IsoMet 1000 Precision Cutter (Figure 3.16). Cross-sectioned sample was potted in epoxy and polished in the same way to prepare microscopic samples as described in section 3.5. After polishing, the epoxy encapsulated sample was mounted rigidly on a 12 mm diameter steel SPM sample puck to reduce system compliance. Initially, the steel puck was cleaned with acetone to remove any oily substance from the surface. After cleaning, a small amount of cyanoacrylate based adhesive (super glue) was applied on the surface. Sample was placed on the adhesive and a firm pressure was applied

on the sample for around 20 second to ensure curing and proper bonding with the steel puck. Since the stage within the nanoindentation system has several magnets, the steel puck will allow the magnetic attraction of one of the magnets to hold the sample firmly on the stage.

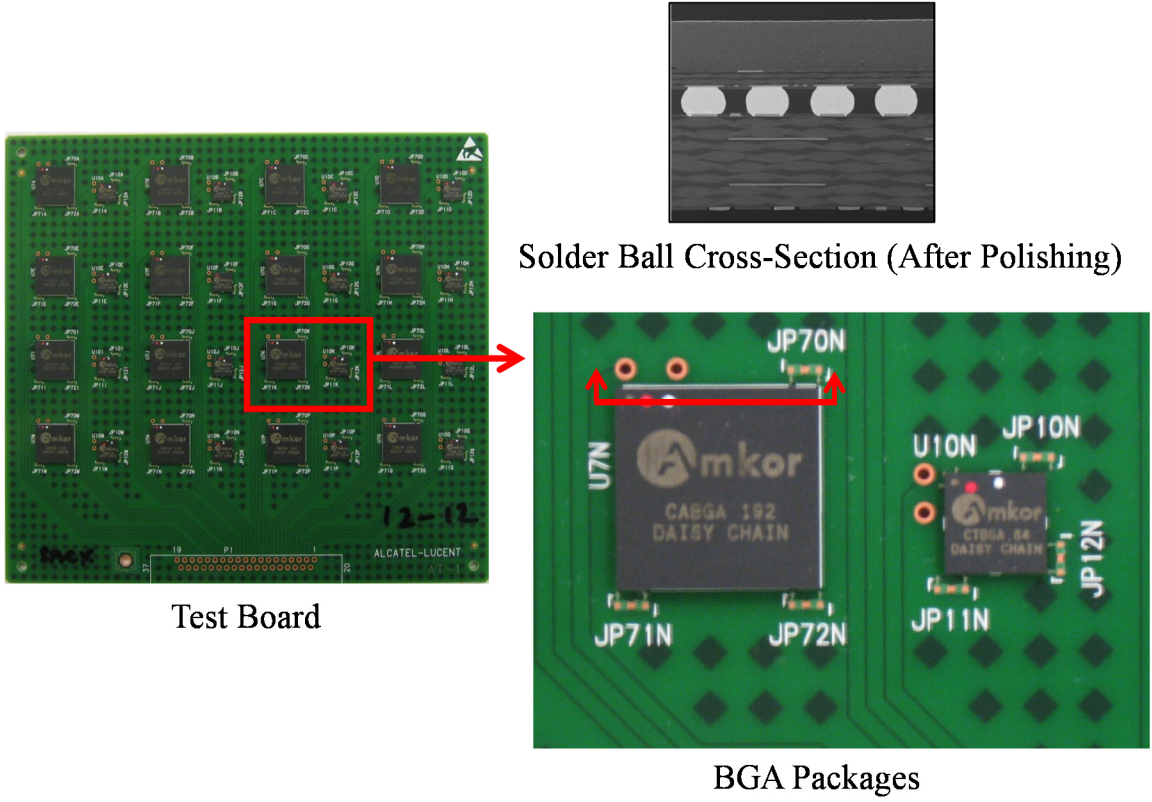


Figure 3.15 iNEMI Test Board and BGA Package



Figure 3.16 IsoMet 1000 Precision Cutter

3.7 Nanoindentation Machine and Test Procedures

The nanoindentation tests in this work were performed using an instrumented Hysitron TI 950 nanoindentation system (Figure 3.17) and a Berkovich indenter tip. During each indentation experiment, load versus indentation displacement response of the test samples in the direction normal to the cross-sectional surface was measured.



Figure 3.17 Hysitron TI950 TriboIndenter

Figure 3.18 shows a typical cross-sectioned SAC305 lead free solder joint sample after nanoindentation testing. A set of 10-30 indents were made, and the measured test data were averaged to obtain statistically relevant results and consistency of inspection. The indents in a set were positioned at least $3b$ apart, where b is the width of a single indent, to avoid interactions between the plastic zones created by the indentations. Figure 3.19 shows a typical example of loading profile used during nanoindentation, for hardness and

modulus testing. The loading profile has three segments 1) loading from 0 mN to 10 mN force, 2) holding 10 mN force for a few seconds, and 3) unloading from 10 mN to 0 mN. Depending on the type of the test material, the different parameters in the loading profile was adjusted to get an accurate measurement.

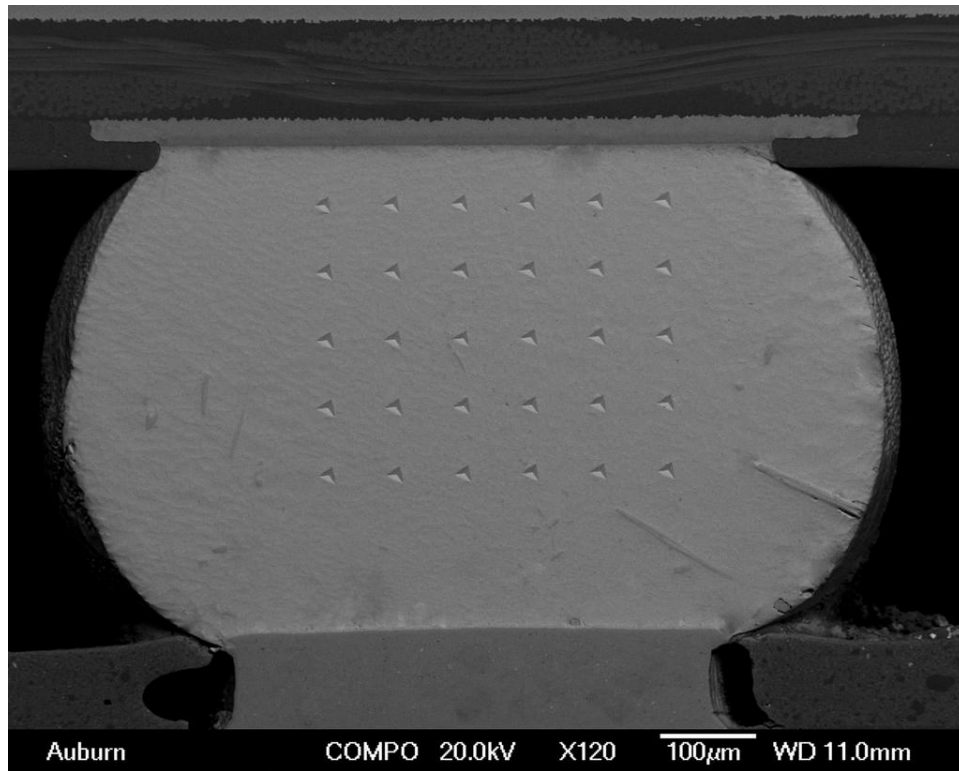


Figure 3.18 SAC305 Solder Joint after Nanoindentation Testing

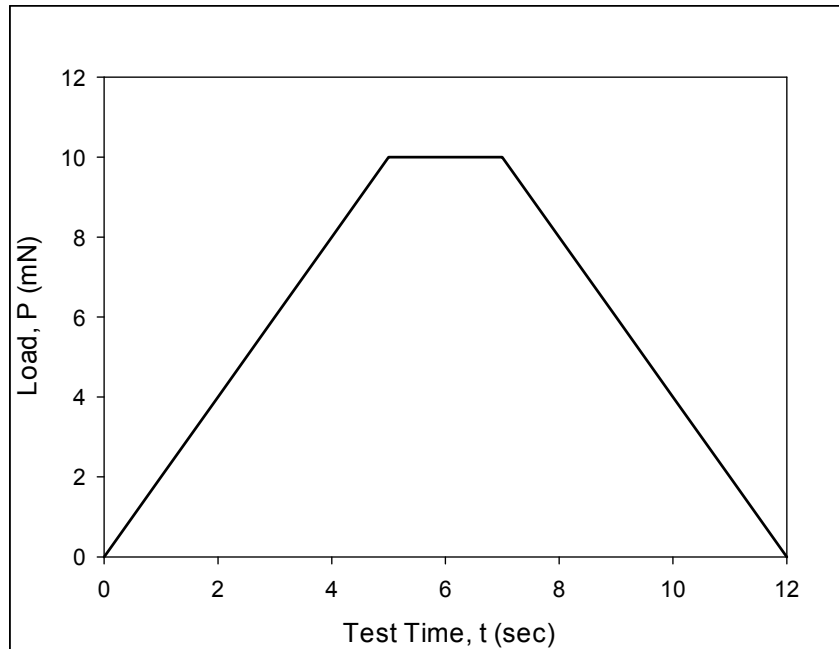


Figure 3.19 An example of the loading profile used during nanoindentation testing

3.8 Measurement of Elastic Modulus and Hardness

A typical load (P) versus displacement (h) curve, obtained after a nanoindentation test, is presented in Figure 3.20. This curve has three different segments where the first, second, and third segments represent the displacements during the loading, holding and unloading period, respectively.

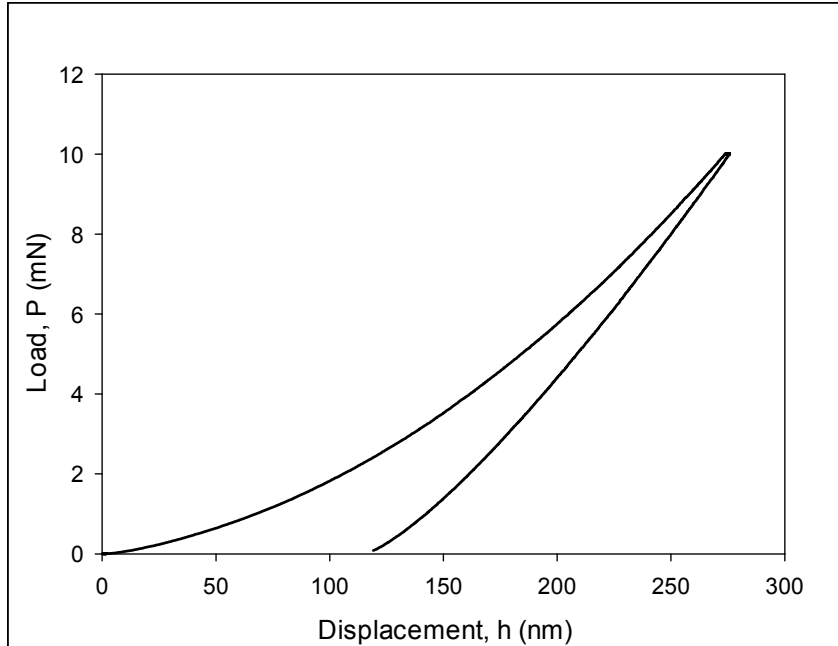


Figure 3.20 An example of the load-displacement curve obtained after nanoindentation testing.

During a nanoindentation experiment, the effects of the non-rigidity of an indenter, during a nanoindentation experiment, can be addressed by introducing a term called reduced modulus (E_r) through the following equation:

$$\frac{1}{E_r} = \frac{(1-\nu^2)}{E} + \frac{(1-\nu_i^2)}{E_i} \quad (3.4)$$

where E is the elastic modulus of the test specimen, E_i is the known elastic modulus of the indenter tip material, ν and ν_i are the Poisson's ratio of the test specimen and the indenter tip, respectively. Typically reduced modulus was measured from an indentation experiment using the following equation

$$E_r = \frac{\sqrt{\pi}}{2} \times \frac{S}{\sqrt{A}} \quad (3.5)$$

where S is the stiffness of the test specimen at the maximum load and A is the projected contact area at the maximum load. Stiffness was determined from the initial slope ($\frac{dP}{dh}$) of the unloading segment of a load displacement curve. The contact area A was measured following the technique proposed by Oliver and Pharr [95] where they assumed the contact area to be a function of contact depth. For an ideal Berkovich tip, it can be expressed as

$$A(h_c) = 24.5h_c^2 \quad (3.6)$$

In order to address any deviation from the ideal Berkovich geometry due to tip blunting, a modified version of equation 3.6 was utilized.

$$A(h_c) = 24.5h_c^2 + C_1h_c^1 + C_2h_c^{1/2} + C_3h_c^{1/4} + C_4h_c^{1/8} + C_5h_c^{1/16} \quad (3.7)$$

where C_1 , C_2 , C_3 , C_4 , and C_5 are fitting constants. In order to determine the values of these constants, multiple indents were made at multiple depths on a quartz sample with known elastic modulus (69.6 GPa). The contact areas at the different known depths were determined from equation 3.5 and these values were plotted to get a A versus h_c plot. The values of constants C_1 to C_5 were determined by fitting the plot by Equation 3.7. Once the values of the constants are known for a particular tip geometry, equation 3.5 was used to determine the value of reduced modulus (E_r) for any unknown material and equation 3.4 was used to convert E_r to elastic modulus E .

Hardness is a material property that defines the resistance of the surface against plastic deformation. During a nanoindentation experiment, hardness H was determined by dividing the maximum load by the projected contact area.

$$H = \frac{P_{\max}}{A} \quad (3.8)$$

Tabor [96, 97] developed an approximate relationship between hardness and yield strength of which is true for many metals.

$$H \approx 3\sigma_Y \quad \text{or} \quad \sigma_Y \approx \frac{H}{3} \quad (3.9)$$

The above equation was used to determine stress during nanoindentation experiments.

3.9 Summary and Discussion

All the experimental procedures and the data processing steps were presented in this chapter. Micro-scale uniaxial tensile specimens were prepared in a rectangular shaped hollow glass tube using a vacuum suction method. Typical dimension of the uniaxial tensile specimens were 80 (length) \times 3 (width) \times 0.5 (height) mm. Uniaxial tensile tests were performed using a micro tension torsion testing system. Nanoindentation experiments were conducted on actual solder joints which were typically extracted from 14 x 14 mm PBGA assemblies (0.8 mm ball pitch, 0.46 mm ball diameter). Nanoindentation experiments were performed using Hysitron TI950 TriboIndenter.

CHAPTER 4

EFFECTS OF AGING ON MECHANICAL PROPERTIES AND ANAND PARAMETERS OF SAC-Bi ALLOYS

4.1 Introduction

In the electronic packaging industry, it is important to be able to make accurate predictions of board level solder joint reliability during thermal cycling exposures. The Anand viscoelastic constitutive model is often used to represent the material behavior of the solder in finite element simulations. This model is defined using nine material parameters, and the reliability prediction results are often highly sensitive to the Anand parameters.

In this chapter, three new SAC_Bi lead free solder materials recommended for high reliability applications have been chemically analyzed and then mechanically tested in order to determine the nine Anand parameters. The alloys are referred to as Ecolloy (SAC_R), CYCLOMAX (SAC_Q), and Innolot by their vendors. The first two SAC-Bi alloys (SAC_R and SAC_Q) were found to be composed of Sn, Ag, Cu, and a single X-element dopant. Such solders are commonly referred to as SAC-X in the literature. For the third material (Innolot), three different dopants are present along with Sn, Ag and Cu. The EDX method was used to determine the approximate chemical composition of the materials, and Bismuth (Bi) was found to be the X-additive for both SAC_R and SAC_Q. In addition, the SAC_R material was found to have no silver (Ag), which is the reason it is marketed as a low cost (economy) material.

For each alloy, three different microstructures were explored using different cooling profiles as well as subsequent isothermal aging. Test specimens were initially solidified with both water quenched (WQ) and reflowed (RF) cooling profiles. In addition,

some of the reflowed samples were subsequently subjected to 3 months of isothermal aging at $T = 100\text{ }^{\circ}\text{C}$ (RF + 3 Months Aging) to further coarsen the reflowed microstructure.

The nine Anand parameters were determined for each unique solder alloy from a set of uniaxial tensile tests performed at several strain rates and temperatures. Testing conditions included strain rates of 0.001, 0.0001, and 0.00001 (sec^{-1}), and temperatures of 25, 50, 75, 100, and 125 $^{\circ}\text{C}$. The Anand parameters were calculated from each set of stress-strain data using an established procedure that is described in detail in the chapter. The mechanical properties and the values of Anand parameters for these new SAC-Bi alloys were compared with those for standard SAC105 and SAC405 lead free alloys.

4.2 Anand Viscoplastic Constitutive Model

The Anand viscoelastic constitutive model [37] is often used to represent the material behavior of the lead free solders in finite element simulations. This model is defined using nine material parameters, and the reliability prediction results are often highly sensitive to the values of the Anand parameters. There are several publications listing values of Anand parameters for particular solder alloys. For example, Anand parameters for alloys such as Sn-3.5Ag, SAC105, SAC305, and SAC387 have been documented [34, 35, 43, 98-100]

4.2.1 Review of Anand Model Equations (1D)

Several authors [34, 35, 41] have previously reviewed the general equations of the Anand constitutive model for one-dimensional (uniaxial) stress states. The theoretical approach is based on a scalar internal variable s , which represents the material resistance to plastic flow. The model includes three equations: (1) stress equation, (2) flow equation, and (3) evolution equation. These expressions unify the rate-independent plastic behavior

and creep behavior of the material. The Anand model does not contain an explicit yield condition or a loading/unloading criterion.

The stress equation is expressed as

$$\sigma = c s; c < 1 \quad (4.1)$$

where s is the scalar internal variable. Quantity c is a function of the temperature and strain rate, and is given by

$$c = c(\dot{\epsilon}_p, T) = \frac{1}{\xi} \sinh^{-1} \left\{ \left[\frac{\dot{\epsilon}_p}{A} e^{\left(\frac{Q}{RT}\right)} \right]^m \right\} \quad (4.2)$$

where $\dot{\epsilon}_p$ is the plastic strain rate, A is the pre-exponential factor, ξ is the multiplier of stress, m is the strain rate sensitivity, Q is the activation energy, R is the universal gas constant, and T is the absolute temperature. By substitution of eq. (4.2) into eq (4.1), the reformatted stress equation becomes:

$$\sigma = \frac{s}{\xi} \sinh^{-1} \left\{ \left[\frac{\dot{\epsilon}_p}{A} e^{\left(\frac{Q}{RT}\right)} \right]^m \right\} \quad (4.3)$$

The Anand model flow equation is found by solving for the strain rate in eq.(4.3):

$$\dot{\epsilon}_p = A e^{-\left(\frac{Q}{RT}\right)} \left[\sinh \left(\xi \frac{\sigma}{s} \right) \right]^{\frac{1}{m}} \quad (4.4)$$

The evolution equation describes the variation of internal variable s with time. In its differential form, it can be expressed as:

$$\begin{aligned} \dot{s} &= h(\sigma, s, T) \dot{\epsilon}_p \\ \dot{s} &= \left[h_0 \left(1 - \frac{s}{s^*} \right)^a \operatorname{sign} \left(1 - \frac{s}{s^*} \right) \right] \dot{\epsilon}_p; \quad a > 1 \end{aligned} \quad (4.5)$$

The term $h(\sigma, s, T)$ in eq. (4.5) is associated with dynamic hardening and recovery, and its initial value is the hardening constant $h(0) = h_0$. Parameter a is the strain rate sensitivity of the hardening process, and parameter s^* is the saturation value of the deformation resistance given by

$$s^* = \hat{s} \left[\frac{\dot{\epsilon}_p}{A} e^{\left(\frac{Q}{RT} \right)} \right]^n \quad (4.6)$$

where \hat{s} is a coefficient, and n is the strain rate sensitivity. Equation (4.5) can be expressed as

$$ds = h_0 \left(1 - \frac{s}{s^*} \right)^a d\epsilon_p \quad (4.7)$$

for $s < s^*$, and then integrated resulting in an evolution expression for the internal variable s :

$$s = s^* - \left[(s^* - s_0)^{1-a} + (a-1) \left\{ (h_0) (s^*)^{-a} \right\} \epsilon_p \right]^{\frac{1}{1-a}} \quad (4.8)$$

where the initial value is $s(0) = s_0$ at time $t = 0$. Combining eq. (4.6) and eq. (4.8) results in an evolution equation for the internal variable s in terms of the plastic strain and plastic strain rate:

$$s = \hat{s} \left[\frac{\dot{\varepsilon}_p}{A} e^{\left(\frac{Q}{RT}\right)} \right]^n - \left[\left(\hat{s} \left[\frac{\dot{\varepsilon}_p}{A} e^{\left(\frac{Q}{RT}\right)} \right]^n - s_0 \right)^{(1-a)} + (a-1) \left\{ (h_0) \left(\hat{s} \left[\frac{\dot{\varepsilon}_p}{A} e^{\left(\frac{Q}{RT}\right)} \right]^n \right)^{-a} \right\} \varepsilon_p \right]^{\frac{1}{1-a}} \quad (4.9)$$

or

$$s = s(\dot{\varepsilon}_p, \varepsilon_p) \quad (4.10)$$

The final versions of the Anand model equations are the stress equation in eq. (4.3), the flow equation in eq. (4.4), and the integrated evolution equation in eq. (4.9). These expressions include 9 material parameters: A , ξ , Q/R , m in eqs. (4.3, 4.4); and constants h_0 , a , s_0 , \hat{s} , and n in eq. (4.9).

4.2.2 Uniaxial Stress-Strain Theoretical Response

Equations (4.3) and (4.9) can be combined to give an expression for the uniaxial stress-strain law (post yield) predicted by the Anand model:

$$\sigma = \frac{1}{\xi} \sinh^{-1} \left\{ \left[\frac{\dot{\varepsilon}_p}{A} e^{\left(\frac{Q}{RT}\right)} \right]^m \right\} \left(\hat{s} \left[\frac{\dot{\varepsilon}_p}{A} e^{\left(\frac{Q}{RT}\right)} \right]^n - \left[\left(\hat{s} \left[\frac{\dot{\varepsilon}_p}{A} e^{\left(\frac{Q}{RT}\right)} \right]^n - s_0 \right)^{(1-a)} + (a-1) \left\{ (h_0) \left(\hat{s} \left[\frac{\dot{\varepsilon}_p}{A} e^{\left(\frac{Q}{RT}\right)} \right]^n \right)^{-a} \right\} \varepsilon_p \right]^{\frac{1}{1-a}} \right) \quad (4.11)$$

$$\sigma = \sigma(\dot{\varepsilon}_p, \varepsilon_p)$$

For a uniaxial tensile test performed at fixed (constant) strain rate $\dot{\varepsilon}_p$ and constant temperature T , this equation represents nonlinear stress-strain behavior in the form of a power law type function after yielding:

$$\sigma = \sigma(\varepsilon_p) \quad (4.12)$$

The yield stress (σ_Y) and the Ultimate Tensile Strength (UTS = maximum or saturation stress) can be obtained from eq. (4.11) by taking the limits for small and large plastic strains. The yield stress is given by the limit as ε_p goes to 0:

$$\sigma_Y = \sigma|_{\varepsilon_p \rightarrow 0} = c s_0 = \frac{1}{\xi} \sinh^{-1} \left\{ \left[\frac{\dot{\varepsilon}_p}{A} e^{\left(\frac{Q}{RT}\right)} \right]^m \right\} s_0 = c s_0 \equiv \sigma_0 \quad (4.13)$$

while the UTS is given by the limit as ε_p goes to ∞ :

$$\text{UTS} = \sigma|_{\varepsilon_p \rightarrow \infty} = \frac{\hat{s}}{\xi} \left[\frac{\dot{\varepsilon}_p}{A} e^{\left(\frac{Q}{RT}\right)} \right]^n \sinh^{-1} \left\{ \left[\frac{\dot{\varepsilon}_p}{A} e^{\left(\frac{Q}{RT}\right)} \right]^m \right\} \equiv \sigma^* \quad (4.14)$$

By substituting eq. (4.14) into eq. (4.11), the stress-strain power law relation after yielding can be expressed as:

$$\sigma = \sigma^* - \left[(\sigma^* - c s_0)^{(1-a)} + (a-1) \left\{ (c h_0) (\sigma^*)^{-a} \right\} \varepsilon_p \right]^{1/(1-a)} \quad (4.15)$$

4.2.3 Procedure for Determining the Anand Model Parameters from Uniaxial

Stress Strain data

Anand [37] suggested using stress-strain data measured over a wide range of temperatures and strain rates to determine the 9 parameters (A , ξ , Q/R , m , h_0 , a , s_0 , \hat{s} , and n) in the viscoelastic constitutive relations presented above. Several previous studies [34,

35, 41], have outlined a procedure for performing this task. Values of the saturation stress ($\sigma^* = \text{UTS}$) can be extracted from the peak stress values on the stress-strain curves for several temperatures and strain rates. Also, stress vs. plastic strain data (σ vs. ε_p) can be extracted from the recorded stress-strain curves (σ, ε) at the various temperatures and strain rates. The conversion of total strain to plastic strain for each data set is performed using:

$$\varepsilon_p = \varepsilon - \frac{\sigma}{E} \quad (4.16)$$

where E is the initial elastic modulus. The sequential procedure for calculating the Anand model parameters consists of:

1. The six Anand parameters \hat{S} , ξ , A, Q/R, n and m are determined using a nonlinear least-squares regression fit of eq. (4.14) to the recorded saturation stress (UTS) vs. temperature and strain rate data.
2. The remaining three Anand parameters (s_0 , h_0 , and a) are found using nonlinear regression fits of eq. (4.15) to the recorded stress vs. plastic strain data at several temperatures and strain rates.

4.3 Chemical Composition of the SAC-Bi Alloys

Chemical compositions of the SAC-Bi alloys are presented in Table 1 along with the compositions of the traditional SAC105 and SAC405 alloys. Innolot has a well published 6-element target composition, while the compositions of SAC_R (Ecolloy) and SAC_Q (CYCLOMAX) are unpublished. Energy Dispersive X-Ray Spectroscopy (EDX) was used to explore the compositions of these two alloys. All three alloys were found to employ Bismuth (Bi) as the primary X-additive. The composition of SAC_R is most

similar to that of SAC 105. However, the SAC_R material does not have any measureable silver (Ag) content, contrary to all other SAC alloys. This is most likely the reason it is marketed as a low cost (economy) material. The silver contents of SAC_Q and Innolot are similar to SAC405, at 3.41% and 3.80%, respectively.

Table 4.1 Chemical Compositions of the Solder Alloys

Alloy	Sn	Ag	Cu	Bi	Ni	Sb
SAC R	96.62	0.00	0.92	2.46	0.00	0.00
SAC 105	98.50	1.00	0.50	0.00	0.00	0.00
SAC Q	92.77	3.41	0.52	3.30	0.00	0.00
SAC 405	95.50	4.00	0.50	0.00	0.00	0.00
Innolot	90.95	3.80	0.70	3.00	0.15	1.40

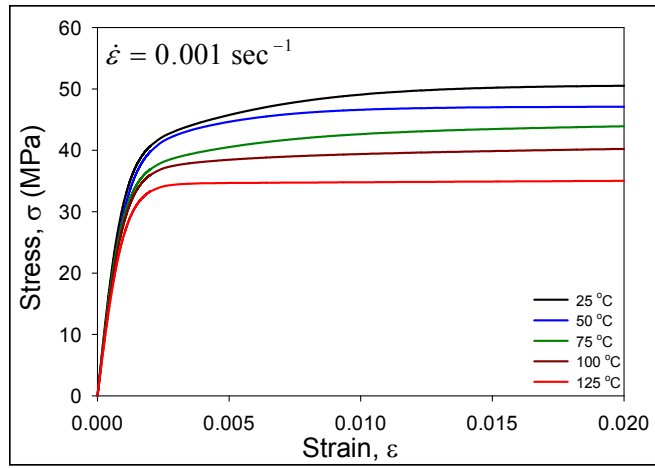
4.4 Effects of Aging on SAC_R (Ecolloy)

Mechanical stress-strain tests have been performed on SAC_R solder samples, and then compared to those measured for SAC105. As mentioned earlier, three different microstructures were explored using different cooling profiles as well as subsequent isothermal aging. Test specimens were initially solidified with both water quenched (WQ) and reflowed (RF) cooling profiles. In addition, some of the reflowed samples were subsequently subjected to 3 months of isothermal aging at $T = 100\text{ }^{\circ}\text{C}$ (RF + 3 Months Aging) to further coarsen the reflowed microstructure. The stress-strain tests were performed at three different strain rates ($\dot{\epsilon} = .001, .0001, \text{ and } .00001\text{ sec}^{-1}$) and five different temperatures ($T = 25, 50, 75, 100, \text{ and } 125\text{ }^{\circ}\text{C}$). From this data, the nine Anand constitutive model parameters were determined for each unique solder alloy and microstructure combination.

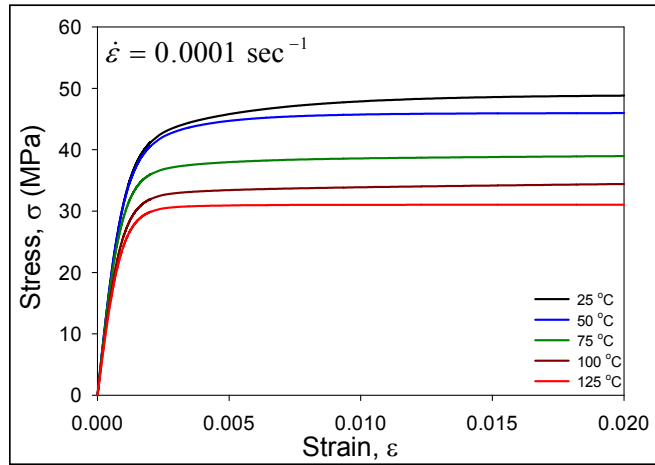
4.4.1 Stress-Strain Data for Various Temperature and Strain Rates

The recorded stress-strain curves for SAC_R (WQ microstructure) at strain rates of 0.001, 0.0001, and 0.00001 sec⁻¹ are shown in Figures 4.1a, 4.1b, and 4.1c, respectively. Each curve in these plots is an “average” stress-strain curve representing the fit of the empirical model in equation 3.2 (chapter 3) to the 5 recorded stress-strain curves for the particular strain rate and temperature. The five different colored curves in each graph are the results for the 5 testing temperatures (T = 25, 50, 75, 100, and 125 °C). As expected, the initial elastic modulus, yield stress, and UTS decrease with increasing temperature. In addition, they also decrease with decreasing strain rate. Analogous results were found for the SAC_R samples with reflowed (RF) microstructure as shown in Figure 4.2, and the SAC_R samples with RF+Aging microstructure as shown in Figure 4.3.

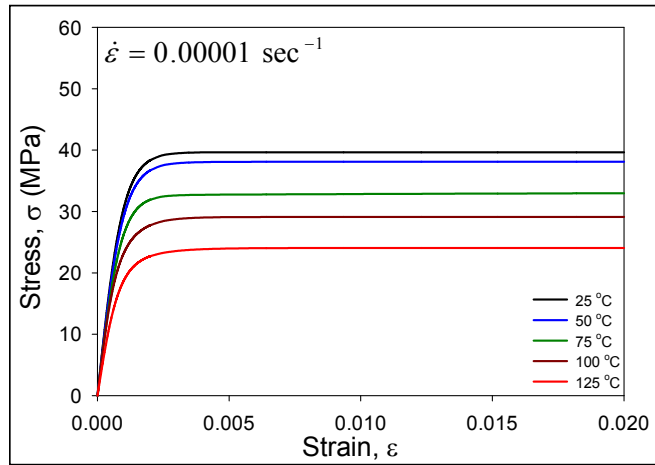
It is observed in each graph in Figures 4.1-4.3 that the effective elastic modulus, yield stress (YS), and ultimate tensile strength (UTS) all decrease monotonically with temperature as expected. These decreases have been found to be nearly linear with the testing temperature for all alloys. By comparing the analogous results for the same temperature and alloy, but different strain rates, it has also been observed that as the strain rate decreases, the effective elastic modulus, yield stress (YS), and ultimate tensile strength (UTS) all decrease. Histogram charts showing the ultimate tensile strength (UTS) with different microstructure, test temperature and strain rate are presented in Figure 4.4.



(a)

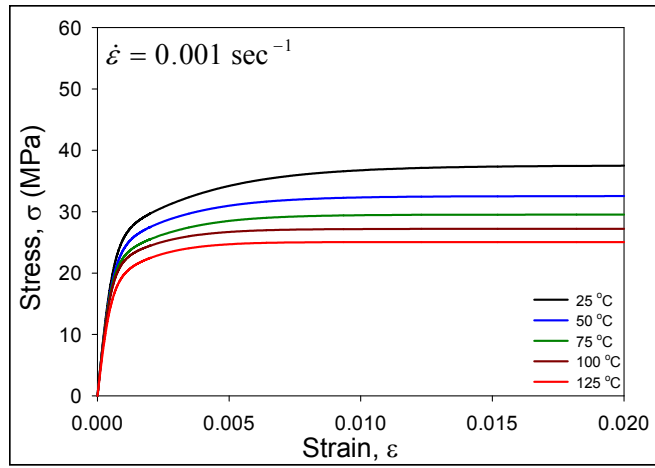


(b)

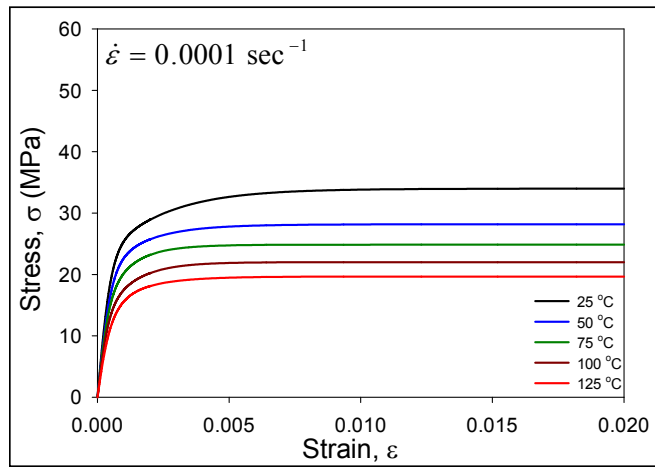


(c)

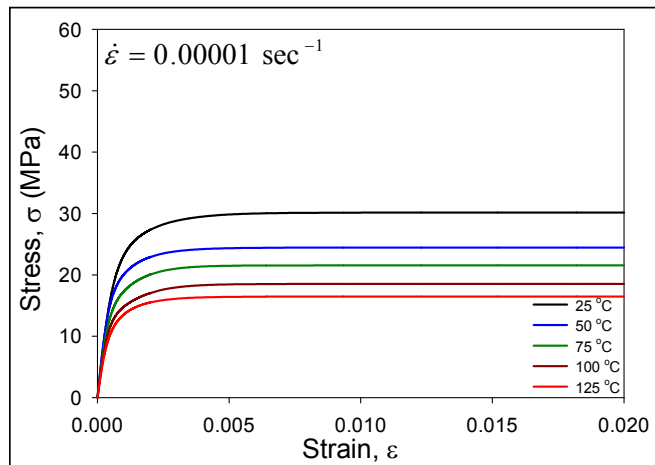
Figure 4.1 (a-c) Stress-Strain Curves for SAC_R (WQ)



(a)

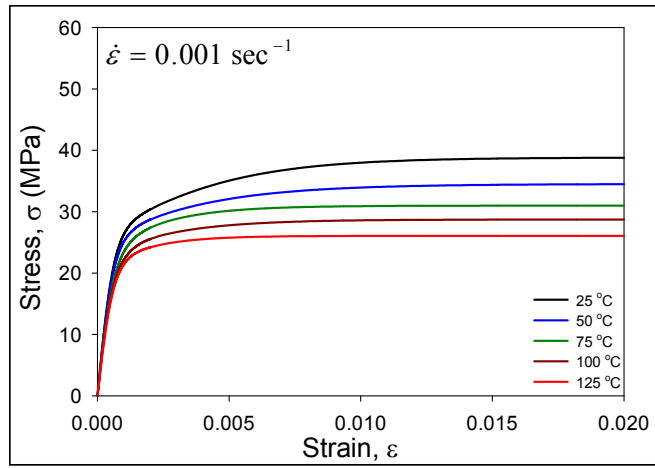


(b)

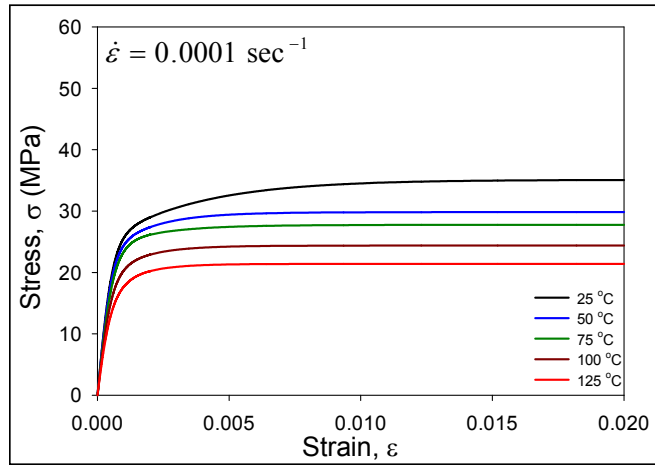


(c)

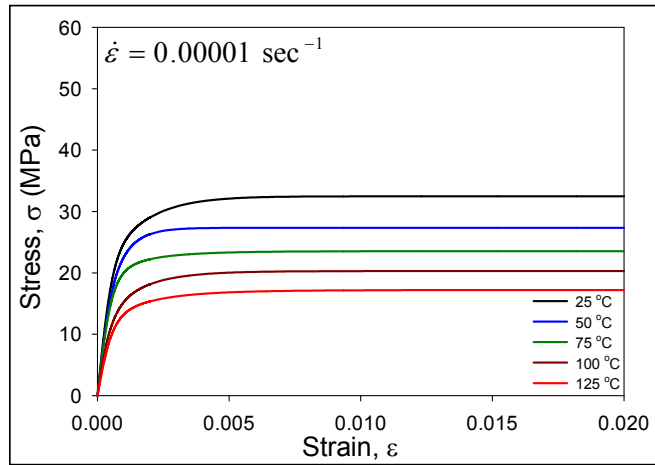
Figure 4.2 (a-c) Stress-Strain Curves for SAC_R (RF)



(a)

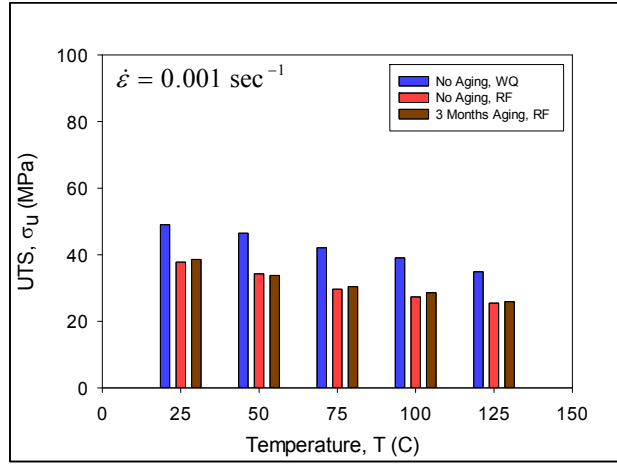


(b)

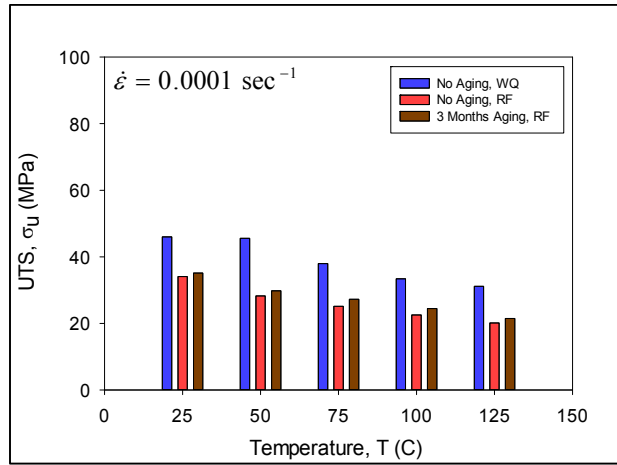


(c)

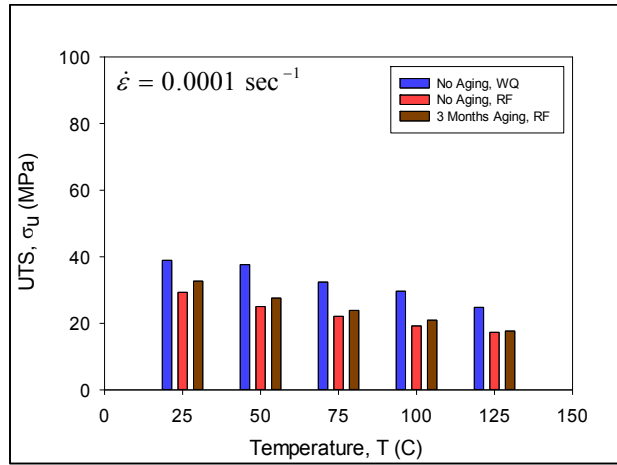
Figure 4.3 (a-c) Stress-Strain Curves for SAC_R (RF+Aging)



(a)



(b)



(c)

Figure 4.4 (a-c) UTS of SAC_R at Different Strain Rates and Test Temperatures

The reductions in ultimate tensile strength (UTS) between the ultrafine WQ microstructure material and the coarser RF microstructure material are visually evident. This matches previous observations for standard SACN05 alloys [101, 102]. However, it is interesting to note that there are no easily apparent visual differences between the results in Figures 4.2 and 4.3, suggesting that the SAC_R alloy is resistant to aging effects. The results presented in Figure 4.4 is summarized in Table 4.2.

Table 4.2 UTS Values of SAC_R

T (°C)	UTS in MPa (STD)								
	$\dot{\epsilon} = 0.001 \text{ sec}^{-1}$			$\dot{\epsilon} = 0.0001 \text{ sec}^{-1}$			$\dot{\epsilon} = 0.00001 \text{ sec}^{-1}$		
	No Aging (WQ)	No Aging (RF)	3M Aging (RF)	No Aging (WQ)	No Aging (RF)	3M Aging (RF)	No Aging (WQ)	No Aging (RF)	3M Aging (RF)
25	49.1 (2.1)	37.8 (4.2)	38.82 (2.2)	46.0 (1.8)	34.0 (0.5)	34.4 (0.7)	38.9 (0.8)	29.3 (2.6)	31.6 (0.6)
50	46.5 (1.2)	31.9 (2.2)	34.3 (2.8)	45.6 (0.8)	28.2 (1.2)	29.7 (0.3)	37.6 (1.9)	25.0 (0.8)	27.6 (0.7)
75	42.1 (3.8)	29.4 (0.8)	30.7 (1.1)	37.9 (2.2)	25.1 (2.2)	27.2 (0.8)	32.4 (1.8)	22.1 (1.7)	23.8 (2.6)
100	39.1 (1.9)	27.2 (2.1)	27.2 (2.4)	33.4 (1.4)	22.5 (0.4)	24.4 (2.1)	29.6 (1.3)	19.2 (1.6)	22.0 (1.3)
125	34.9 (1.1)	24.9 (1.6)	24.5 (2.1)	31.1 (0.6)	20.1 (0.8)	21.4 (1.6)	24.8 (1.9)	17.3 (1.8)	18.6 (0.2)

4.4.2 The Anand Parameters for SAC_R

The Anand model parameters for the SAC_R lead free solder materials, for the three different microstructures, have been determined from the temperature and strain rate dependent stress-strain data in Figures 4.1-4.3. The curves in each Figure were first processed to extract saturation stress (UTS) vs. strain rate and temperature data for each

alloy, as well as stress vs. plastic strain data at several strain rates and temperatures for each alloy. From the extracted data from each Figure, the nine Anand parameters were calculated for each alloy using equations 4.13 and 4.15, and the nonlinear regression analysis procedure discussed in section 4.2.3. The results are tabulated in Table 4.3.

Table 4.3 Anand Parameters for SAC_R

Par. No.	Anand Par.	Units	WQ	RF	RF+Aging
1	s_0	MPa	34.72	30.59	30.59
2	Q/R	1/K	11100	11100	11100
3	A	sec ⁻¹	1000	2000	2000
4	ξ	-	6	6	6
5	m	-	0.15	0.12	0.12
6	h_0	MPa	145640	141180	143540
7	\hat{S}	MPa	71.71	61.165	64.89
8	n	-	0.0010	0.0009	0.0009
9	a	-	1.55	1.63	1.63

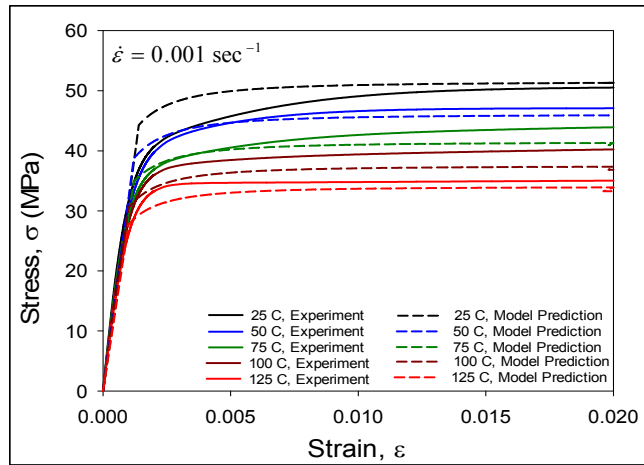
Once the Anand constants are determined for each alloy, it is possible to predict the stress (σ) vs. plastic strain (ϵ_p) curve at a particular set of temperature, strain rate, and alloy using equation 4.11. This result can be adjusted to a stress (σ) vs. total strain curve (ϵ) by adding the elastic strain to the plastic strain:

$$\epsilon = \epsilon_e + \epsilon_p \quad \epsilon_e = \frac{\sigma}{E} \quad (4.17)$$

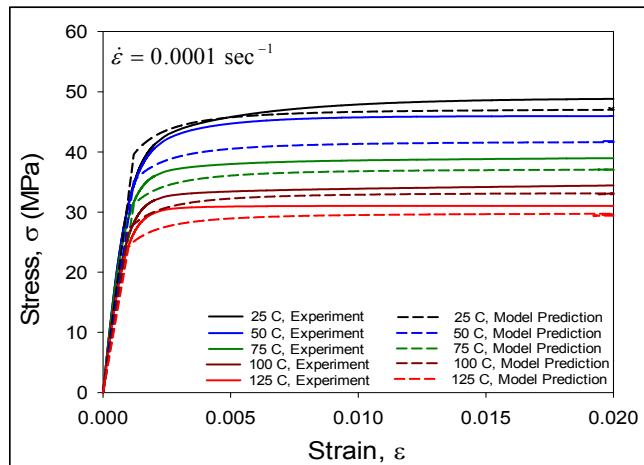
where E is the initial elastic modulus at the particular temperature, strain rate, and aging conditions.

Figure 4.5 illustrates the correlation between the model predictions and the experimental stress-strain curves for SAC_R (WQ). In this case, the Anand model constants from Table 4.3 for the alloy SAC_R were utilized. The experimental curves were

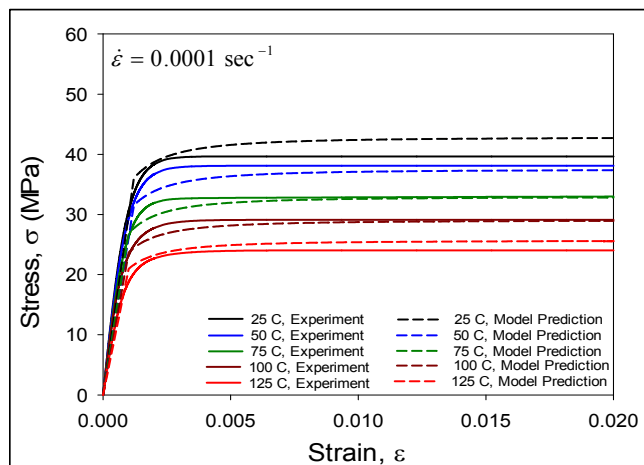
those shown earlier in Figure 4.1. Good correlations are obtained, with the Anand model able to represent the stress-strain curves accurately over a wide range of temperatures and strain rates. Analogous comparisons for SAC_R (RF) and SAC_R (RF+3 Months Aging) are shown in Figures 4.6 and 4.7, respectively. In these cases, the appropriate Anand model constants from Table 4.3 were utilized, along with the experimental curves from Figures 4.2 and 4.3. Again, good correlations were obtained



(a)

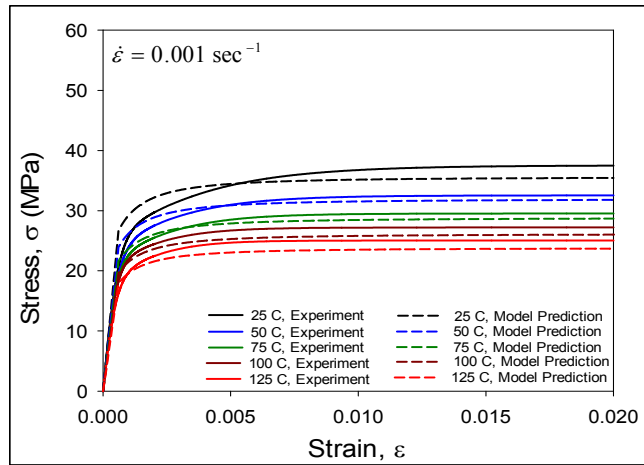


(b)

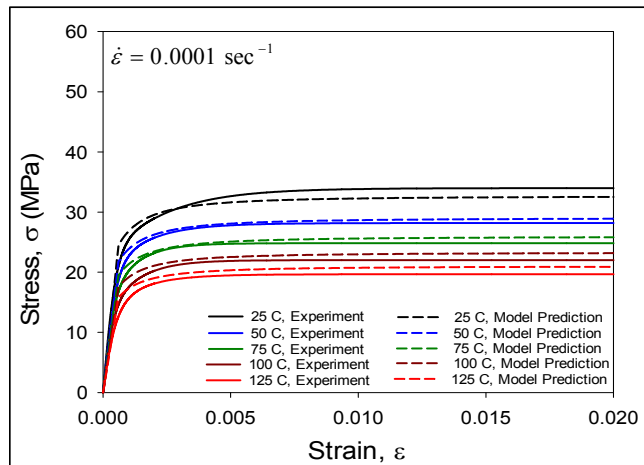


(c)

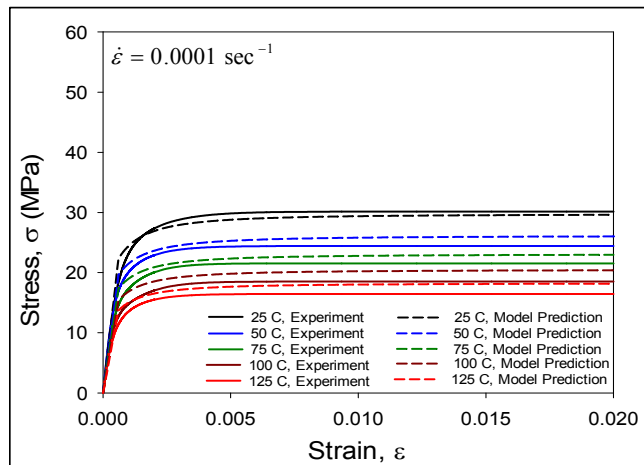
Figure 4.5 (a-c) Comparisons between Anand Model Predictions and Experimental Data (SAC_R, WQ)



(a)

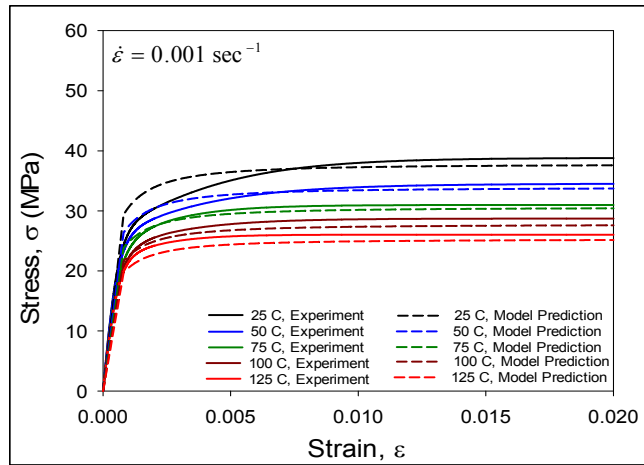


(b)

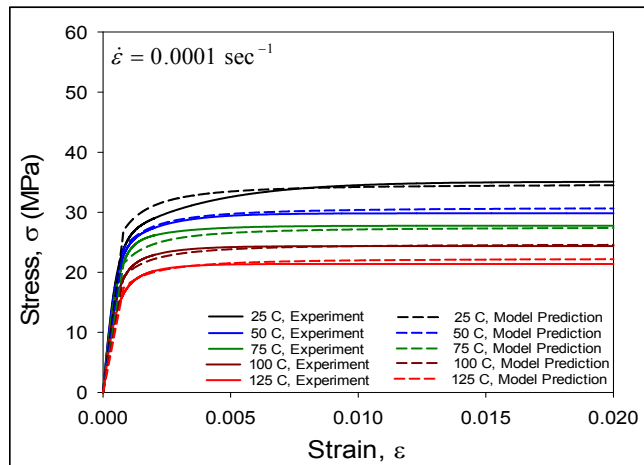


(c)

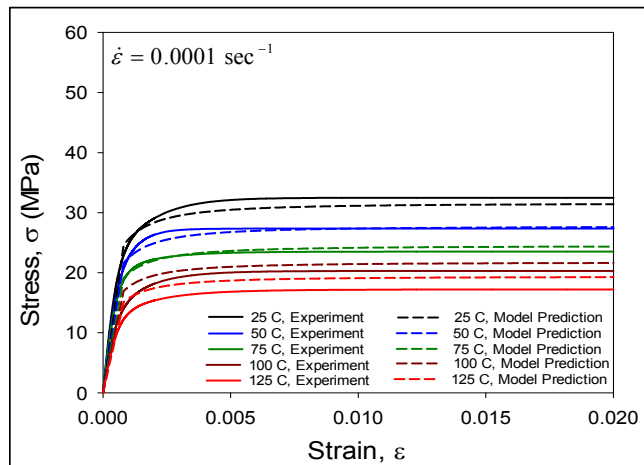
Figure 4.6 (a-c) Comparisons between Anand Model Predictions and Experimental Data (SAC_R, RF)



(a)



(b)



(c)

Figure 4.7 (a-c) Comparisons between Anand Model Predictions and Experimental Data (SAC_R, RF+3 Months Aging)

4.4.3 Stress-Strain Data Comparison (SAC_R and SAC105)

Selected stress-strain curves for SAC_R in Figures 4.1-4.3 have been replotted in Figure 4.8 for a strain rate of $\dot{\epsilon} = 0.001 \text{ sec}^{-1}$, temperatures of $T = 25$ and $125 \text{ }^\circ\text{C}$, and the three solder microstructures (WQ, RF, RF+Aging). The analogous curves for SAC105 [101] are plotted in Figure 4.9. It is observed that large aging induced degradations occur for the SAC105 alloy at both testing temperatures (the dashed curves for the RF+Aging microstructure are significantly below the solid curves for the RF microstructure). For the SAC_R alloy, there appear to be no aging induced degradations at either testing temperature. In fact, there was a small increase in strength with aging, as both of the curves for the RF+Aging microstructure are slightly higher than the corresponding curves for the RF microstructure. These observations are further demonstrated in Figure 4.10, where analogous results for SAC_R and SAC105 are directly compared. In addition, similar results were found for all 5 testing temperatures and 3 strain rates. In a previous study on SAC-Bi alloys [28], it was demonstrated that addition of only 0.1% Bi significantly reduced aging effects in SAC solders.

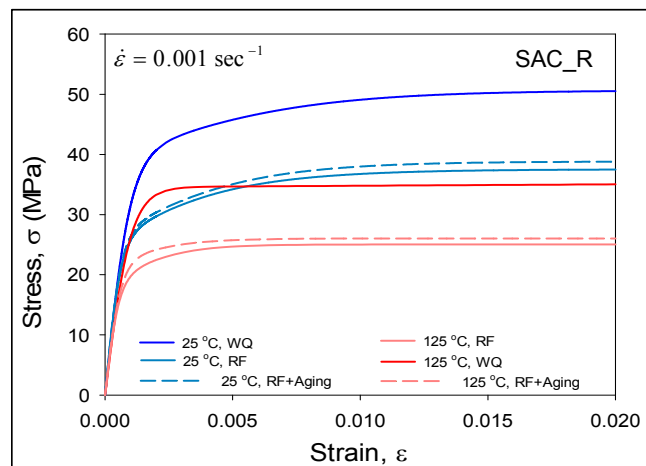


Figure 4.8 Stress-Strain Curve Comparisons for SAC_R

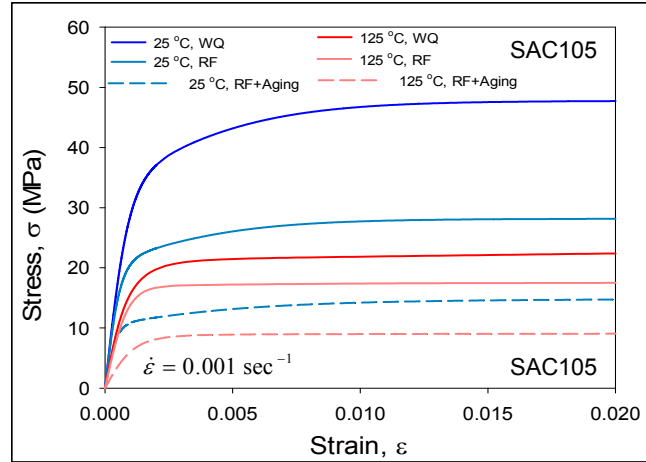


Figure 4.9 Stress-Strain Curve Comparisons for SAC105

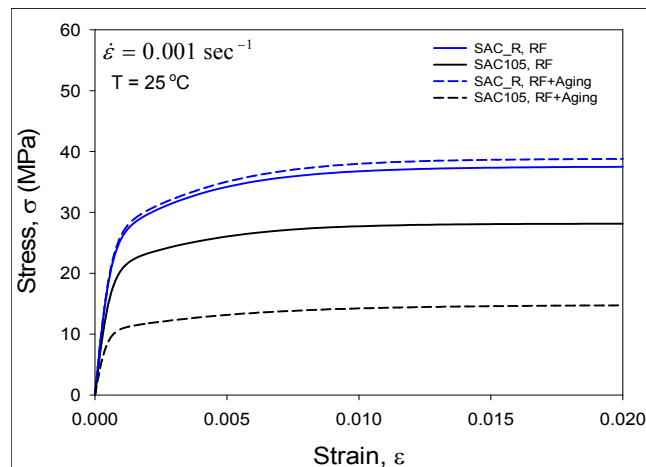


Figure 4.10 Comparisons of Stress-Strain Curves for SAC_R and SAC105
($T = 25 \text{ }^\circ\text{C}$, $\dot{\epsilon} = 0.001 \text{ sec}^{-1}$)

4.4.4 Microstructure Analysis

The microstructure of SAC105 is mainly composed of a β -Sn matrix and two different intermetallic compounds (IMC) namely, Ag_3Sn and Cu_6Sn_5 . The reduction of strength of SAC105 after aging can be attributed to 2 major facts [103]. First, aging causes coarsening of the Ag_3Sn and Cu_6Sn_5 intermetallic compounds and hence reduces their ability to block dislocation movements. Second, the β -Sn phase also coarsens/grows with aging, and hence reduces the strength of the alloy.

For the SAC_R alloy, there is no silver and thus no Ag_3Sn intermetallics. In addition, Bi doesn't form any IMC with Sn. Therefore, the only IMC that should present in microstructure of SAC_R is Cu_6Sn_5 . From the Sn-Bi phase diagram (see Figure 1.11), it is observed that Bi has a good (~1.8%) solid solubility in Sn at room temperature. Hence Bi contributes to some enhancement in strength of the SAC-Bi alloy before aging by the solid solution strengthening mechanism.

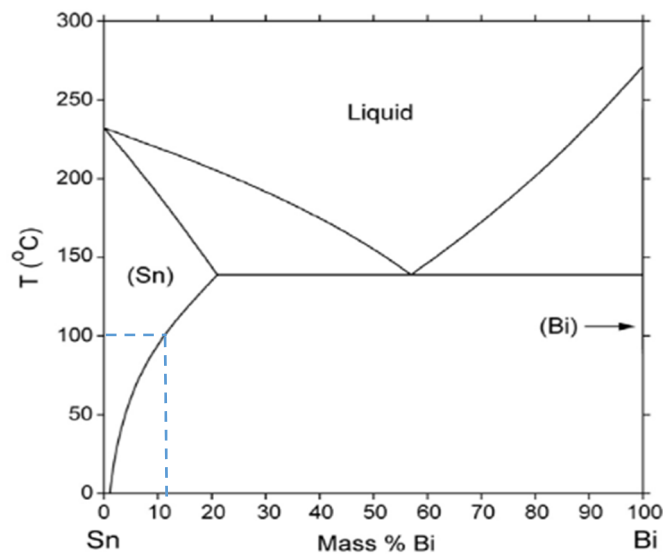
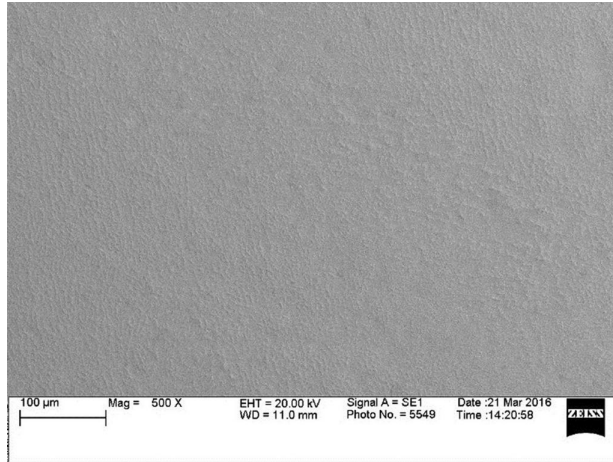


Figure 4.11 Sn-Bi Phase Diagram
<http://www.metallurgy.nist.gov/>

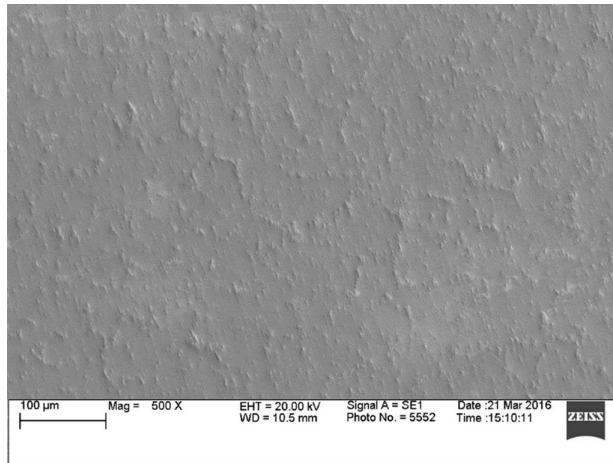
During aging, intermetallic coarsening effects in SAC_R are reduced relative to SAC105 because of a relative lack of IMC particles. In addition, Cai and coworkers [28] have demonstrated that additional Bi will go into solution in the β -Sn matrix during the aging of SAC-Bi alloys. As seen in Figure 4.11, the solid solution solubility of Bi increases from 1.8% at $T = 25^\circ\text{C}$, to about 14% at 100°C . Thus, the Bi present in the as solidified microstructure of SAC_R as a separate Bi phase will have the tendency to go into the solution with the β -Sn matrix during aging. This will lead to additional solid solution

strengthening of the SAC-Bi alloy. A hypothesis was developed to explain the experimental observation. The hypothesis is the observed slight enhancement of strength of SAC_R during aging is due to the increases in strength from solid solution strengthening exceeding any reductions in strength caused by IMC and β -Sn phase coarsening.

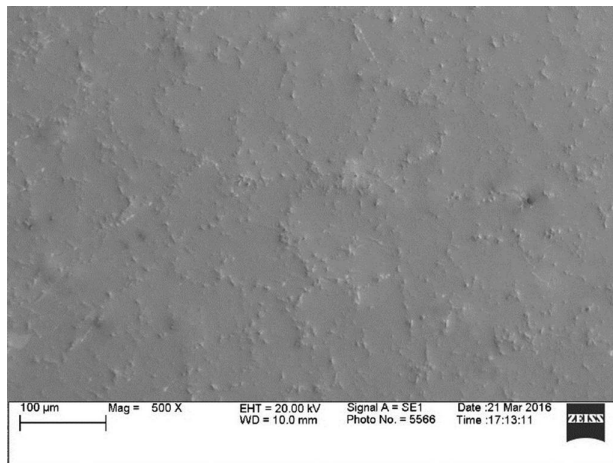
To support the proposed mechanism for mitigation of aging effects in SAC-Bi alloys, a study on the microstructure of SAC_R was performed as shown in the secondary electron (SEI) imaging in Figure 4.12, and backscattered electron (BSE) imaging in Figure 4.13. In each Figure, images are shown for the WQ, RF, and RF+Aging microstructures. From Figure 4.12(a), the fine microstructure of the WQ samples is clearly evident. The RF and RF+Aging samples illustrate coarser microstructures in Figures 4.12(b) and 4.12(c), and aging can be seen to result in growth of the β -Sn phases and Cu_6Sn_5 IMC particles. From Figure 4.13, the BSE images exhibit traces of white particles in the microstructure. This is most evident at higher magnification (Figure 4.13(b)). EDS analysis of these white particles has confirmed that they are Bi rich phases/regions with more than 80% Bi. After aging, these particles are not evident, suggesting that the Bi has completely dissolved into the β -Sn matrix providing solid solution strengthening. Thus, the microstructure results strongly support the hypothesis for aging mitigation.



(a)

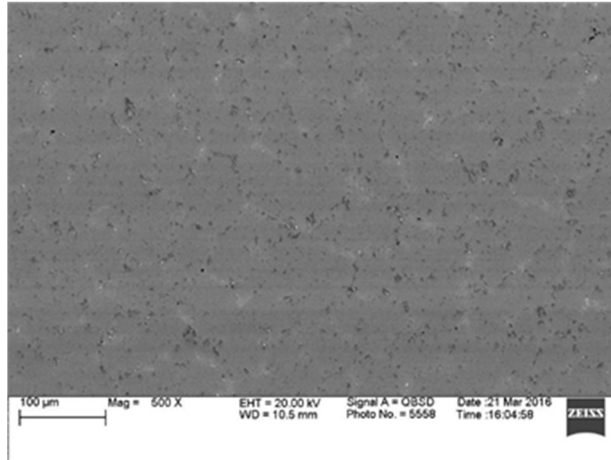


(b)

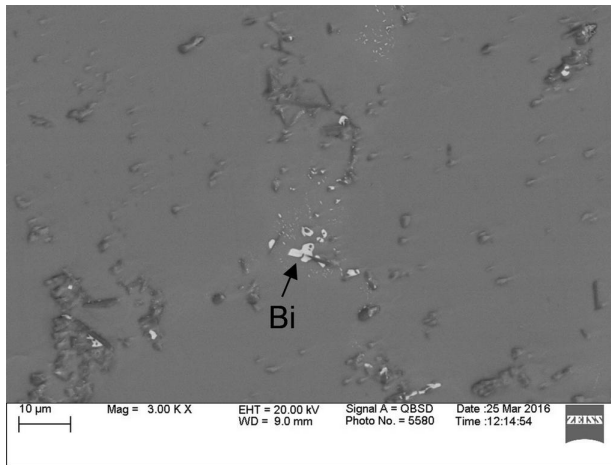


(c)

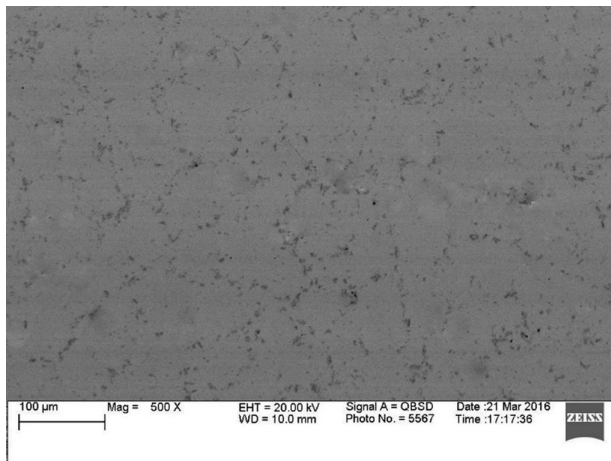
Figure 4.12 (a-c) SEM Images for SAC_R Microstructure (SEI)



(a)



(b)



(c)

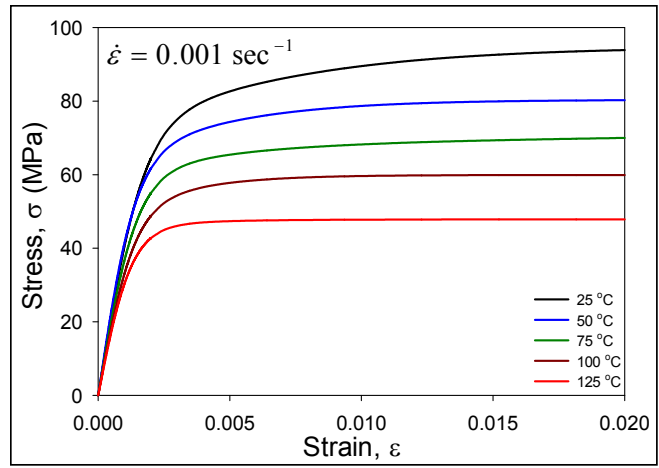
Figure 4.13 (a-c) SEM Images for SAC_R Microstructure (BSE)

4.5 Effects of Aging on SAC_Q (CYCLOMAX)

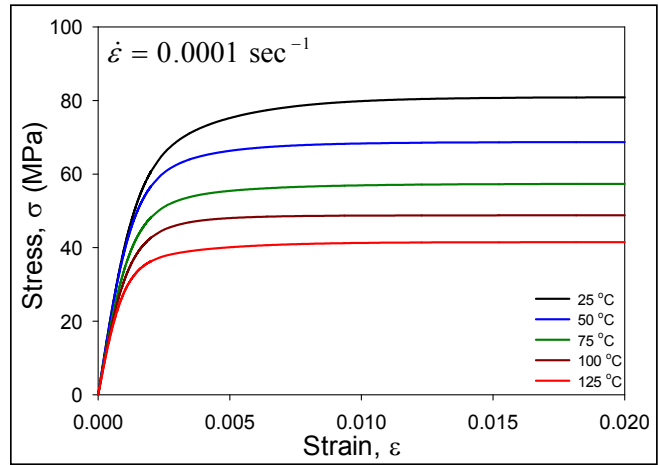
Mechanical stress-strain tests have been performed on SAC_Q solder samples. Test specimens were first prepared using WQ cooling profile (WQ) and then a portion of the prepared solder sample was passed through a nine-zone reflow (RF) oven with a preset temperature profile (RF) which is typical for a BGA solder joint preparation. Some of the reflowed samples were exposed to isothermal aging at $T = 100\text{ }^{\circ}\text{C}$ (RF + 3 Months Aging) for 3 months. The stress-strain tests were performed before and after aging, at 15 different test conditions achieved by a combination of three strain rates ($\dot{\epsilon} = 0.001, 0.0001, \text{ and } 0.00001\text{ sec}^{-1}$) and five test temperatures ($T = 25, 50, 75, 100, \text{ and } 125\text{ }^{\circ}\text{C}$). From the experimental stress-strain data, the nine Anand constitutive model parameters were determined for the alloy SAC_Q in three different conditions (i.e. WQ, RF and RF + 3 Months Aging).

4.5.1 Stress-Strain Data for Various Temperature and Strain Rates

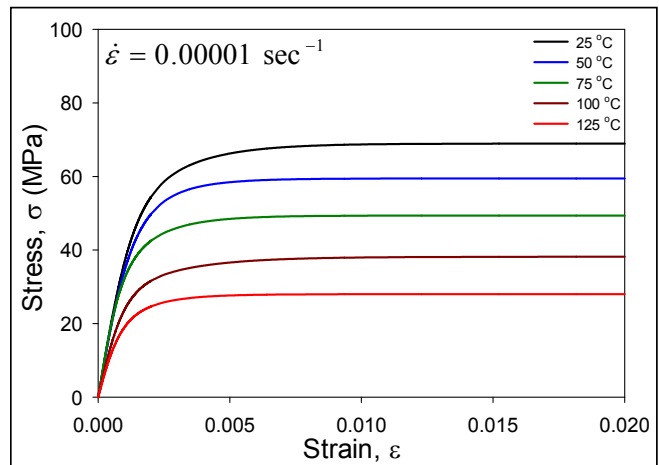
The recorded stress-strain curves for SAC_Q (WQ) at strain rates of 0.001, 0.0001, and 0.00001 sec⁻¹ are shown in Figures 4.14a, 4.14b, and 4.14c, respectively. Each curve in these plots is an “average” stress-strain curve representing the fit of the empirical model in eq. (3.2) to the 5 recorded stress-strain curves for the particular strain rate and temperature. The five different colored curves in each graph are the results for the 5 testing temperatures ($T = 25, 50, 75, 100, \text{ and } 125\text{ }^{\circ}\text{C}$). As expected, the initial elastic modulus, yield stress, and UTS decrease with increasing temperature. In addition, they also decrease with decreasing strain rate. Analogous results were found for the SAC_Q samples with RF and RF + Aging conditions as shown in Figures 4.15 and 4.16, respectively. The UTS of SAC_Q at different test temperatures and strain rates are presented in Figure 4.17.



(a)

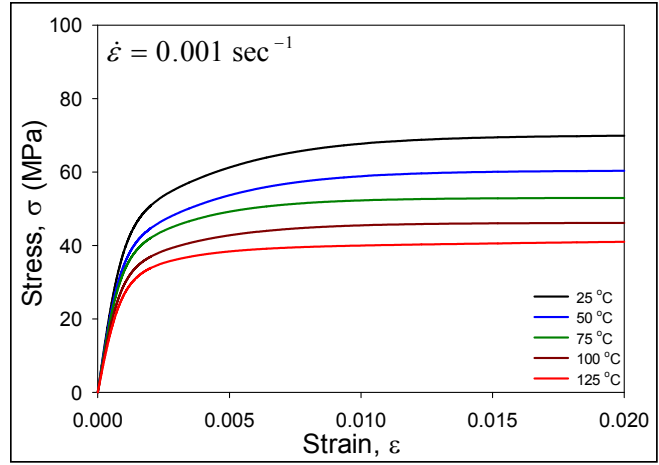


(b)

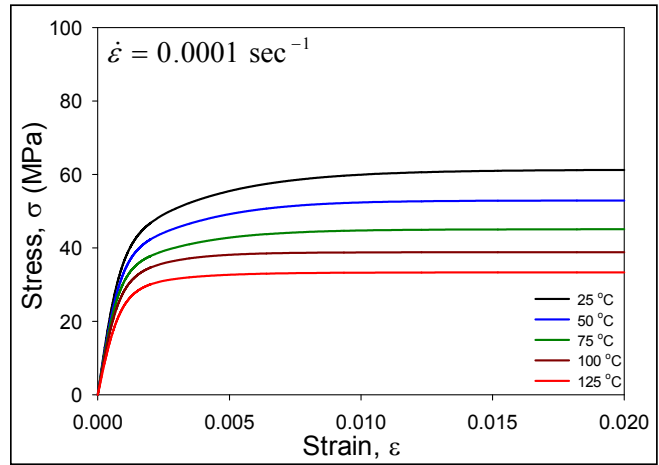


(c)

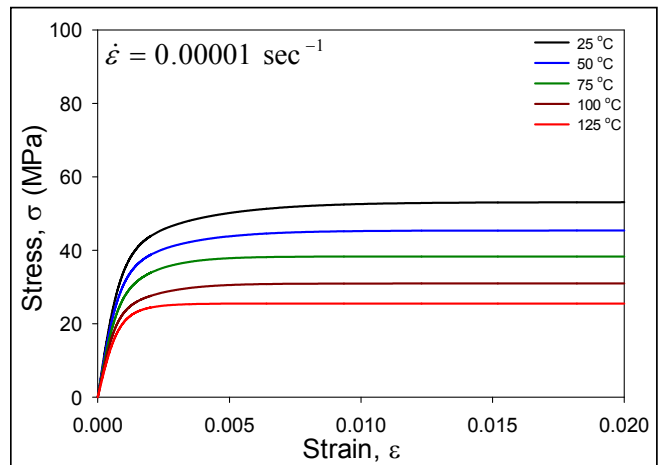
Figure 4.14 (a-c) Stress-Strain Curves Obtained for SAC_Q (WQ)



(a)

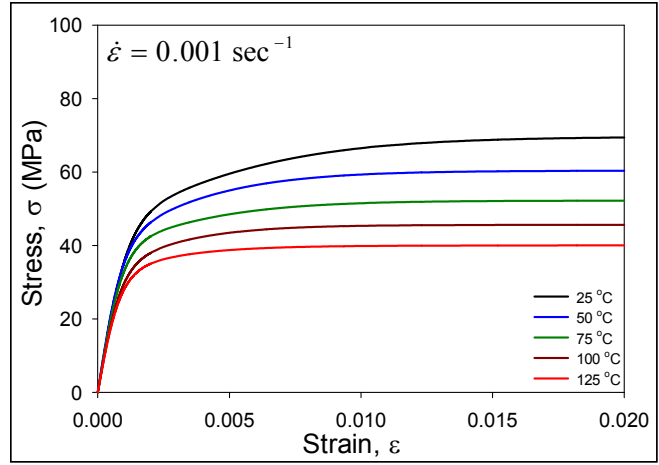


(b)

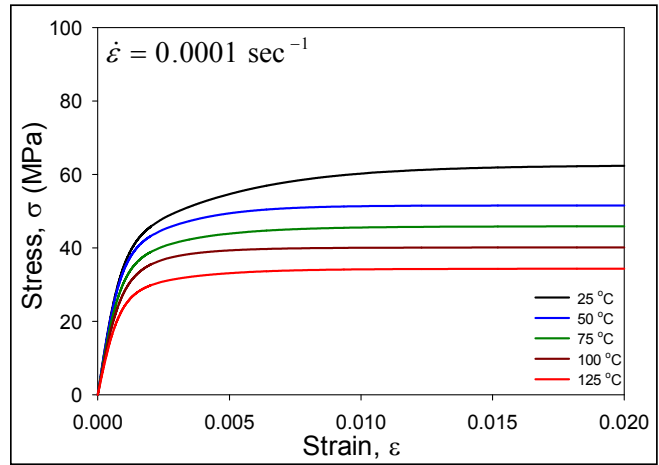


(c)

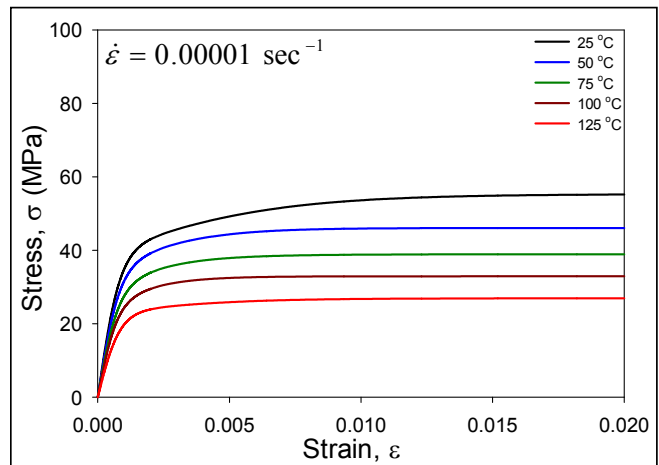
Figure 4.15 (a-c) Stress-Strain Curves Obtained for SAC_Q (RF, No Aging)



(a)

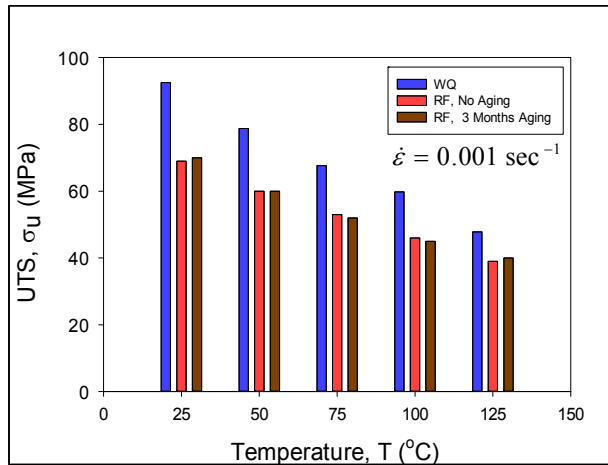


(b)

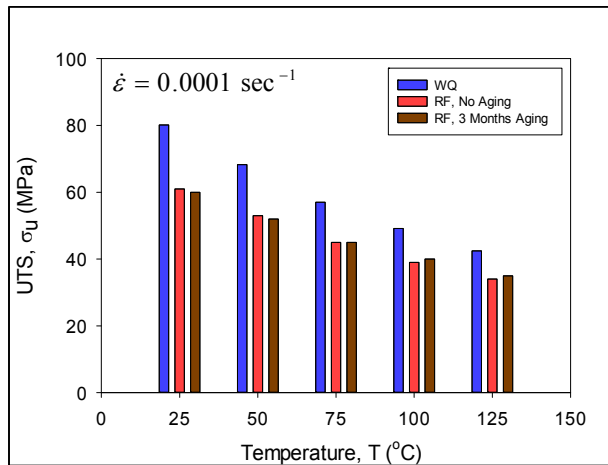


(c)

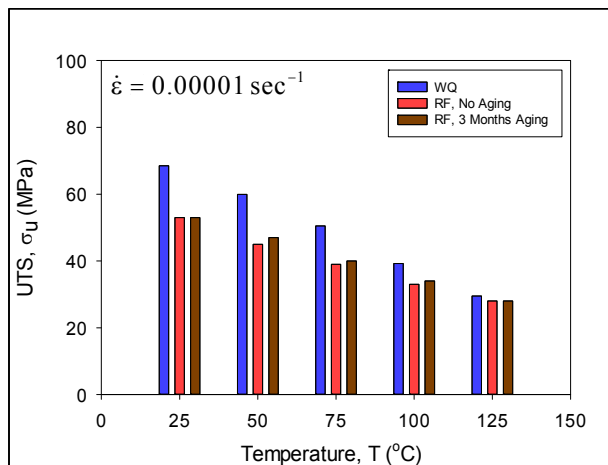
Figure 4.16 (a-c) Stress-Strain Curves Obtained for SAC_Q (RF, 3 Months Aging)



(a)



(b)



(c)

Figure 4.17 (a-c) UTS of SAC_Q at Different Strain Rates and Test Temperatures

The UTS data for SAC_Q presented in Figure 4.17 are summarized in Table 4.4. It is obvious from the figure and the table that the highest UTS values were obtained for WQ samples. Also, Aging of the RF samples at 100 °C for 3 months didn't cause any change in the UTS value of the solder. This observation was true for all the 15 test conditions obtained by a combination of 5 temperatures and 3 strain rates.

Table 4.4 UTS Values of SAC_Q

T (°C)	UTS in MPa (STD)								
	$\dot{\epsilon} = 0.001 \text{ sec}^{-1}$			$\dot{\epsilon} = 0.0001 \text{ sec}^{-1}$			$\dot{\epsilon} = 0.00001 \text{ sec}^{-1}$		
	No Aging (WQ)	No Aging (RF)	3M Aging (RF)	No Aging (WQ)	No Aging (RF)	3M Aging (RF)	No Aging (WQ)	No Aging (RF)	3M Aging (RF)
25	92.5 (3.6)	69.0 (5.1)	70.3 (3.2)	80.2 (3.8)	60.7 (4.5)	60.1 (2.8)	68.5 (3.2)	52.7 (1.5)	53.0 (1.9)
50	78.8 (3.9)	60.0 (3.4)	59.8 (2.3)	68.3 (3.3)	52.7 (1.4)	51.6 (1.0)	59.9 (2.5)	45.5 (1.2)	46.6 (2.3)
75	67.7 (2.1)	52.6 (2.1)	52.1 (2.6)	57.0 (4.0)	45.1 (1.3)	45.7 (3.1)	50.5 (2.1)	39.2 (1.4)	39.6 (2.8)
100	59.8 (4.2)	45.6 (2.3)	45.4 (2.3)	49.2 (1.6)	38.9 (2.8)	40.2 (2.5)	39.2 (1.9)	33.2 (2.2)	34.0 (0.9)
125	47.8 (3.3)	39.1 (2.6)	39.8 (2.2)	42.4 (1.6)	33.6 (2.4)	34.7 (2.8)	29.5 (0.7)	27.5 (0.8)	27.8 (0.8)

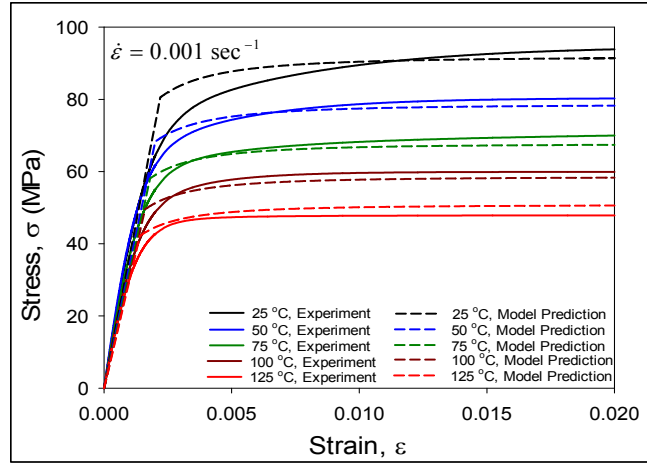
4.5.2 The Anand Parameters for SAC_Q

The data in Figures 4.14-1.16 were used to extract the nine Anand parameters for the SAC_Q material for each conditions (WQ, RF and RF+Aging). As discussed previously, a least-squares regression fitting procedure was utilized to extract the optimal set of Anand parameters using the stress-strain curves for each pre-test conditions at 5 different temperatures and 3 different strain rates. The calculated Anand parameters are tabulated in Table 4.5.

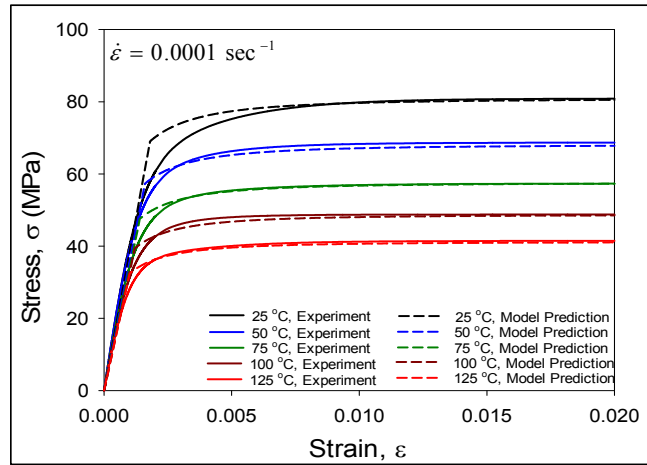
Table 4.5 Anand Parameters for SAC_Q

Par. No.	Anand Par.	Units	WQ	RF	RF+Aging
1	s_0	MPa	32.95	27.93	27.90
2	Q/R	1/K	10742	10750	10750
3	A	sec ⁻¹	7000	8500	6500
4	ξ	-	6	6	6
5	m	-	0.35	0.32	0.32
6	h_0	MPa	95433	65200	65200
7	\hat{S}	MPa	60.48	54	54
8	n	-	0.0077	0.0039	0.0032
9	a	-	1.50	1.56	1.56

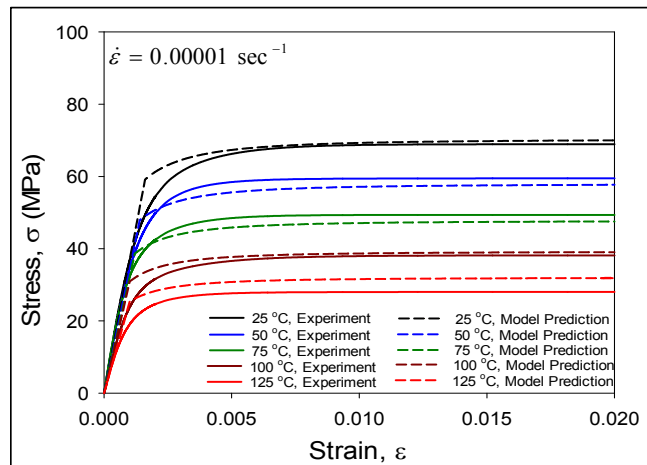
The calculated values of the Anand parameters were used to predict stress-strain behavior for the SAC_Q solder alloy with the various microstructures. For example, the results for SAC_Q (WQ) are presented in Figures 4.18(a), 4.18(b) and 4.18(c) for 3 different strain rates (i.e. 0.001, 0.0001 and 0.00001 sec⁻¹). Reasonable correlations were found for all of the temperatures. Analogous results were found for the other aging condition as well and are presented in Figures 4.19 and 4.20.



(a)

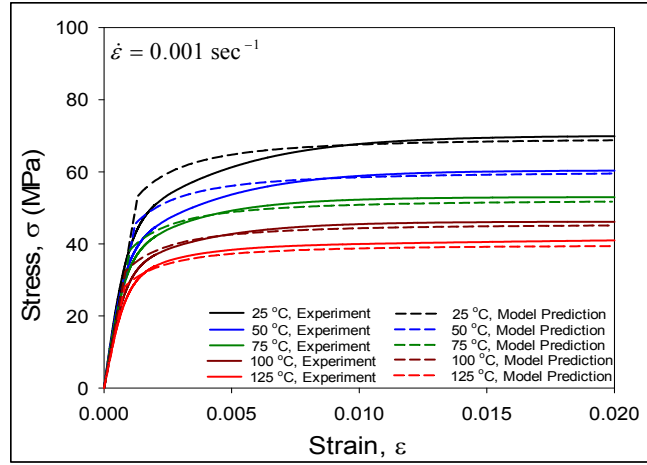


(b)

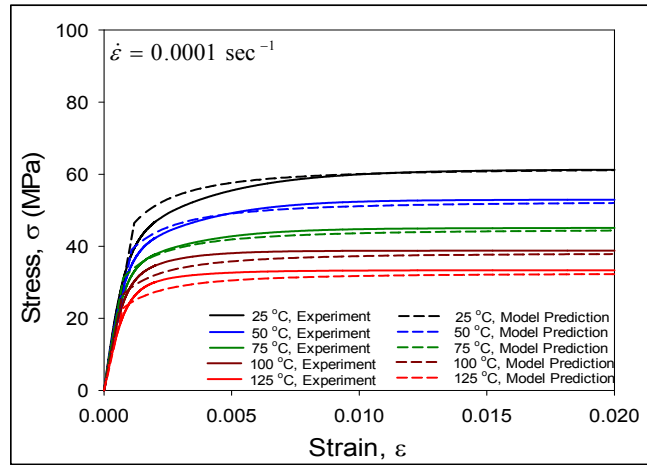


(c)

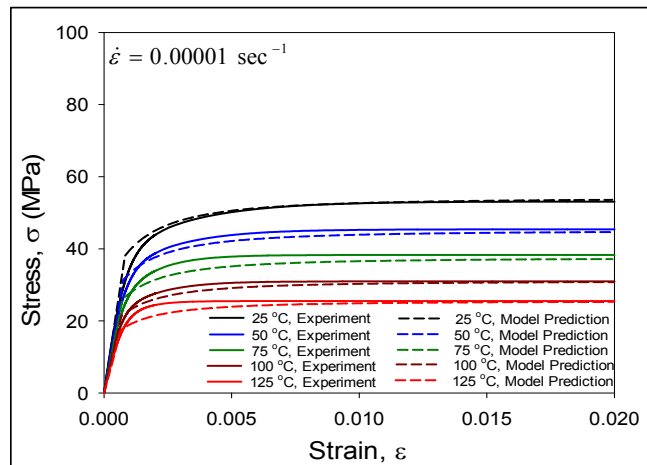
Figure 4.18 (a-c) Comparison between Anand Model Predictions and Experimental Data for SAC_Q (WQ)



(a)

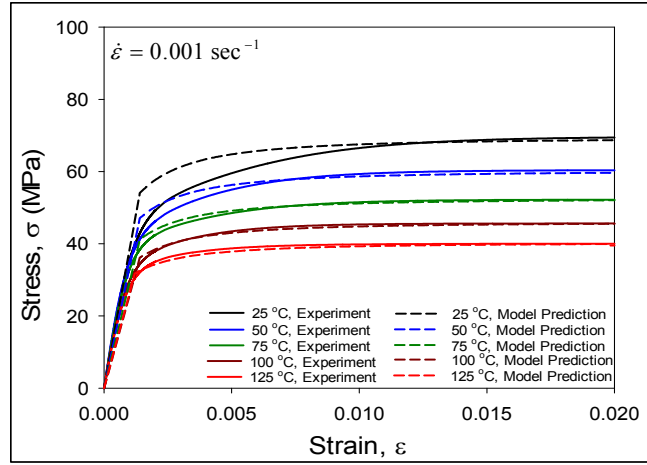


(b)

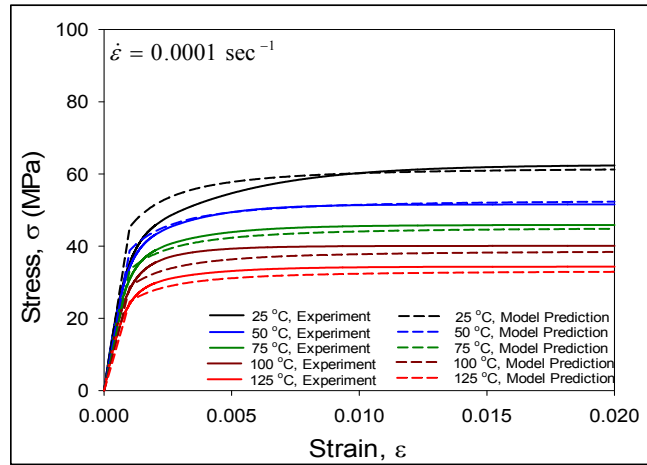


(c)

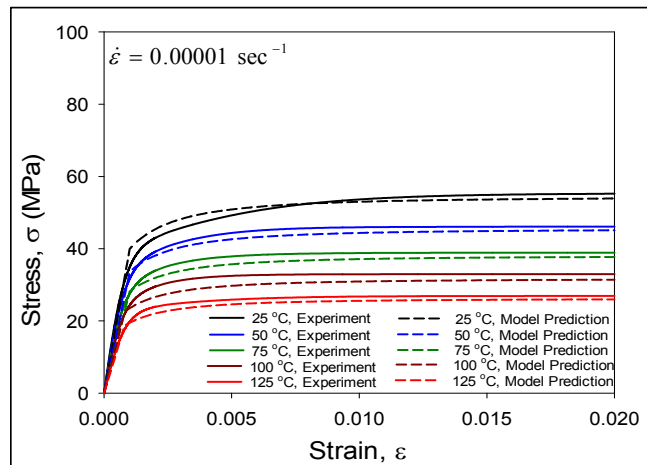
Figure 4.19 (a-c) Comparison between Anand Model Predictions and Experimental Data for SAC_Q (RF, No Aging)



(a)



(b)



(c)

Figure 4.20 (a-c) Comparison between Anand Model Predictions and Experimental Data for SAC_Q (RF, 3 Months Aging)

4.5.3 Stress-Strain Data Comparison (SAC_Q and SAC305)

Selected stress-strain curves for SAC_Q in Figures 4.14-4.16 have been replotted in Figure 4.21 for a strain rate of $\dot{\epsilon} = 0.001 \text{ sec}^{-1}$, temperatures of $T = 25 \text{ }^\circ\text{C}$, and the two aging conditions (no aging and 3 months aging). The analogous curves for SAC305 [101] are plotted in Figure 4.22. It is observed that large aging induced degradations occur for the SAC305 alloy (the dashed curves for the RF+Aging microstructure are significantly below the solid curves for the RF microstructure). For the SAC_Q alloy, there appear to be no aging induced degradations. These observations are further demonstrated in Figure 4.23, where analogous results for SAC_Q and SAC305 are directly compared. In addition, similar results were found for all 5 testing temperatures and 3 strain rates. Previous study on SAC-Bi alloys [28] demonstrated that addition of only Bi significantly reduced or eliminate aging effects in SAC solders.

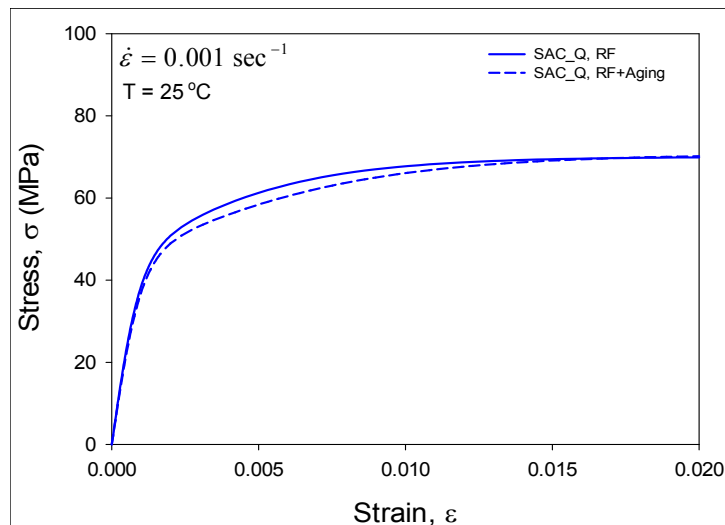


Figure 4.21 Stress-Strain Curves for SAC_Q with and without Prior Aging

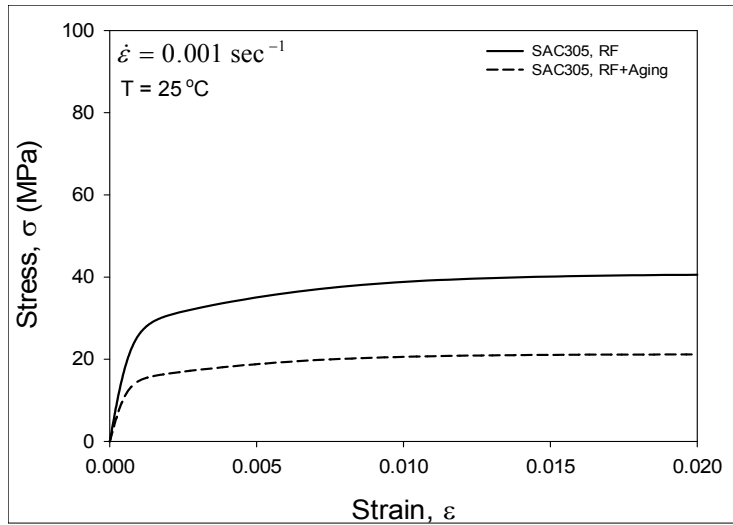


Figure 4.22 Stress-Strain Curves for SAC305 with and without Prior Aging

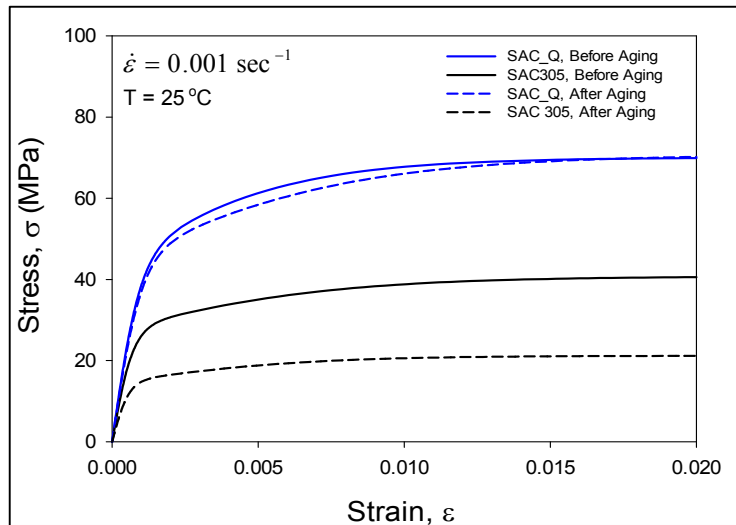


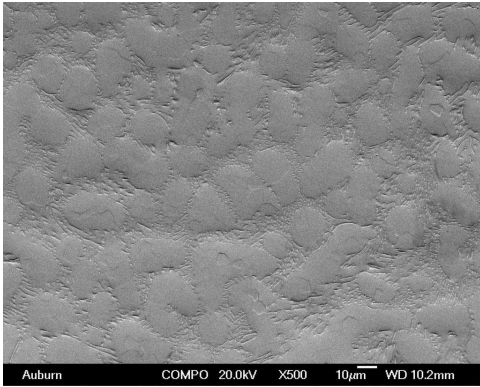
Figure 4.23 Comparison of Stress-Strain Curves for SAC305 and SAC_Q

4.5.4 Microstructure Analysis

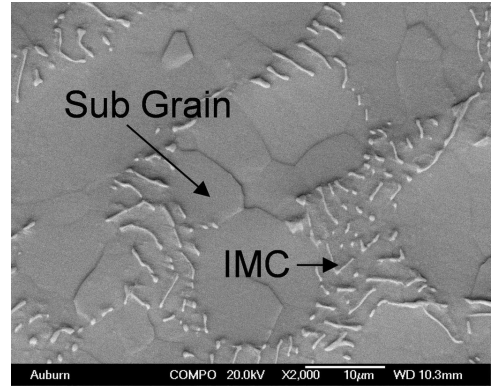
The microstructure of SAC305 is mainly composed of a β - Sn matrix and two different intermetallic compounds (IMC) namely, Ag_3Sn and Cu_6Sn_5 . The reduction of strength of SAC305 after aging can be attributed to 2 major facts [103]. First, aging causes coarsening of the Ag_3Sn and Cu_6Sn_5 intermetallic compounds and hence reduces their ability to block dislocation movements. Second, the β -Sn phase also coarsens/grows with

aging, and hence reduces the strength of the alloy. For the SAC_Q alloy, Bi doesn't form any IMC with Sn. Therefore, the IMC's that should present in microstructure of SAC_Q are same as SAC305 (i.e. Ag₃Sn and Cu₆Sn₅). From the Sn-Bi phase diagram (see Figure 4.11), it is observed that Bi has a good (~1.8%) solid solubility in Sn at room temperature. Hence Bi contributes to some enhancement in strength of the SAC-Bi alloy before aging by the solid solution strengthening mechanism.

Non-aged microstructures of SAC305 and SAC_Q are presented in Figures 4.24 and 4.25, respectively. As expected, a similarity was found between the microstructure of SAC305 and SAC_Q at low magnification (4.24(a) and 4.25(a)). But at higher magnification, the precipitation of remaining Bismuth (Bi), which could not go to the solid solution with Sn, was found in the microstructure. As discussed in section 4.4.4, Bi phase present in the as reflowed microstructure goes into β -Sn matrix during aging at 100 °C and enhance strength by solid solution strengthening. The increases in strength from solid solution strengthening nullify any reductions in strength caused by IMC and β -Sn phase coarsening. As a result, no significant difference was evident in stress-strain behavior, before and after aging. Figure 4.26 shows the absence of separate Bi phase in the SAC_Q microstructure after aging.

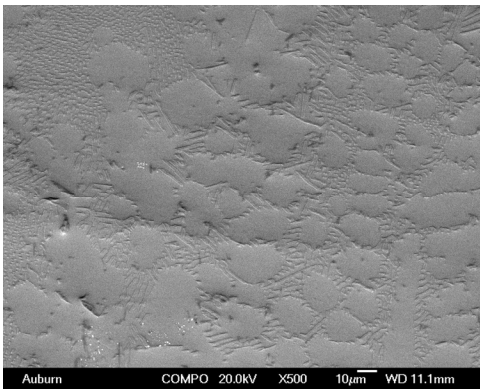


(a)

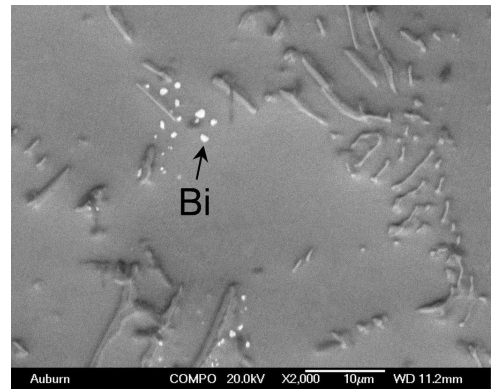


(b)

Figure 4.24 SEM Image for SAC305 Microstructure (a) Low Magnification (500X) and (b) High Magnification (2000X)

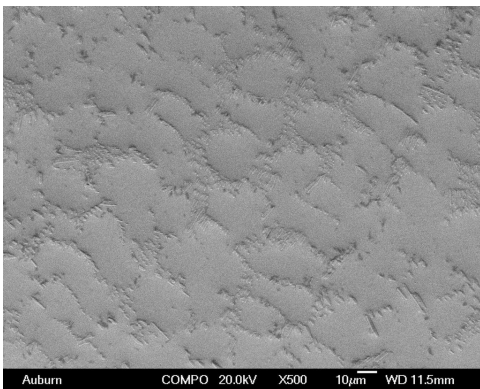


(a)

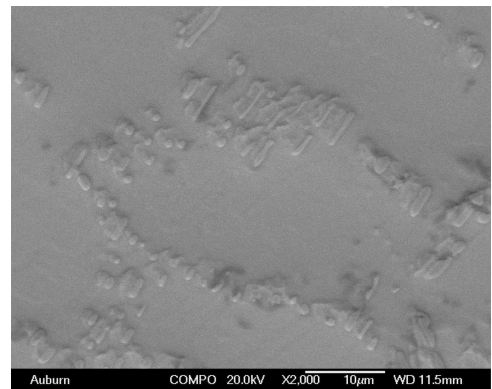


(b)

Figure 4.25 SEM Image for SAC_Q Microstructure (a) Low Magnification (500X) and (b) High Magnification (2000X)



(a)



(b)

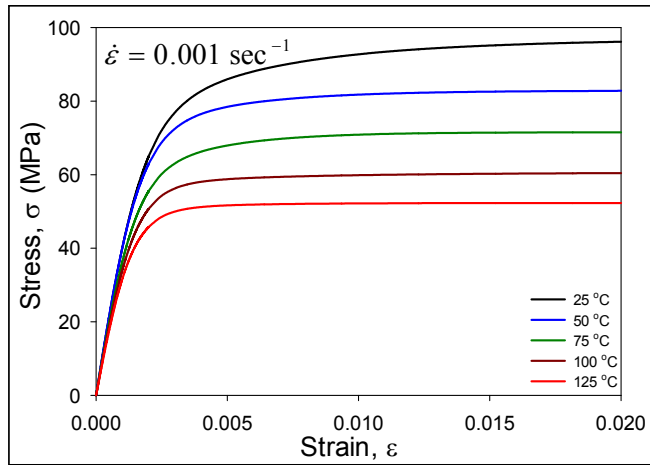
Figure 4.26 SEM Image for Aged SAC_Q Microstructure (a) Low Magnification (500X) and (b) High Magnification (2000X)

4.6 SAC-Bi Alloy Innolot

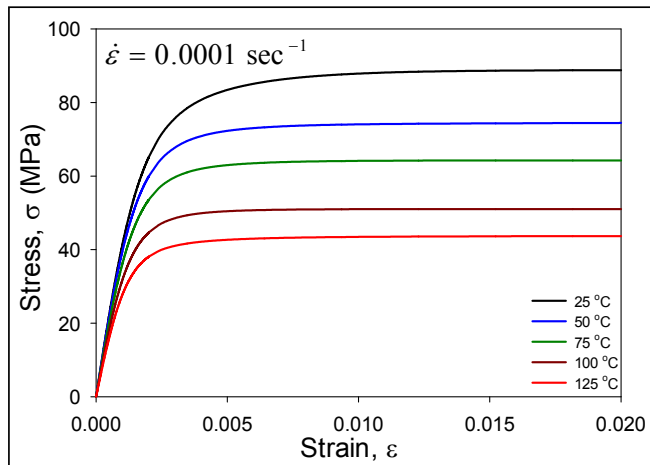
Three different dopants, Bi, Ni and Sb are present in Innolot along with Sn, Ag and Cu. The chemical composition of Innolot is presented in Table 4.1. Stress-strain tests on the SAC-Bi lead free solder samples were performed for samples prepared using a water quenched cooling profile. For Innolot, stress-strain experiments were performed at five temperatures ($T = 25, 50, 75, 100, \text{ and } 125 \text{ }^\circ\text{C}$), and three strain rates ($\dot{\epsilon} = .001, .0001, \text{ and } .00001 \text{ sec}^{-1}$). Using the measured stress-strain data and calculation procedure presented in section 4.2.3, the nine Anand model parameters have been determined for the SAC-Bi alloy Innolot.

4.6.1 Stress-Strain Data for Various Temperature and Strain Rates

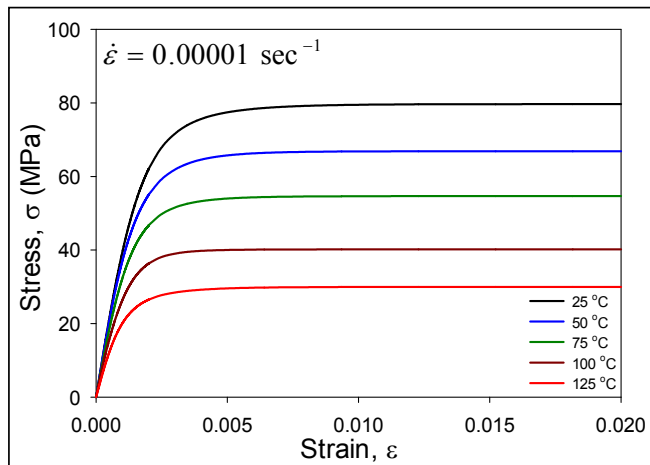
Uniaxial tensile testing of the water quenched Innolot lead free solder specimens has been performed. Stress-strain data were measured at three strain rates and five temperatures. Figures 4.27(a), 4.27(b), 4.27(c) illustrates typical stress-strain curves for Innolot for strain rates of $0.001, 0.0001, \text{ and } 0.00001 \text{ sec}^{-1}$, respectively. In each plot, the 5 colored curves are the stress-strain results for temperatures of $T = 25, 50, 75, 100, \text{ and } 125 \text{ }^\circ\text{C}$. Each curve is the “average” stress-strain curve representing the fit of equation. 3.2 (chapter 3) to the 5 recorded raw stress-strain curves for a given set of temperature and strain rate. For example, the top (black) curve in each plot is the average stress-strain curve at room temperature ($25 \text{ }^\circ\text{C}$), and the bottom (red) curve in each plot is the average stress-strain curve at $125 \text{ }^\circ\text{C}$.



(a)



(b)



(c)

Figure 4.27 (a-c) Stress-Strain Curves for Innolot

It is observed in each graph in Figure 4.27 that the effective elastic modulus, yield stress (YS), and ultimate tensile strength (UTS) all decrease monotonically with temperature as expected. These decreases have been found to be nearly linear with the testing temperature for all alloys. By comparing the analogous results for the same temperature and alloy, but different strain rates, it has also been observed that as the strain rate decreases, the effective elastic modulus, yield stress (YS), and ultimate tensile strength (UTS) all decrease. The UTS values of Innolot obtained at different test temperatures and strain rates are summarized in Table 4.6.

Table 4.6 UTS Values of Innolot

T (°C)	UTS in MPa (STD)		
	$\dot{\epsilon} = 0.001 \text{ sec}^{-1}$	$\dot{\epsilon} = 0.0001 \text{ sec}^{-1}$	$\dot{\epsilon} = 0.00001 \text{ sec}^{-1}$
25	92.4 (5.8)	86.8 (4.7)	77.9 (2.0)
50	81.9 (3.2)	74.1 (3.8)	67.2 (3.8)
75	70.6 (4.1)	63.2 (3.1)	55.3 (1.1)
100	59.3 (2.7)	50.5 (3.5)	41.1 (2.1)
125	51.9 (1.9)	44.0 (2.3)	31.3 (2.4)

4.6.2 The Anand Parameters for Innolot

The data in Figures 4.27 were used to extract the nine Anand parameters for the Innolot solder. As discussed previously, a least-squares regression fitting procedure was utilized to extract the optimal set of Anand parameters. The calculated Anand parameters are tabulated in Table 4.7.

Table 4.7 Anand Parameters for Innotot

Par. No.	Anand Par.	Units	Innotot (WQ)
1	s_0	MPa	32.42
2	Q/R	1/K	12441
3	A	sec ⁻¹	25000
4	ξ	-	7
5	m	-	0.35
6	h_0	MPa	88875
7	\hat{S}	MPa	56.76
8	n	-	0.0097
9	a	-	1.45

The calculated values of the Anand parameters were used to predict stress-strain curves and a reasonable correlations (Figure 4.28) were found with the experimental results.

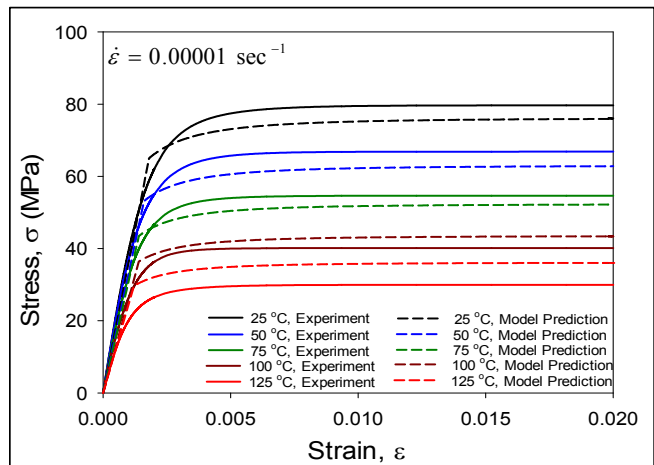
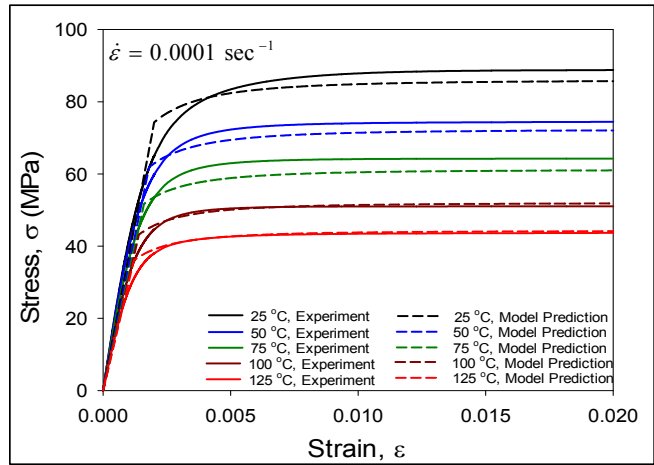
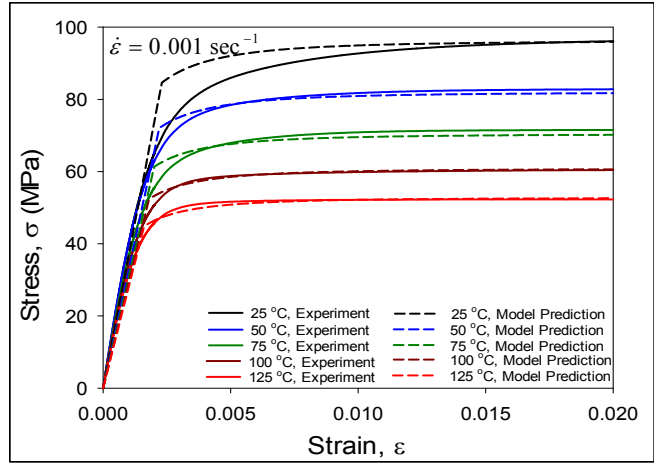
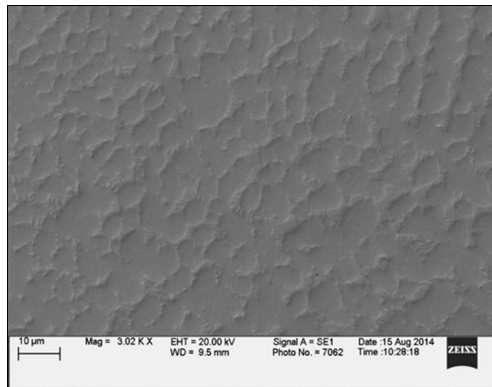


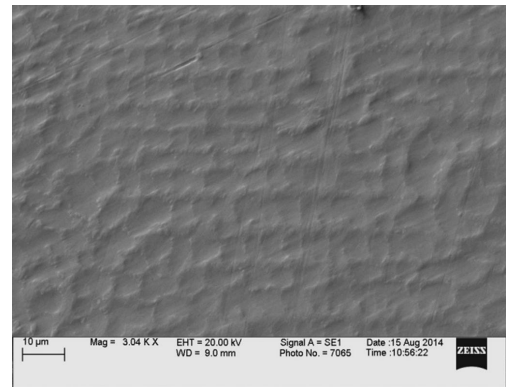
Figure 4.28 (a-c) Comparison between Anand Model Predictions and Experimental Data for Innolot (WQ)

4.7 Comparison of the Microstructure of SAC_R, SAC_Q and Innolot

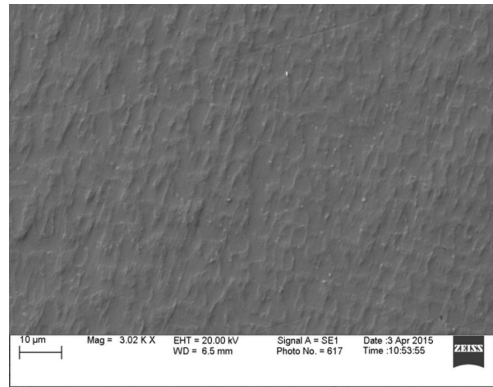
SEM images of the microstructures of the three SAC-Bi alloys are presented in Figure 4.29. It is evident that the amount of IMC (Intermetallic Compound) in the microstructure of SAC_Q was more than in the microstructure of SAC_R. This was due to the presence of higher amount of dopant in SAC_Q compared to SAC_R (Table 4.1). Besides, the microstructure characteristic sizes were found to be much smaller for Innolot. The presence of the additional micro-alloying elements (Ni and Sb) are believed to be the reason for the observed finer microstructure.



(a) SAC_R



(b) SAC_Q



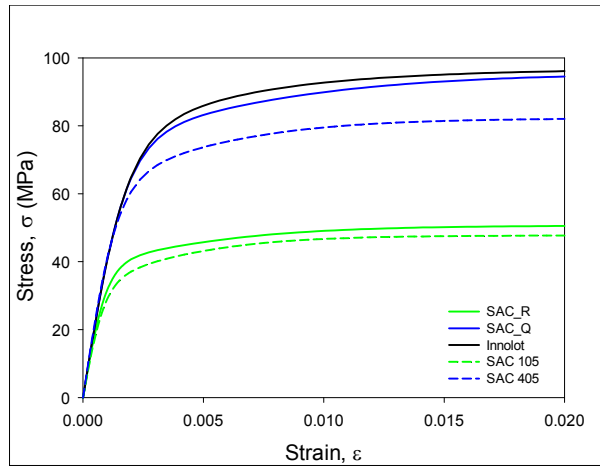
(c) Innolot

Figure 4.29 Microstructure of the SAC-Bi Solder Alloys

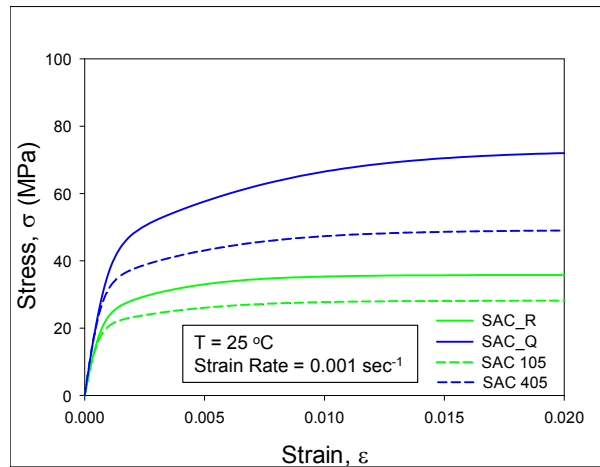
4.7.1 Comparison of Stress-Strain Data of SAC-Bi Alloys with Traditional SAC Alloys

Uniaxial tensile test results of the new SAC-Bi alloys were compared with SAC105 and SAC405. As shown in Figure 4.30 (a), among all three SAC-Bi alloys, Innolot has the highest strength whereas SAC_R has lowest strength which is about 50% of that of Innolot. The presence of Bi along with Ni and Sb is the reason for superior mechanical properties of Innolot. While comparing with SAC105, it was found that although SAC_R does not have any Ag, it has better mechanical properties than SAC105. The presence of Bi along with slightly more Cu is the reason for that. Analogous results (Figure 4.30 (b)) were also obtained when tests were performed with reflowed samples.

Another comparison of the stress-strain curves of different temperatures but same strain rate (0.001 sec⁻¹) was made between SAC_R (WQ) and SAC 105 (WQ) and presented in Figure 4.31. It was found that the strength of SAC105 was 47 MPa when tested at 25 °C and the strength dropped to 22 MPa at 125 °C testing temperature. Reduction of strength was found to be 53%. Whereas the strength of SAC_R dropped from 49 MPa (at 25 °C) to 34 MPa (at 125 °C), which indicates only 30% reduction in strength. Hence it can be said that the strength of SAC_R is less sensitive of testing temperature than SAC105.



(a)



(b)

Figure 4.30 Comparison of Stress-Strain Curves of New SAC-Bi Alloys with SAC105 and SAC405 (a) WQ Samples and (b) (RF Samples)

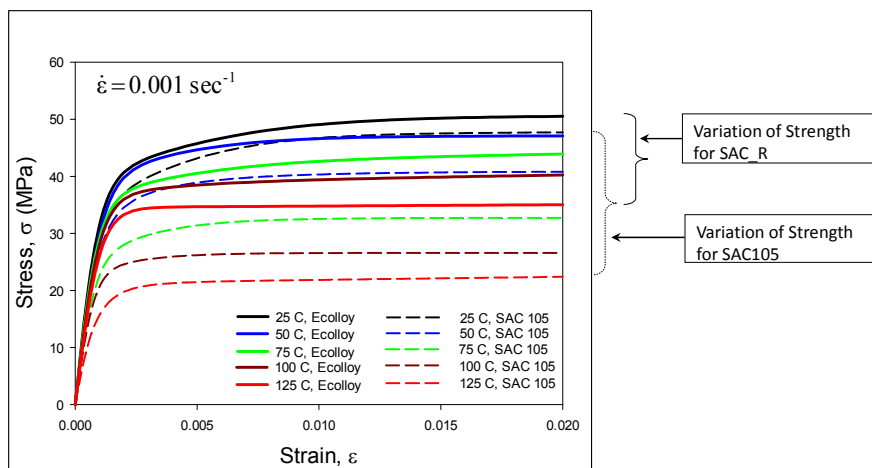


Figure 4.31 Variation of Strength for Different Temperatures

4.8 Summary and Discussion

In this chapter, three new SAC-Bi lead free solder materials recommended for high reliability applications have been chemically analyzed and then mechanically tested in order to determine the nine Anand parameters. For each alloy, three different microstructures were explored using different cooling profiles as well as subsequent isothermal aging. Test specimens were initially solidified with both water quenched (WQ) and reflowed (RF) cooling profiles. In addition, some of the reflowed samples were subsequently subjected to 3 months of isothermal aging at $T = 100\text{ }^{\circ}\text{C}$ (RF + 3 Months Aging) to further coarsen the reflowed microstructure. Uniaxial tensile tests were performed with the SAC-Bi alloy at different cooling profiles and aging times. Test condition includes three different strain rates (0.001 , 0.0001 and 0.00001 sec^{-1}) and five different test temperatures ($25\text{ }^{\circ}\text{C}$, $50\text{ }^{\circ}\text{C}$, $75\text{ }^{\circ}\text{C}$, $100\text{ }^{\circ}\text{C}$ and $125\text{ }^{\circ}\text{C}$). Tensile test results of the SAC-Bi alloy, before and after aging, were compared with those of standard SACN05 alloys.

Anand parameters of the SAC-Bi alloys for different solidification and aging conditions were determined from stress-strain test results. A good correlation was found between Anand model predicted and experimentally obtained results. Although the SAC_R material does not have any silver, it was shown to have better mechanical behavior than SAC 105 due to the presence of Bismuth (Bi) along with a little higher percentage of Copper (Cu). The Innolot and SAC_Q materials were shown to have higher strengths than SAC405. SAC-Bi Alloy SAC_R and SAC_Q have been found to be highly resistant to aging induced degradations. Microstructural analysis has shown that the improved aging

resistance is due to solid solution strengthening where the Bi-phases go into the solution in the β -Sn matrix during aging and enhance strength.

CHAPTER 5

CHARACTERIZATION OF SAC SOLDER JOINTS AT HIGH TEMPERATURE USING NANOINDENTATION

5.1 Introduction

In this chapter, nanoindentation methods were utilized to explore the creep behavior, and aging effects of SAC305 solder joints at several elevated testing temperatures from 25 to 125 °C. A special high temperature stage and test protocol was used within the nanoindentation system to carefully control the testing temperature, and make the measurements insensitive to thermal drift problems. Solder joints were extracted from 14 x 14 mm PBGA assemblies (0.8 mm ball pitch, 0.46 mm ball diameter) that were built as part of the iNEMI Characterization of Pb-Free Alloy Alternatives Project. Since the properties of SAC solder joints are highly dependent on crystal orientation, polarized light microscopy was utilized to determine the orientation of the tested joints. For all the experiments, only single grain solder joints were used to avoid introducing any unintentional variation from changes in the crystal orientation across the joint cross-section. After extraction, the single grain solder joints were subjected to various aging conditions. Nanoindentation testing was then performed on the aged specimens at five different testing temperatures ($T = 25, 50, 75, 100, \text{ and } 125 \text{ }^\circ\text{C}$). In order to understand creep response of the solder joints at different temperatures, a constant force at max indentation was applied for 900 sec while the creep displacements were monitored. With this approach, creep strain rate was measured as a function of both temperature and prior aging conditions. As expected, indent/testing temperature was found to have a significant impact on the mechanical properties and creep strain rate of solder joints. The measured

data have also shown that the effects of aging on solder joints properties become much more significant as the testing temperature increases. In particular, the aging induced degradation rates at high temperatures (100-125 °C) were more than 100X those seen at room temperature. Nanoindentation pile-up effects, although insignificant at room temperature, were observed during high-temperature testing and corrections were made to limit their influence on the test results.

5.2 Sample Preparation for High Temperature Nanoindentation

Sample cross-sectioning and polishing procedure outlined in chapter 3 section 3.5 and 3.6 was followed to prepare samples for high temperature nanoindentation experiments. The space inside the high temperature stage, attached with the nanoindentation system, is limited. The maximum allowable sample height is around 3 mm, which impose a restriction of using an epoxy mounted sample inside the high temperature stage. As a result, an alternative approach was developed to polish solder joint samples without any epoxy encapsulate. As shown in Figure 5.1, cross-sectional samples were mounted on a cylindrical epoxy preform by double-sided tape to facilitate polishing. The polished solder joint array cross-sections were then carefully extracted from the preform.

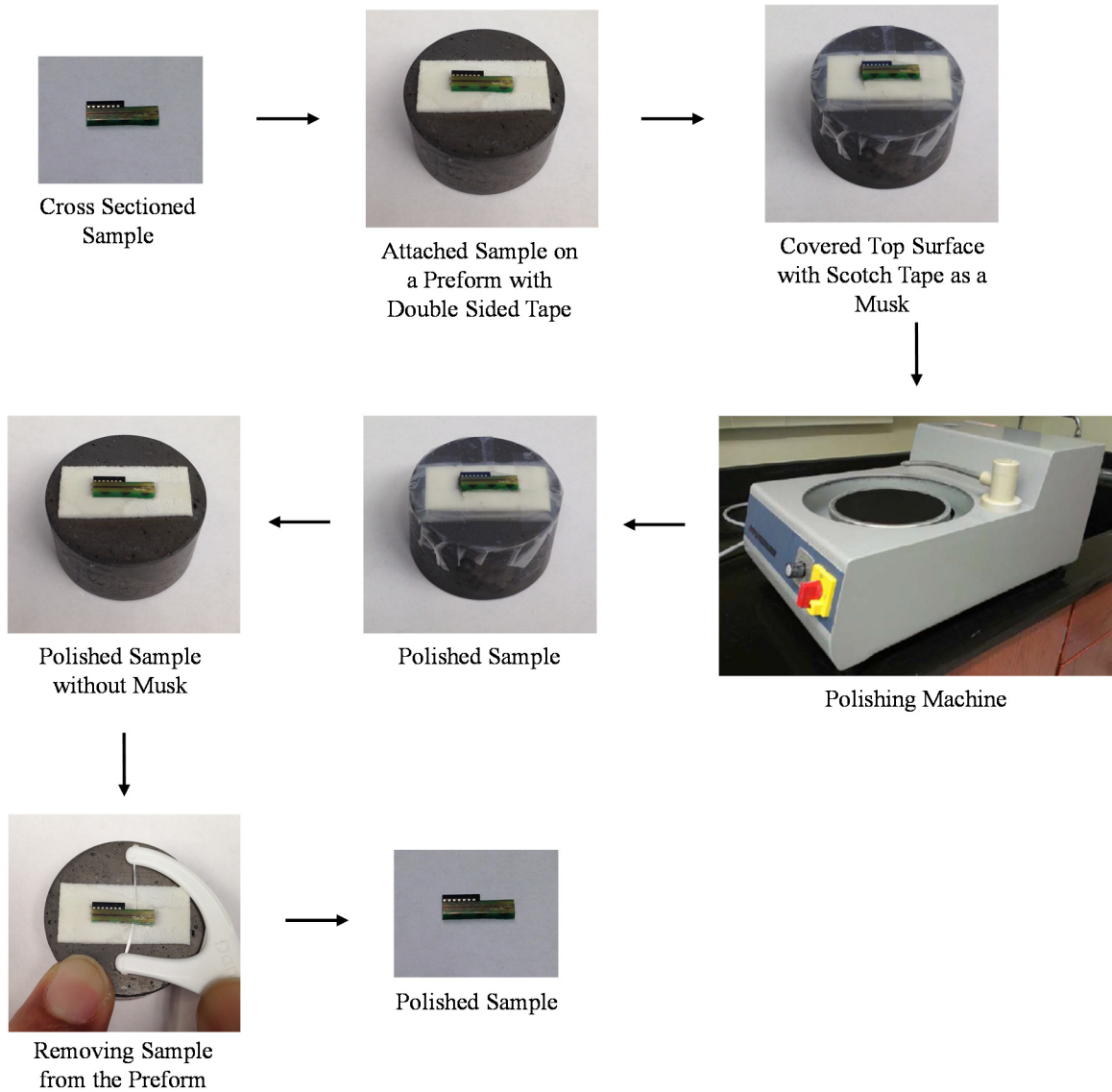
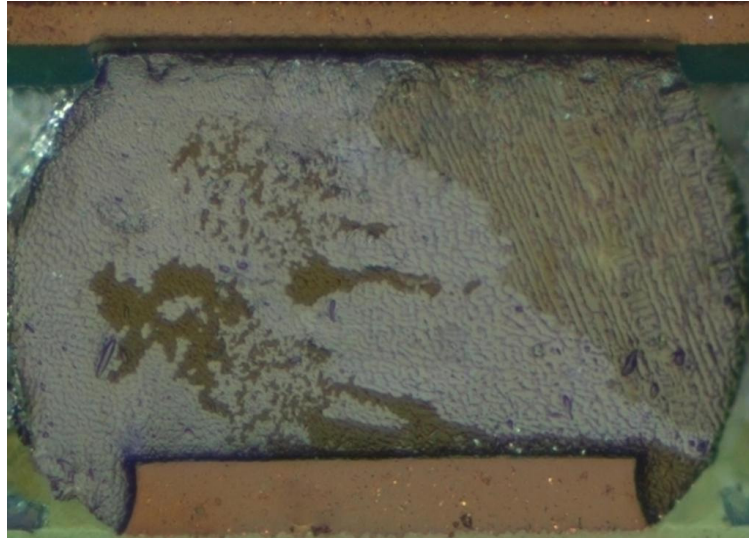


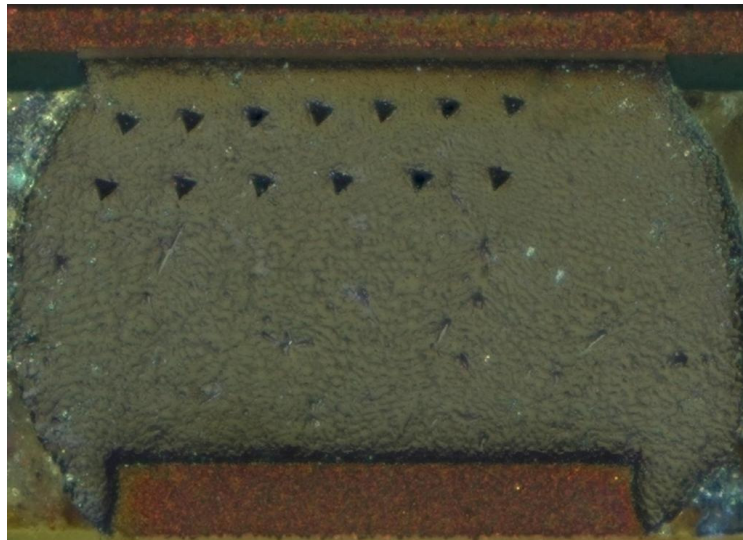
Figure 5.1 Sample Preparation for High Temperature Nanoindentation

Since the properties of SAC solder joints are highly dependent on crystal orientation, polarized light microscopy was utilized to determine the orientation of the tested joints. For all the experiments, only single grain solder joints were used to avoid introducing any unintentional variation from changes in the crystal orientation across the joint cross-section. Among the identified single grain joints, ones with the most uniform

IMC distributions were used for nanoindentation. Figures. 5.2(a) and (b) show polarized light images of multi-grain and single grain solder joint samples.



(a)



(b)

Figure 5.2 (a) Multi-Grain Solder Joint, (b) Single Grain Solder Joint

5.3 High Temperature Nanoindentation System and Test Procedures

The nanoindentation tests in this work were performed using an instrumented Hysitron TI 950 nanoindentation system (Figure 3.17) and a Berkovich indenter tip. The

system was equipped with an xSOL 400 high temperature stage to facilitate elevated temperature material characterization. During each indentation experiment, load versus indentation displacement response of the solder material in the direction normal to the cross-sectional surface was measured. Figure 5.3 shows the high temperature stage within the nanoindentation system, while Figure 5.4 shows images of a test sample in the high temperature stage.

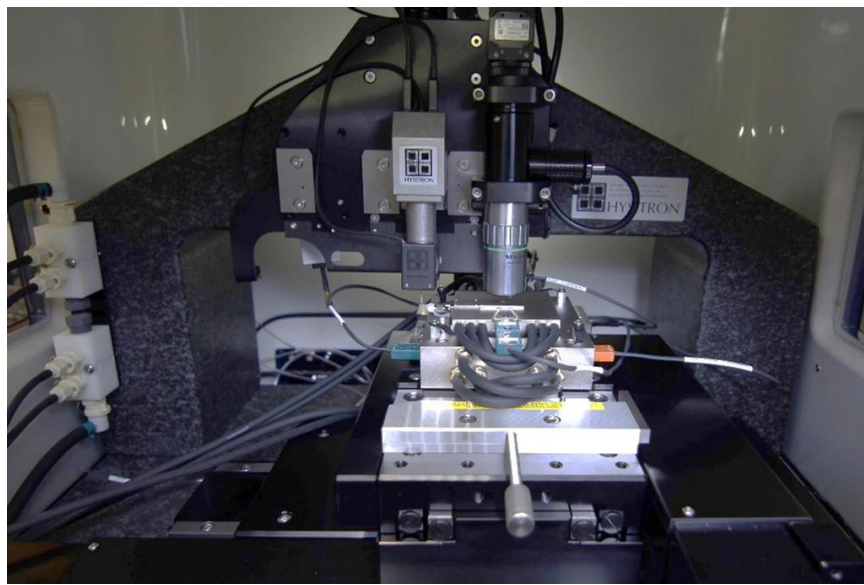
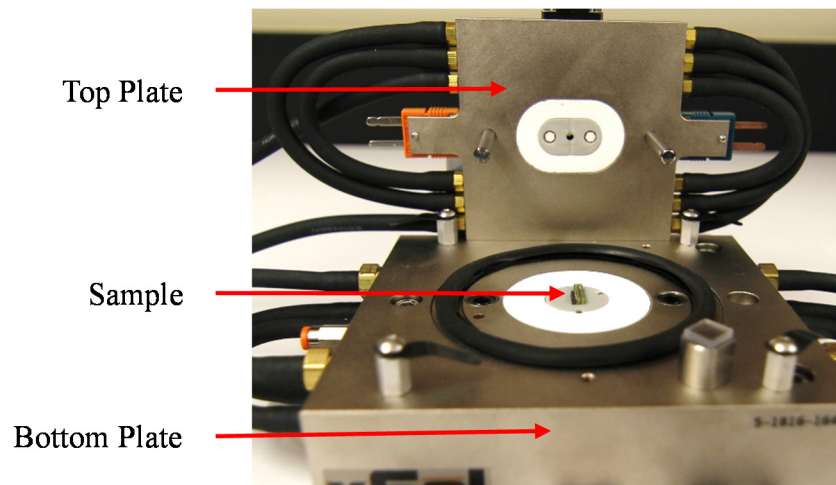
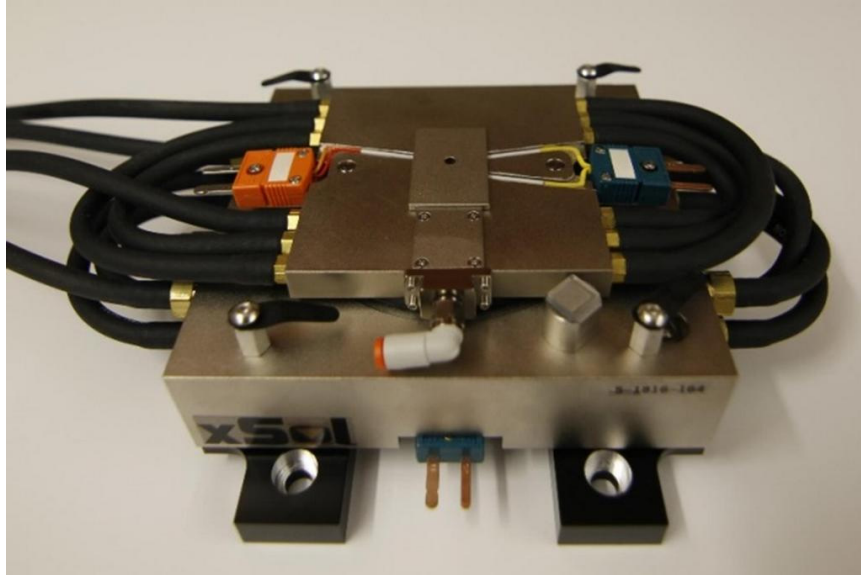


Figure 5.3 High Temperature Nanoindentation System



(a)



(b)

Figure 5.4 Solder Joint Sample in the High Temperature Stage in (a) Open and (b) Close Conditions

An SEM image of a typical permanent indentation mark after completing an indentation is shown Figure 5.5. For each set of experimental test conditions (e.g. temperature and prior aging conditions), a set of 6-10 indents were made, and the measured test data were averaged to obtain statistically relevant results and consistency of inspection. The indents in a set were positioned 30-50 μm apart, to avoid interactions between the plastic zones created by the indentations.

As discussed in the previous section (5.2), all tests in this work were performed on single grain (Sn crystal) solder joints, so that there were no orientation effects caused by an indentation array covering two or more grain boundaries of grains with different crystal orientations (different material properties).

For nanoindentation creep experiments, the maximum load in the performed tests was selected to be 10 mN. As shown in Figure 5.5, this ensured that the indentation marks were large enough to cover all the phases of lead free solder material. Therefore, the

nanoindentation tests characterized the averaged global mechanical properties of the SAC305 solder joints, rather than the localized properties in the β -Sn dendrites or the Ag_3Sn and Cu_6Sn_5 intermetallic particles in the eutectic regions between dendrites. Calibration of the indenter tip shape was performed on a standard fused quartz sample.

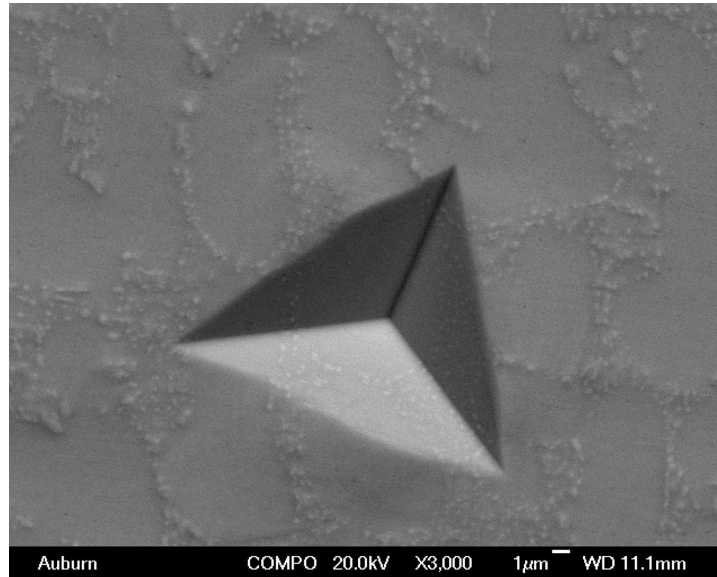


Figure 5.5 Permanent Indentation After Testing

After reaching the peak load of 10 mN, indentation creep tests were performed by holding the load constant for 900 sec. A load versus time graph for a single indentation test performed in this work is shown in Figure 5.6. A very small sinusoidal load was applied along with the static load of 10 mN during the peak load dwell period. Since the effects of thermal drift will be negligible during the first few seconds at constant load, a so-called “reference segment” of 5 sec duration was introduced at the beginning of the creep deformations. The purpose of this reference segment was to calculate the modulus of the material from the indent displacements. After the reference segment was completed, the calculated modulus was utilized to calculate the area of indent throughout the creep test (instead of using the indent depth). Thus, the reference segment makes the experiments

relatively insensitive to thermal drift problems. An example of a load vs. indent displacement graph obtained after a nanoindentation creep test is shown in Figure 5.7. The displacement during the Dwell/Creep region of the curve was utilized to obtain creep properties of the solder joint.

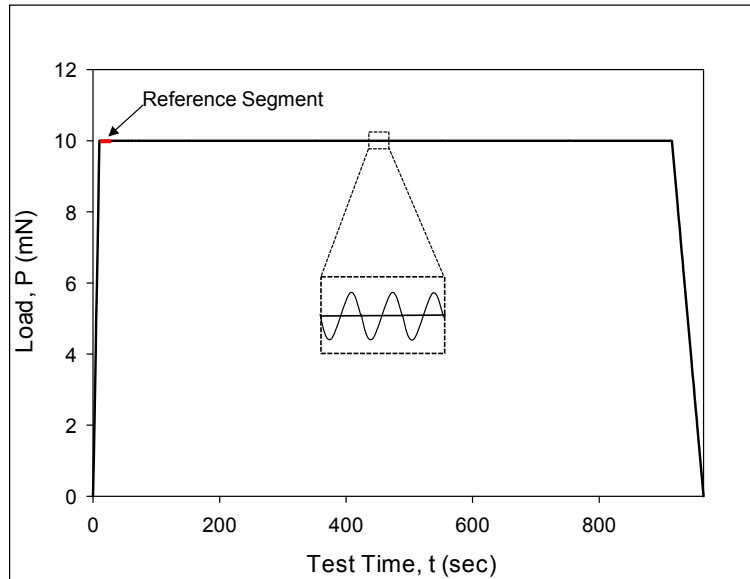


Figure 5.6 Loading Profile Used for Nanoindentation Creep Tests

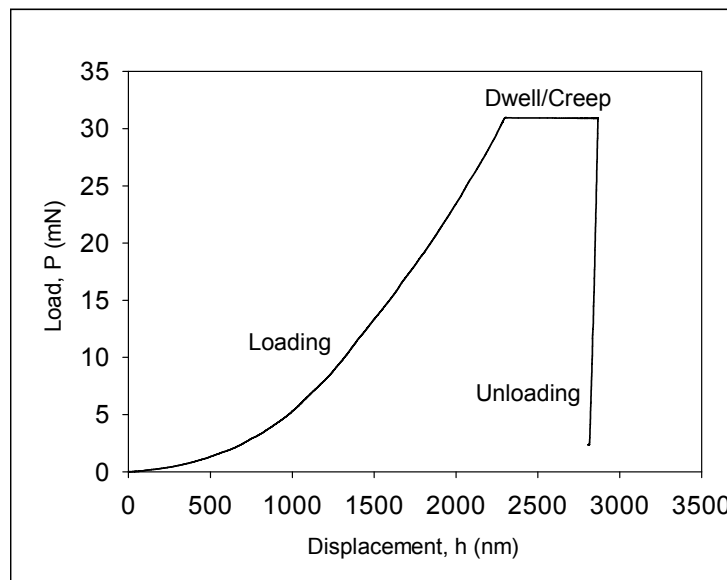


Figure 5.7 Load-Displacement Curve Obtained from a Nanoindentation Creep Test

5.4 Pile-up Correction for High Temperature Nanoindentation Tests

Accumulation of material near the edges of an indent is known as pile-up. Although normally insignificant for room temperature testing, pile-up was observed in the high-temperature tests in this work, especially at $T = 100$ and 125 °C. From the 3D SPM image of a single indent (Figure 5.8) on SAC305 solder, obtained at 100 °C test temperature, pile up is apparent. The semi-ellipse method for pile-up correction proposed by Kese, et al. [77] was used here to adjust our nanoindentation creep data. According to this method, the corrected contact area A is given by:

$$A = A_{OP} + A_{PU} = A_{OP} + 5.915h_c \sum_{i=1}^3 a_i \quad (5.1)$$

where A_{OP} is the contact area obtained from the normal calculations based on the tip shape, A_{PU} is the additional pile-up area, h_c is contact depth, and a_i ($i = 1, 2, 3$) are the height of pile-ups mid-way along the three edges. In this investigation, A_{OP} and h_c were obtained from the normal indentation results reported by the system. In order to determine a_i , the profile of each indent was scanned using SPM imaging. A sample of the topographic SPM image obtained for one typical indent and the location of a_i is shown in Figure 5.9. The surface profile was measured along three different sections as shown in Figure 5.10 to determine the value of a_i along each edges.

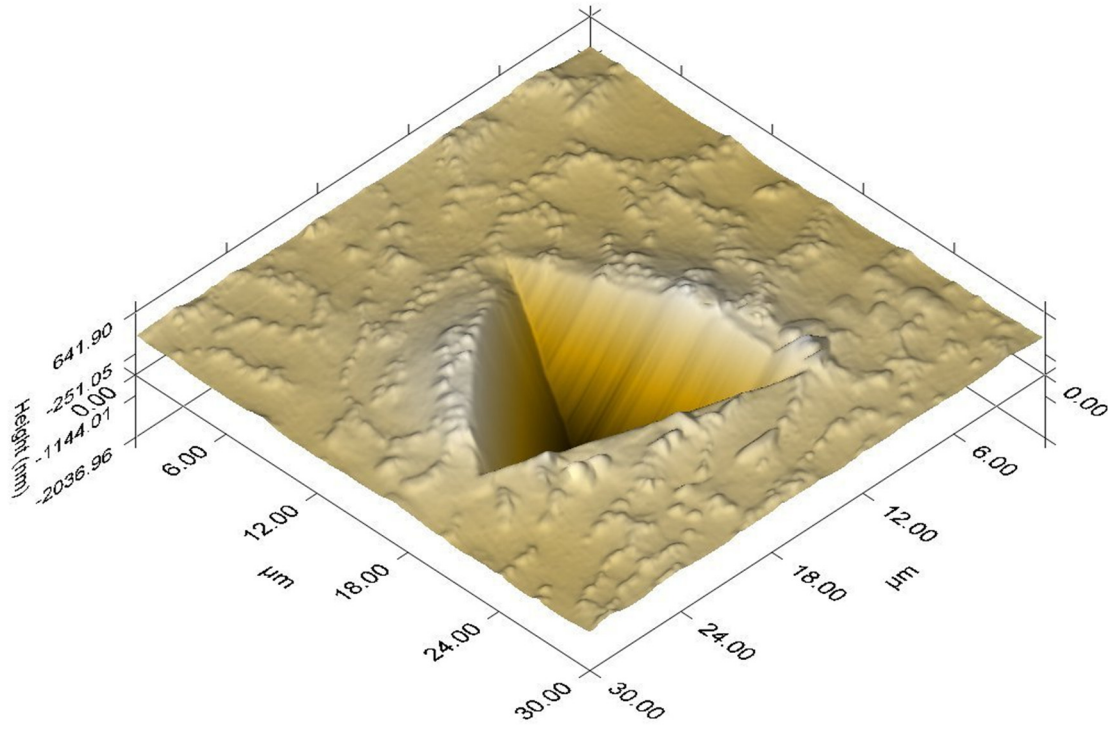


Figure 5.8 3D SPM Image of a Single Indent

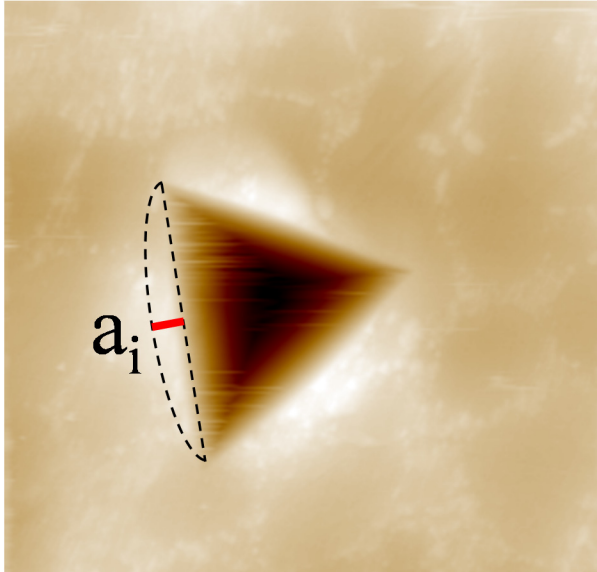


Figure 5.9 2D SPM Topography Data for a Single Indent

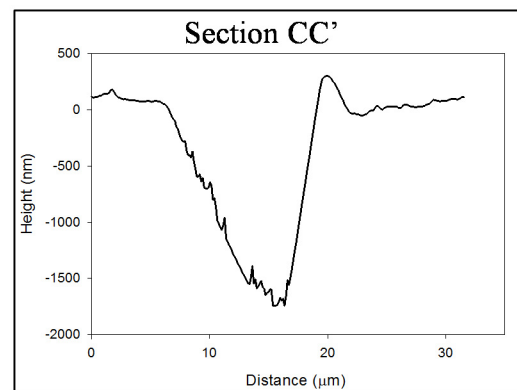
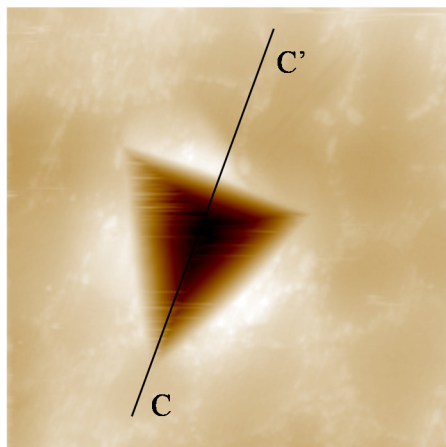
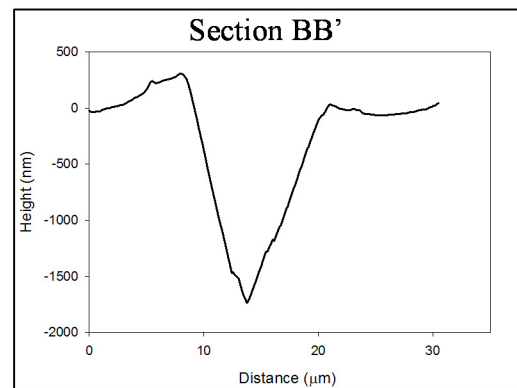
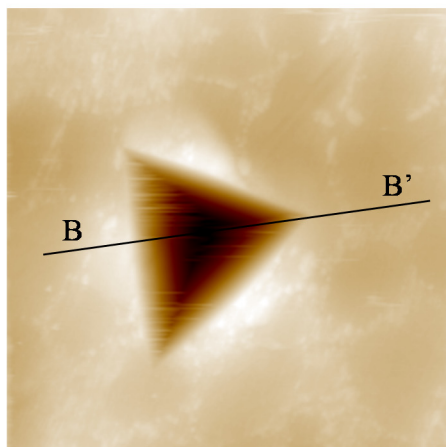
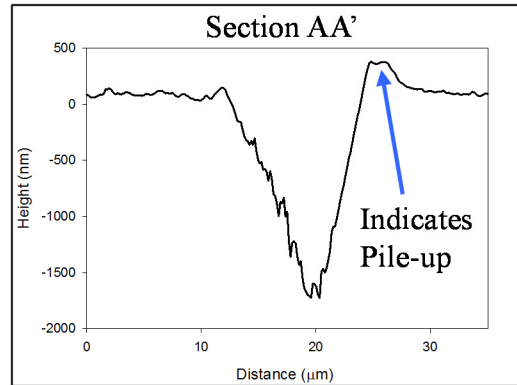
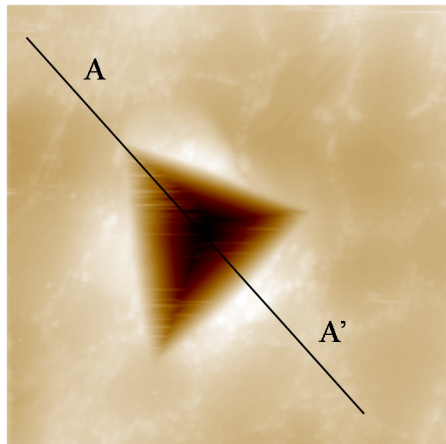


Figure 5.10 SPM Topography Data for a Single Indent and Pile-up Measurement

5.5 Measurement of Creep Behavior

The displacement during the hold period of 900 second at the maximum load of 10 mN was utilized to obtain creep properties of the solder joint. An example of the measured displacement during the hold period versus time plot, for an array of indents performed on a single grain solder joint under similar test conditions, is presented in Figure 5.11.

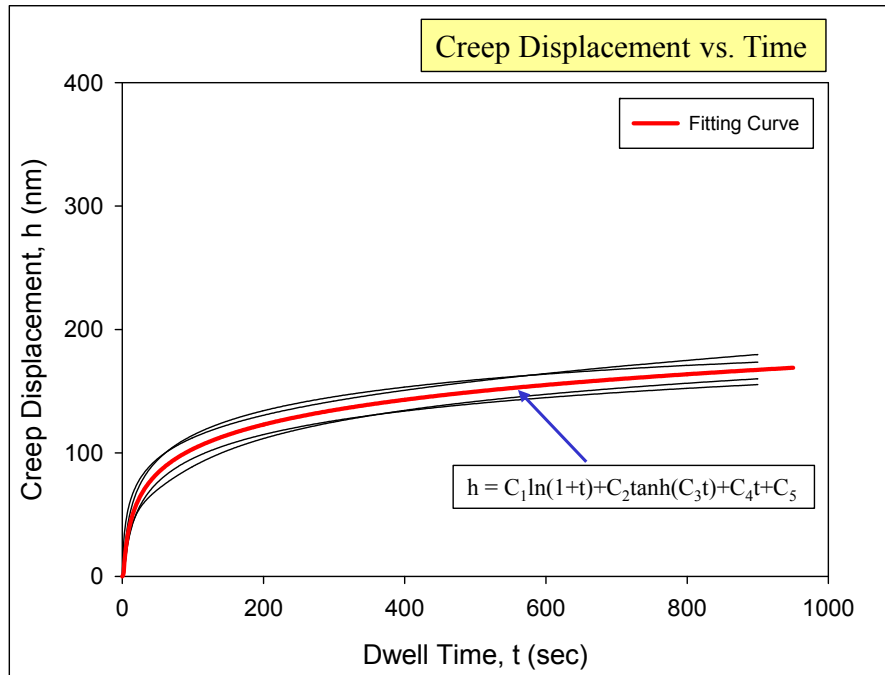


Figure 5.11 Nanoindentation Creep Displacement on SAC305 Joint

The log hyperbolic tangent creep model proposed by Chhanda, et al. [104] has been used to fit and model the recorded indentation depth versus time data during the creep loading.

$$h(t) = C_1 \ln(1+t) + C_2 \tanh(C_3 t) + C_4 t + C_5 \quad (5.2)$$

where C_1 , C_2 , C_3 , C_4 , and C_5 are fitting constants. All the black curves in Figure 5.11 represents the fit of equation 5.2 to the creep data from several individual indentation

experiments whereas the red color curve represents a mathematical average of the series of indentations. In addition, the method for calculating the creep strain rate proposed by Mayo and Nix [105, 106] has been adopted in this study. According to the method, creep strain rate can be determined from instantaneous creep deformation and deformation rate using the following equation

$$\dot{\epsilon} = \frac{1}{h} \frac{dh}{dt} \quad (5.3)$$

In order to determine creep strain rate, the derivative of equation 5.2 with respect to time was divided by corresponding instantaneous displacement. A plot of creep strain rate versus time for the deformation data from Figure 5.11 is shown in Figure 5.12 and it was found that after 900 seconds of holding time, creep strain was nearly constant with a value of 1.83×10^{-4} . In reality, a constant strain rate was never achieved in a nanoindentation creep test.

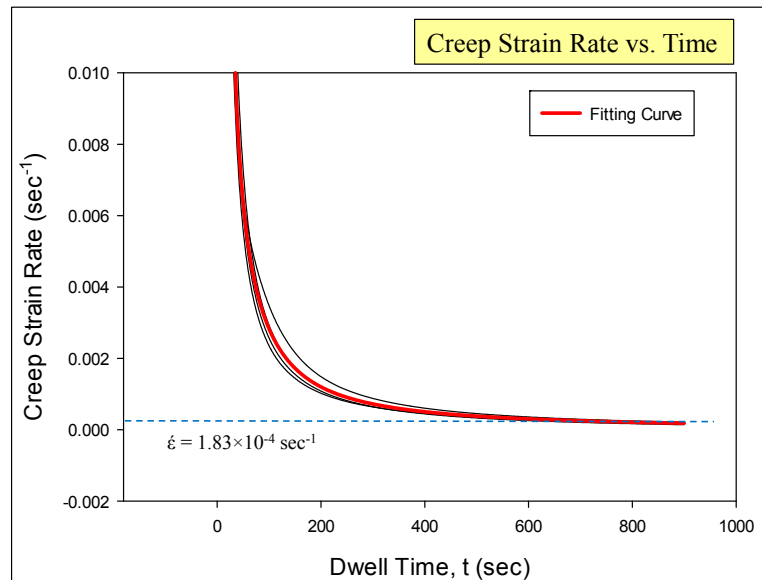


Figure 5.12 Variation of Creep Strain Rate with Holding Time for SAC305 Solder Joint

Since the applied load was fixed (10 mN) and the projected area under the indenter tip increases continuously during the creep deformation period, the stress changes over the time. For example, the variation of stress, for the same set of experiments presented in Figure 5.11, as a function of dwell time is presented in Figure 5.13 where the red curve represents an average for the series of indents.

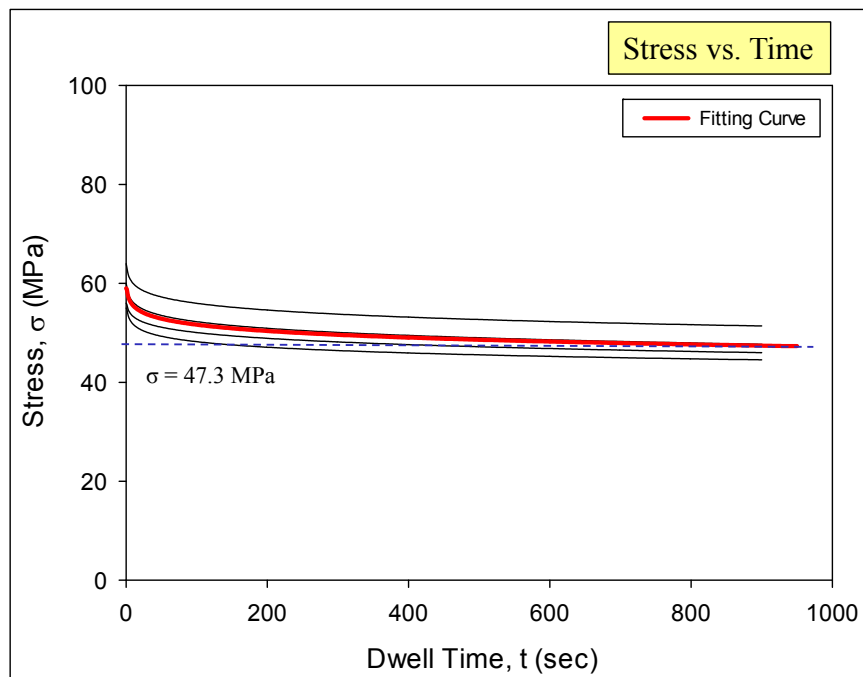


Figure 5.13 Variation of Stress with Holding Time for SAC305 Solder Joint

Data from Figures 5.12-5.13 was combined to generate the creep strain rate versus applied stress plot as shown in Figure 5.14.

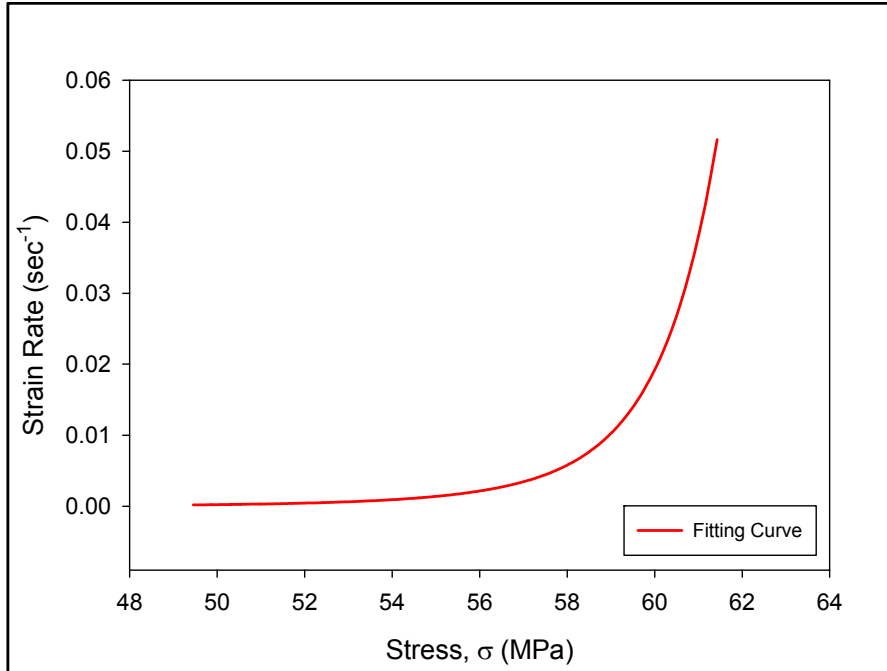


Figure 5.14 Creep Strain Rate vs. Applied Stress Plot Obtained from Nanoindentation Creep Experiment

The stress level attained during the test ranges from 50-62 MPa whereas the stress level typically used during a tensile creep experiment of SAC305 solder is 10-30 MPa [11, 24-26]. Since, the stress applied during the nanoindentation test is compressive in nature, the stress level attained during the test is well above the desired range. Garofalo creep model, as shown in equation 5.4, was used to extrapolate nanoindentation creep results to a lower stress level.

$$\dot{\epsilon} = C_1 [\sinh(C_2 \sigma)]^{C_3} e^{\frac{-C_4}{T}} \quad (5.4)$$

where C_1 - C_4 are fitting constants and T is the test temperature. A log-log plot of strain rate vs. stress for the fitted experimental data (solid red curve) and the extrapolation using Garofalo creep model (blue dotted curve) is presented in Figure 5.15.

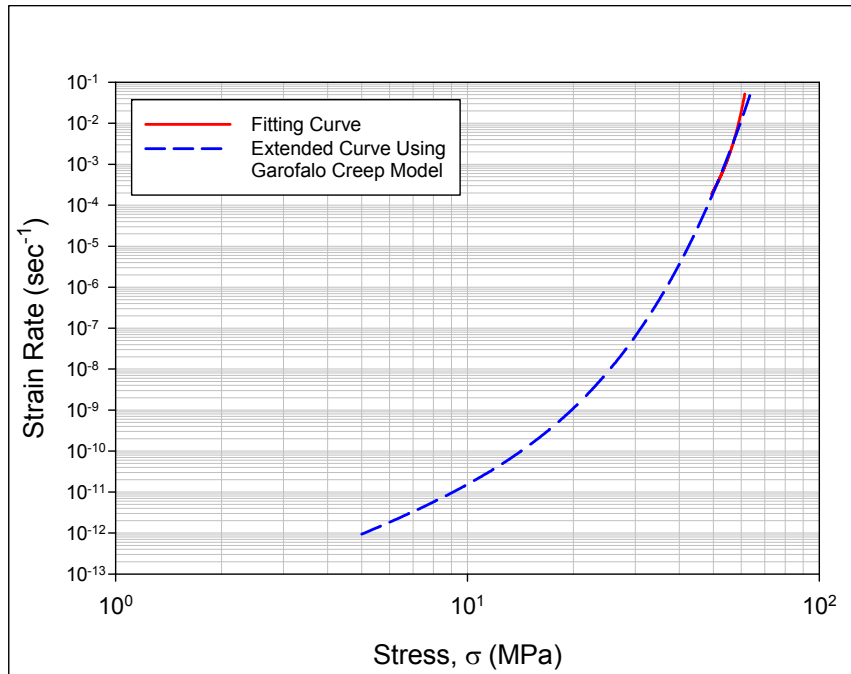


Figure 5.15 Creep Strain Rate vs. Applied Stress Plot Using Garofalo Creep Model

5.6 High Temperature Nanoindentation Test Matrix

High temperature tests were performed by placing cross-sectioned and polished single grain solder joint samples into the heating chamber mounted within the nanoindentation system. Five testing temperatures were utilized including $T = 25, 50, 75, 100,$ and $125\text{ }^{\circ}\text{C}$. A unique joint was used for each of the testing temperatures. Therefore, the test sample set consisted of six single crystal SAC305 solder joints. One joint was used to study only the effect of test temperatures while the rest 5 joints were used to study the combined effect of aging time and test temperatures on the creep properties. For each tested joint and temperature, five unique sets of aging conditions are being explored: no aging; and 1, 5, 10 and 30 days of prior aging at $T = 125\text{ }^{\circ}\text{C}$. For each aging condition and temperature, 6-10 indentations were performed.

5.7 Effects of Test Temperature

Using the nanoindentation creep procedures discussed above (sections 5.3-5.5), the dependence of the creep response of SAC305 solder joints on test temperature was characterized. For all of the tests, a constant peak load of 10 mN and a dwell time of 900 sec were used during the hold periods. A series of indents were made at each test temperature as shown in Figure 5.16. Different rows of indents were made at different temperature. For example, the indents at the bottom row represents 25 °C test temperature whereas the indents at the top row represents 125 °C test temperature. It is obvious from the figure that the indent size is getting bigger with increasing test temperature, as expected.

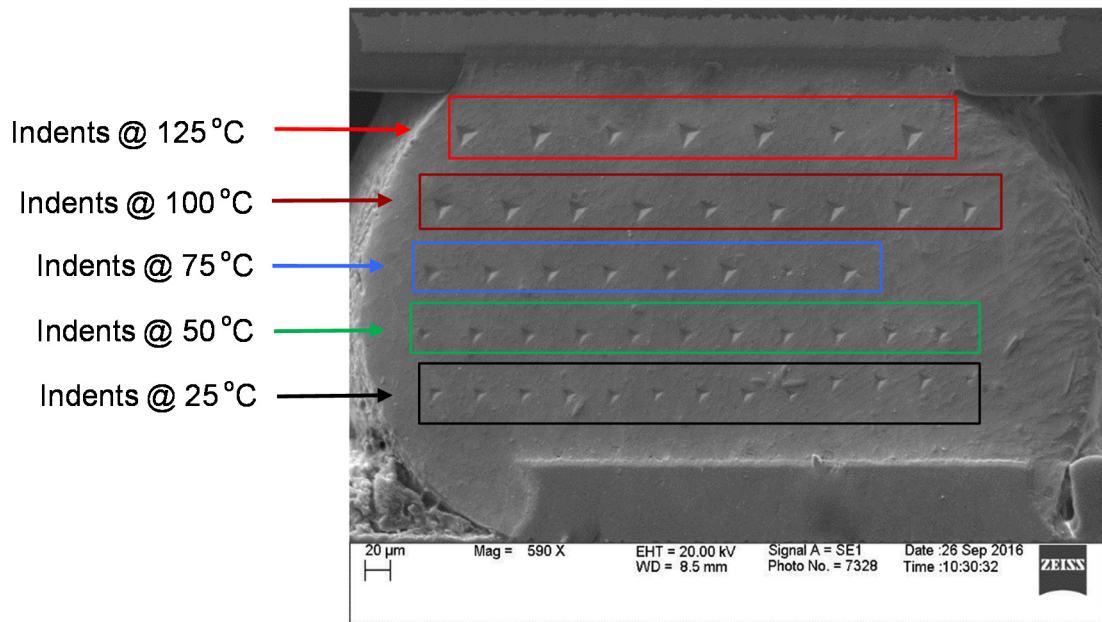


Figure 5.16 SAC305 Solder Joint after Nanoindentation Testing at Different Temperatures

Using the recorded creep indentation displacement vs. time data, the creep strain rate vs. applied stress curves were generated as outlined in section 5.5. Figure 5.17 shows typical load vs. total indentation depth curves, and Figure 5.18 shows typical creep

displacement vs. time curves for temperatures of $T = 25, 50, 75, 100,$ and $125\text{ }^{\circ}\text{C}$. As expected, the total and creep displacements increased with increasing test temperature.

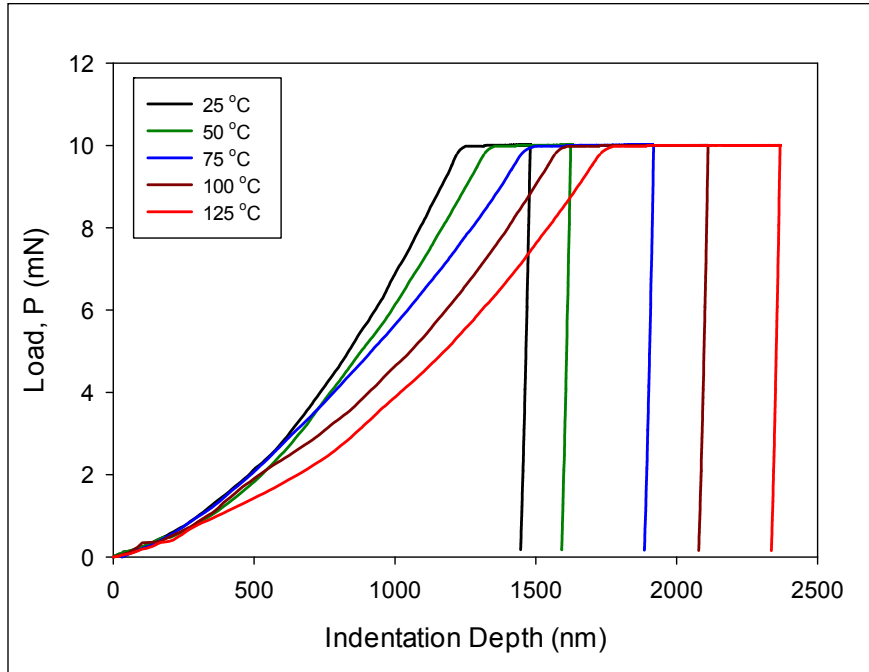


Figure 5.17 Nanoindentation Load vs. Indentation Depth Curves

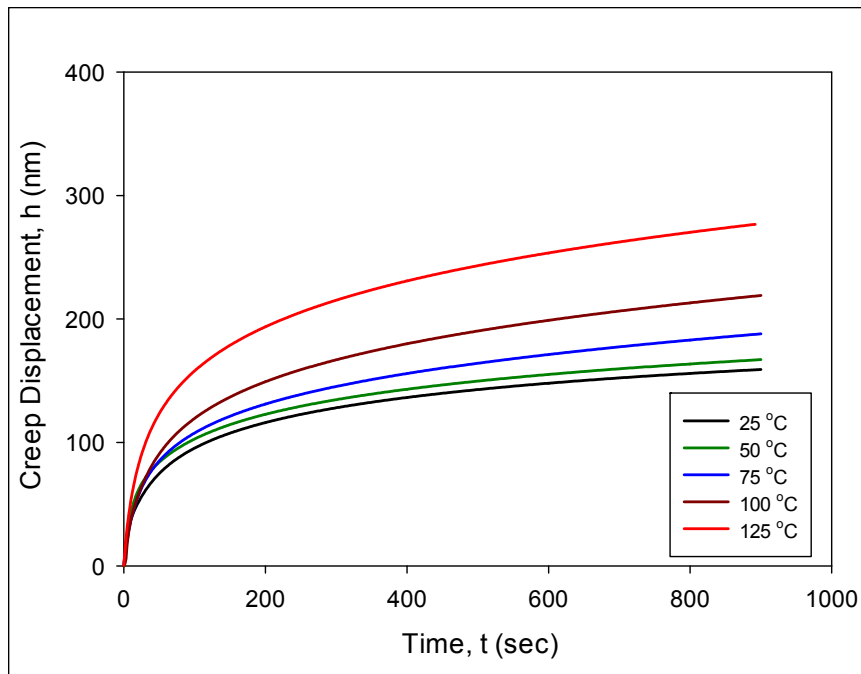


Figure 5.18 Nanoindentation Creep Displacement vs. Time Curves

The effects of the test temperature on the applied stress vs. time curves during the creep deformations are shown in Figure 5.19. Although the applied load was kept constant during the creep tests, the applied stress under the indenter tip decreased with time due to the contact area continually increasing. The applied stresses decreased with increasing temperature, since the indentation depth and thus the contact area increased with test temperature.

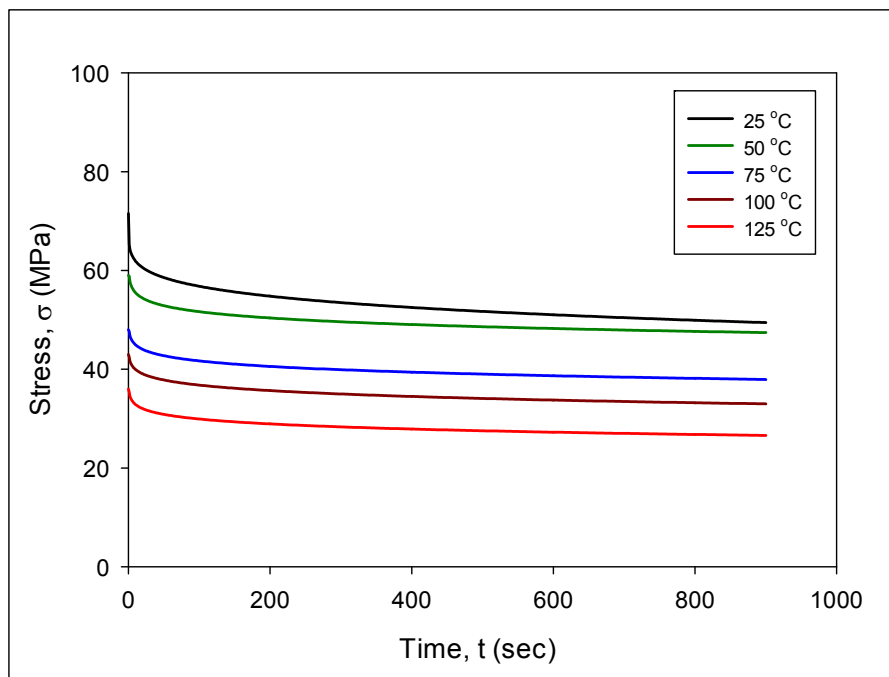


Figure 5.19 Variation of Applied Stress with Time During Constant Loading

Creep strain rate vs. applied stress plots obtained at different test temperatures are shown in Figure 5.20. As expected, the test temperature had a significant influence on measured creep strain rate, changing it several orders of magnitude for a fixed applied stress level. The corresponding extrapolated curves to the lower stress levels, using Garofalo creep model, are presented in Figure 5.21. The values of equivalent creep strain rates at 15 MPa stress level for all the test temperatures are tabulated in Table 5.1.

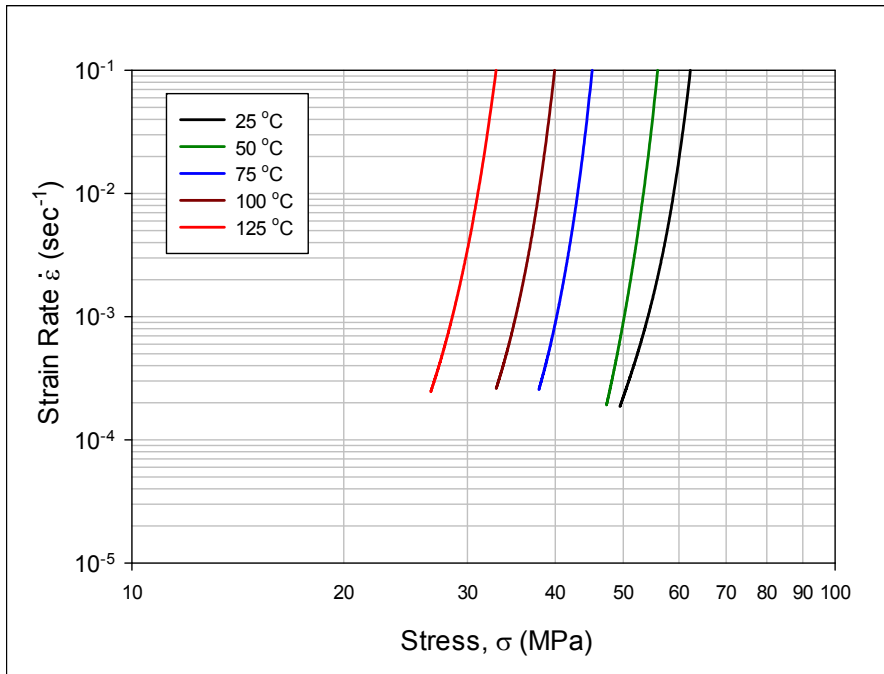


Figure 5.20 Variation of Creep Strain Rate with Applied Stress

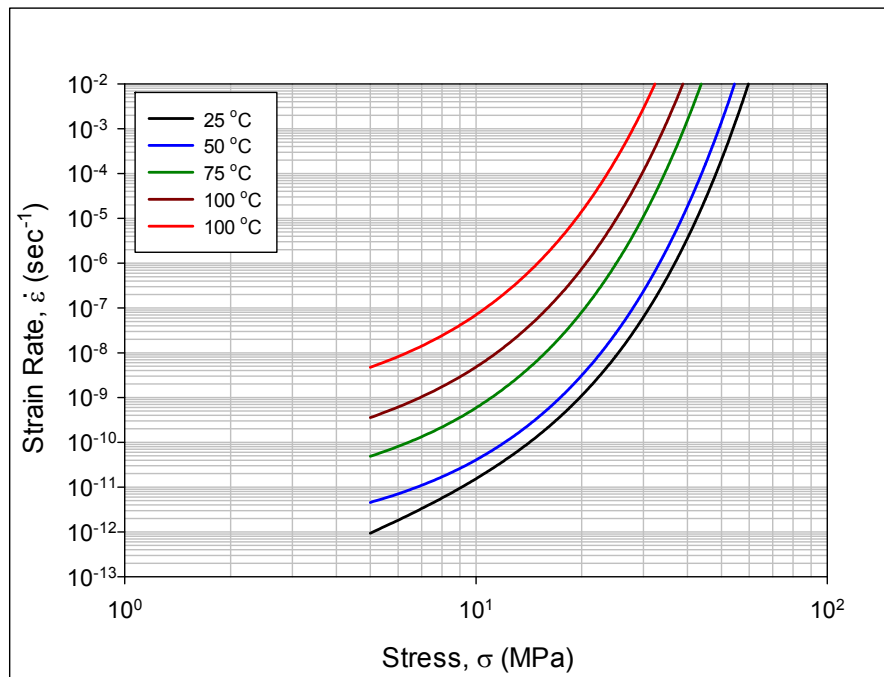


Figure 5.21 Creep strain vs. stress curves extrapolated to a lower stress level

Table 5.1 Equivalent Creep Strain Rates at 15 MPa Stress Level

Test Temperature	Strain Rate ($\times 10^{-10} \text{ sec}^{-1}$)
25 °C	1.4
50 °C	3.5
75 °C	70
100 °C	601
125 °C	10,050

5.8 Effects of Aging

A series of indents were made on 5 single grain SAC305 solder joints at 5 different test temperatures as shown in Figure 5.22. In this case, test temperature for each joint was kept constant and indents were made at different aging time. After having the initial series of indents in no aging condition, all the joints were kept inside an oven at 100 °C for 1 day. After removing the samples from the aging oven, another series of indents (1 day aging) were made on each joint and then kept them back for the next aging cycle. In the same way, nanoindentation creep experiments were conducted in 5 different aging conditions. Images of the five single grain solder joints after indentation creep experiments at five different test temperature and five different aging conditions are presented in Figure 5.23. As mentioned earlier, the row of indents on the top of each joint were obtained in no aging condition while the row of indents at the bottom of each joint were obtained after 1 month of aging at 100 °C.

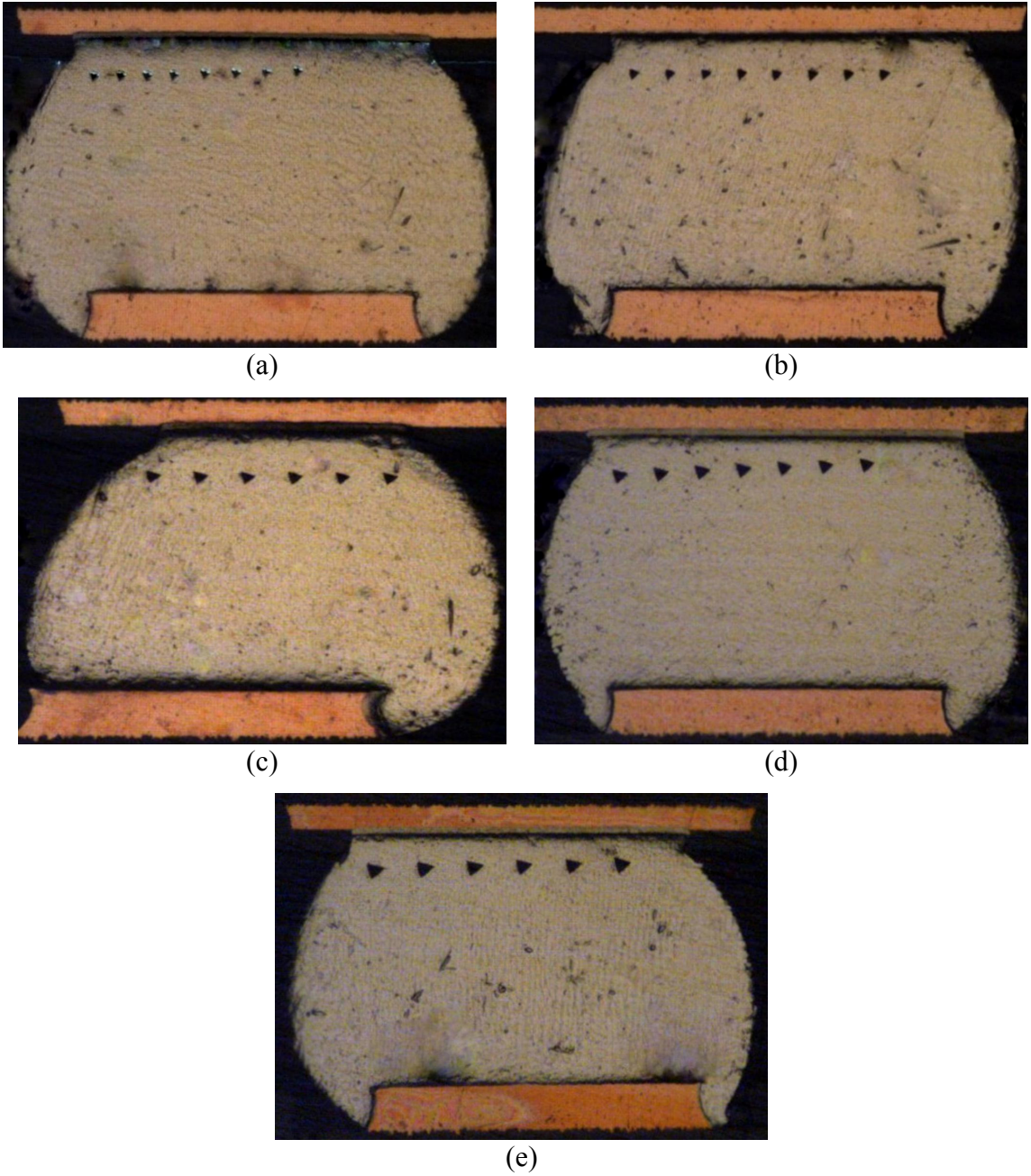


Figure 5.22 Indents on SAC305 Solder Joints in No Aging Conditions Obtained at (a) 25 °C, (b) 50 °C, (c) 75 °C, (d) 100 °C, and (e) 125 °C

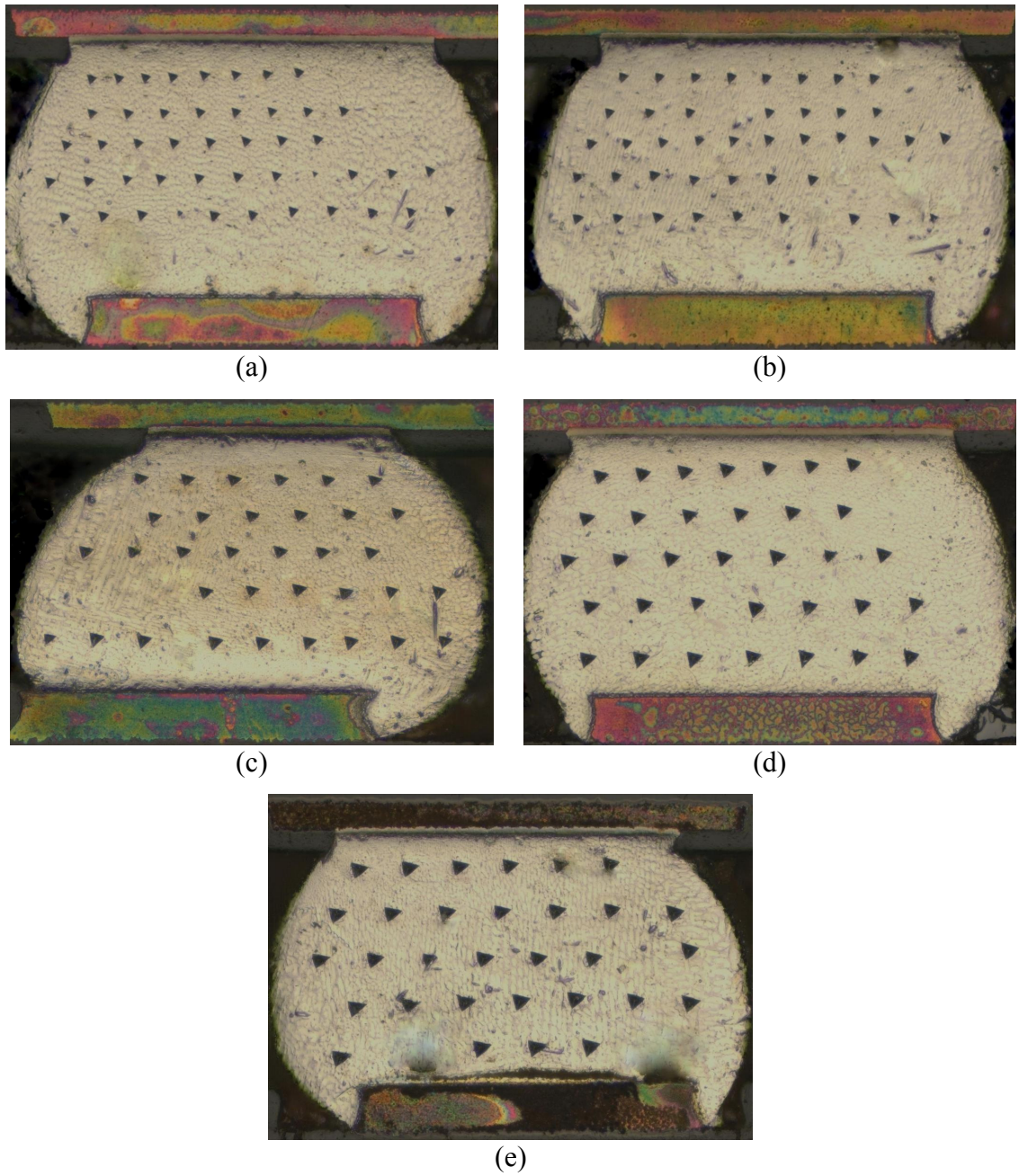


Figure 5.23 Indents on SAC305 Solder Joints at Different Aging Conditions Obtained at (a) 25 °C, (b) 50 °C, (c) 75 °C, (d) 100 °C, and (e) 125 °C

Example results for the effects of aging on the temperature dependent creep data of SAC305 solder joints are shown in Figures 5.24-5.28. Each of the five plots for different test temperatures illustrates the strain rate vs. applied stress curves for no aging (black), 1 day (blue), 5 days (green), 10 days (dark red) and 30 days (red) of prior aging at $T = 125$ °C. As we can see from the figures, at any particular temperature, the strain rate vs. stress curve shifts towards the left with increasing aging time. This indicates that for any fixed stress level, creep strain rate increases with increasing aging time. Although the short-term aging had only a small influence on the room temperature creep response, the creep rates at high temperature increased significantly with prior aging time. For example, the creep rate at $T = 125$ °C increased over 1000X at $\sigma = 30$ MPa only after 10 days of aging (Figure 5.26). The effects of aging on the creep rate vs. stress response became larger and larger as the testing temperature increased.

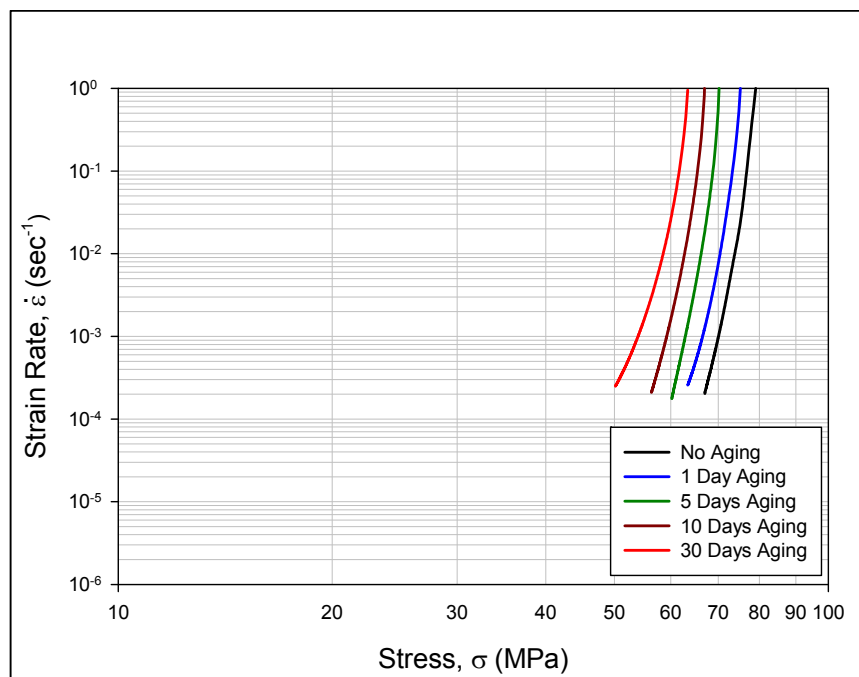


Figure 5.24 Effects of Aging on Creep Response at 25 °C

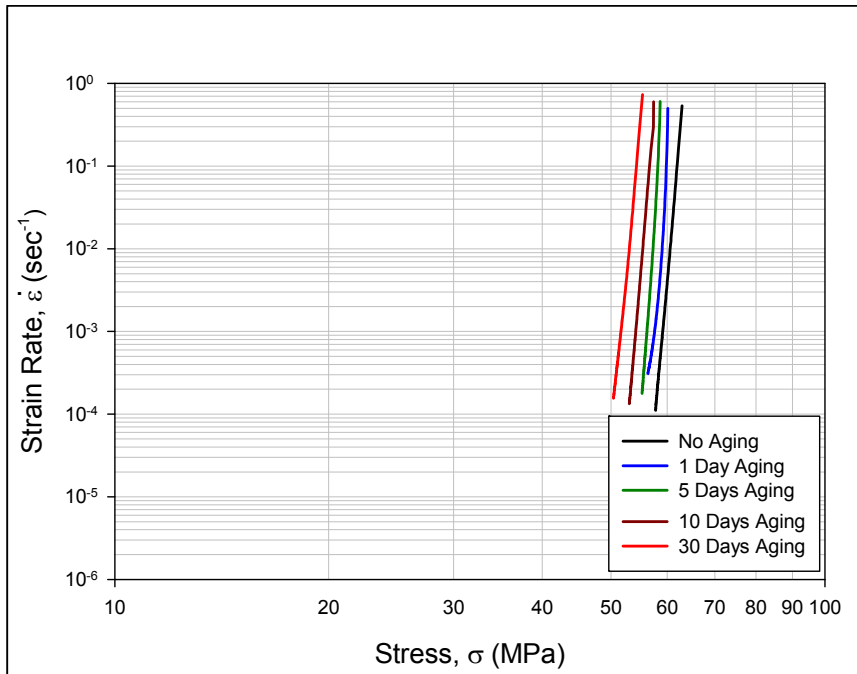


Figure 5.25 Effects of Aging on Creep Response at 50 °C

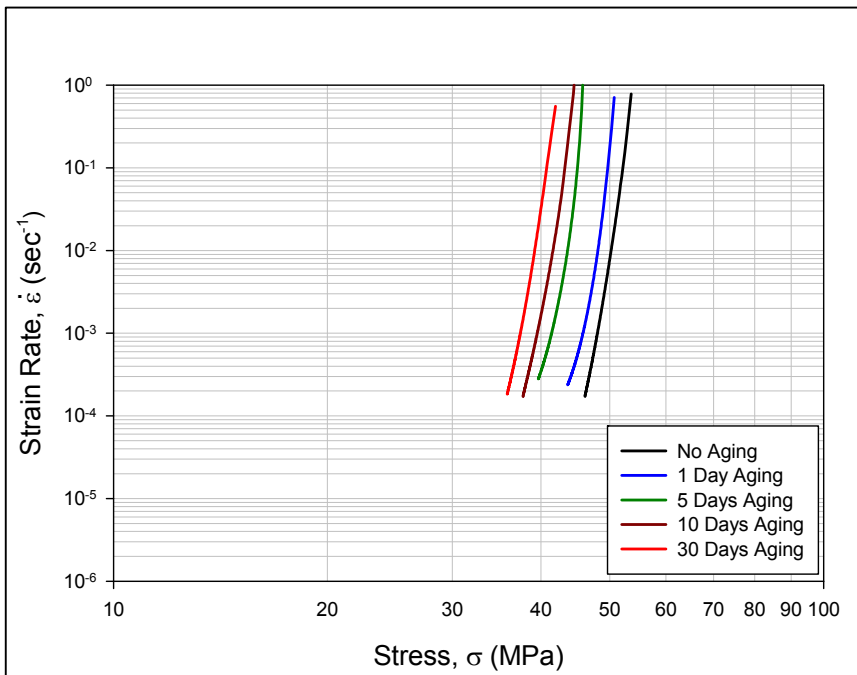


Figure 5.26 Effects of Aging on Creep Response at 75 °C

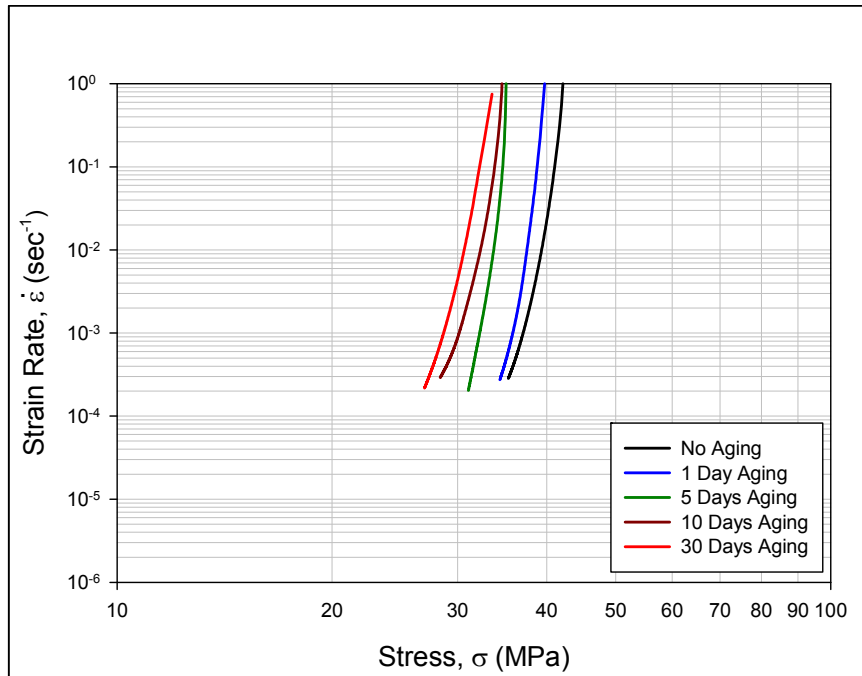


Figure 5.27 Effects of Aging on Creep Response at 100 °C

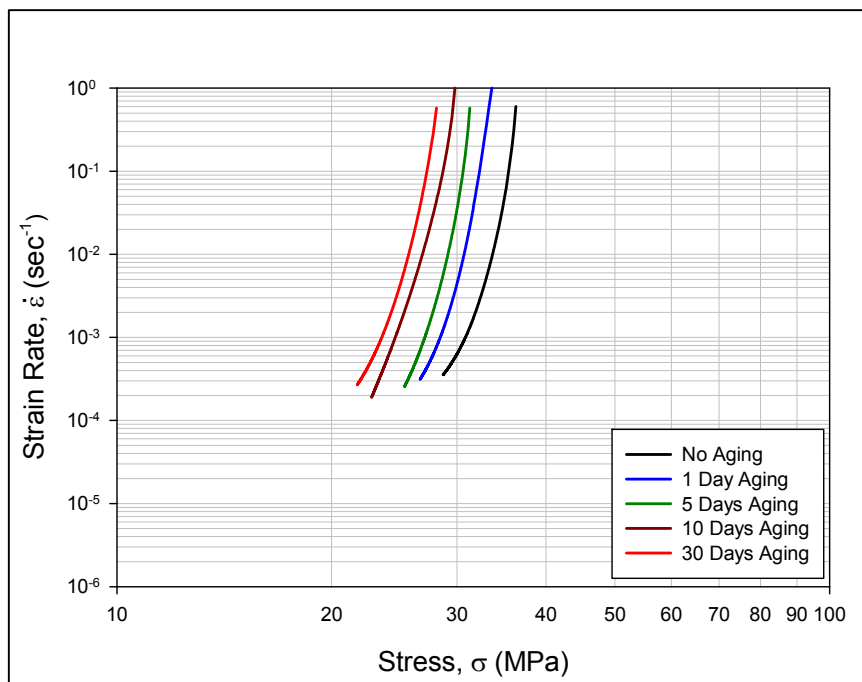


Figure 5.28 Effects of Aging on Creep Response at 125 °C

5.9 Summary and Discussion

In this chapter, nanoindentation methods were used to explore the creep behavior, and aging effects of SAC305 solder joints at several elevated testing temperatures from 25 to 125 °C. A special high temperature stage and test protocol was used within the nanoindentation system to carefully control the testing temperature, and make the measurements insensitive to thermal drift problems. Since the properties of SAC solder joints are highly dependent on crystal orientation, only single grain solder joints were used to avoid introducing any unintentional variation from changes in the crystal orientation across the joint cross-section.

Nanoindentation creep testing was performed on the non-aged and aged solder joint specimens at five different testing temperatures ($T = 25, 50, 75, 100,$ and 125 °C). As expected, the results have shown that indent/testing temperature has a significant impact on the mechanical properties and creep strain rate of solder joints. The measured data have also shown that the effects of aging on solder joint creep response are highly temperature dependent. At any particular temperature, creep rate increases with increasing aging time. The creep rates at high temperature increased significantly with just a few days of prior aging. In particular, the aging induced degradation rates at high temperatures (100-125 °C) were more than 100X those seen at room temperature. The effects of aging on the creep rate vs. stress response became larger and larger as the testing temperature increased. Nanoindentation pile-up effects, although insignificant at room temperature, were observed during high-temperature testing and corrections were made to limit their influence on the test results.

CHAPTER 6

EVALUATION OF AGING INDUCED MICROSTRUCTURAL EVOLUTION IN LEAD FREE SOLDERS USING SCANNING PROBE MICROSCOPY

6.1 Introduction

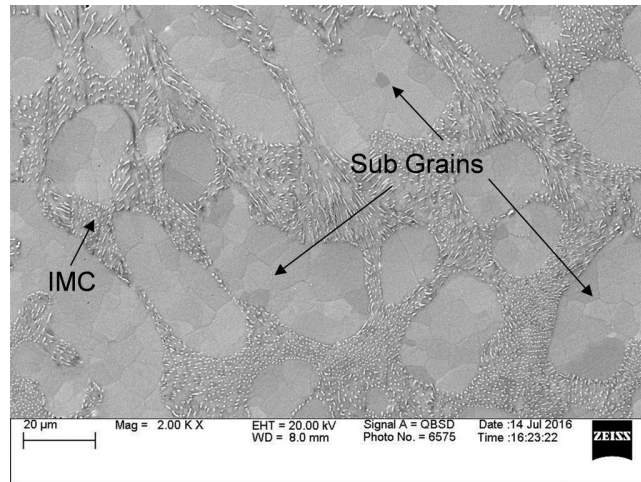
The changes in solder mechanical behavior that occur during isothermal aging are a result of the evolution of the SAC solder microstructure. The most well-known and widely observed changes are coarsening of the Ag_3Sn and Cu_6Sn_5 intermetallic compounds (IMCs) present in the eutectic regions between beta-Sn dendrites. Some researchers have proposed empirical models to describe the growth of these secondary phase particles as a function of aging temperature and aging time, and related this growth to mechanical property changes. In most of the prior investigations, microstructural changes during aging have been observed by comparing two different solder joints subjected to different aging conditions. Thus, the comparisons made were qualitative in nature (e.g. average IMC particle size) since the two microstructures were from different samples and could not be directly compared.

In the current work, new procedures were developed to capture solder microstructure while the sample is being heated inside an oven (in-situ aging study). The heating stage and scanning probe microscopy (SPM) facility within a nanoindentation system were utilized to achieve the goal. The sample was kept within the nanoindentation system and exposed to a high temperature aging using the heating stage present in the instrument. In particular, aging was performed at $T = 125\text{ }^\circ\text{C}$ for up to 26 hours, and the topography of the microstructure of a fixed region (10×10 microns) was continuously scanned using the SPM system and recorded after one hour time intervals. This process

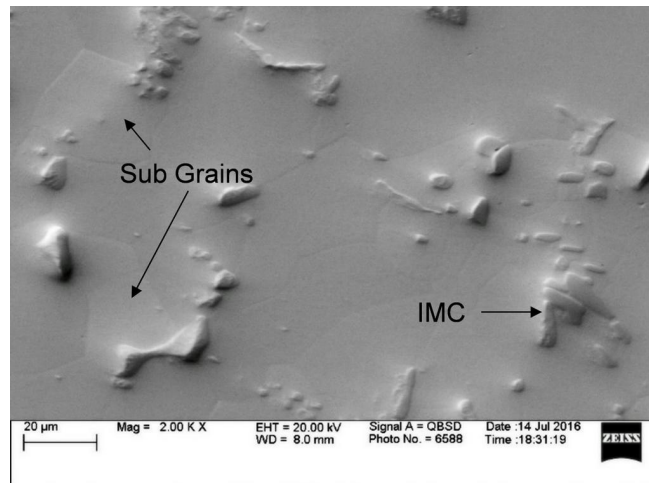
generated several images of the microstructure as the aging progressed. When placed together sequentially, these images have been used as frames to create an experimentally recorded movie of the microstructural evolution in SAC solder joints exposed to aging. Image analysis software was utilized to quantify microstructural changes (total area, number and average diameter of IMC particles, interparticle spacing etc.) with respect to aging time.

6.2 Effects of Aging on the Microstructure of SAC305 Solder

The microstructure of SAC305 solder consists of β -Sn dendrites surrounded by eutectic region which is a mixture of Ag_3Sn , Cu_6Sn_5 , and β -Sn phase. The IMCs (Ag_3Sn , Cu_6Sn_5) in the eutectic region helps to improve strength of the solder alloy restricting dislocation motion. Due to their low melting temperatures, lead free solders are exposed to high homologous temperatures in most product applications. Thus, there is a continuous state of active diffusion processes in the solder alloys, and their microstructures are inherently unstable and will continually evolve during normal operating temperature conditions of electronic packaging assemblies. Typical microstructure evolution in lead free solders includes coarsening of intermetallic phases and subgrains, breakdown of dendrite structures, as well as potential recrystallization at Sn grain boundaries. Such changes in solder microstructure are accompanied by dramatic changes in mechanical response and failure behavior, and these multifaceted evolutions occurring in the material are typically referred to as solder aging phenomena. An example of SAC305 solder microstructure evolution after 1 year of aging at 100 °C is presented in Figure 6.1.



(a)



(b)

Figure 6.1 Microstructure of SAC305 Solder (a) Before Aging and (b) After Aging

Many researchers have studied effects of aging on the evolution of solder microstructure. The most well known and widely observed changes are coarsening of the Ag_3Sn and Cu_6Sn_5 IMCs present in the eutectic regions between β -Sn dendrites. Several researchers [61, 80, 82, 85, 86, 107-110] have also proposed empirical models to describe the growth of IMC particles or layers as a function of aging temperature and aging time. In many studies on the effects of aging on solder microstructure, observations were made on two different solder joints (one non-aged and one aged). Thus, the comparisons made

were often qualitative in nature since the two microstructures were from different samples and could not be directly compared. Figure 6.2 represents the variations of SAC305 microstructure based on the locations of the same sample. All the images were taken at the same magnification from the same sample but in different locations or regions. It is evident from all the images in Figure 6.2 (a-d) that the microstructure of SAC305 is also dependent on the locations. As a result, in order to avoid region based variation in the microstructure, aging study should conduct at a fixed location of the same sample (not different sample). This kind of careful studies are expected to produce a more realistic quantitative analysis results for aging induced IMC coarsening experiments.

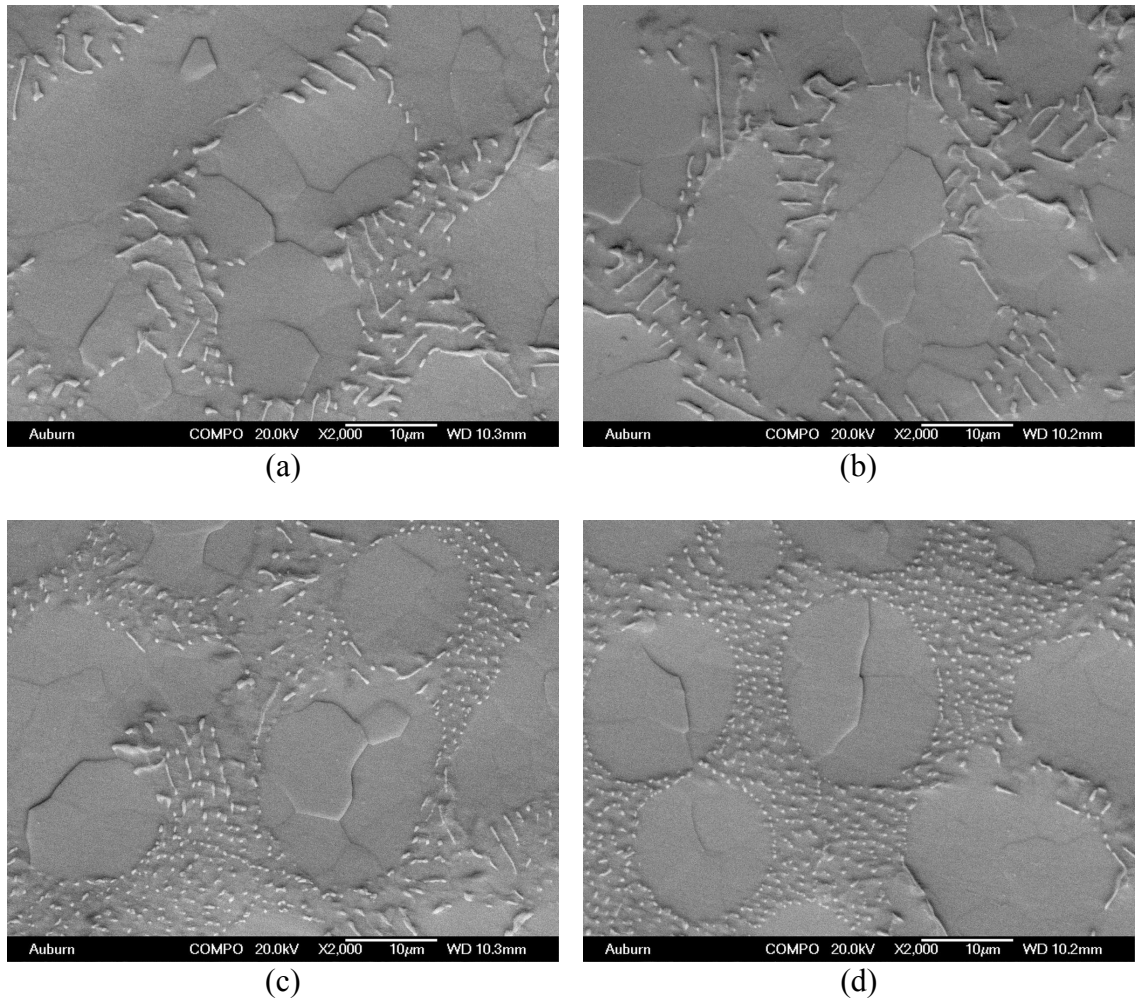


Figure 6.2 (a-d) Location Based Variation in the Microstructure of SAC305 Solder

6.3 In-situ Imaging Process

Scanning Probe Microscopy attached with Hysitron TI 950 (Figure 3.17) was used to monitor microstructure evolution was. In this technique, a sharp tipped probe (radius <math><50\text{ nm}</math>) was used to scan the topography of a sample surface. The contact force between the tip and the specimen surface was very small (<math>< 250\text{ nN}</math>). Thus, surface damage was minimized when profiling the surface. Using the high temperature stage within the Hysitron nanoindentation system, the aging of the sample was performed within the system and in-situ SPM scans of SAC305 microstructures were performed as the sample was

aging. Three-dimensional representations of the surface topography of the solder microstructures were generated using the SPM data.

The lead free The lead free solder joint samples used in the SPM study were extracted from BGA assemblies as shown in Figure. 6.3. The cross-sectional specimens were prepared in a special way to avoid encapsulation in a microscopy potting compound, which would have made them too tall for use in the nanoindentation thermal stage. To facilitate polishing, the samples were first mounted on a cylindrical epoxy preform using double-sided tape. Details of the high temperature chamber and the sample polishing procedure was presented in chapter 3, section 3.6 and 3.7. Then, the thin polished samples were removed from the preform and placed within the nanoindentation system. Four indents were used to define a region of interest for SPM observations. The prepared samples were aged at $T = 125\text{ }^{\circ}\text{C}$ for up to 26 hours. During the aging, SPM measurements were made in-situ on one hour increments.

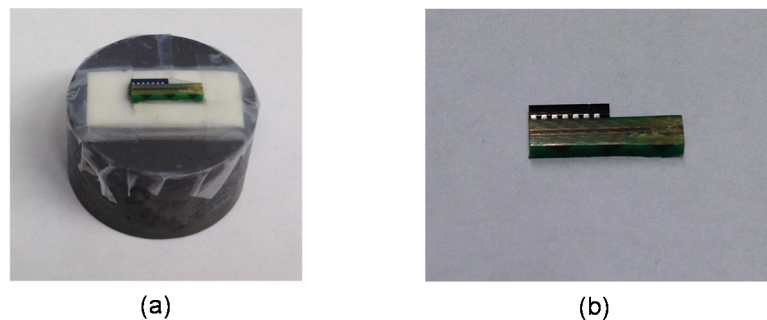


Figure 6.3 SPM Sample, (a) on Preform, (b) Final Polished Sample.

6.4 SPM Image of SAC305 Solder

In this chapter, example results for a typical RF SAC305 sample were presented. Typical SPM topography data are shown in Figure 6.4 for a single β -Sn dendrite in one of the regions studied. In this case, the region encompassing the dendrite is $30 \times 30\text{ }\mu\text{m}$ in

size. The microstructural evolution was characterized in the smaller 10 x 10 μm subregion in the interdendritic eutectic area identified by the dashed line square. Figure 6.5 shows the initial topography of the two different eutectic regions that were examined in detail.

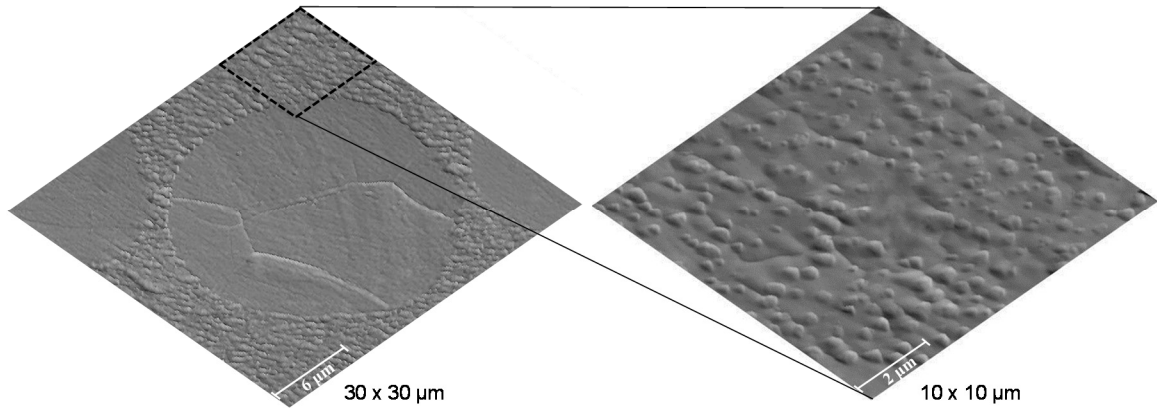
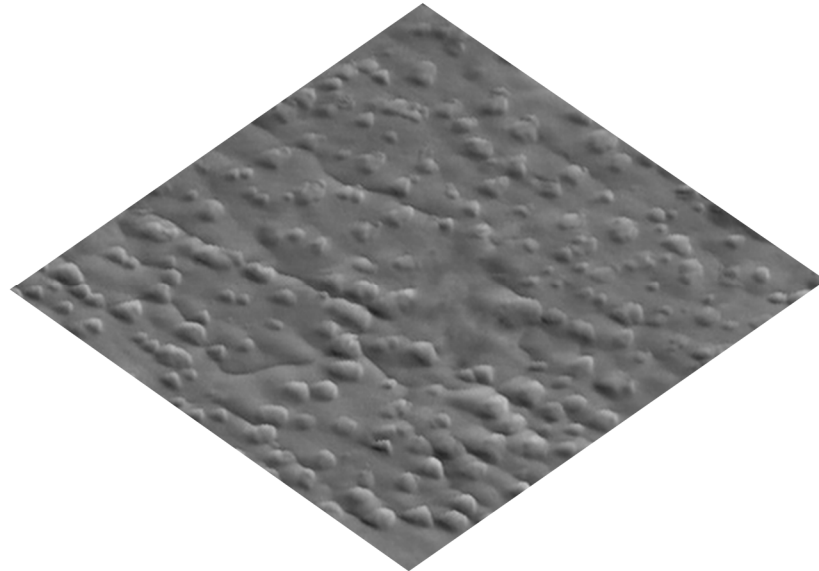
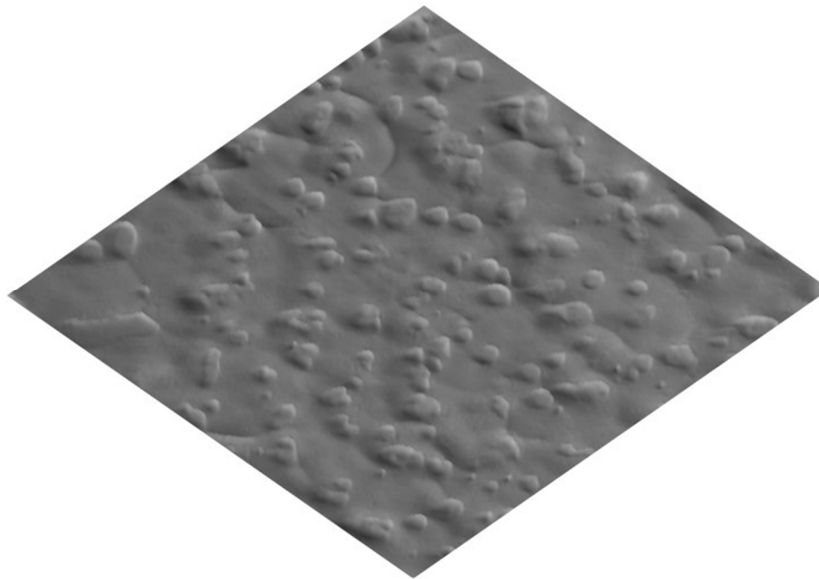


Figure 6.4 SPM Topography Image of a Typical SAC305 Sample Showing β -Sn Dendrite, Subgrain Boundaries, and Eutectic Region (No Aging).



(a)



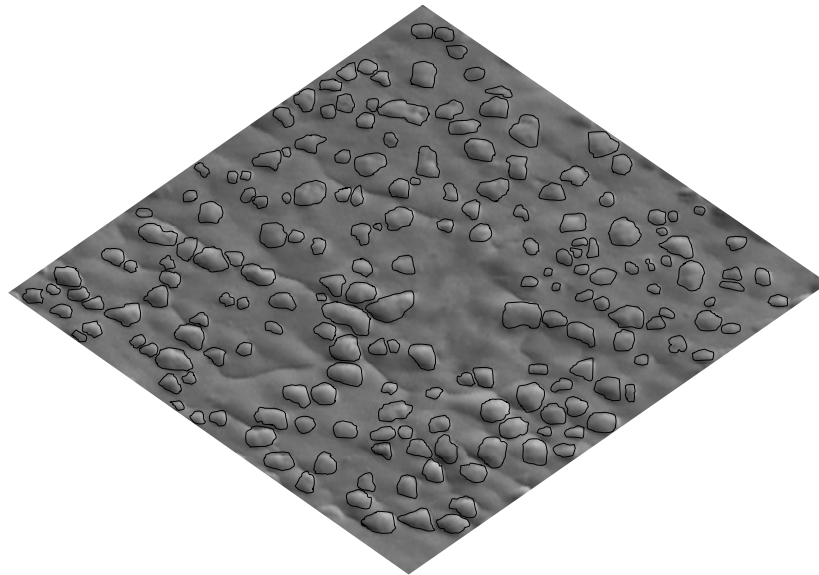
(b)

Figure 6.5 (a-b) Initial Topographies of the Studied SAC305 Samples Before Aging.

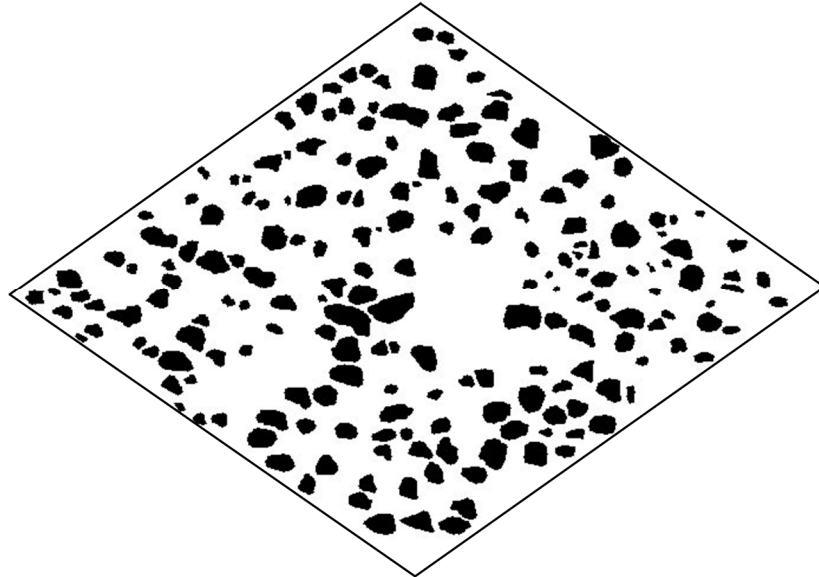
6.5 Measurement of Area and Number of IMC

IMC particle size of the captured SPM images were measured using image analysis software ImageJ. The particle size measurement process involves 3 major steps. First, all the particles were outlined. Then the gray scale image were converted into a binary image.

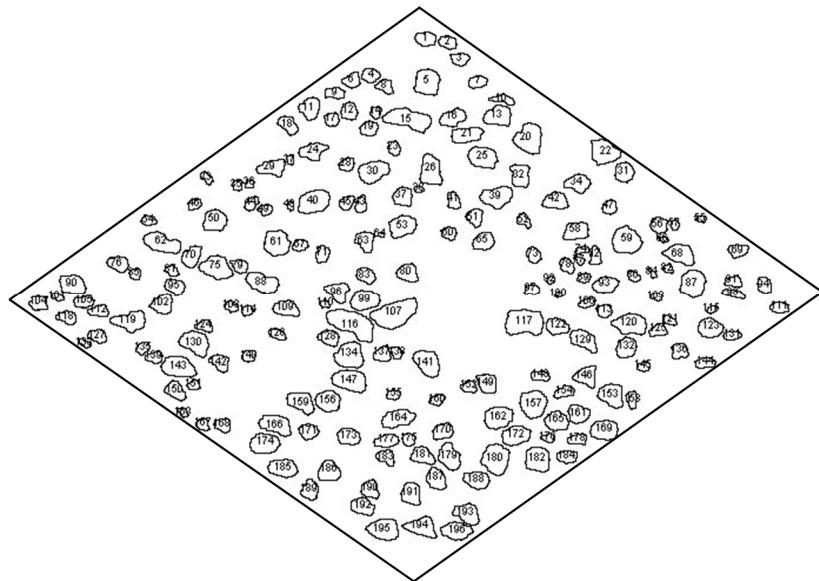
Lastly, the number as well as the average area of the black spots, in the binary image, were calculated using an image analysis software (ImageJ). An example of a SPM image with all the IMC particle outlined are presented in Figure 6.6(a). Similarly, Figure 6.6(b) represents the corresponding binary image that was obtained after conversion. Figure 6.6(c) shows the image obtained from the ImageJ software after particle area calculations. It is evident from this image that the software was capable to accurately identify all the individual particle in the field of view.



(a)



(b)



(c)

Figure 6.6 Image Processing Steps for IMC Particle Area Calculations (a) After Outlining All the Particles (b) Binary Image and (c) Final Image from ImageJ.

6.6 Measurement of Particle Diameter

As shown for an ideal spherical IMC particle in Figure. 6.7, the amount of the particle that is visible on the polished cross-sectional surface is actually unknown. Here,

the black portion of the particle represents the polished surface exposed to the surrounding in air, while the gray shaded portion is the portion of the IMC below the surface. As indicated in Figures. 6.7-6.8, the observed particle diameter (apparent diameter) for a particle is actually less than or equal to the actual particle diameter. Thus, the measured (apparent) average particle diameter must be adjusted to calculate the actual average particle diameter.

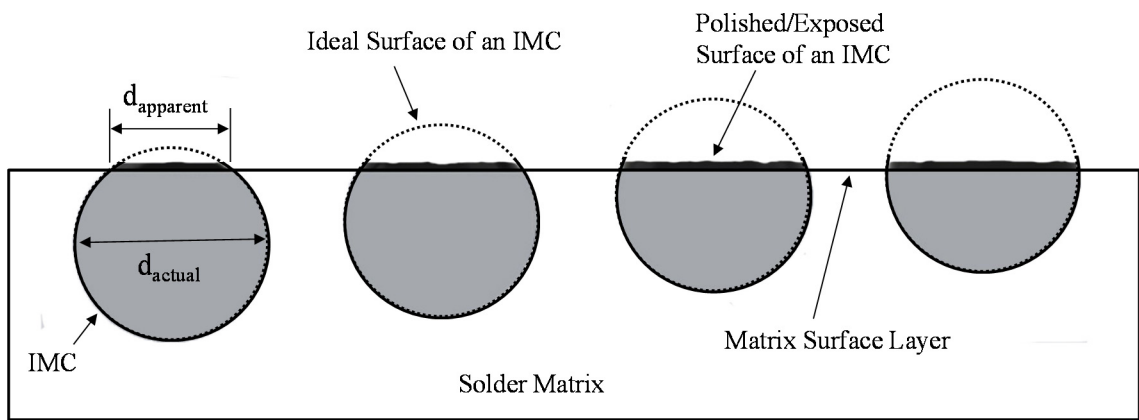


Figure 6.7 A Schematic Representation of An IMC with Several Possible Exposed Area Above The Surface Layer.

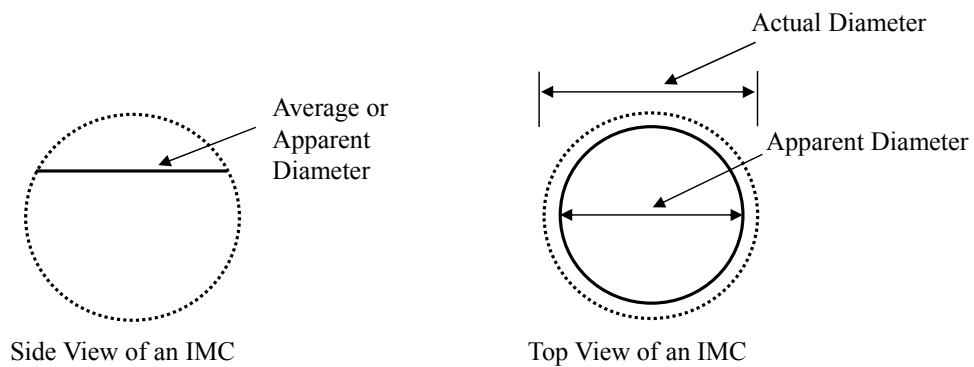


Figure 6.8 Side And Top View of An Ideal Spherical IMC Particle Showing Actual And Apparent Diameters.

For a fixed particle with diameter d , the apparent/measured particle diameter d_{apparent} can be several different values based on the vertical position of the particle (Figure 6.7). The average value of d_{apparent} can be found mathematically by averaging all possible values obtained from all possible vertical positions for the particle:

$$(d_{\text{apparent}})_{\text{ave}} = 2 \times (R_{\text{apparent}})_{\text{ave}} = \frac{2}{R} \int_0^R \sqrt{(R^2 - x^2)} dx \quad (6.1)$$

$$(d_{\text{apparent}})_{\text{ave}} = \frac{2}{R} \times \frac{\pi R^2}{4} = \frac{\pi}{4} d_{\text{actual}} \quad (6.2)$$

$$d_{\text{actual}} = \frac{4}{\pi} (d_{\text{apparent}})_{\text{ave}} \quad (6.3)$$

Equation 6.3 was used to estimate the actual diameter of each particle by adjusting the measured (apparent) diameter.

If the particles are spherical, the apparent diameter of the exposed surface of each particle can be calculated by assuming a circular relation between particle surface area and apparent diameter:

$$A_{\text{apparent}} = \pi R^2 = \frac{\pi}{4} (d_{\text{apparent}})^2 \quad (6.4)$$

$$d_{\text{apparent}} = \frac{2}{\sqrt{\pi}} \sqrt{A_{\text{apparent}}} \quad (6.5)$$

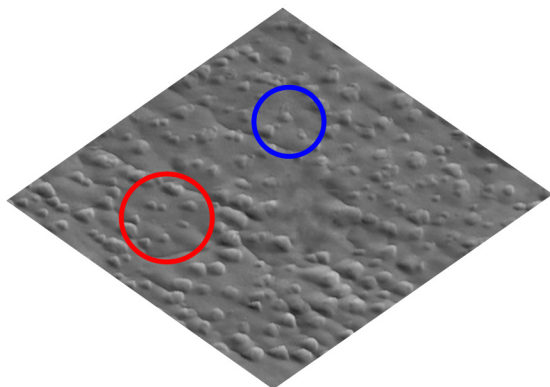
Combining of equations (6.3, 6.5) yields the relation for the particle diameter in terms of the measured/particle surface area:

$$d_{\text{actual}} = \frac{4}{\pi} (d_{\text{apparent}})_{\text{ave}} = \frac{8}{\pi^{3/2}} \sqrt{(A_{\text{apparent}})_{\text{ave}}} \quad (6.6)$$

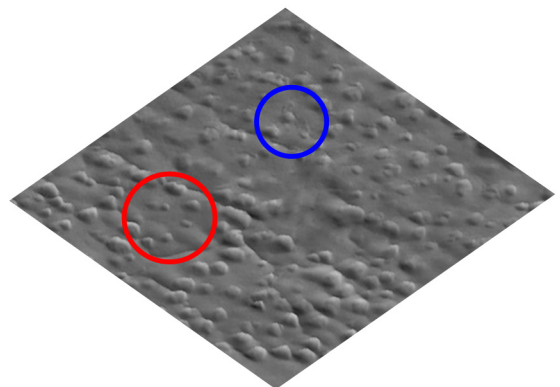
In addition to the averaging assumptions made above, this analysis also assumes that the particle does not move vertically during the aging process.

6.7 Changes in Microstructure During Aging

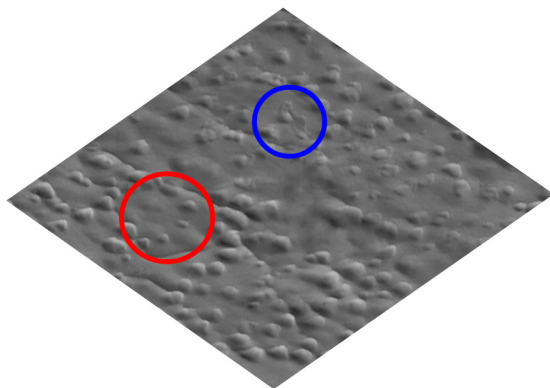
Figure 6.9 shows a series of images illustrating an example microstructural evolution observed at several aging times up to 26 hours. In this case, the results were from Region 1 (Figure 6.5(a)). The expected coarsening of intermetallics occurred, with some IMC particles growing in size, and some IMC particles decreasing in size and eventually disappearing altogether. This resulted in: (1) a decrease in the number of IMC particles, (2) an increase in the average particle size, and (3) an increase in the average particle separation distance. These effects are illustrated in Figure. 6.9, where blue circles show example positions where particles were growing, red circles illustrate positions where the particles decreased in size and disappeared.



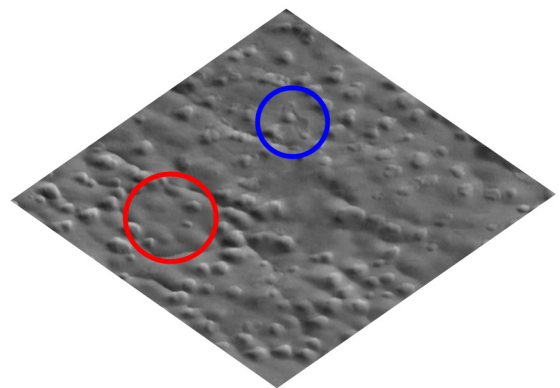
(a) No aging



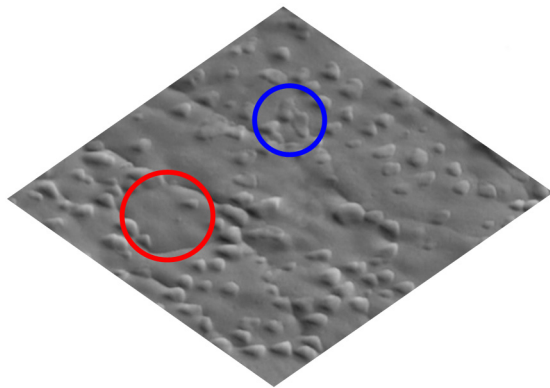
(b) 1 hour of aging



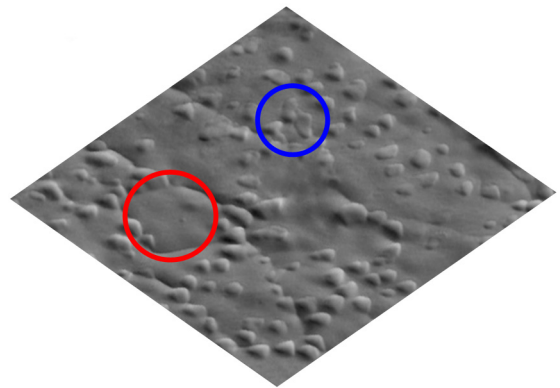
(c) 2 hours aging



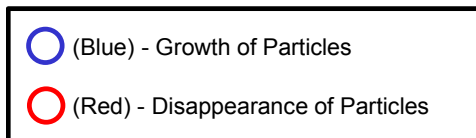
(d) 3 hours of aging

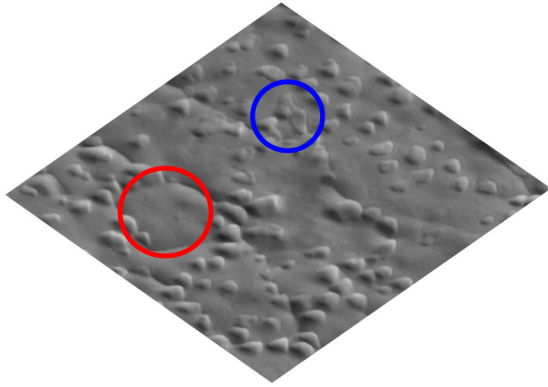


(e) 4 hours aging

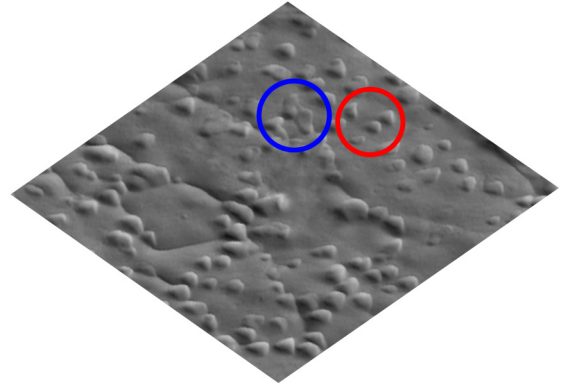


(f) 5 hours of aging

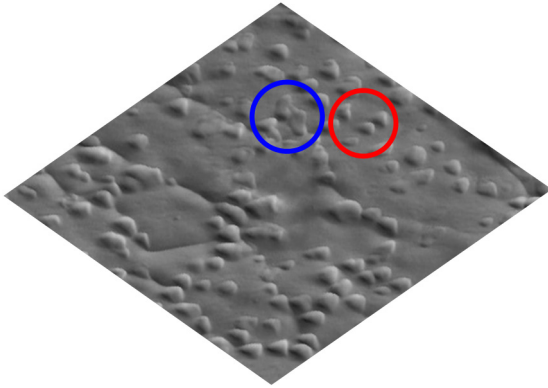




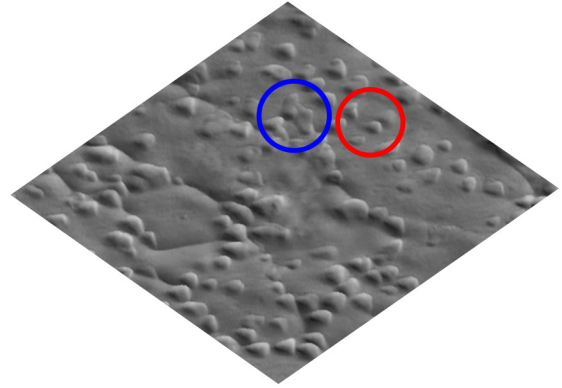
(g) 6 hours aging



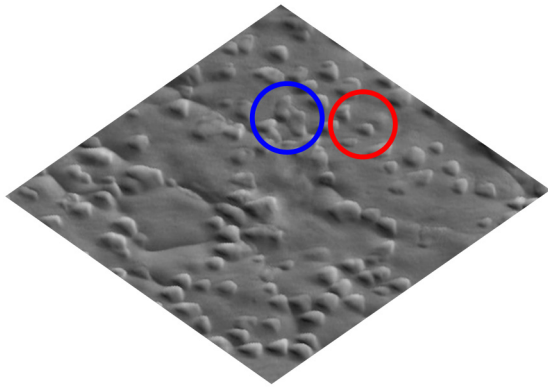
(h) 7 hours of aging



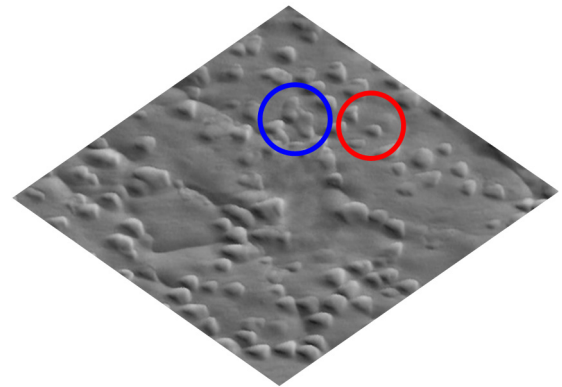
(i) 8 hours aging



(j) 9 hours of aging

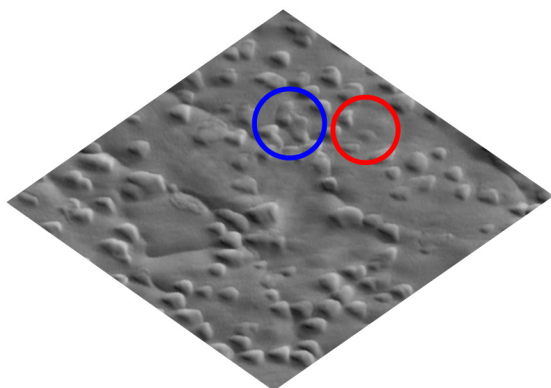


(k) 10 hours aging

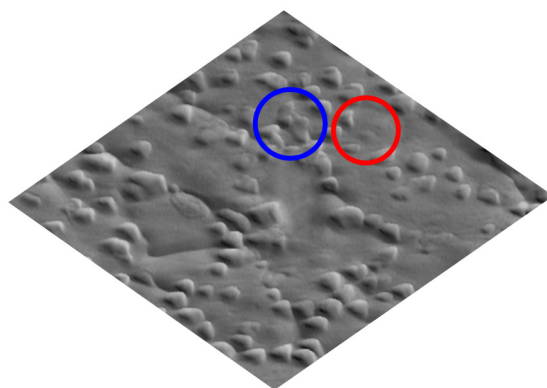


(l) 12 hours of aging

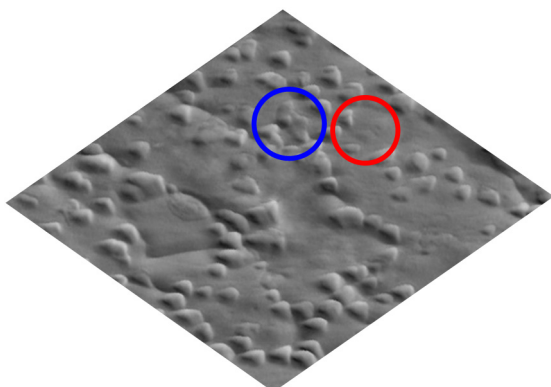
○ (Blue) - Growth of Particles
○ (Red) - Disappearance of Particles



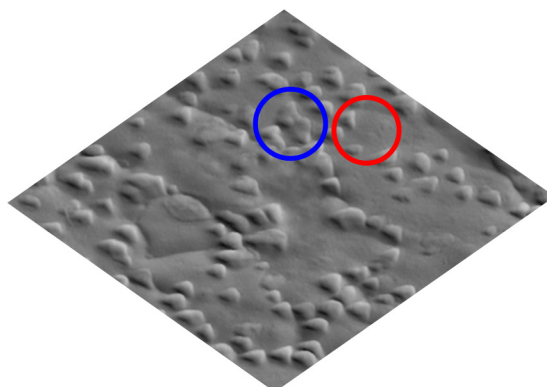
(m) 14 hours aging



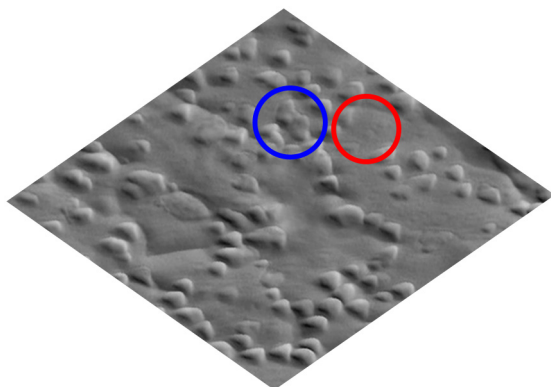
(n) 16 hours of aging



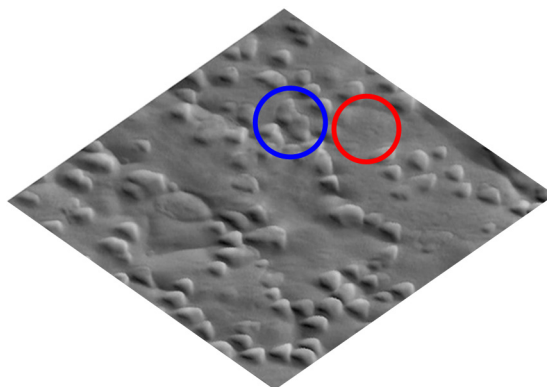
(o) 18 hours aging



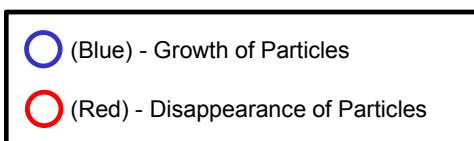
(p) 20 hours of aging



(q) 22 hours aging



(r) 24 hours of aging



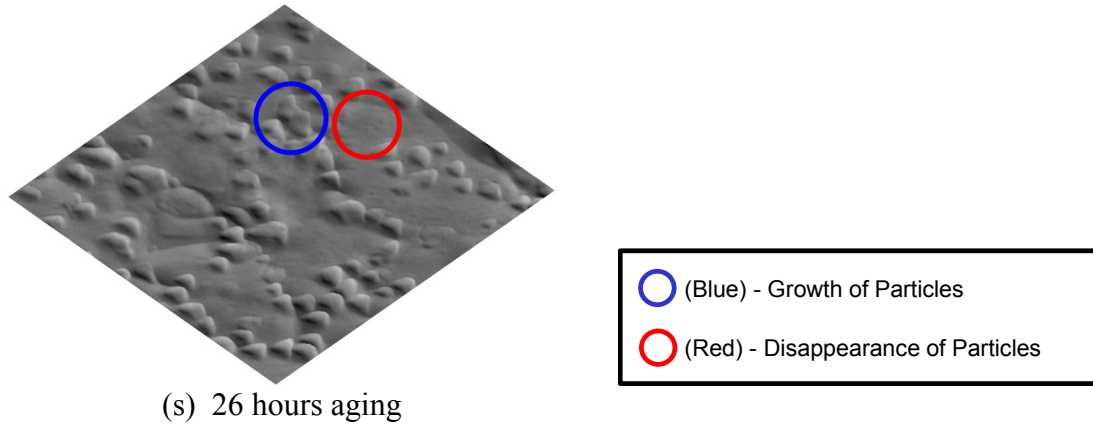


Figure 6.9 (a-s) Example SAC305 Microstructural Evolution Observed by SPM Imaging (Aging at $T = 125\text{ }^{\circ}\text{C}$).

Image processing and analysis steps as outlined before in sections 6.5 and 6.6 were followed to calculate the number and average diameter of the IMC particles of all the images of Region 1 (presented in Figure 6.9) and Region 2 (all the images are not shown here). The quantitative analysis results are summarized in Table 6.1. Graphical representations of the changes in number, size, and total area of the particles for region 1 are shown in Figures 6.10 – 6.12. It is evident from the Figures 6.10 and 6.11 that the average size of the particles increases while the number of the particles decreases with increasing aging time. At the same time the total area of the particles (Figure 6.12) does not have any significant change as expected.

Table 6.1 IMC Particle Diameter of Different Locations After Different Aging Duration

Time (Hour)	No. of Particles		Avg. Diameter (nm)	
	R - 1	R - 2	R - 1	R - 2
0	196	134	365	404
1	167	98	396	433
2	147	91	415	451
3	138	88	423	466
4	120	78	464	500
5	114	67	478	520
6	113	62	481	540
7	113	61	488	544
8	112	61	494	563
9	111	60	498	571
10	110	60	502	569
12	107	61	508	594
14	103	61	521	590
16	102	61	529	594
18	101	58	538	615
20	99	58	549	616
22	98	57	547	633
24	94	57	555	630
26	92	57	564	643

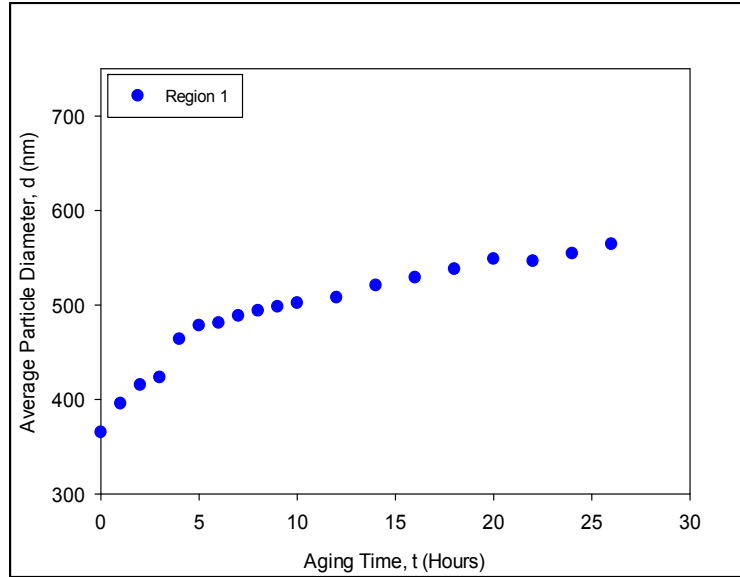


Figure 6.10 Changes in IMC Particle Diameter with Aging Time

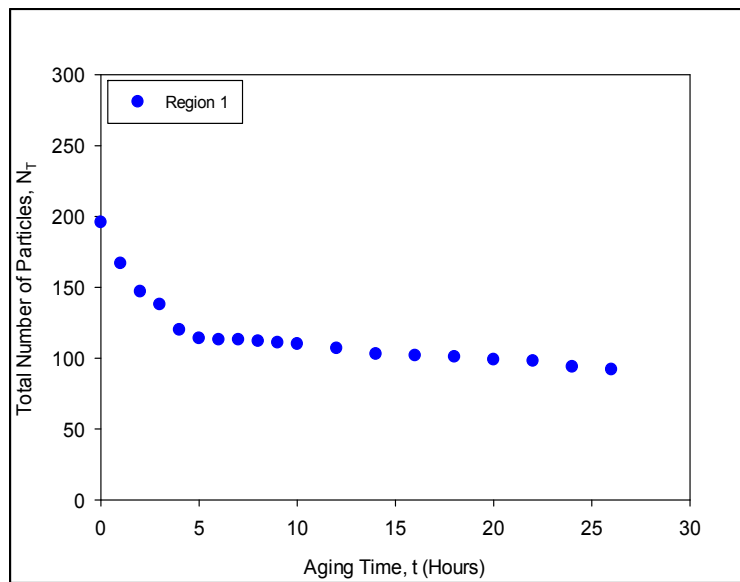


Figure 6.11 Changes in IMC Particle Number with Aging Time

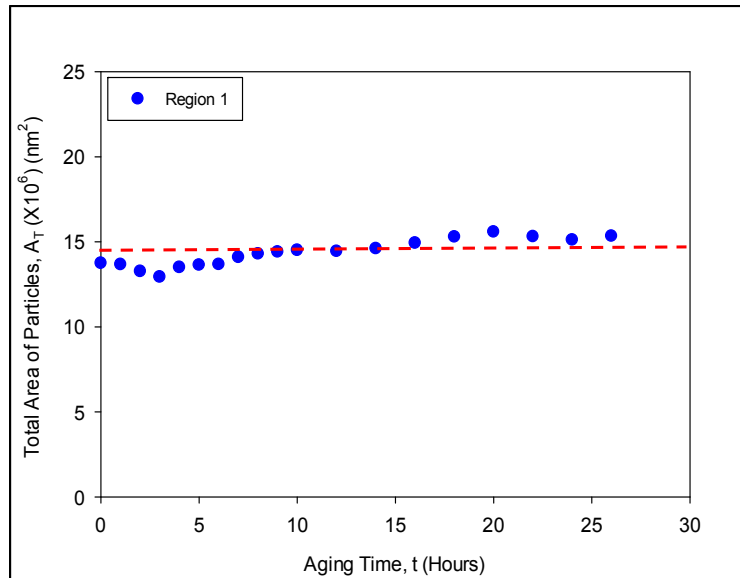


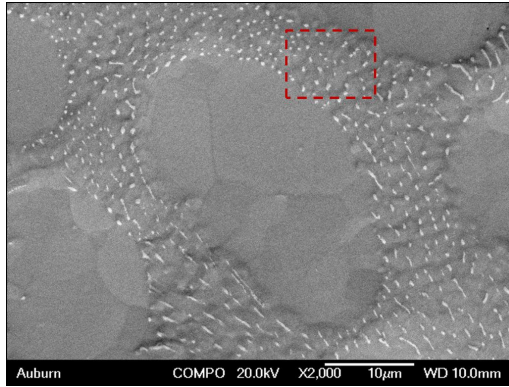
Figure 6.12 Variation in Total IMC Particle Area with Aging Time

6.8 Study Using SEM

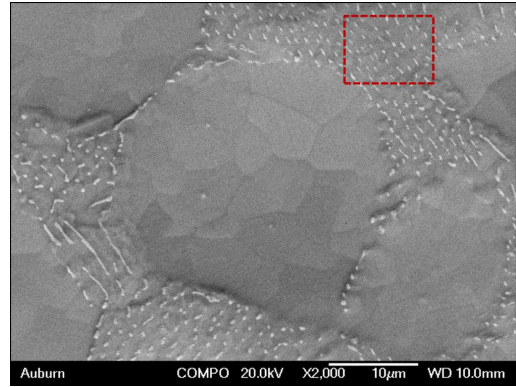
In a parallel study [111], Scanning Electron Microscopy (JEOL JSM-7000F) was utilized to examine the aging induced microstructural changes occurring within lead free solders. Solder cross-sectional specimens were first encapsulated in epoxy mold and then polished using standard procedures. Regions of interest with typical Sn-Ag-Cu (SAC) microstructures were identified to monitor within the polished samples. These consisted of β -Sn dendrites surrounded by interdendritic eutectic regions incorporating a fine dispersion of Ag_3Sn and Cu_6Sn_5 intermetallic particles in β -Sn. To facilitate locating the same regions multiple times after various aging durations, small indentation marks were added to the cross-sections. The polished solder samples with indentation marks were aged at $T = 125^\circ\text{C}$ for various durations. After each aging increment, the microstructures of the regions of interest in the samples were captured using SEM microscopy. Several different regions from several different SAC305 joints were examined, and both short term (up to 50 hours) and long term (up to 2750 hours) aging of the joints have been performed. For

example, Figure 6.13 shows the three regions monitored for the short term aging experiments with up to 50 hours of aging. The microstructures in the regions of interest were recorded after predetermined time intervals of aging. For the short term aging experiments, a 1 hour increment was utilized (up to 50 hours). For the long term aging experiments, a 250 hour increment was utilized (up to 1500 hours). The red boxes in each images indicates regions used for analytical analysis.

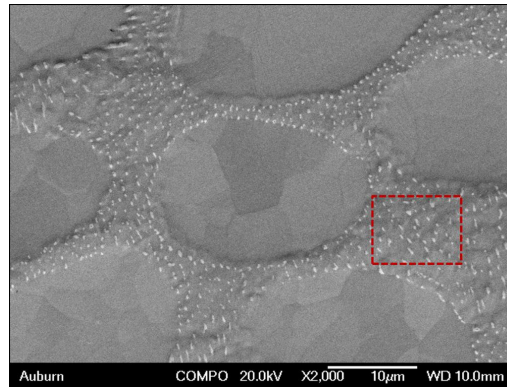
Figure 6.14 shows a series of images illustrating an example microstructural evolution observed at several aging times up to 52 hours. In this case, the results were from Region 1 (Figure 6.13(a)). Similar to the SPM results, coarsening of intermetallics occurred, with some IMC particles growing in size, and some IMC particles decreasing in size and eventually disappearing altogether. This resulted in: (1) a decrease in the number of IMC particles, (2) an increase in the average particle size, and (3) an increase in the average particle separation distance. These effects are illustrated in Figure 6.14, where blue circles show example positions where particles were growing, red circles illustrate positions where the particles decreased in size and disappeared. In addition, the particles tended to shift to more spherical shapes, with needle shaped IMC particles splitting into several smaller particles as shown in the black circles in Figure 6.14. There were no significant changes observed in the size and shape of the dendrites. An example of long term changes in the solder microstructure is presented in Figure 6.15.



(a)

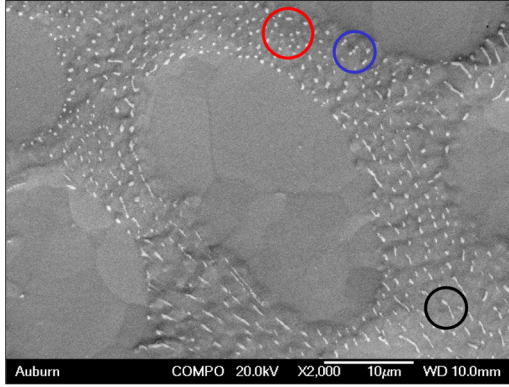


(b)

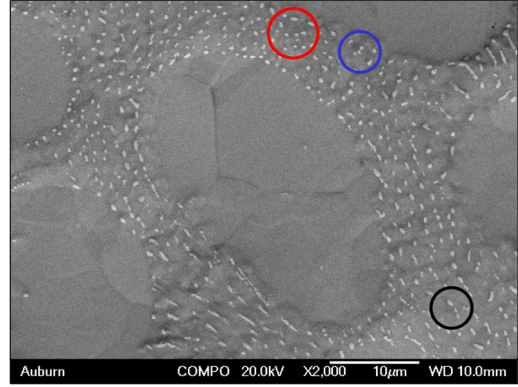


(c)

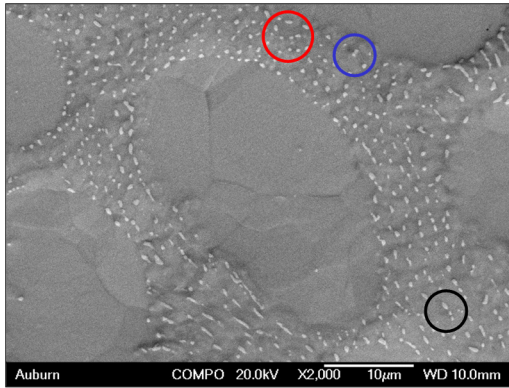
Figure 6.13 (a-c) Monitored Regions in The Short Term Aging Experiments with SEM (Red Boxes Indicate Regions Used for Analytical Analysis).



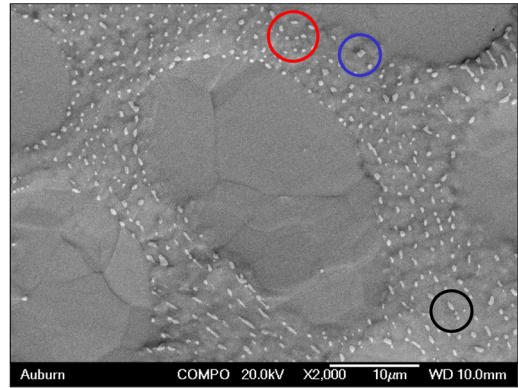
(a) No Aging



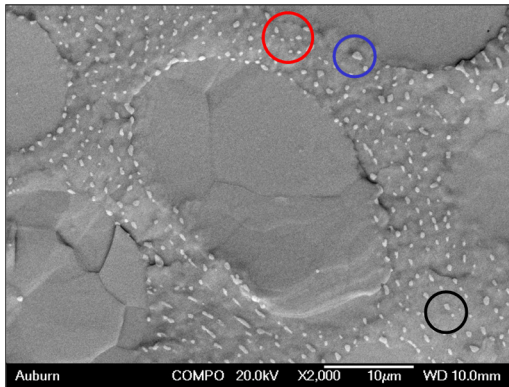
(b) 1 Hour of Aging



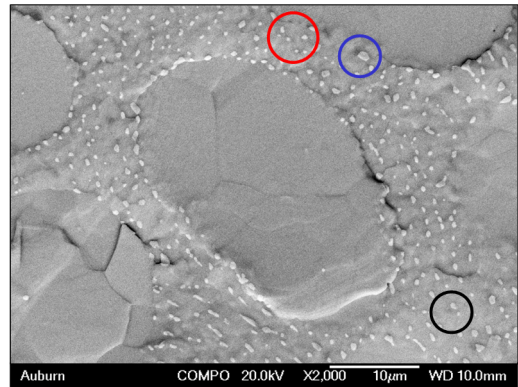
(c) 2 Hours of Aging






(d) 4 Hours of Aging

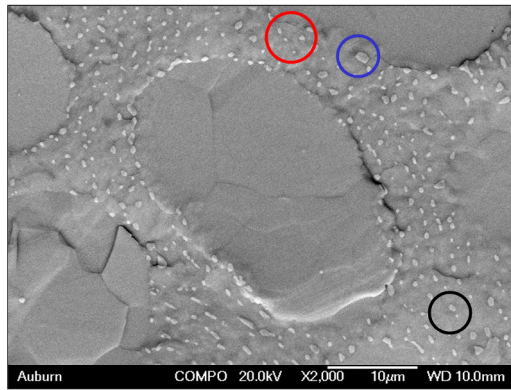


(e) 8 Hours of Aging

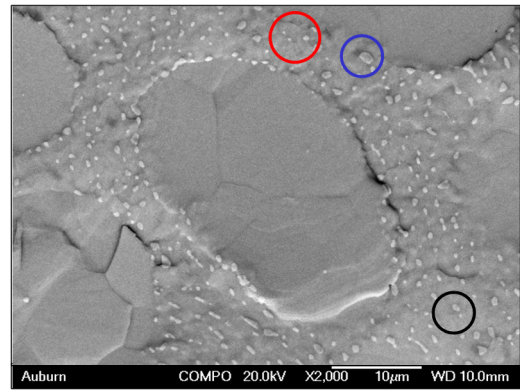


(f) 12 Hours of Aging

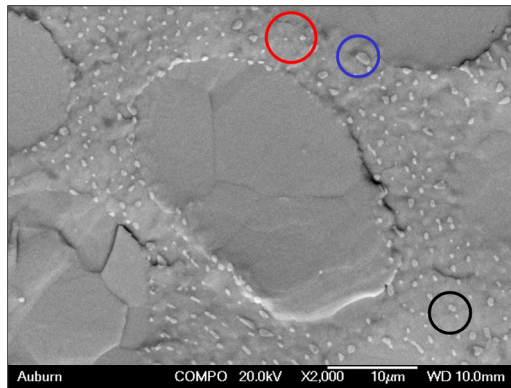
-  (Blue) - Growth and Coalescence of Particles
-  (Red) - Disappearance of Particles
-  (Black) - Splitting of Needle-Shaped IMCs



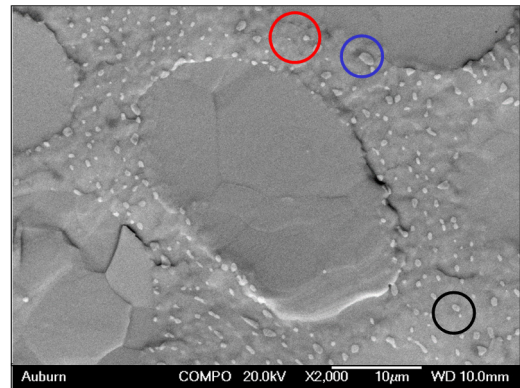
(g) 20 Hours of Aging



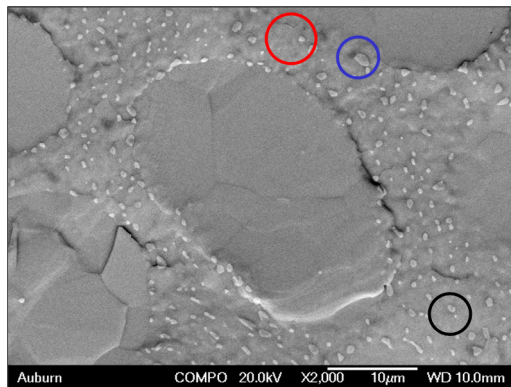
(h) 28 Hours of Aging



(i) 36 Hours of Aging



(j) 44 Hours of Aging



(k) 36 Hours of Aging

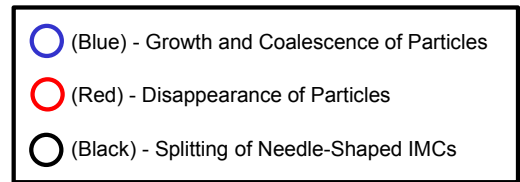


Figure 6.14 (a-k) Example SAC305 Short Term Microstructural Evolution Observed by SEM Microscopy (Aging at $T = 125\text{ }^{\circ}\text{C}$).

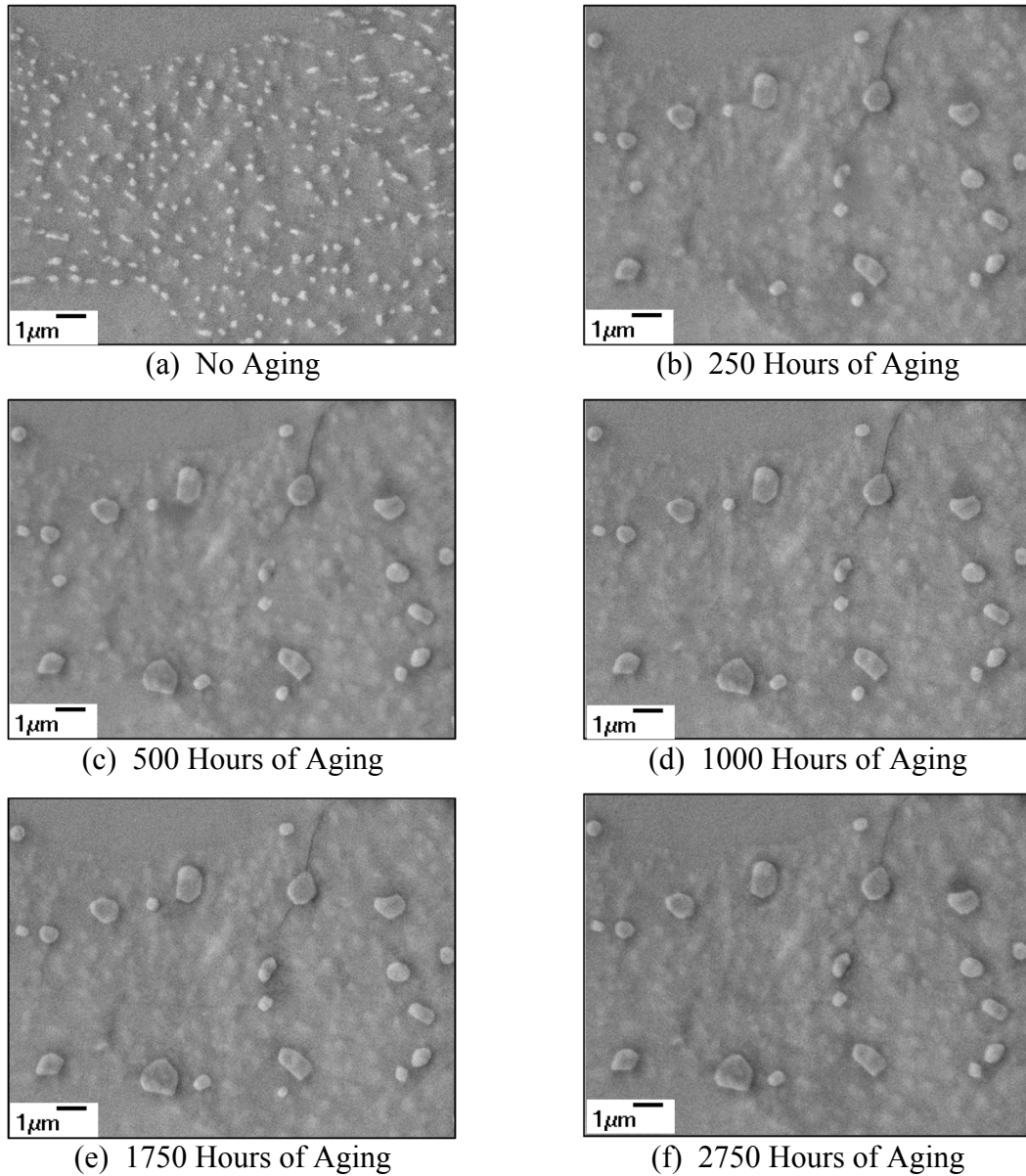


Figure 6.15 (a-f) Example SAC305 Long Term Microstructural Evolution Observed by SEM Microscopy (Aging at $T = 125\text{ }^{\circ}\text{C}$).

6.9 Discussion of IMC Evolution During Aging

Typically, IMC particles tend to become more round (spherical) with aging. Atoms on the surface of a particle have higher energy than the atoms inside a particle due to unsatisfied bonds in the surface atoms. A cylindrical or elongated particle has a higher

fraction of surface atoms (or higher surface to volume ratio) compared to a spherical (round) particle with the same volume. As a result, the free energy per atom of an elongated particle or several small particle is higher than a big round particle with equal volume. This free energy difference is the driving force that causes the transition of IMC particles from smaller to a bigger size as seen in Figures 6.9-6.10, 6.14-6.15.

This IMC coarsening phenomenon is also known as Ostwald Ripening. According to the Gibbs-Thompson effect [112-114], an increase in particle size is accompanied by a decrease of the solute concentration in the matrix surrounding the particle. This leads to a concentration gradient, and solute atoms near smaller particles will diffuse towards the larger particles where the reductions in solute concentration has occurred. In addition, atoms from the smaller particles will go back into solution. The overall effects are shrinkage of smaller particles, and growth of larger particles. A schematic of the variation of solute concentration around a small and a large particles is shown in Figure 6.16. Since Ostwald Ripening is a diffusion-based process, use of higher aging temperatures will increase the rate of coarsening significantly.

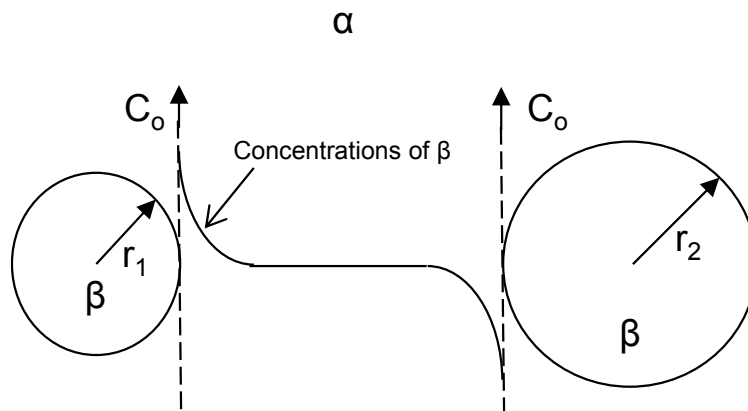


Figure 6.16 Schematic of Solute Concentration in Front of A Small and a Large Particle [114].

The coarsening and coalescing of IMC particles during aging is known to play a critical role in the degradations of solder mechanical properties. IMC particles will pin and block the movement of dislocations. However, aging leads to both a smaller number of larger IMC particles and increased spacing between the IMC particles. The interparticle spacing λ can be calculated from the following equation:

$$\lambda = \frac{4(1-f)r}{3f} \quad (6.7)$$

where f is the volume fraction of the particles and r is the particle radius. Hence for a fixed volume fraction of the IMC particles, spacing between the particles increases with increasing particle diameter. Orowan proposed a mechanism that when a dislocation crosses incoherent precipitate particles (like the IMC particles in present case), it will bow and leave a loop of stress field around the particle [113-115]. A schematic of the interaction between a dislocation and IMC particles is shown in Figure 6.17

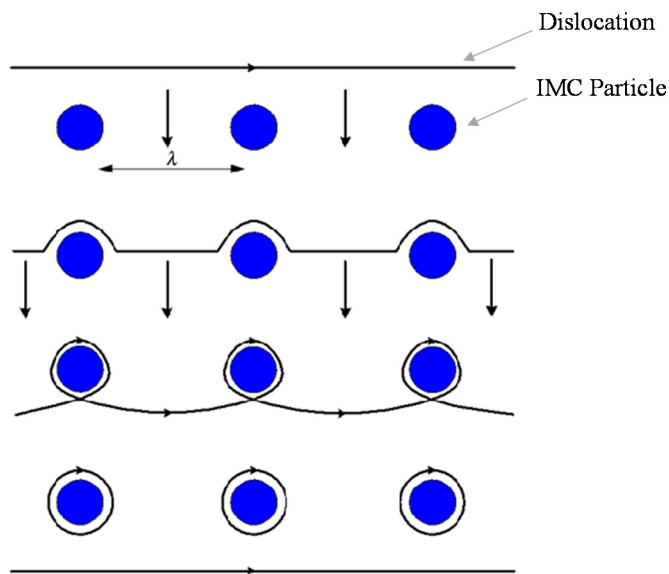


Figure 6.17 Schematic Representation of a Dislocation Passing IMCs (Orowan Looping)

[115]

The yield stress and strength of a material depends on the shear stress (also known as the Orowan stress) that is required for a dislocation to pass through the particles. This shear stress will decrease as the inter-particle spacing increases during aging as shown in equation 6.8 [113, 114, 116]

$$\tau_o = \frac{Gb}{\lambda} \quad (6.8)$$

where τ_o is the shear stress required for a dislocation to pass through the particles, G is the shear modulus, and b is the magnitude of the burgers vector. Therefore, aging leads to the coarsening of the IMC particles which causes to increase the interparticle spacing (equation 6.7). The yield stress and strength of a material decrease after aging due to the increased interparticle spacing.

6.10 Fitting Equation

Early quantitative modeling of Ostwald ripening was Performed by Lifshitz and Slyozov, and Wagner in 1961 (known as the LSW Theory) [108, 109]. According to the model, the diameter of a particle at any arbitrary time during thermal exposure can be represented as

$$\frac{d^3}{8} - \frac{d_o^3}{8} = \left[\frac{8\Omega^2\gamma C_o D}{9RT} \right] t \quad (6.9)$$

where d is the average diameter of all particles at time t, d_o is the average diameter of all particles at time $t = 0$, Ω is the molar volume of the particle material, γ is the particle surface energy, C_o is the solubility of the particle material, D is the diffusion coefficient of

the particle material, R is the ideal gas law constant, T is the absolute temperature, and t is the time. Equation (6.9) can be simplified as

$$d = (C_1 t + C_2)^{1/3} \quad (6.10)$$

where C_1 and C_2 are constants.

To fit our experimental data well, it was found that equations (6.9, 6.10) needed to be slightly modified by adding an extra constant C_3 as below

$$d = (C_1 t + C_2)^{1/3} + C_3 \quad (6.11)$$

The black and blue curves in Figure 6.18 indicate regression fits of eq. (6.11) to the data present in each plot for region 1 and region 2, respectively.

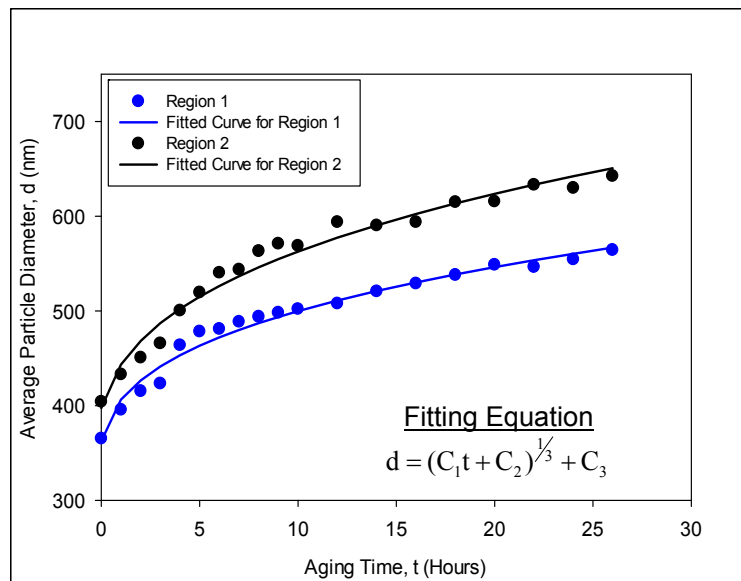


Figure 6.18 Changes in IMC Particle Diameter with Aging Time.

The slight deviation from the LSW theory could arise from the non-spherical shape of the IMC particles. In addition, the quantitative analysis results reported in this work are

based on coarsening phenomenon observed at the solder surface. In many cases, the surface diffusion rates in the plane of the sample surface are different than those in the sample bulk. The observations in question involve both bulk and surface diffusion phenomena.

6.11 Comparison Between SPM and SEM Results with Mechanical Properties

Analytical analysis results obtained from SPM and SEM images, for all the regions are presented in Figures 6.19 and 6.20, respectively. It is clear that the results obtained from SPM analysis are consistent with those obtained from the SEM analysis.

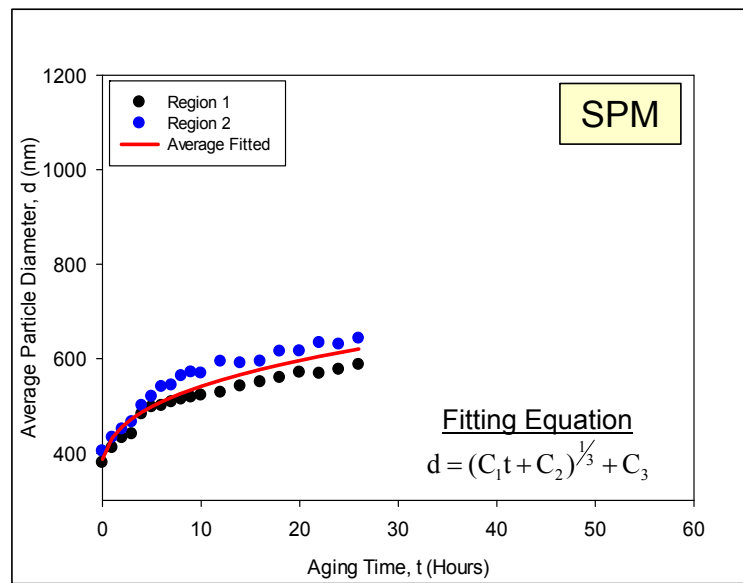


Figure 6.19 Variation of IMC Particle Diameter with Aging Time (SPM, Short Term Aging).

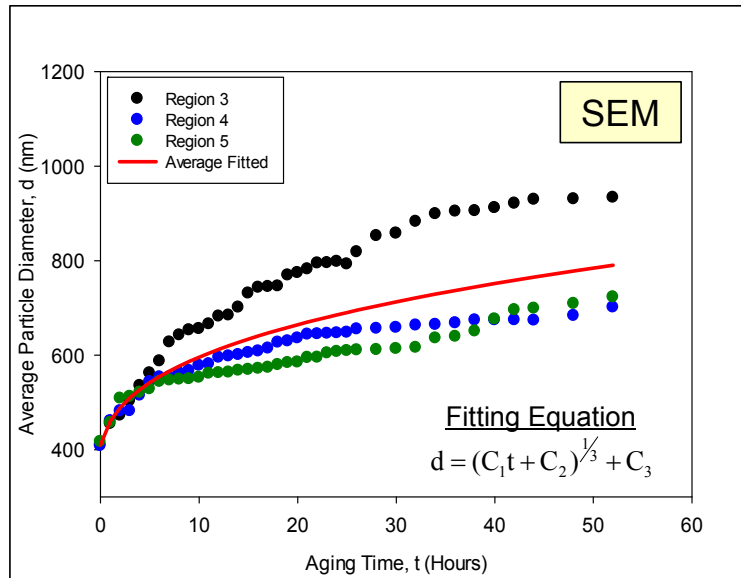


Figure 6.20 Variation of IMC Particle Diameter with Aging Time (SEM, Short Term Aging).

A combined graph of short and long term studies with both SPM and SEM is plotted in Figure 6.21. In the same figure, the changes in mechanical strength (UTS) of the same alloy plotted as a function of aging time. It is clear from figure 6.21 that the initial rapid degradation of the mechanical strength of the SAC solder can relate to the rapid coarsening rate at the first few hours

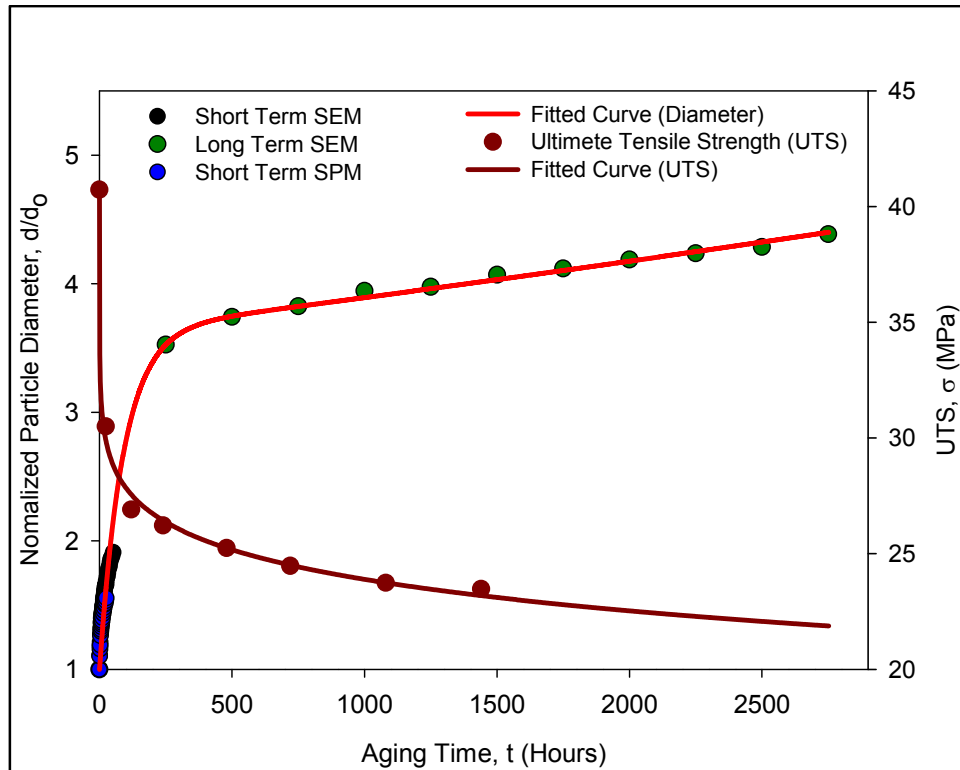
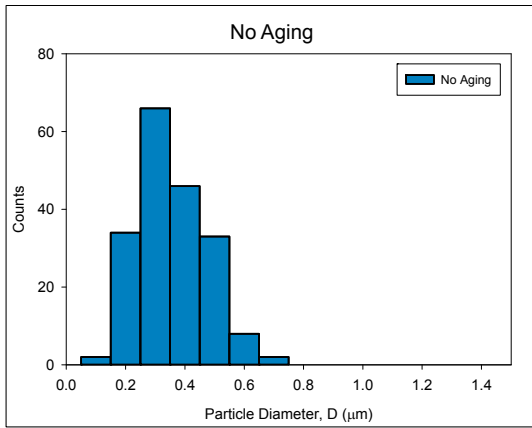


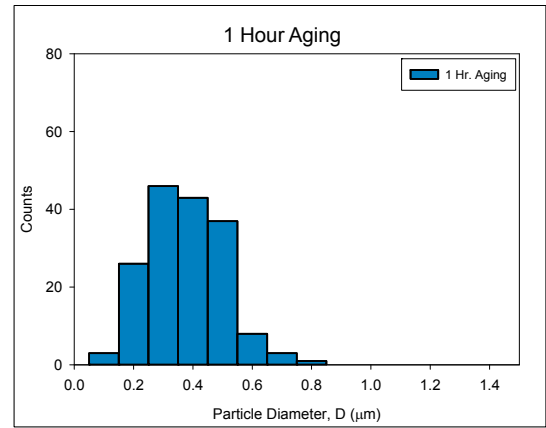
Figure 6.21 Variation of IMC Particle Diameter (Short Term and Long Term Aging Data) and Mechanical Strength with Aging Time.

6.12 Distribution of IMC Particles

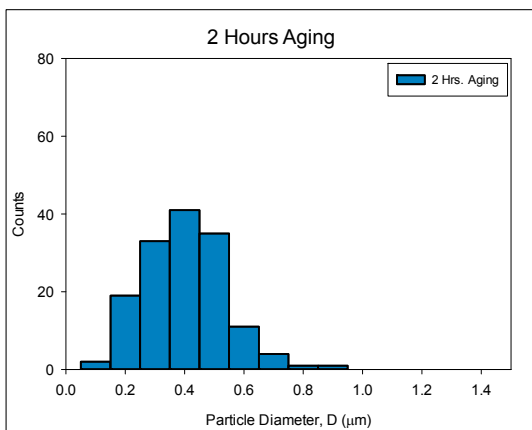
Figure 6.14 illustrates results (from region 1) for the variations of the particle size distribution in a fixed region with aging time. In as reflowed conditions (no aging), a narrow and tall distribution profile was obtained (Figure 6.22(a)). As the aging progresses (Figures 6.22(b-s)), the height of the distribution profile decreases, whereas the width increases. This transition in the distribution profile also reflects the fact that the larger IMC particles keep growing at the expense of the smaller IMC particles during aging.



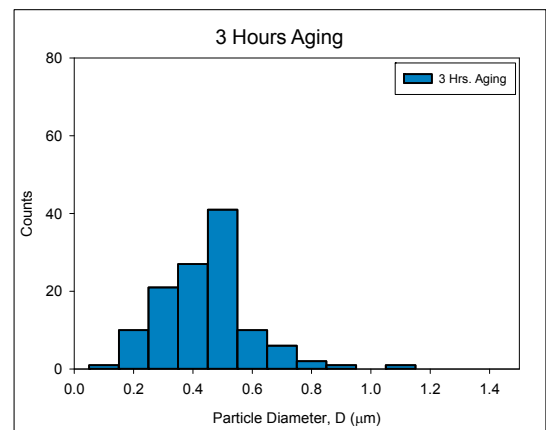
(a)



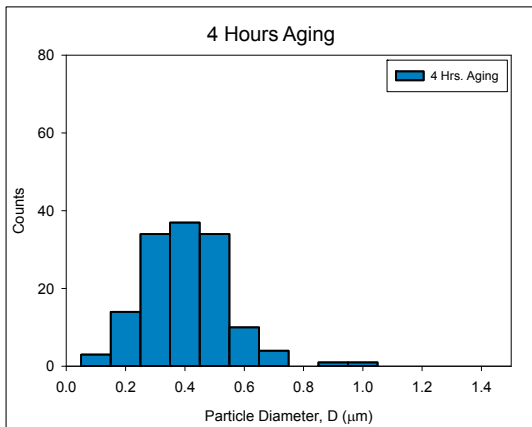
(b)



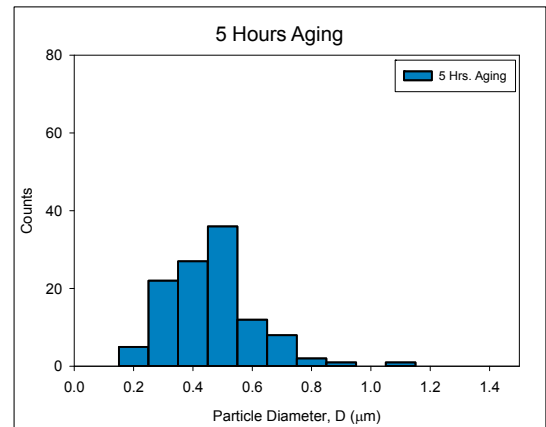
(c)



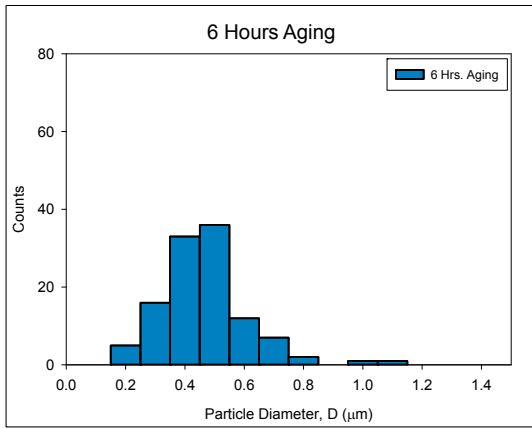
(d)



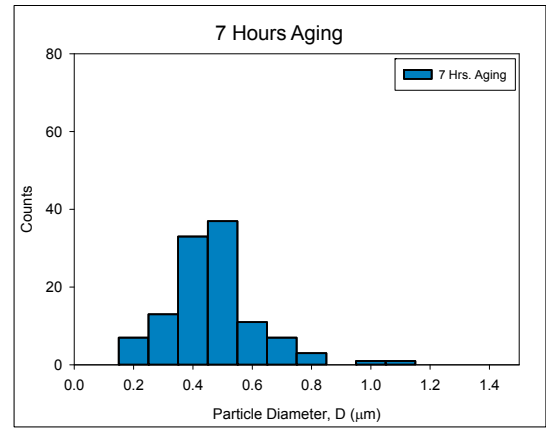
(e)



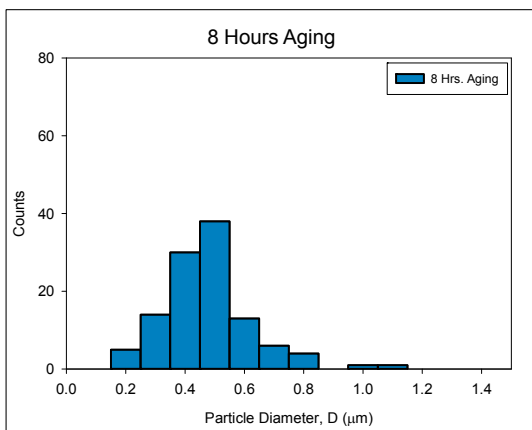
(f)



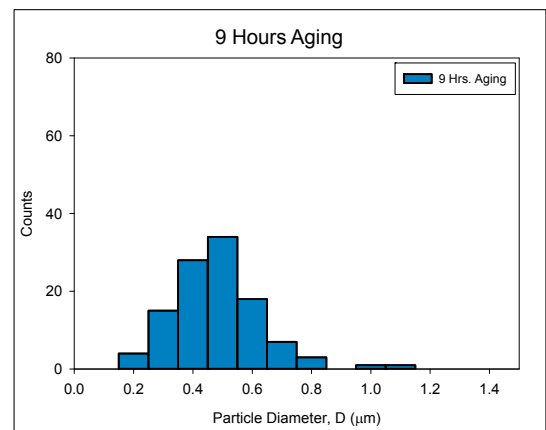
(g)



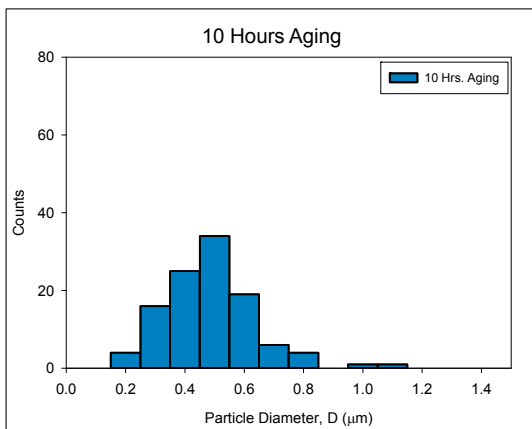
(h)



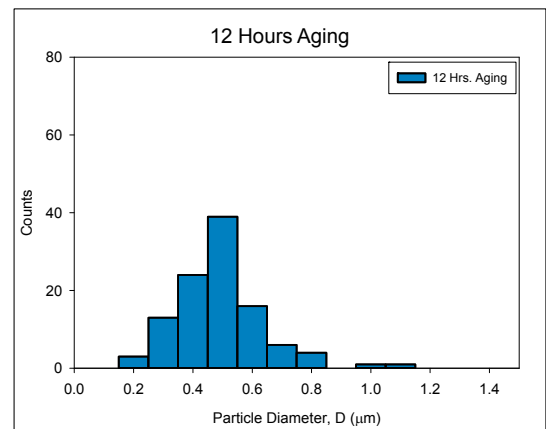
(i)



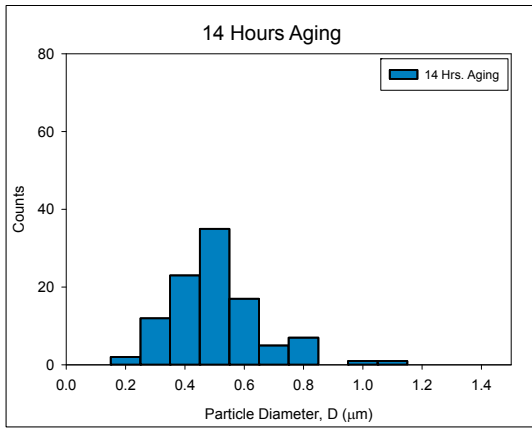
(j)



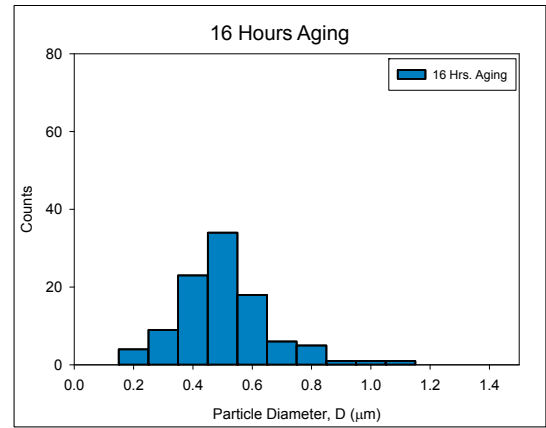
(k)



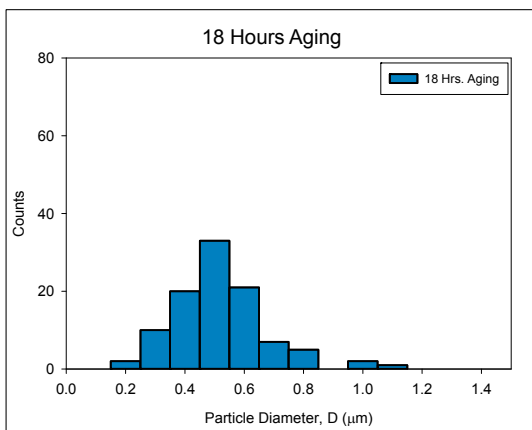
(l)



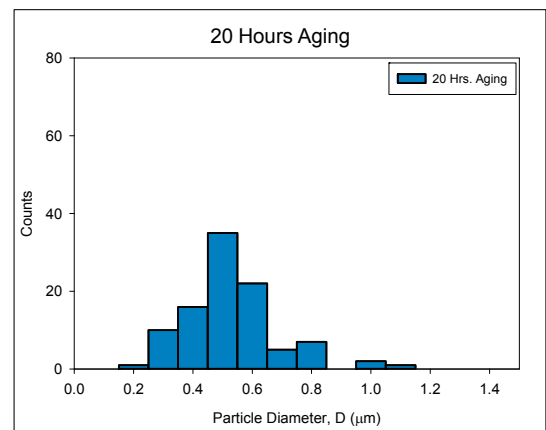
(m)



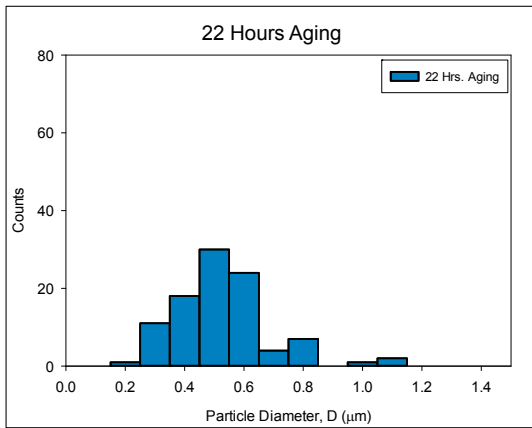
(n)



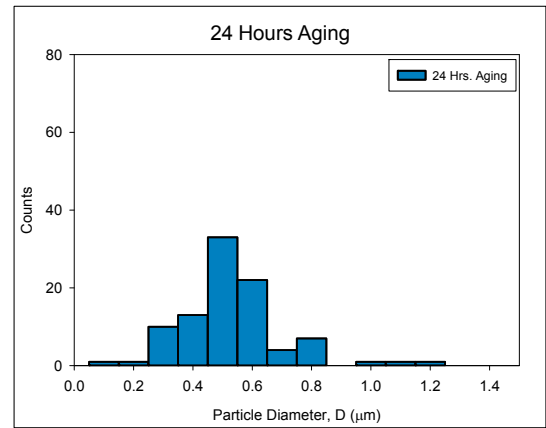
(o)



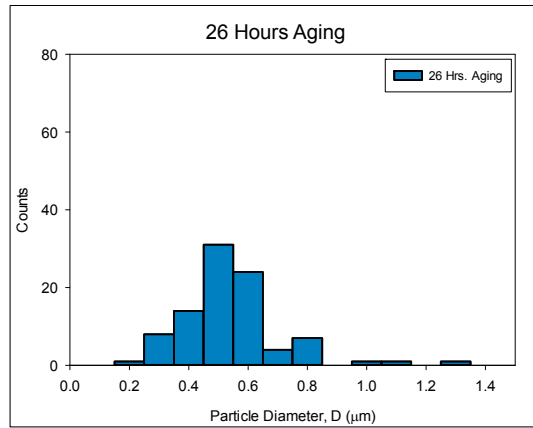
(p)



(q)



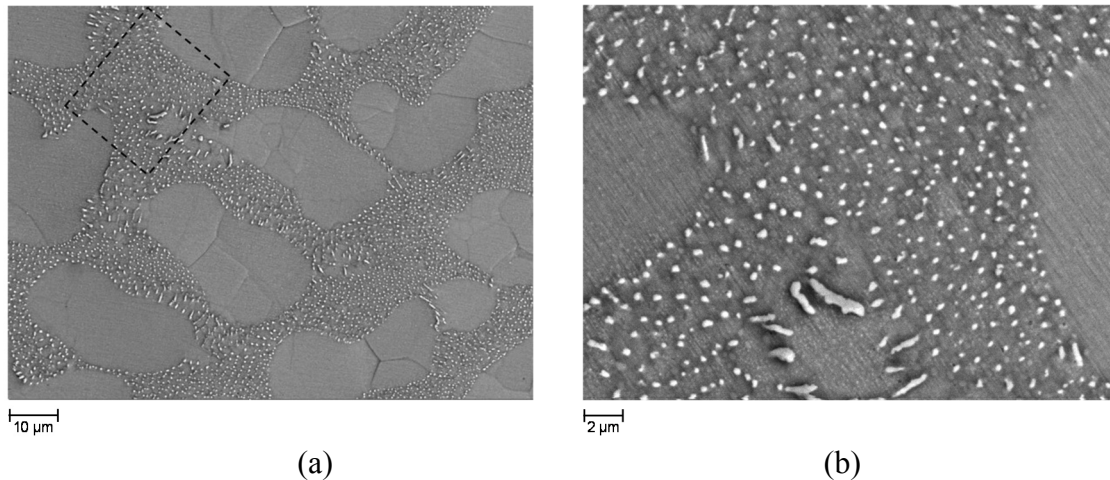
(r)



(s)

Figure 6.22 (a-s) Distributions of IMC Particle Sizes After Various Aging Times.

The IMC particles observed during SEM/SPM imaging were similar to the ice bergs, where a tiny portion of an ice burg is exposed above the water layer and the rest of it is underneath the water. Focused Ion Beam (FIB) was used to observe the size of the IMC particles underneath the exposed surface. Microstructure of SAC305 solder and the location of the eutectic region where FIB analysis was performed is shown in Figure 6.22.



(a)

(b)

Figure 6.23 (a) SAC305 Microstructure and (B) Region Selected for FIB Analysis.

A portion of the selected region was coated with Platinum (Pt) to prevent surface damage during ion bombardment. Figure 6.24 shows platinum coating and the condition of the surface after FIB analysis.

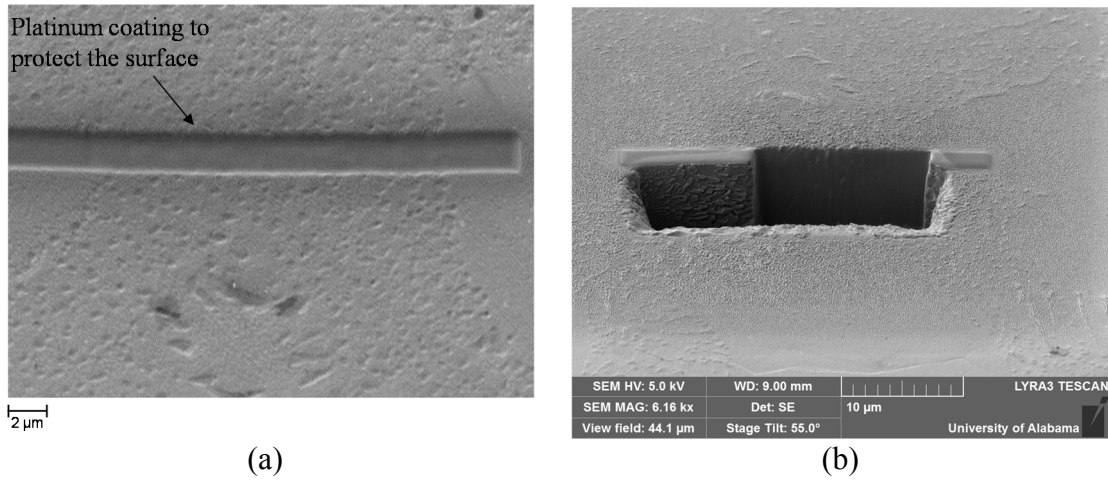
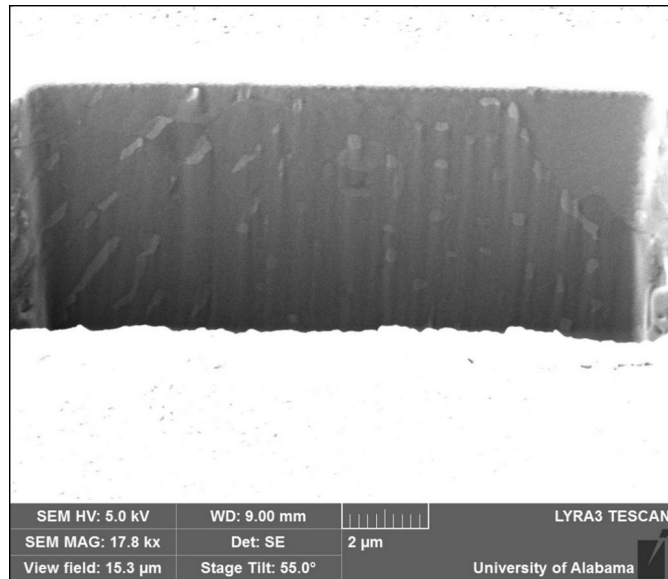
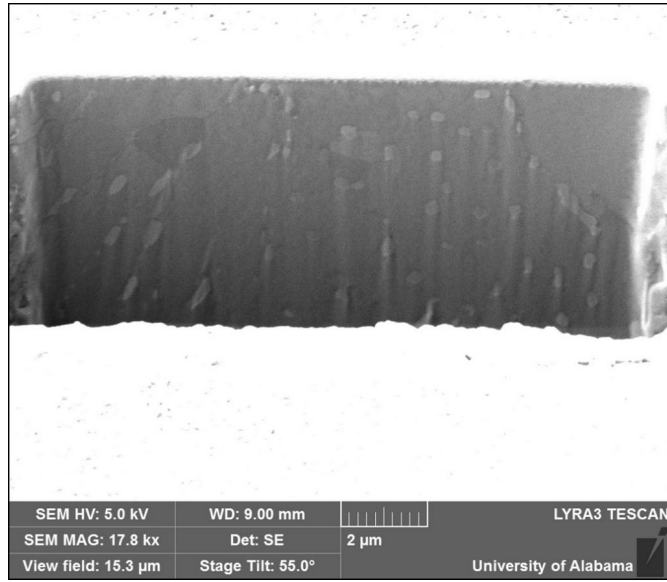


Figure 6.24 SAC305 Microstructure (a) After Platinum Coating and (b) After FIB Analysis

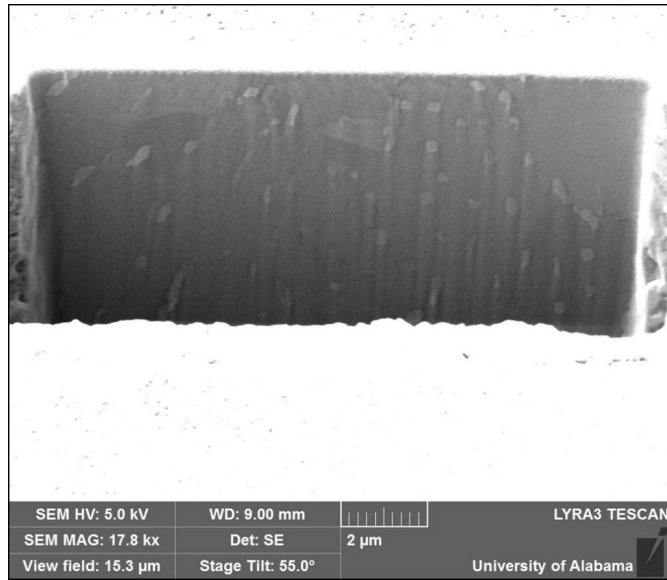
After the initial coarse cutting, during the FIB analysis, several fine cuts were made with 100 nm increment. All the images obtained during the FIB analysis are presented in Figure 6.25. It is clear from all the FIB images that the IMC particle size measured from the surface are similar to the IMC particle size inside the surface.



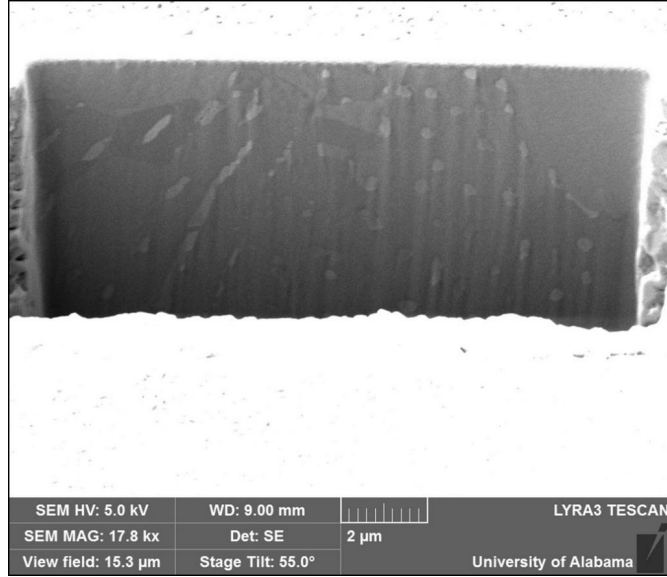
(a) 1st Slice: 0 nm



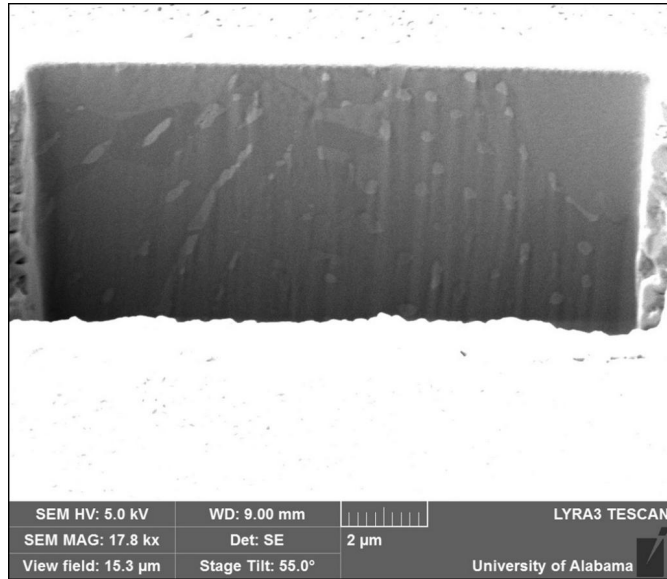
(b) 2nd Slice: 100 nm



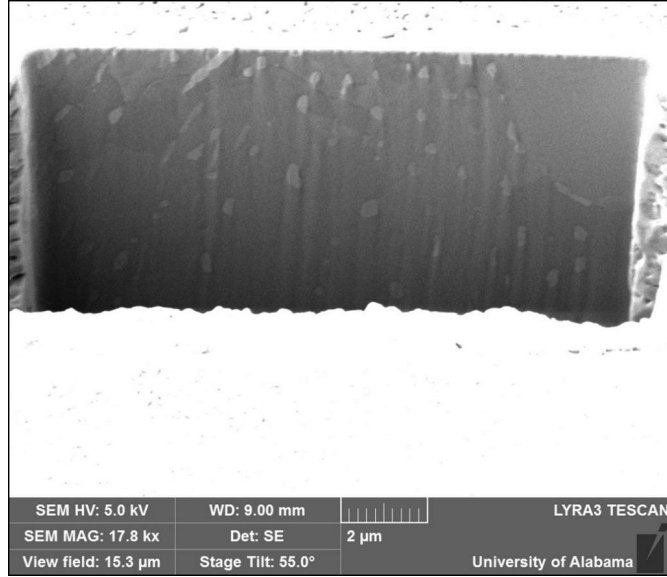
(c) 3rd Slice: 200 nm



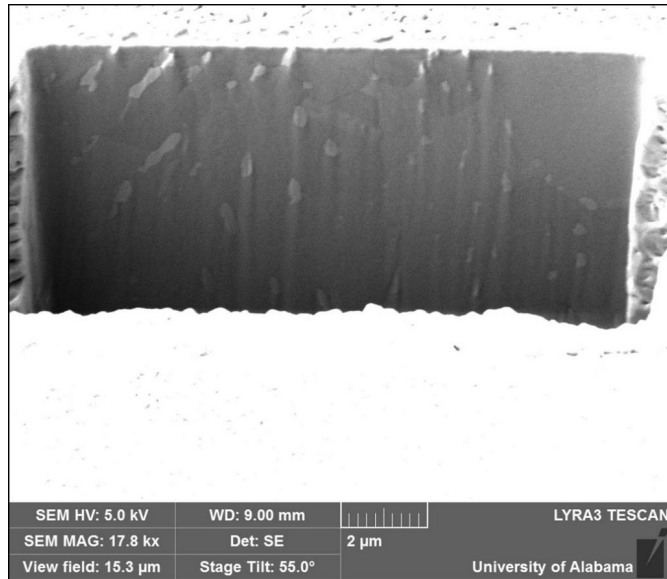
(d) 4th Slice: 300 nm



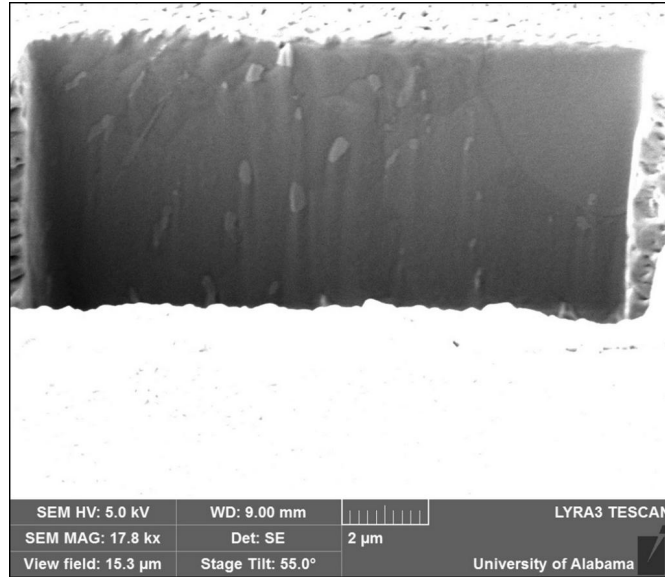
(e) 5th Slice: 400 nm



(f) 6th Slice: 500 nm



(g) 7th Slice: 600 nm



(h) 8th Slice: 700 nm

Figure 6.25 (a-h) FIB Images of SAC305 Solder Showing the IMC Particles Underneath the Surface

6.13 Summary

New procedures were developed to capture solder microstructure while the sample is being heated inside an oven (in-situ aging study). The heating stage and scanning probe microscopy (SPM) facility within a nanoindentation system were utilized to achieve the goal. The sample was kept within the nanoindentation system and exposed to a high temperature aging using the heating stage present in the instrument. In particular, aging was performed at $T = 125\text{ }^{\circ}\text{C}$ for 26 hours, and the topography of the microstructure of two different fixed region (10×10 microns) was continuously scanned using the SPM system and recorded after one hour time intervals. This process generated several images of the microstructure as the aging progressed. When placed together sequentially, these images have been used as frames to create an experimentally recorded movie of the microstructural evolution in SAC solder joints exposed to aging. Image analysis software was utilized to

quantify microstructural changes (total area, number and average diameter of IMC particles, etc.) with respect to aging time.

Quantitative analysis of the microstructures has shown that the number of IMC particles decreases during aging, while the average diameter of the particles increases significantly. Conventional models for IMC particle coarsening could not fit the experimental data found in this study. Histogram charts were also used to illustrate distribution of the particle sizes present at each aging time, and to show that that changes occurred during aging. In particular, the number of particles of any given size decreased with aging, while the width of the histogram increased, indicating a larger distribution of different particle sizes as aging progressed. FIB analysis shows that the IMC size underneath the surface of the solder is similar to the ones on the surface.

CHAPTER 7

CHARACTERIZATION OF SBGA PACKAGE FOR RELIABILITY ANALYSIS

7.1 Introduction

In this chapter, the board level thermal cycling reliability of Super Ball Grid Array (SBGA) packages has been investigated by simulation and experimental testing. A typical SBGA design has a facedown cavity structure for chip attachment, where the chip is directly attached to an integrated copper heatsink. This copper plate gives SBGA components better heat dissipation efficiencies than standard PBGAs. However, since the constructions of SBGA packages are quite different than other PBGA (Plastic Ball Grid Array) packages; they have different reliability behaviors and can have different compatibilities with Printed Circuit Board (PCB) materials and surface finishes. Nanoindentation and strain gauge based CTE (coefficient of thermal expansion) measurement methods were utilized to extract mechanical and thermal properties of different layers such as substrates, mold, die, solder mask, Cu-pad, solder, adhesive material etc. of a 31 mm SBGA package. Extensive microscopic study was performed to understand the construction of SBGA package, FR-4 and Megtron-6 PCB laminates. Finite element modeling was used to predict the reliability of SBGA assemblies for different PCB laminate materials. The FEA results have been validated through correlation with thermal cycling accelerated life testing experimental data. One general finding is that SBGA packages are more reliable when mounted on Megtron-6 PCB material.

7.2 Nanoindentation on SBGA Package

The nanoindentation tests were conducted on solder joint, copper heat spreader, copper ring, die, die adhesive, solder mask, solder ball, copper pad, and mold layer of the

SBGA package using an instrumented Hysitron TI 950 nanoindentation system shown in Figure 3.17 (chapter 3). Package cross sectioning, epoxy potting, grinding and polishing procedure described in chapter 3 sections 3.5 and 3.6 were followed to prepare sample for nanoindentation experiment. The load vs. displacement (depth of indentation) in the direction normal to the cross-sectional surface of specimen was recorded during each nanoindentation test.

Figure 7.1 shows half of the cross section and a few example of indents achieved on solder joint (SAC305), heat sink, and copper pad of the SBGA package. The zoom in area of permanent indentation are also presented in the figure. 15-30 indents were performed to attain a statistically meaningful results and the consistency of inspection. It can be noted that the indents in a set were positioned at least $3b \mu\text{m}$ apart, where b is the width of a single indent, to avoid interactions between the plastic zones created by the indentations. The calibration of the indenter tip shape was performed on a standard fused quartz sample. Based on the type of the material present in the SBGA assembly, both high load and low load transducers of the indentation machine were utilized. Images of both transducers along with stages are presented in Figure 7.2.

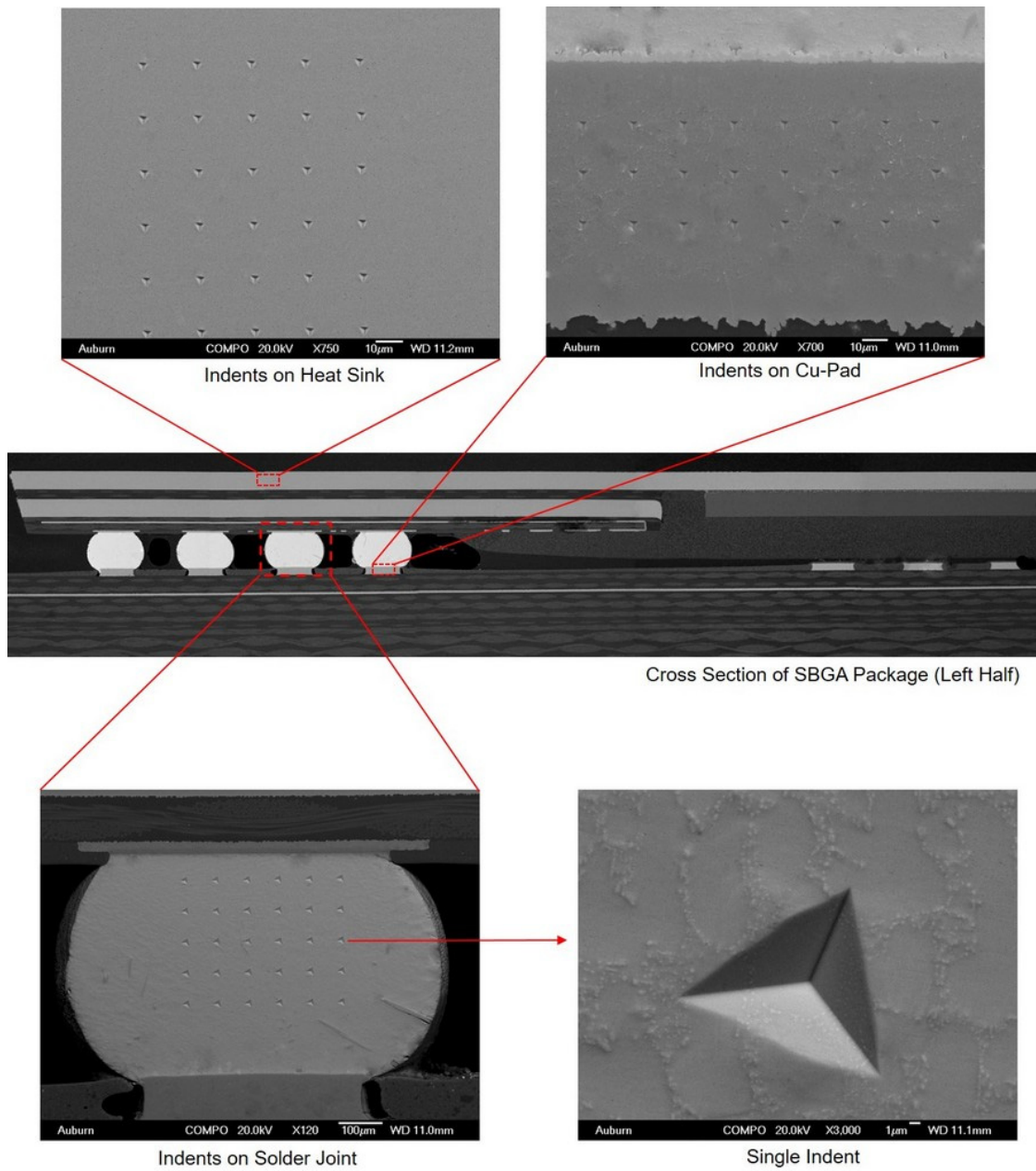


Figure 7.1 Cross Section of SBGA Package and a Few Examples of Indents.

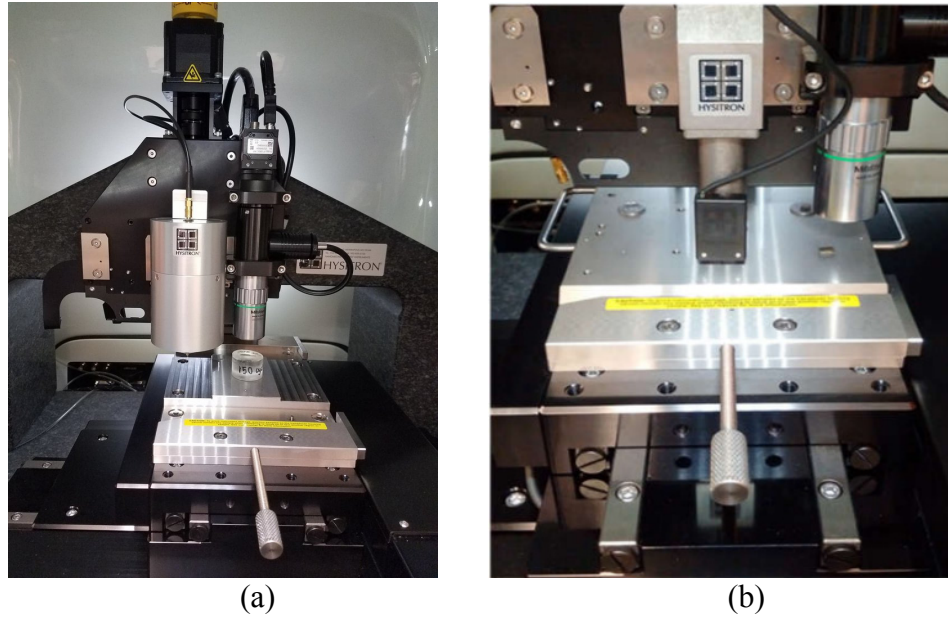


Figure 7.2 (a) High Load Transducer and Stage, (b) Low Load Transducer and Stage

Different loading profiles, as shown in Figures 7.3-7.7, were used for nanoindentation on different materials of the SBGA assembly. Same loading profile, as shown in Figure 7.3, was used for Cu pad, heat sink, Cu-ring, and Si die. The maximum load used was 10 mN with 5 second loading, 2 second holding, and 5 second unloading time. The loading profiles used for solder joint, solder mask, die adhesive, and mold are presented in Figures 7.4, 7.5, 7.6, and 7.7 respectively. Figure 7.4 represents the loading profile used for nanoindentation in the solder joint. The maximum load used was 30 mN to ensure that the load is large enough to cover all the phases in the microstructure. Holding time was increased to 5 second while the unloading time was reduced to 2 second. These changes were made to avoid bowing in the unloading portion of the load vs. indentation depth curve. Since modulus was measured by taking the slope of the unloading portion of the load-displacement curve (Oliver-Pharr method [95, 117]), bowing would yield a wrong result. Bowing is typically observed when the test material shows excessive creep deformation during the test. Since the creep rate is very high at the beginning, increasing

holding time will ensure a majority of the primary creep deformation to take place during the holding period at the maximum load. Besides, reducing the unloading time, will give less chance to the material for creep deformation during the unloading period. An example of load displacement curve with and without bowing is shown in Figure 7.8. For each material, the test parameters were optimized by performing several trial run, to obtain the correct results. A summary of the nanoindentation test results are presented in Table 7.1

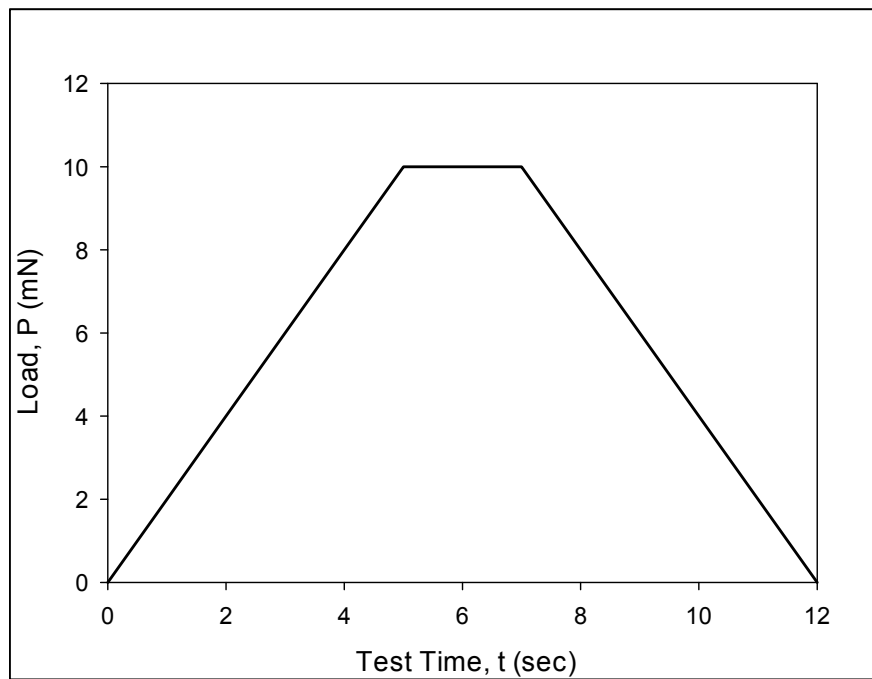


Figure 7.3 Loading Profile Used for Cu Pad, Heat Sink, Cu Ring, and Si Die

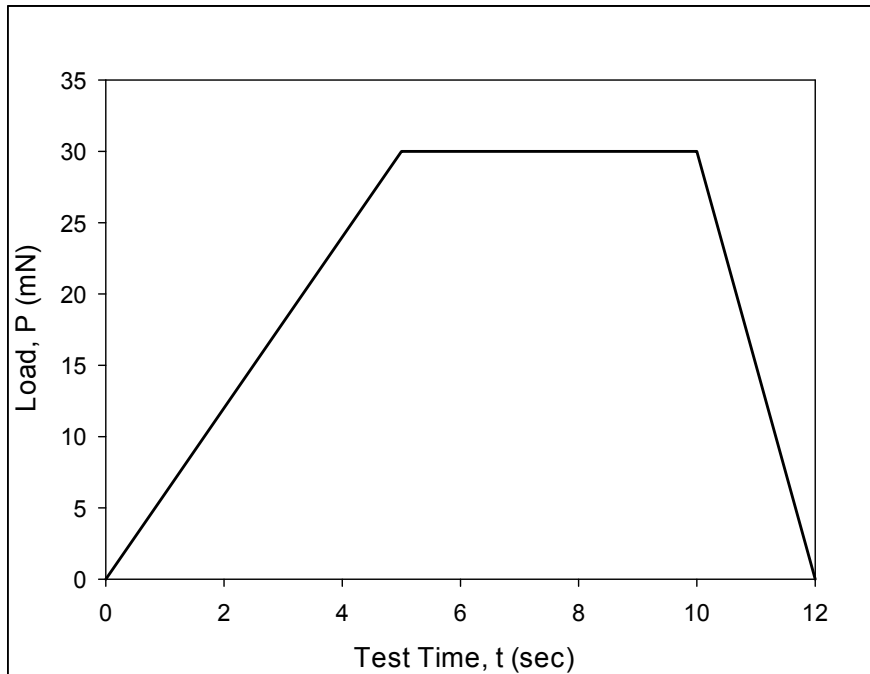


Figure 7.4 Loading Profile Used for Solder Joint

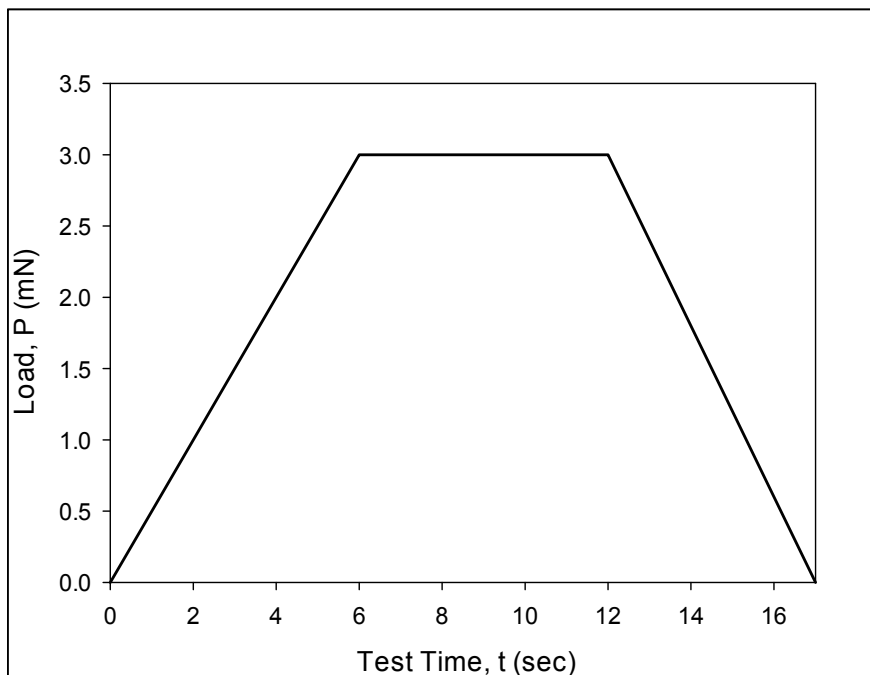


Figure 7.5 Loading Profile Used for Solder Mask

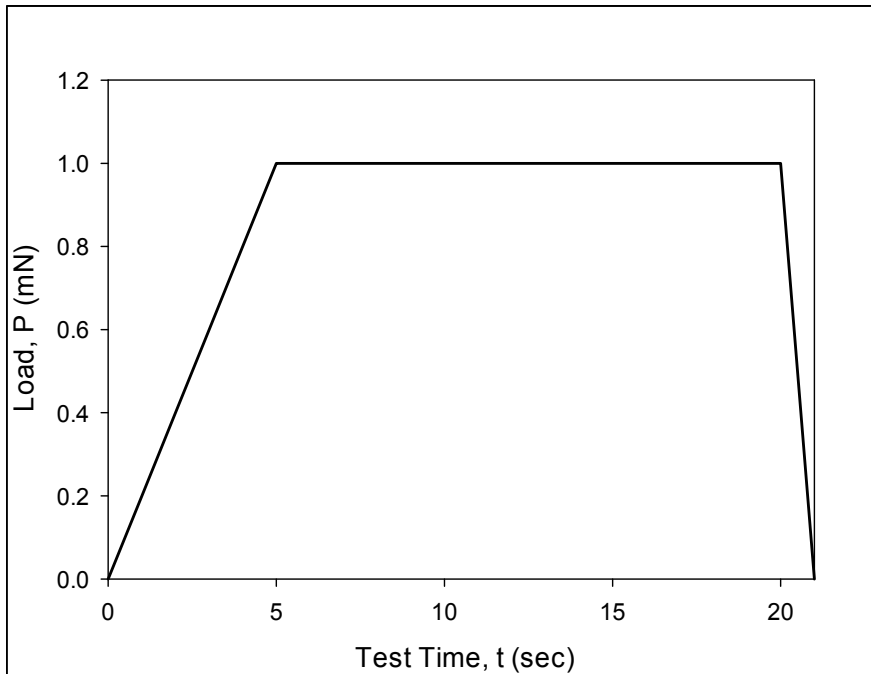


Figure 7.6 Loading Profile Used for Die Attach Adhesive

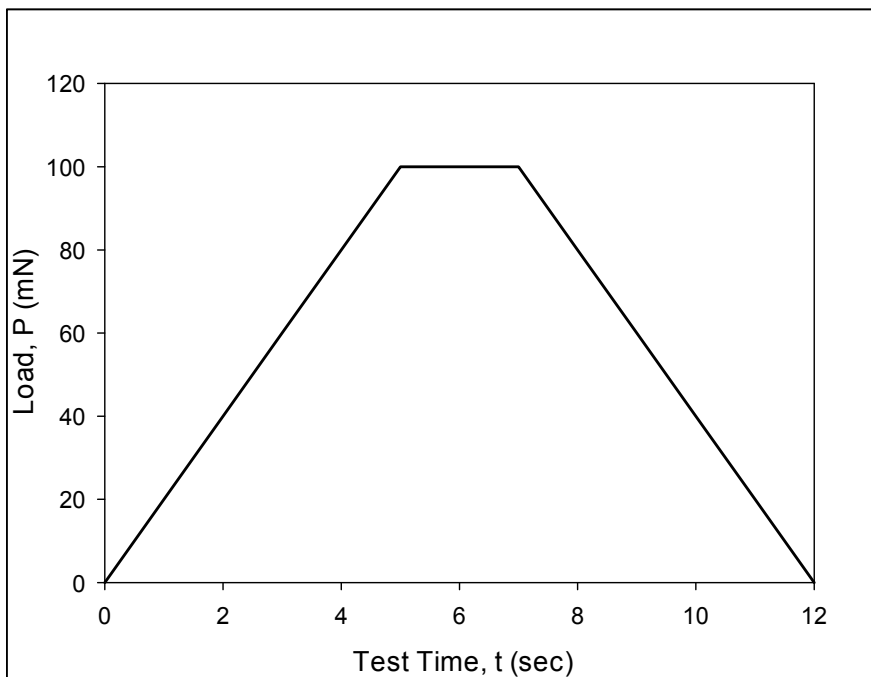
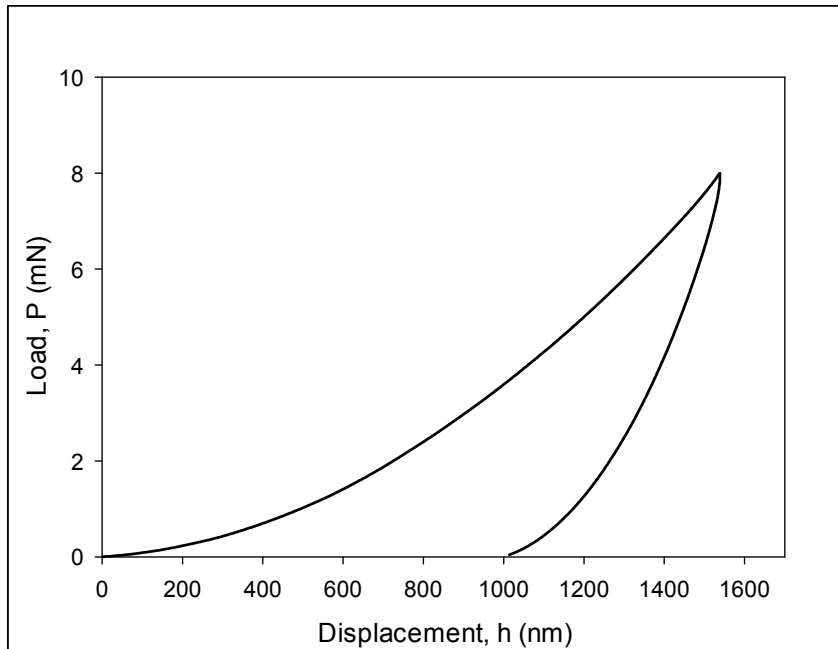
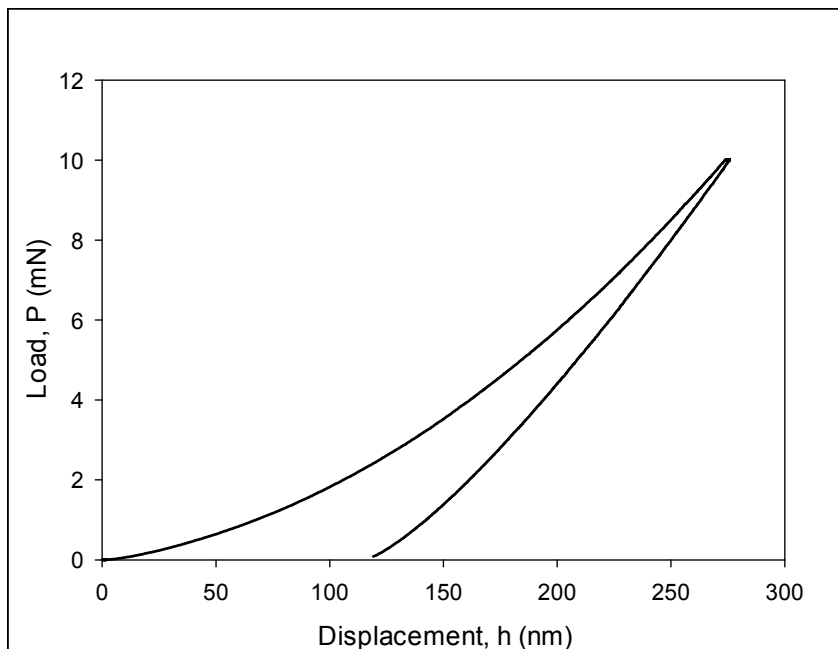


Figure 7.7 Loading Profile Used for Mold Compound



(a)



(b)

Figure 7.8 Nanoindentation Load-Displacement Curves (a) Bowing and (b) No Bowing in the Unloading Curve

Table 7.1 A Summary of the Nanoindentation Test Results

Material	Load Applied (mN)	No. of Indents	Average Reduced Modulus, E_r (GPa)	Average Elastic Modulus, E (GPa)
Cu Ring	10	26	116.4 (3.0)	114.6 (3.3)
Cu Heat Sink	10	28	116.9 (2.1)	115.2 (2.3)
Solder Ball	30	25	54.6 (2.5)	50.3 (2.2)
Si Die	10	30	144.2 (1.0)	152 (0.9)
Cu Pad	10	27	93.3 (2.8)	89.9 (2.9)
Solder Mask	3	19	7.2 (0.3)	6.8 (0.2)
Die Adhesive	1	15	1.4 (0.3)	1.2 (0.3)
Mold	100	27	11.5 (1.5)	10.9 (1.4)

7.3 Measurement of Thermal Property (CTE)

CTE of FR-4 and Megtron-6 were measured by a Wheatstone Bridge based Vishay Measurement Group 2120 strain indicator with a model MG2000 Analog to Digital Converter as shown in Figure 7.9. This system allowed the Wheatstone bridge voltage signals from the strain gages to be conditioned and transformed into digital readings. A LabView program recorded both the temperature and strain gage readings. The testing equipment has the ability to track and record 8 channels simultaneously. The excitation voltages on all the channels were calibrated with a HP 3478A digital multimeter with errors not larger than ± 0.001 VDC.



Figure 7.9 Vishay Strain Gage Signal Processing Equipment

The well-established procedure for strain gage based CTE measurement requires strain gages to be mounted on the surface of the test specimen and then subjected to controlled temperature change. The strain gage will capture any expansion caused by the temperature change. The measurements obtained in this process adds up the expansion of strain gauge along with the expansion of the test specimen and thus introduce thermally induced strain gauge error. To avoid this error, a reference material with extremely low CTE, titanium silicate ($CTE \approx 30 \times 10^{-9}/K$), was used along with the test specimen. A similar type of strain gauges were mounted on both test material and the reference material and both of them were subjected to the same controlled temperature change. The CTE of the test specimen are calculated using the following equation [24]:

$$(\epsilon_S)_{APP} - (\epsilon_R)_{APP} = (\alpha_S - \alpha_R) \times T - (\alpha_S - \alpha_R) \times T_0 \quad (7.1)$$

where α_R is the CTE of a known reference material, α_S is the unknown CTE of the test specimen, $(\epsilon_S)_{APP}$ is the thermal output (apparent strain) of the specimen strain gage, $(\epsilon_R)_{APP}$ is the thermal output (apparent strain) of the reference material strain gage, T is the testing temperature, and T_0 is the initial (zero strain) temperature (normally room temperature). Equation (7.1) can be rewritten as

$$\alpha_S = \frac{(\epsilon_S)_{APP} - (\epsilon_R)_{APP}}{T - T_0} + \alpha_R \quad (7.2)$$

In order to ensure calibration of the test system, an Aluminum bar with known CTE was used as a test sample at the beginning of the test. For all the materials experiments were conducted at least 2 times to ensure repeatability. The results of the CTE measurement tests on Aluminum, FR-4, and Megtron-6 are summarized in Table 7.2.

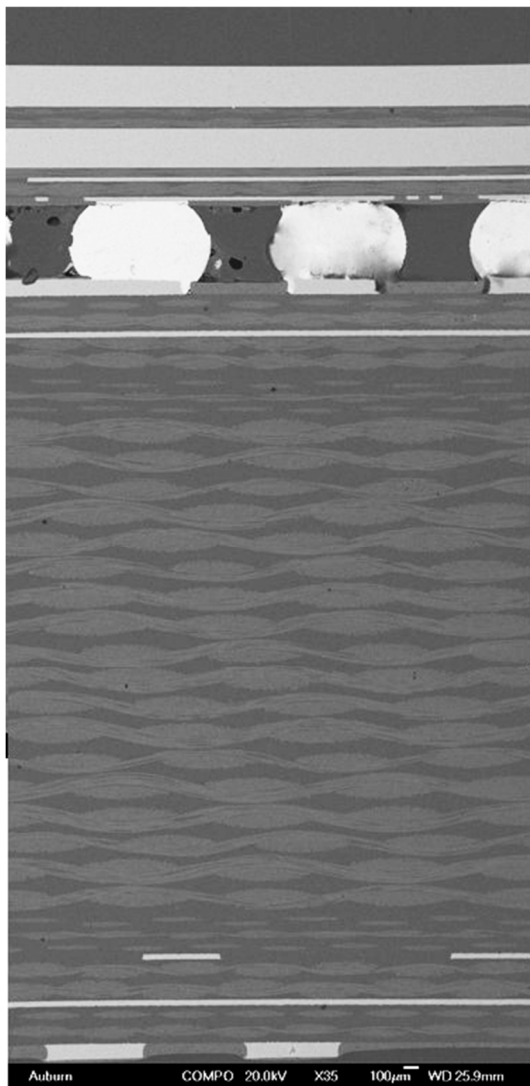
Table 7.2 CTE Measurement Results for the PCBs

Direction	CTE(1/°C)		
	Aluminum Bar	FR-4 Board	Megtron-6 Board
Longitudinal	25.18×10^{-6}	12.41×10^{-6}	16.32×10^{-6}
Transverse	25.41×10^{-6}	15.59×10^{-6}	16.37×10^{-6}

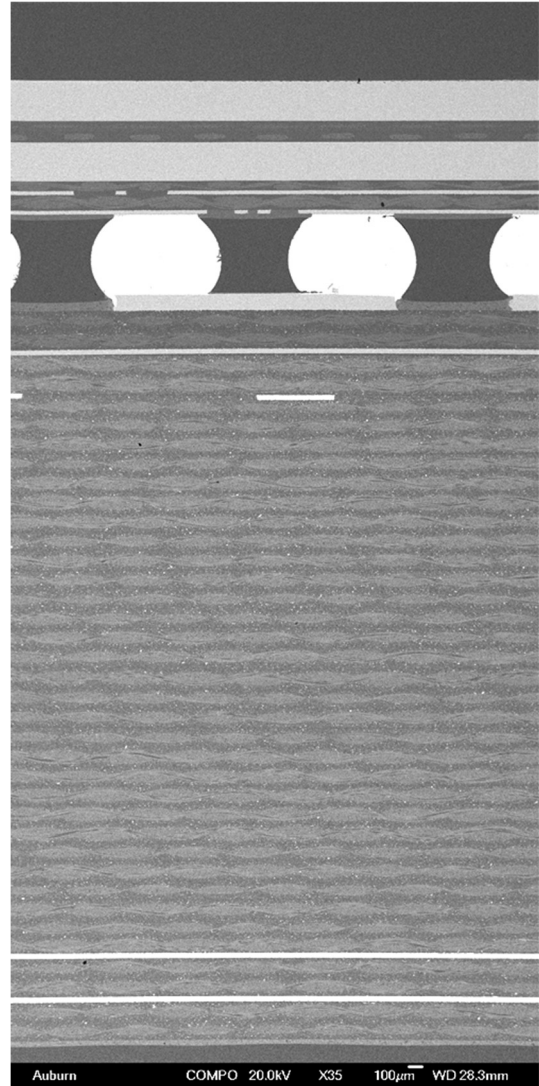
7.4 Microstructure of FR-4 and Megtron-6 PCBs

The SEM images of the cross section of FR-4 and Megtron-6 PCBs are shown in Figure 7.10. It is evident from the image that size of laminates used in both PCBs are different. A variety of laminate thickness was found in FR-4 while Megtron-6 was found to have only one type of laminate. In order to understand the construction of each laminate, SEM images were also taken at higher magnifications and are presented in Figures 7.11 and 7.12. Presence of around 10 μm diameter glass filler was found in the laminates of the

both PCBs. Although an additional kind of submicron level glass filler was identified in the Megtron-6 board. Backscattered Electron (BSE) images at the higher magnifications reveal the presence of white phase in both PCBs. Elemental analysis results by EDS showed that the white phases in FR-4 is a compound of Bromine (Br), Magnesium (Mg), Silicon (Si), and Oxygen (O) whereas the white phase in Megtron-6 is mainly composed of Bromine which is typically used in the PCBs as a fire retardant.



(a)



(b)

Figure 7.10 SEM Image of the Cross Section of (a) FR-4 and (b) Megtron-6 PCB

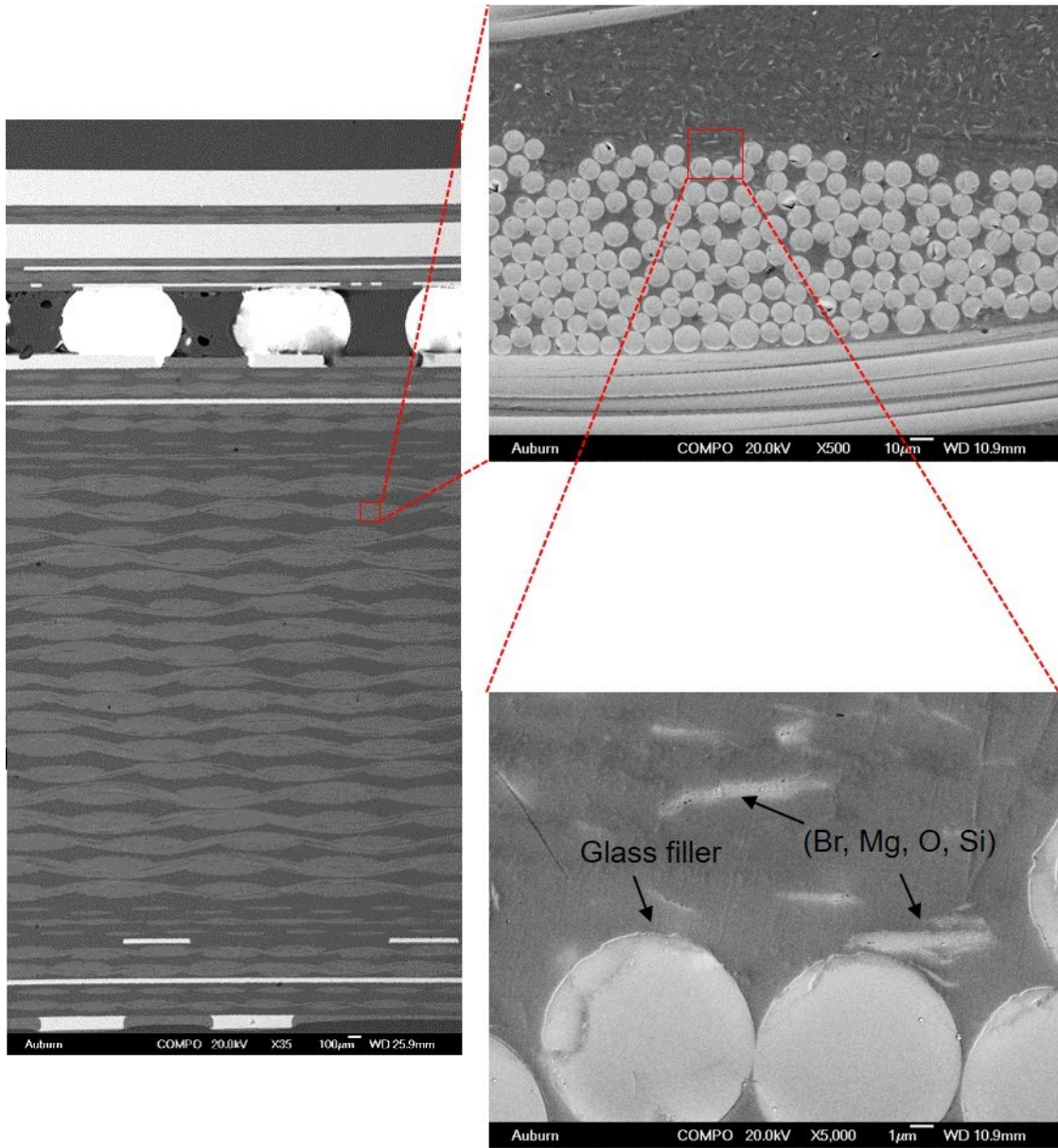


Figure 7.11 Images of FR-4 Laminate at Higher Magnifications

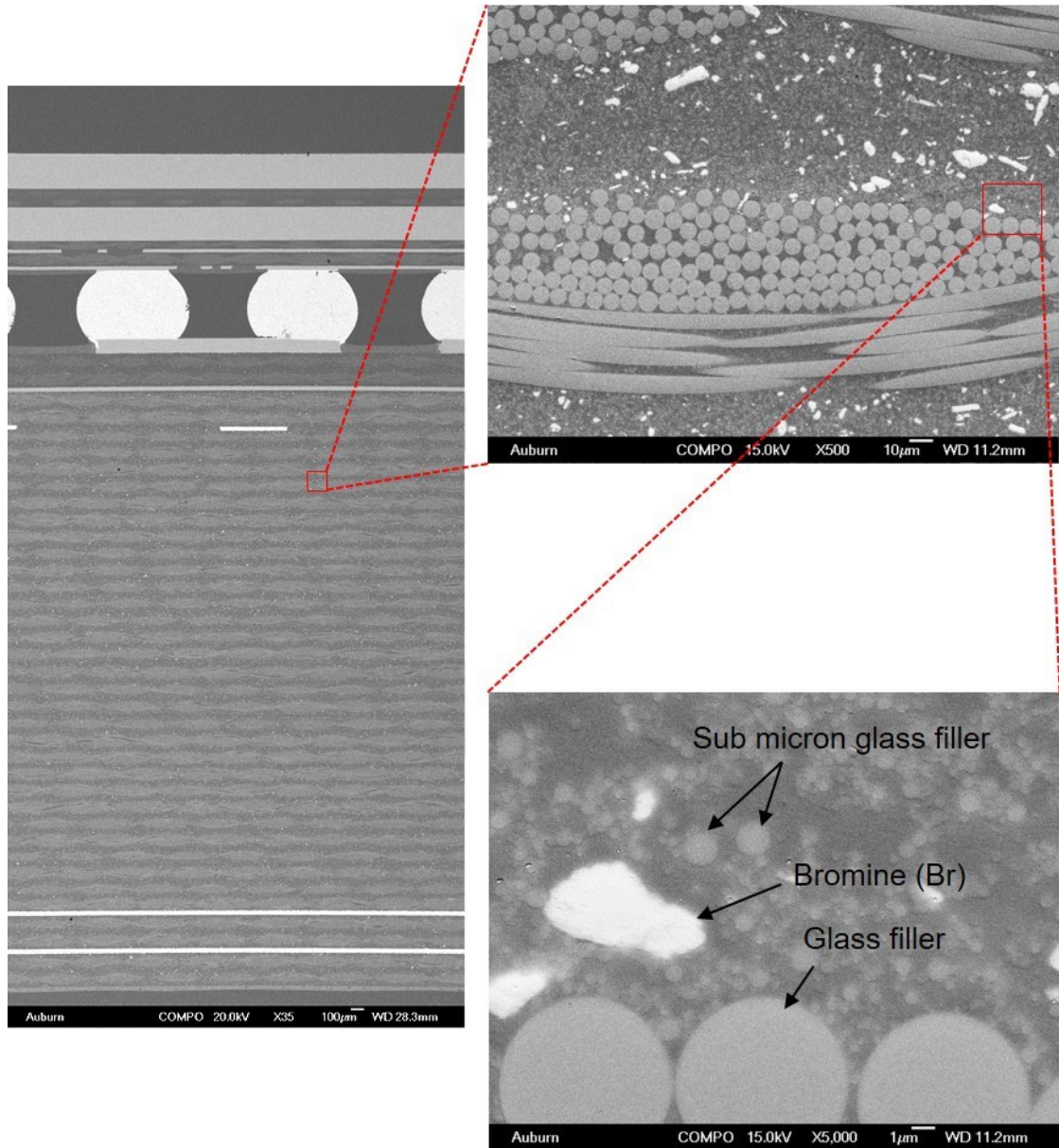


Figure 7.12 Images of Megtron-6 Laminate at Higher Magnifications

7.5 FEA Model for SBGA Package

It was found in a previous study [118] that the thermal cycling life of a SBGA package is higher if it is mounted on a Megtron-6 board than on a FR-4 board. In a parallel study the material properties of SBGA package, FR-4 and Megtron-6 boards reported in

this chapter was used to simulate the thermal cycling life using appropriate boundary conditions. The accumulated plastic energy per cycle (after third cycle) was used in Darveaux model [119] to predict thermal cycling characteristic life and compared with experimentally obtain values. First of all, a model of the SBGA package was developed based on the dimensions obtained from package cross section. Details of the package dimensions are presented in Table 7.3 and a schematic cross section of the package is shown in Figure 7.13. A three dimensional finite element model of the package is also presented in Figure 7.14.

Table 7.3 Geometry of a 35 mm SBGA package

I/O Count	304
Pitch	1.27 mm
Die Size	11.2x11.2 mm
Epoxy	0.63 mm thick
Die	0.35 mm thick
Die Attach	0.05 mm thick
Solder Mask	0.05mm thick
Substrate	0.10 mm thick
Copper Pad	0.108 mm thick
Copper Heat Spreader	0.25 mm thick
Bonding Material	0.15 and 0.08 mm thick

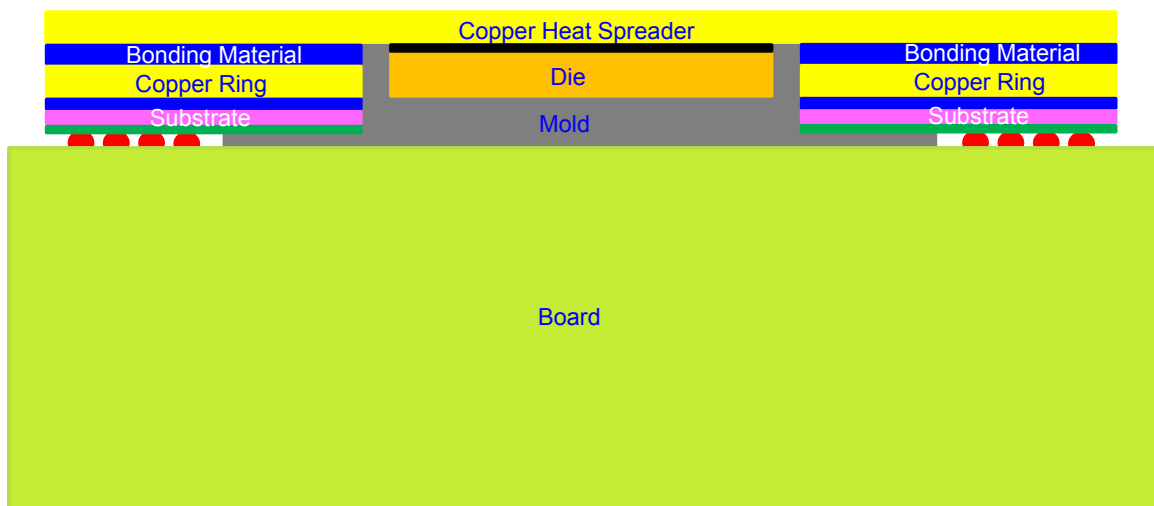


Figure 7.13 Schematic Cross Section of the SBGA Package

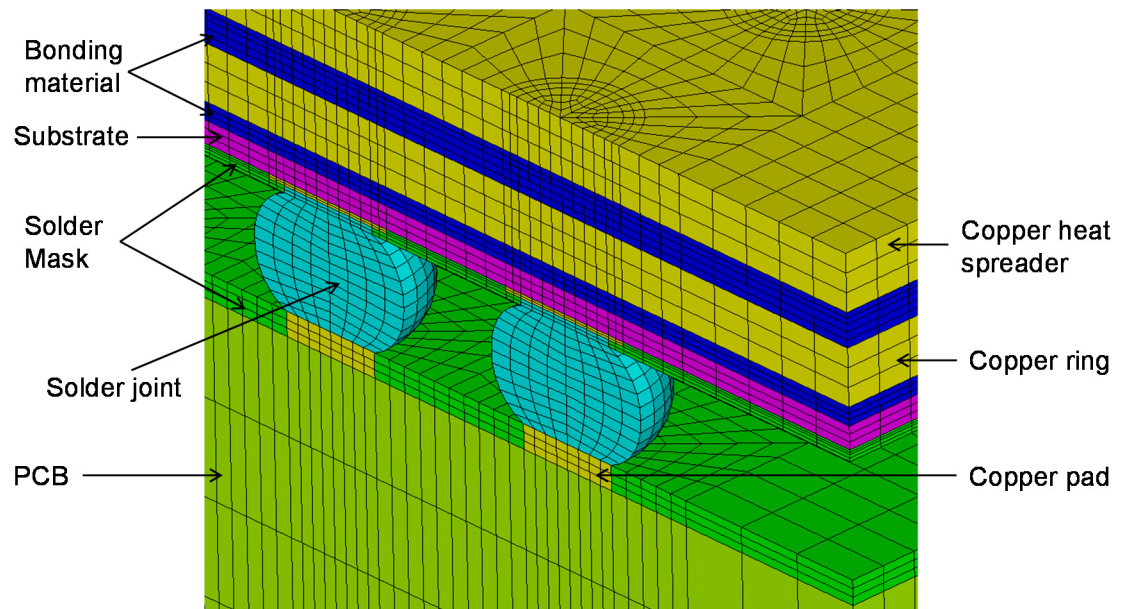


Figure 7.14 3D Finite Element Model of the SBGA Package

The material properties used in the simulation are presented in Table 7.4. Most of the properties were determined by designing and conducting appropriate experiments, as reported in this chapter while the others were collected from previous literature. A quarter symmetric model was used to reduce calculation time. The characteristic life of the SBGA package obtained from the finite element simulation are presented in Table 7.5 along with the experimental thermal cycling results.

Table 7.4 Material Properties of Different Layers used During Simulation

Material	Elastic Modulus (GPa)	Poisson's Ratio	CTE (1/°C)
Solder Ball	54, 50, 41, 38, 34, 30 GPa, at -40, 25, 50, 75, 100, 125 °C	0.35	24.5×10^{-6}
Copper Heat Spreader	115.2	0.34	16.3×10^{-6}
Copper Ring	114.6	0.34	16.3×10^{-6}
Copper Pad	89.9	0.34	16.3×10^{-6}
Silicon Die	152	0.28	2.5×10^{-6}
Die Adhesive	1.2	0.35	83.6×10^{-6}
Solder Mask	6.8	0.3	30.0×10^{-6}
Mold	10.9	0.25	10.0×10^{-6}
PCB (FR-4)	16.1 (x, y, 25°C)	0.11 (xy)	12.41×10^{-6} (x)
	8.8 (x, y, 125°C)		15.59×10^{-6} (y)
	12.5 (z, 25°C)	0.39 (xz, yz)	45×10^{-6} (z)
	6.8 (z, 125°C)		
PCB (Megtron-6)	16.9 (x, y, 25°C)	0.11 (xy)	16.32×10^{-6} (x)
	10.5 (x, y, 125°C)		16.37×10^{-6} (y)
	13.8 (z, 25°C)	0.39 (xz, yz)	45×10^{-6} (z)
	8.7 (z, 125°C)		
BT Substrate	17.89 (x, y)	0.11 (xy)	12.42×10^{-6} (x, y)
	7.85 (z)	0.39 (xz, yz)	57×10^{-6} (z)

Table 7.5 Characteristic Life of a 31 mm SBGA Package During Thermal Cycling

Board Type	Experimental (N_f)	FEA (N_f)
FR-4	2550	2383
Megtron-6	3000	3023

A contour plot of the accumulated plastic work (MPa) in the solder joints of FR-4 boards per cycle is presented in Figure 7.15. It is clear from the plot that the maximum damage is done on the corner joint which is consistent with the DNP (distance from neutral point) formula. From the enlarge image of the corner joint it is clear that the highest plastic work was accumulated near the top and bottom end of the joint. Failure analysis results as

presented in Figure 7.16 clearly shows the presence of cracks near both end of a solder joint and thus supports the FEA results.

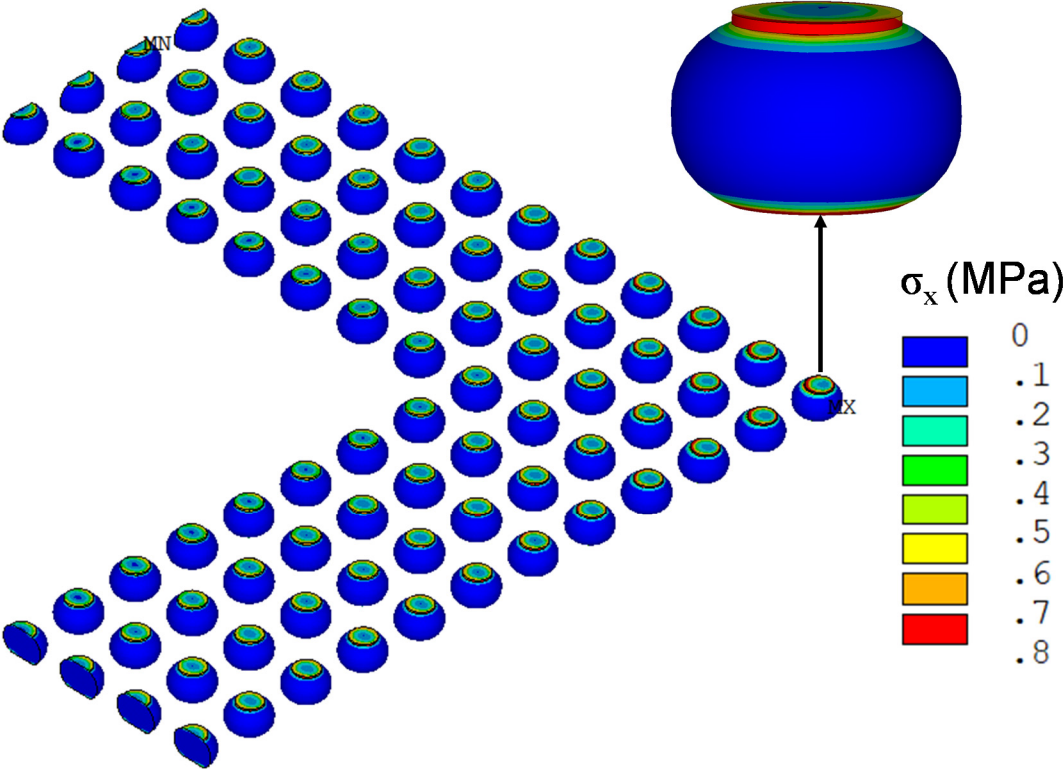


Figure 7.15 Accumulated Plastic Work (MPa) Contours Plot for the Solder Joints of FR-4 Board

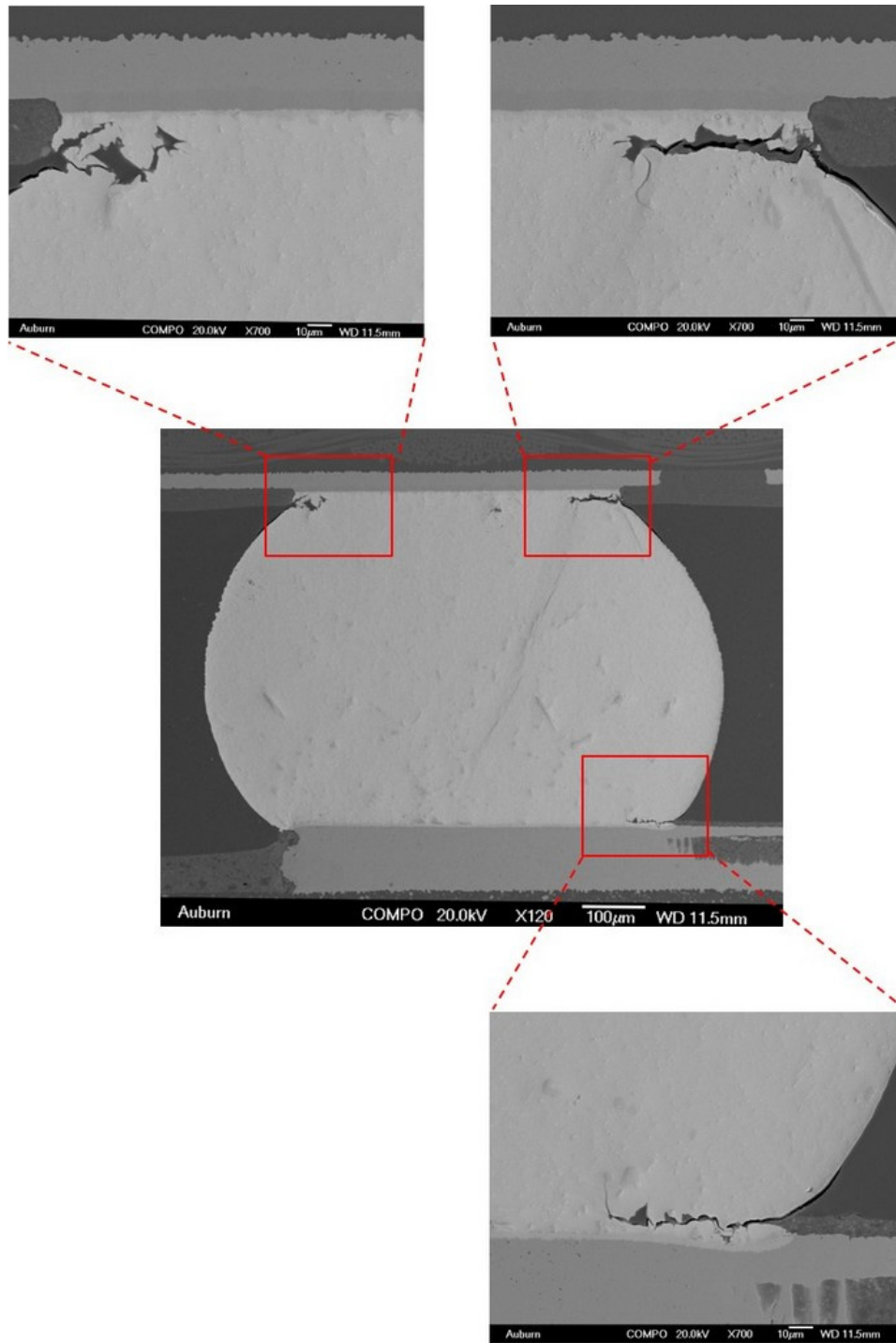


Figure 7.16 Failure Analysis Results Showing the Locations of the Cracks

Both experimental and FEA results (Table 7.5) shows that the characteristic life of SBGA package is higher when mounted on a Megtron-6 board than on FR-4 board. Fatigue

failure of the solder joints is the main failure mechanism during a thermal cycling experiment. The magnitude of the fatigue stress imposed on the solder joints, during thermal cycling, mainly depends on the extent of CTE mismatch between the layers below and above the joint. As shown in Table 7.4, the x-direction CTE of FR-4 and Megtron-6 boards are 12.4×10^{-6} and 16.3×10^{-6} respectively. As it can be seen that the Figures 7.1 and 7.10-7.13, multiple Cu layer with the CTE of 16.3×10^{-6} presents on the other side of the joint. Hence the CTE mismatch was large for FR-4 board compared to Megtron-6 board resulting the higher characteristic life of the SBGA package on a Megtron-6 board.

7.6 Summary and Discussion

The reliability of super ball grid array package (SBGA) is compared for the assemblies mounted on two different types of board. Nano-mechanical technique, and thermo-mechanical analysis were conducted to characterize the material properties of different layers of SBGA package. Extensive microscopic study was performed to understand the construction of SBGA package, FR-4 and Megtron-6 PCB laminates. Finite element analysis were employed for this reliability study of SBGA package. FEA results were validated through the experimental outcomes.

A number of different loading profile for nanoindentation on different layers of the package was established to get correct modulus values. Strain gauge based CTE measurement technique was utilized to measure CTE of FR-4 and Megtron-6 boards. Microstructure study of FR-4 and Megtron-6 PCBs revealed that their construction is different. Bromine (Br) was found in the matrix of both PCB composite as a fire retardant. Besides, the presence of sub-micron glass filler was identified in the Megtron-6 board.

The material properties obtained from mechanical and thermal analysis of SBGA package, FR-4 and Megtron-6 boards were utilized to simulate the thermal cycling life of the package and then compared with the experimental results. Both experimental and simulation results show that SBGA packages has better performance when it is mounted on the Megtron-6 board compared to the FR4 board. This was due to the better compatibility (low CTE mismatch) of SBGA and Megtron-6 board. Contour plot of the accumulated plastic work in the solder joints shows that maximum work was done on the corner joint especially near the top and bottom end of the joint. After failure analysis, cracks were found near both end of a solder joint which supports the contour plot of the FEA results.

CHAPTER 8

CONCLUSIONS

8.1 Literature Review

The mechanical properties of a solder are strongly influenced by its microstructure, which is controlled by its thermal history including its solidification rate and thermal exposures after solidification. Aging of lead free solders leads to degradations in their constitutive and failure behaviors. For example, research in the literature has shown that aging leads to large reductions in solder material properties including shear strength, elastic modulus, nanoindentation joint modulus and hardness, high strain rate mechanical behavior, creep response, and Anand model parameters. Other studies have shown that aging causes severe degradations in uniaxial cyclic stress-strain curves and fatigue life, shear cyclic stress-strain curves and fatigue life, fracture behavior, drop reliability, and thermal cycling reliability.

Dopants have been found to strongly influence the properties and behaviors of lead free solders. For Example, Bi helps to reduce solidification temperature, increases strength by means of precipitation hardening, helps to reduce IMC (Intermetallic Compound) layer thickness, and also reduce aging induced degradation of mechanical properties in lead free solder materials. Ni helps to improve thermal fatigue life and drop test performance by refining Sn grain size and reducing the IMC layer formation near the Cu pad. The effects of rear earth (RE) elements and nanoparticle addition on the properties of lead free solder was also discussed in this chapter.

Nanoindentation methods have shown great potential for characterizing solder materials and aging effects at the joint scale. Nanoindentation is mainly used to extract

elastic modulus and hardness of solder joints. Some of the prior works have also used nanoindentation technique to characterize the creep properties although most of the nanoindentation experiments, on solder joints, were conducted at room temperature.

The changes in solder mechanical behavior are a result of the evolution of the SAC solder microstructure that occurs during aging. The most well-known and widely observed changes are coarsening of the Ag₃Sn and Cu₆Sn₅ intermetallic compounds (IMCs) present in the eutectic regions between beta-Sn dendrites. Several researchers have proposed empirical models to describe the growth of these secondary phase particles as a function of aging temperature and aging time, and related this growth to mechanical property changes.

8.2 Experimental

All the experimental procedures and the data processing steps were presented in chapter 3. Micro-scale uniaxial tensile specimens were prepared in a rectangular shaped hollow glass tube using a vacuum suction method. Typical dimension of the uniaxial tensile specimens were 80 (length) × 3 (width) × 0.5 (height) mm. Uniaxial tensile tests were performed using a micro tension torsion testing system. Nanoindentation experiments were conducted on actual solder joints which were typically extracted from 14 x 14 mm PBGA assemblies (0.8 mm ball pitch, 0.46 mm ball diameter). Nanoindentation experiments were performed using Hysitron TI950 TriboIndenter.

8.3 Effects of Aging on Mechanical Properties and Anand Parameters of SAC-Bi Alloys

Three new SAC-Bi lead free solder materials recommended for high reliability applications have been chemically analyzed and then mechanically tested in order to determine the nine Anand parameters. For each alloy, three different microstructures were

explored using different cooling profiles as well as subsequent isothermal aging. Test specimens were initially solidified with both water quenched (WQ) and reflowed (RF) cooling profiles. In addition, some of the reflowed samples were subsequently subjected to 3 months of isothermal aging at $T = 100\text{ }^{\circ}\text{C}$ (RF + 3 Months Aging) to further coarsen the reflowed microstructure. Uniaxial tensile tests were performed with the SAC-Bi alloy at different cooling profiles and aging times. Test condition includes three different strain rates (0.001, 0.0001 and 0.00001 sec^{-1}) and five different test temperatures (25 $^{\circ}\text{C}$, 50 $^{\circ}\text{C}$, 75 $^{\circ}\text{C}$, 100 $^{\circ}\text{C}$ and 125 $^{\circ}\text{C}$). Tensile test results of the SAC-Bi alloy, before and after aging, were compared with those of standard SACN05 alloys.

Anand parameters of the SAC-Bi alloys for different solidification and aging conditions were determined from stress-strain test results. A good correlation was found between Anand model predicted and experimentally obtained results. Although the SAC_R material does not have any silver, it was shown to have better mechanical behavior than SAC 105 due to the presence of Bismuth (Bi) along with a little higher percentage of Copper (Cu). The Innolot and SAC_Q materials were shown to have higher strengths than SAC405. SAC-Bi Alloy SAC_R and SAC_Q have been found to be highly resistant to aging induced degradations. Microstructural analysis has shown that the improved aging resistance is due to solid solution strengthening where the Bi-phases go into the solution in the β -Sn matrix during aging and enhance strength.

8.4 Characterization of SAC Solder Joints at High Temperature Using

Nanoindentation

In chapter 5, nanoindentation methods were used to explore the creep behavior, and aging effects of SAC305 solder joints at several elevated testing temperatures from 25 to

125 °C. A special high temperature stage and test protocol was used within the nanoindentation system to carefully control the testing temperature, and make the measurements insensitive to thermal drift problems. Since the properties of SAC solder joints are highly dependent on crystal orientation, only single grain solder joints were used to avoid introducing any unintentional variation from changes in the crystal orientation across the joint cross-section.

Nanoindentation creep testing was performed on the non-aged and aged solder joint specimens at five different testing temperatures ($T = 25, 50, 75, 100, \text{ and } 125 \text{ }^\circ\text{C}$). As expected, the results have shown that indent/testing temperature has a significant impact on the mechanical properties and creep strain rate of solder joints. The measured data have also shown that the effects of aging on solder joint creep response are highly temperature dependent. At any particular temperature, creep rate increases with increasing aging time. The creep rates at high temperature increased significantly with just a few days of prior aging. In particular, the aging induced degradation rates at high temperatures (100-125 °C) were more than 100X those seen at room temperature. The effects of aging on the creep rate vs. stress response became larger and larger as the testing temperature increased. Nanoindentation pile-up effects, although insignificant at room temperature, were observed during high-temperature testing and corrections were made to limit their influence on the test results.

8.5 Evaluation of Aging Induced Microstructural Evolution in Lead Free Solders Using Scanning Probe Microscopy

New procedures were developed to capture solder microstructure while the sample is being heated inside an oven (in-situ aging study). The heating stage and scanning probe

microscopy (SPM) facility within a nanoindentation system were utilized to achieve the goal. The sample was kept within the nanoindentation system and exposed to a high temperature aging using the heating stage present in the instrument. In particular, aging was performed at $T = 125\text{ }^{\circ}\text{C}$ for 26 hours, and the topography of the microstructure of two different fixed region (10×10 microns) was continuously scanned using the SPM system and recorded after one hour time intervals. This process generated several images of the microstructure as the aging progressed. When placed together sequentially, these images have been used as frames to create an experimentally recorded movie of the microstructural evolution in SAC solder joints exposed to aging. Image analysis software was utilized to quantify microstructural changes (total area, number and average diameter of IMC particles, etc.) with respect to aging time.

Quantitative analysis of the microstructures has shown that the number of IMC particles decreases during aging, while the average diameter of the particles increases significantly. Conventional models for IMC particle coarsening could not fit the experimental data found in this study. Histogram charts were also used to illustrate distribution of the particle sizes present at each aging time, and to show that that changes occurred during aging. In particular, the number of particles of any given size degraded with aging, while the width of the histogram increased, indicating a larger distribution of different particle sizes as aging progressed. FIB analysis shows that the IMC size underneath the surface of the solder is similar to the ones on the surface

8.6 Characterization of SBGA Package for Reliability Analysis

The reliability of super ball grid array package (SBGA) is compared for the assemblies mounted on two different types of board. Nano-mechanical technique, and

thermal-mechanical analysis were conducted to characterize the material properties of different layer of SBGA package. Extensive microscopic study was performed to understand the construction of SBGA package, FR-4 and Megtron6 PCB laminates. Finite element analysis were employed for this reliability study of SBGA package. FEA results were validated through the experimental outcomes.

A number of different loading profile for nanoindentation on different layers of the package was established to get correct modulus values. Strain gauge based CTE measurement technique was utilized to measure CTE of FR-4 and Megtron6 boards. Microstructure study of FR-4 and Megtron6 PCBs revealed that their construction is different. Bromine (Br) was found in the matrix of both PCB composite as a fire retardant. Besides, the presence of sub-micron glass filler was identified in the Megtron6 board.

The material properties obtained from mechanical and thermal analysis of SBGA package, FR-4 and Megtron6 boards were utilized to simulate the thermal cycling life of the package and then compared with the experimental results. Both experimental and simulation results show that SBGA packages has better performance when it is mounted on the Megtron6 board compared to the FR4 board. This was due to the better compatibility (low CTE mismatch) of SBGA and Megtron6 board. Contour plot of the accumulated plastic work in the solder joints shows that maximum work was done on the corner joint especially near the top and bottom end of the joint. After failure analysis, cracks were found near both end of a solder joint which supports the contour plot of the FEA results.

8.7 Summary

In this Dissertation, the effects of high temperature aging on the mechanical properties and microstructure of lead free solders were investigated. Previous studies reported a significant degradation of mechanical properties of SAC solders during aging due to the coarsening of the microstructure. In this study, it was found that Bi can help the solder alloy to become resistant to aging induced degradation. Microstructural analysis has shown that the improved aging resistance of SAC-Bi alloys is due to solid solution strengthening where the Bi-phases go into the solution in the β -Sn matrix during aging and enhance strength. This enhancement in strength of the alloy balances any reduction of strength during aging caused by the grain coarsening. To understand the effect of aging on the actual solder joint at elevated temperatures, a test procedure was developed to perform high temperature creep experiments using nanoindentation tool. It was found that the creep strain rate decreases with increasing test temperature and aging time. The negative effect of aging was found to be even more pronounced when the joints were tested at elevated temperatures.

Since IMC coarsening is the main reason for the mechanical property degradation during aging, a novel in-situ imaging technique was developed to monitor the changes in IMC size with aging time. The coarsening of the IMCs, with aging, was correlated with the degradation of the mechanical strength of SAC305 solder. Finite element simulation technique was utilized to simulate the mechanical response of the solder joints in a SBGA package, on FR-4 and Megtron-6 PCBs, in a thermal cycling environment. Mechanical and thermal analysis techniques were used to obtain material properties of the different

layers of the package. The results suggests that the SBGA package is more compatible (higher characteristic life) on Megtron-6 board than on FR-4 board.

8.8 Future Work

Following future work can be performed to extend the findings of this dissertation:

- Anand parameters of the 3 SAC-Bi alloys can be determined extremely high temperature (125-200 °C) applications.
- The 3 SAC-Bi alloys studied in this dissertation was found to be resistant to aging induced degradation after aging at 100 °C. The effects of low temperature aging (25-100 °C) on these solder alloys are need to be investigated.
- The effects of test temperatures on the creep properties of SAC305 solder joints were investigated from 25-125 °C temperature range by nanoindentation. This work can be extended to an even higher temperature range of 125-200 °C.
- Creep properties of individual IMCs and the β -Sn matrix can also be performed using nanoindentation.
- Nanoindentation experiments can be performed on the other SACN05 and SAC-Bi solder joints.
- The microstructure evolution study presented in this dissertation can be extended to a higher aging time. Based on the short and long term aging induced IMC coarsening data, a mathematical model can be developed to predict solder joint reliability as a function of aging time and temperature.

- The evolution of the microstructure of SAC-Bi alloys with aging can also be performed to understand how the changes in the microstructure making them resistant to aging induced degradations.

REFERENCES

- [1] M. Abtey and G. Selvaduray, "Lead-free solders in microelectronics," *Materials Science and Engineering: R: Reports*, vol. 27, no. 5, pp. 95-141, 2000.
- [2] P. T. Vianco, "Development of alternatives to lead-bearing solders," Proceeding of the Technical Program on Surface Mount International, San Jose, CA, 1993.
- [3] N. C. Lee, "Getting Ready for Lead-free Solders," *Soldering & Surface Mount Technology*, vol. 9, no. 2, pp. 65-69, 1997.
- [4] G. Zeng, S. D. McDonald, Q. Gu, K. Sweatman, and K. Nogita, "Effects of element addition on the $\beta \rightarrow \alpha$ transformation in tin," *Philosophical Magazine Letters*, vol. 94, no. 2, pp. 53-62, 2014.
- [5] W. J. Plumbridge, "Tin pest issues in lead-free electronic solders," *Lead-Free Electronic Solders*, Springer, 2006, pp. 307-318.
- [6] S. Cheng, C.-M. Huang, and M. Pecht, "A review of lead-free solders for electronics applications," *Microelectronics Reliability*, vol. 75, pp. 77-95, 2017.
- [7] Q. B. Tao, L. Benabou, L. Vivet, V. N. Le, and F. B. Ouezdou, "Effect of Ni and Sb additions and testing conditions on the mechanical properties and microstructures of lead-free solder joints," *Materials Science and Engineering: A*, vol. 669, pp. 403-416, 2016.
- [8] M. Hasnine, B. Tolla, and M. Karasawa, "Effect of Ge addition on wettability, copper dissolution, microstructural and mechanical behavior of SnCu-Ge solder alloy," *Journal of Materials Science: Materials in Electronics*, vol. 28, no. 21, pp. 16106-16119, 2017.
- [9] K. S. Kim, S. H. Huh, and K. Suganuma, "Effects of intermetallic compounds on properties of Sn-Ag-Cu lead-free soldered joints," *Journal of Alloys and Compounds*, vol. 352, no. 1, pp. 226-236, 2003.
- [10] D. Q. Yu and L. Wang, "The growth and roughness evolution of intermetallic compounds of Sn-Ag-Cu/Cu interface during soldering reaction," *Journal of Alloys and Compounds*, vol. 458, no. 1, pp. 542-547, 2008.
- [11] H. Ma, J. C. Suhling, Y. Zhang, P. Lall, and M. J. Bozack, "The influence of elevated temperature aging on reliability of lead free solder joints," *Proceeding of the 57th Electronic Components and Technology Conference*, pp. 653-668, 2007.
- [12] P. T. Vianco, "Fatigue and creep of lead-free solder alloys: Fundamental properties," *ASM International*, pp. 67-106, 2005.
- [13] S. Wiese *et al.*, "Constitutive behaviour of lead-free solders vs. lead-containing solders-experiments on bulk specimens and flip-chip joints," *Proceeding of the 51st Electronic Components and Technology Conference*, pp. 890-902, 2001
- [14] R. J. McCabe and M. E. Fine, "Athermal and thermally activated plastic flow in low melting temperature solders at small stresses," *Scripta Materialia(USA)*, vol. 39, no. 2, pp. 189-195, 1998.
- [15] H. Ma and J. C. Suhling, "A review of mechanical properties of lead-free solders for electronic packaging," *Journal of Materials Science*, vol. 44, no. 5, pp. 1141-1158, 2009.
- [16] J. H. Lau and Y.-H. Pao, *Solder joint reliability of BGA, CSP, flip chip, and fine pitch SMT assemblies*, McGraw-Hill, New York, 1997.

- [17] R. W. Hertzberg, R. P. Vinci, and J. L. Hertzberg, *Deformation and Fracture Mechanics of Engineering Materials*, Wiley New York, 1996.
- [18] A. C. Fischer-Cripps, *Nanoindentation*, Third ed. Springer, 2011.
- [19] K. Zeng and K.-N. Tu, "Six cases of reliability study of Pb-free solder joints in electronic packaging technology," *Materials Science and Engineering: R: Reports*, vol. 38, no. 2, pp. 55-105, 2002.
- [20] S. Terashima, Y. Kariya, T. Hosoi, and M. Tanaka, "Effect of silver content on thermal fatigue life of Sn-xAg-0.5 Cu flip-chip interconnects," *Journal of Electronic Materials*, vol. 32, no. 12, pp. 1527-1533, 2003.
- [21] M. Amagai, Y. Toyoda, and T. Tajima, "High solder joint reliability with lead free solders," in *Proceedings of 53rd Electronic Components and Technology Conference*, pp. 317-322, 2003.
- [22] F. Che, W. Zhu, E. S. Poh, X. Zhang, and X. Zhang, "The study of mechanical properties of Sn-Ag-Cu lead-free solders with different Ag contents and Ni doping under different strain rates and temperatures," *Journal of Alloys and Compounds*, vol. 507, no. 1, pp. 215-224, 2010.
- [23] F. Zhu, H. Zhang, R. Guan, and S. Liu, "Effects of temperature and strain rate on mechanical property of Sn96.5Ag3Cu0.5," *Journal of Alloys and Compounds*, vol. 438, no. 1-2, pp. 100-105, 2007.
- [24] H. Ma, J. C. Suhling, P. Lall, and M. J. Bozack, "Reliability of the aging lead free solder joint," *Proceeding of the 56th Electronic Components and Technology Conference*, pp. 849-864, 2006.
- [25] Y. Zhang, Z. Cai, J. C. Suhling, P. Lall, and M. J. Bozack, "The effects of aging temperature on SAC solder joint material behavior and reliability," *Proceedings of the 58th Electronic Components and Technology Conference*, pp. 99-112, 2008.
- [26] Y. Zhang, Z. Cai, J. C. Suhling, P. Lall, and M. J. Bozack, "The effects of SAC alloy composition on aging resistance and reliability," *Proceedings of the 59th Electronic Components and Technology Conference*, pp. 370-389, 2009.
- [27] Y. Zhang, K. Kurumaddali, J. C. Suhling, P. Lall, and M. J. Bozack, "Analysis of the mechanical behavior, microstructure, and reliability of mixed formulation solder joints," *Proceedings of the 59th Electronic Components and Technology Conference*, pp. 759-770, 2009.
- [28] Z. Cai, Y. Zhang, J. C. Suhling, P. Lall, R. W. Johnson, and M. J. Bozack, "Reduction of lead free solder aging effects using doped SAC alloys," *Proceedings of the 60th Electronic Components and Technology Conference*, pp. 1493-1511, 2010.
- [29] M. Mustafa, Z. Cai, J. C. Suhling, and P. Lall, "The effects of aging on the cyclic stress-strain behavior and hysteresis loop evolution of lead free solders," *Proceedings of the 61st Electronic Components and Technology Conference*, pp. 927-939, 2011.
- [30] M. Mustafa, J. C. Roberts, J. C. Suhling, and P. Lall, "The effects of aging on the fatigue life of lead free solders," *Proceedings of the 64th Electronic Components and Technology Conference*, pp. 666-683, 2014.
- [31] J. Zhang, Thirugnanasambandam, S., Evans, J. L., Bozack, M. J., Zhang, Y., Suhling, J. C., "Correlation of aging effects on the creep rate and reliability in lead free solder joints," *SMTA Journal*, vol. 25(3), pp. 19-28 2012.

- [32] J. Zhang *et al.*, "Thermal aging effects on the thermal cycling reliability of lead-free fine pitch packages," *IEEE Transactions on Components, Packaging and Manufacturing Technology*, vol. 3, no. 8, pp. 1348-1357, 2013.
- [33] Z. Hai *et al.*, "Reliability comparison of aged SAC fine-pitch ball grid array packages versus surface finishes," *IEEE Transactions on Components, Packaging and Manufacturing Technology*, vol. 5, no. 6, pp. 828-837, 2015.
- [34] M. Motalab *et al.*, "Improved predictions of lead free solder joint reliability that include aging effects," *Proceedings of the 62nd Electronic Components and Technology Conference*, pp. 513-531, 2012.
- [35] M. Motalab *et al.*, "Correlation of reliability models including aging effects with thermal cycling reliability data," *Proceedings of the 63rd IEEE Electronic Components and Technology Conference*, pp. 986-1004, 2013.
- [36] P. Lall, S. Shantaram, J. Suhling, and D. Locker, "Effect of aging on the high strain rate mechanical properties of SAC105 and SAC305 leadfree alloys," *Proceedings of the 63rd IEEE Electronic Components and Technology Conference*, pp. 1277-1293, 2013.
- [37] L. Anand, "Constitutive equations for the rate-dependent deformation of metals at elevated temperatures," *Journal of Engineering Materials and Technology*, vol. 104, no. 1, pp. 12-17, 1982.
- [38] F. X. Che, H. L. J. Pang, W. H. Zhu, W. Sun, and A. Y. S. Sun, "Modeling constitutive model effect on reliability of lead-free solder joints," in *Proceedings of the 7th International Conference on Electronics Packaging Technology*, pp. 1-6, 2006.
- [39] M. Pei and J. Qu, "Constitutive modeling of lead-free solders," *Proceedings of the International Symposium on Advanced Packaging Materials*, pp. 45-49, 2005.
- [40] K. Mysore, G. Subbarayan, V. Gupta, and R. Zhang, "Constitutive and aging behavior of Sn3. 0Ag0. 5Cu solder alloy," *Electronics Packaging Manufacturing, IEEE Transactions on*, vol. 32, no. 4, pp. 221-232, 2009.
- [41] M. Motalab, Z. Cai, J. C. Suhling, and P. Lall, "Determination of Anand constants for SAC solders using stress-strain or creep data," *Proceedings of ITherm*, pp. 910-922, 2012.
- [42] N. Bai, X. Chen, and H. Gao, "Simulation of uniaxial tensile properties for lead-free solders with modified Anand model," *Materials & Design*, vol. 30, no. 1, pp. 122-128, 2009.
- [43] M. Amagai, M. Watanabe, M. Omiya, K. Kishimoto, and T. Shibuya, "Mechanical characterization of Sn–Ag-based lead-free solders," *Microelectronics Reliability*, vol. 42, no. 6, pp. 951-966, 2002.
- [44] Y. Kim, H. Noguchi, and M. Amagai, "Vibration fatigue reliability of BGA-IC package with Pb-free solder and Pb–Sn solder," *Microelectronics Reliability*, vol. 46, no. 2, pp. 459-466, 2006.
- [45] M. Huang and L. Wang, "Effects of Cu, Bi, and In on microstructure and tensile properties of Sn-Ag-X (Cu, Bi, In) solders," *Metallurgical and Materials Transactions A*, vol. 36, no. 6, pp. 1439-1446, 2005.
- [46] M. Matahir, L. Chin, K. Tan, and A. Olofinjana, "Mechanical strength and its variability in Bi-modified Sn-Ag-Cu solder alloy," *Journal of Achievement in Materials and Manufacturing Engineering*, vol. 46, pp. 50-56, 2011.

- [47] R. S. Pandher, B. G. Lewis, R. Vangaveti, and B. Singh, "Drop shock reliability of lead-free alloys—effect of micro-additives," *Proceedings 57th Electronic Components and Packaging Technology Conference*, pp. 669-676, 2007.
- [48] Z. Zhao, L. Wang, X. Xie, Q. Wang, and J. Lee, "The influence of low level doping of Ni on the microstructure and reliability of SAC solder joint," *Proceedings of 9th International Conference on Electronic Packaging Technology & High Density Packaging*, pp. 1-5, 2008.
- [49] I. De Sousa, D. W. Henderson, L. Parry, S. K. Kang, and D.-Y. Shih, "The influence of low level doping on the thermal evolution of SAC alloy solder joints with Cu pad structures," *Proceeding of the 56th Electronic Components and Technology Conference*, pp. 1454-1461, 2006.
- [50] J. H. Lee, S. Kumar, H. J. Kim, Y. W. Lee, and J. T. Moon, "High thermo-mechanical fatigue and drop impact resistant Ni-Bi doped lead free solder," in *Proceedings of the 64th Electronic Components and Technology Conference*, pp. 712-716, 2014.
- [51] T.-S. Yeung, H. Sze, K. Tan, J. Sandhu, C.-W. Neo, and E. Law, "Material characterization of a novel lead-free solder material—SACQ," *Proceedings of the 64th IEEE Electronic Components and Technology Conference*, pp. 518-522, 2014.
- [52] L. Sun and L. Zhang, "Properties and microstructures of Sn-Ag-Cu-X lead-free solder joints in electronic packaging," *Advances in Materials Science and Engineering*, vol. 2015, 2015.
- [53] M. Sadiq, R. Pesci, and M. Cherkaoui, "Impact of thermal aging on the microstructure evolution and mechanical properties of lanthanum-doped tin-silver-copper lead-free solders," *Journal of electronic materials*, vol. 42, no. 3, pp. 492-501, 2013.
- [54] H.-T. Lee, Y.-F. Chen, T.-F. Hong, K.-T. Shih, and C.-w. Hsu, "Microstructural evolution of Sn-3.5 Ag solder with lanthanum addition," *Proceedings of International Conference on Electronic Packaging Technology & High Density Packaging*, pp. 617-622, 2009.
- [55] H. Hao, Y. Shi, Z. Xia, Y. Lei, and F. Guo, "Microstructure evolution of SnAgCuEr lead-free solders under high temperature aging," *Journal of Electronic Materials*, vol. 37, no. 1, pp. 2-8, 2008.
- [56] D. B. Witkin, "Influence of microstructure on mechanical behavior of Bi-containing Pb-Free solders," *Proceedings of IPC APEX EXPO Conference and Exhibition*, pp. 540-547, 2013.
- [57] A. Delhaise, D. Perovic, and P. Snugovsky, "The effects of Bi and aging on the microstructure and mechanical properties of Sn-rich alloys," *Proceedings of the International Conference on Soldering and Reliability*, 2015.
- [58] J. H. Pang, T. Low, B. Xiong, X. Luhua, and C. Neo, "Thermal cycling aging effects on Sn–Ag–Cu solder joint microstructure, IMC and strength," *Thin solid films*, vol. 462, pp. 370-375, 2004.
- [59] R. Darveaux, "Shear deformation of lead free solder joints," *Proceedings of the 55th IEEE Electronic Components and Technology Conference*, pp. 882-893, 2005.
- [60] S. Wiese and K. J. Wolter, "Creep of thermally aged SnAgCu-solder joints," *Microelectronics Reliability*, vol. 47, no. 2, pp. 223-232, 2007.

- [61] I. Dutta, D. Pan, R. A. Marks, and S. G. Jadhav, "Effect of thermo-mechanically induced microstructural coarsening on the evolution of creep response of SnAg-based microelectronic solders," *Materials Science and Engineering: A*, vol. 410, pp. 48-52, 2005.
- [62] M. Hasnine, M. Mustafa, J. C. Suhling, B. C. Prorok, M. J. Bozack, and P. Lall, "Characterization of aging effects in lead free solder joints using nanoindentation," *Proceedings of the 63rd IEEE Electronic Components and Technology Conference*, pp. 166-178, 2013.
- [63] M. Hasnine, J. C. Suhling, B. C. Prorok, M. J. Bozack, and P. Lall, "Exploration of aging induced evolution of solder joints using nanoindentation and microdiffraction," *Proceedings of the 64th IEEE Electronic Components and Technology Conference*, pp. 379-394, 2014.
- [64] M. Hasnine, J. C. Suhling, B. C. Prorok, M. J. Bozack, and P. Lall, "Nanomechanical characterization of sac solder joints-reduction of aging effects using microalloy additions," *Proceedings of the 65th IEEE Electronic Components and Technology Conference*, pp. 1574-1585, 2015.
- [65] M. Hasnine, J. Suhling, B. Prorok, M. Bozack, and P. Lall, "Anisotropic mechanical properties of SAC solder joints in microelectronic packaging and prediction of uniaxial creep using nanoindentation creep," *Experimental Mechanics*, vol. 57, no. 4, pp. 603-614, 2017.
- [66] H. Rhee, J. Lucas, and K. Subramanian, "Micromechanical characterization of thermomechanically fatigued lead-free solder joints," *Journal of Materials Science: Materials in Electronics*, vol. 13, no. 8, pp. 477-484, 2002.
- [67] R. Chromik, R. Vinci, S. Allen, and M. Notis, "Measuring the mechanical properties of Pb-free solder and Sn-based intermetallics by nanoindentation," *Jom*, vol. 55, no. 6, pp. 66-69, 2003.
- [68] X. Deng, N. Chawla, K. Chawla, and M. Koopman, "Deformation behavior of (Cu, Ag)-Sn intermetallics by nanoindentation," *Acta Materialia*, vol. 52, no. 14, pp. 4291-4303, 2004.
- [69] Y. Sun, J. Liang, Z.-H. Xu, G. Wang, and X. Li, "Nanoindentation for measuring individual phase mechanical properties of lead free solder alloy," *Journal of Materials Science: Materials in Electronics*, vol. 19, no. 6, pp. 514-521, 2008.
- [70] F. Gao, H. Nishikawa, T. Takemoto, and J. Qu, "Mechanical properties versus temperature relation of individual phases in Sn-3.0 Ag-0.5 Cu lead-free solder alloy," *Microelectronics Reliability*, vol. 49, no. 3, pp. 296-302, 2009.
- [71] Y. Han, H. Jing, S. Nai, L. Xu, C. Tan, and J. Wei, "Temperature dependence of creep and hardness of Sn-Ag-Cu lead-free solder," *Journal of Electronic Materials*, vol. 39, no. 2, pp. 223-229, 2010.
- [72] M. Sadiq, J.-S. Lecomte, and M. Cherkaoui, "Individual phase mechanical properties at different temperatures of Sn-Ag-Cu lead-free solders incorporating special pileup effects using nanoindentation," *Journal of Electronic Packaging*, vol. 137, no. 3, pp. 0310051-0310055, 2015.
- [73] S. Lotfian, J. M. Molina-Aldareguia, K. Yazzie, J. Llorca, and N. Chawla, "Mechanical characterization of lead-free Sn-Ag-Cu solder joints by high-temperature nanoindentation," *Journal of Electronic Materials*, vol. 42, no. 6, pp. 1085-1091, 2013.

- [74] V. Marques, C. Johnston, and P. Grant, "Nanomechanical characterization of Sn–Ag–Cu/Cu joints—Part 1: Young's modulus, hardness and deformation mechanisms as a function of temperature," *Acta Materialia*, vol. 61, no. 7, pp. 2460-2470, 2013.
- [75] V. Marques, B. Wunderle, C. Johnston, and P. Grant, "Nanomechanical characterization of Sn–Ag–Cu/Cu joints—Part 2: Nanoindentation creep and its relationship with uniaxial creep as a function of temperature," *Acta Materialia*, vol. 61, no. 7, pp. 2471-2480, 2013.
- [76] J. L. Hay and G. M. Pharr, "Instrumented indentation testing," *ASM Handbook, Mechanical Testing and Evaluation*, vol. 8, pp. 232-243, 2000.
- [77] K. O. Kese, Z.-C. Li, and B. Bergman, "Method to account for true contact area in soda-lime glass during nanoindentation with the Berkovich tip," *Materials Science and Engineering: A*, vol. 404, no. 1-2, pp. 1-8, 2005.
- [78] M. Cabibbo, D. Ciccarelli, and S. Spigarelli, "Nanoindentation hardness measurement in piling up SiO₂ coating," *Physics Procedia*, vol. 40, pp. 100-112, 2013.
- [79] G. J. Chou, "Microstructure evolution of SnPb and SnAg/Cu BGA solder joints during thermal aging," *Proceedings of the 8th International Symposium on Advanced Packaging Materials*, pp. 39-46, 2002.
- [80] L. Xu, J. H. Pang, K. H. Prakash, and T. Low, "Isothermal and thermal cycling aging on IMC growth rate in lead-free and lead-based solder interface," *IEEE Transactions on Components and Packaging Technologies*, vol. 28, no. 3, pp. 408-414, 2005.
- [81] R. L. Ubachs, P. J. Schreurs, and M. G. Geers, "Microstructure evolution of tin-lead solder," *IEEE Transactions on Components and Packaging Technologies*, vol. 27, no. 4, pp. 635-642, 2004.
- [82] U. Sahaym, B. Talebanpour, S. Seekins, I. Dutta, P. Kumar, and P. Borgesen, "Recrystallization and Ag₃Sn particle redistribution during thermomechanical treatment of bulk Sn–Ag–Cu solder alloys," *IEEE Transactions on Components, Packaging and Manufacturing Technology*, vol. 3, no. 11, pp. 1868-1875, 2013.
- [83] M. Maleki, J. Cugnoni, and J. Botsis, "Isothermal ageing of SnAgCu solder alloys: three-dimensional morphometry analysis of microstructural evolution and its effects on mechanical response," *Journal of Electronic Materials*, vol. 43, no. 4, pp. 1026-1042, 2014.
- [84] A. Telang *et al.*, "Grain-boundary character and grain growth in bulk tin and bulk lead-free solder alloys," *Journal of Electronic Materials*, vol. 33, no. 12, pp. 1412-1423, 2004.
- [85] S. L. Allen, M. R. Notis, R. R. Chromik, and R. P. Vinci, "Microstructural evolution in lead-free solder alloys: Part I. Cast Sn–Ag–Cu eutectic," *Journal of Materials Research*, vol. 19, no. 5, pp. 1417-1424, 2004.
- [86] P. Kumar, B. Talenbanpour, U. Sahaym, C. Wen, and I. Dutta, "Microstructural evolution and some unusual effects during thermo-mechanical cycling of Sn-Ag-Cu alloys," *Proceedings of ITherm* pp. 880-887, 2012.
- [87] P. Chauhan, S. Mukherjee, M. Osterman, A. Dasgupta, and M. Pecht, "Effect of isothermal aging on microstructure and creep properties of SAC305 solder: a micromechanics approach," *Proceedings of InterPACK*, 2013.

- [88] W. Yang, R. W. Messler, and L. E. Felton, "Microstructure evolution of eutectic Sn-Ag solder joints," *Journal of Electronic Materials*, vol. 23, no. 8, pp. 765-772, 1994.
- [89] T.-C. Chiu, K. Zeng, R. Stierman, D. Edwards, and K. Ano, "Effect of thermal aging on board level drop reliability for Pb-free BGA packages," *Proceedings of the 54th Electronic Components and Technology Conference*, pp. 1256-1262, 2004.
- [90] A. R. Fix, W. Nüchter, and J. Wilde, "Microstructural changes of lead-free solder joints during long-term ageing, thermal cycling and vibration fatigue," *Soldering & Surface Mount Technology*, vol. 20, no. 1, pp. 13-21, 2008.
- [91] S. Ahat, M. Sheng, and L. Luo, "Microstructure and shear strength evolution of SnAg/Cu surface mount solder joint during aging," *Journal of Electronic Materials*, vol. 30, no. 10, pp. 1317-1322, 2001.
- [92] W. K. Choi and H. M. Lee, "Effect of soldering and aging time on interfacial microstructure and growth of intermetallic compounds between Sn-3.5 Ag solder alloy and Cu substrate," *Journal of Electronic Materials*, vol. 29, no. 10, pp. 1207-1213, 2000.
- [93] A. Z. Akhtar, K. H. Wirda, I. S. R. Aisha, and I. Mahadzir, "Microstructure evolution at the solder joint during isothermal aging," *Proceedings of the 36th International Electronic Manufacturing Technology Conference*, pp. 1-5, 2014.
- [94] M. Berthou, P. Retailleau, H. Frémont, A. Guédon-Gracia, and C. Jéphos-Davennel, "Microstructure evolution observation for SAC solder joint: Comparison between thermal cycling and thermal storage," *Microelectronics Reliability*, vol. 49, no. 9-11, pp. 1267-1272, 2009.
- [95] W. C. Oliver and G. M. Pharr, "An improved technique for determining hardness and elastic modulus using load and displacement sensing indentation experiments," *Journal of Materials Research*, vol. 7, no. 6, pp. 1564-1583, 1992.
- [96] D. Tabor, *The Hardness of Metals*. Oxford university press, 2000.
- [97] P. Zhang, S. Li, and Z. Zhang, "General relationship between strength and hardness," *Materials Science and Engineering: A*, vol. 529, pp. 62-73, 2011.
- [98] D. Herkommer, J. Punch, and M. Reid, "A reliability model for SAC solder covering isothermal mechanical cycling and thermal cycling conditions," *Microelectronics Reliability*, vol. 50, no. 1, pp. 116-126, 2010.
- [99] G. Z. Wang, Z. N. Cheng, K. Becker, and J. Wilde, "Applying Anand model to represent the viscoplastic deformation behavior of solder alloys," *Journal of Electronic Packaging*, vol. 123, no. 3, pp. 247-253, 2001.
- [100] D. Bhate, D. Chan, G. Subbarayan, T. C. Chiu, V. Gupta, and D. R. Edwards, "Constitutive behavior of Sn3. 8Ag0. 7Cu and Sn1. 0Ag0. 5Cu alloys at creep and low strain rate regimes," *IEEE Transactions on Components and Packaging Technologies*, vol. 31, no. 3, pp. 622-633, 2008.
- [101] M. Basit, M. Motalab, J. C. Suhling, and P. Lall, "Viscoplastic constitutive model for Lead-free solder including effects of silver content, solidification profile, and severe aging," *Proceedings of InterPACK*, pp. 1-18, 2015.
- [102] M. M. Basit, M. Motalab, J. C. Suhling, and P. Lall, "The effects of aging on the Anand viscoplastic constitutive model for SAC305 solder," *Proceedings of ITherm* pp. 112-126, 2014.

- [103] Z. Cai, J. C. Suhling, P. Lall, and M. J. Bozack, "Mitigation of lead free solder aging effects using doped SAC-X alloys," *Proceedings of ITherm*, pp. 896-909, 2012.
- [104] N. J. Chhanda, J. C. Suhling, and P. Lall, "Experimental characterization and viscoplastic modeling of the temperature dependent material behavior of underfill encapsulants," *Proceedings of InterPACK*, pp. 749-761, 2011.
- [105] M. Mayo and W. Nix, "A micro-indentation study of superplasticity in Pb, Sn, and Sn-38 wt% Pb," *Acta Metallurgica*, vol. 36, no. 8, pp. 2183-2192, 1988.
- [106] M. Mayo, R. Siegel, A. Narayanasamy, and W. Nix, "Mechanical properties of nanophase TiO₂ as determined by nanoindentation," *Journal of Materials Research*, vol. 5, no. 5, pp. 1073-1082, 1990.
- [107] I. Dutta, "A constitutive model for creep of lead-free solders undergoing strain-enhanced microstructural coarsening: A first report," *Journal of Electronic Materials*, vol. 32, no. 4, pp. 201-207, 2003.
- [108] I. Dutta, P. Kumar, and G. Subbarayan, "Microstructural coarsening in Sn-Ag-based solders and its effects on mechanical properties," *Journal of Metals*, vol. 61, no. 6, pp. 29-38, 2009.
- [109] P. Kumar *et al.*, "Microstructurally adaptive model for primary and secondary creep of Sn-Ag-based solders," *IEEE Transactions on Components, Packaging and Manufacturing Technology*, vol. 2, no. 2, pp. 256-265, 2012.
- [110] P. Borgesen, "Microstructurally adaptive constitutive relations and reliability assessment protocols for lead free solder," *SERDP Project WP-1752 Final Report*, 2015.
- [111] J. Wu, N. Fu, S. Ahmed, J. C. Suhling, and P. Lall, "Investigation of microstructural evolution in SAC solders exposed to short-term and long-term aging," *Proceedings of the ITherm*, pp. 1234-1242, 2018.
- [112] D. A. Porter, K. E. Easterling, and M. Sherif, *Phase Transformations in Metals and Alloys, (Revised Reprint)*, CRC press, 2009.
- [113] R. E. Smallman, *Modern physical metallurgy*, 4th ed. Elsevier, 2016.
- [114] R. Boistelle and J. Astier, "Crystallization mechanisms in solution," *Journal of Crystal Growth*, vol. 90, no. 1-3, pp. 14-30, 1988.
- [115] Y. D. Han *et al.*, "A modified constitutive model for creep of Sn-3.5Ag-0.7Cu solder joints," *Journal of Physics D: Applied Physics*, vol. 42, no. 12, p. 125411, 2009.
- [116] G. E. Dieter and D. J. Bacon, *Mechanical Metallurgy*, McGraw-hill New York, 1986.
- [117] G. Pharr, W. C. Oliver, and F. Brotzen, "On the generality of the relationship among contact stiffness, contact area, and elastic modulus during indentation," *Journal of Materials Research*, vol. 7, no. 3, pp. 613-617, 1992.
- [118] S. Thirugnanasambandam, T. Sanders, J. Evans, M. Bozack, W. Johnson, and J. Suhling, "Component level reliability for high temperature power computing with SAC305 and alternative high reliability solders," *Proceedings of SMTA International*, pp. 144-150, 2015.
- [119] R. Darveaux, "Effect of simulation methodology on solder joint crack growth correlation," *Proceedings of the 50th IEEE Electronic Components and Technology Conference*, pp. 1048-1058, 2000.